In vivo lipidomic and metabolomic analysis of dermatosis by real-time mass spectrometry using the SpiderMass technology

Philippe Saudemont

Université de Lille

École Doctorale Biologie Santé Lille

Laboratoire PRISM Inserm U1192 | Pierre Fabre Dermocosmétique

Analyse métabolomique et lipidomique *in vivo* de dermatoses par spectrométrie de masse en temps réel par la technologie SpiderMass

Thèse de Doctorat présenté par Philippe Saudemont

En vue de l'obtention du grade de Docteur es Science de l'Université de Lille en Aspects moléculaires et cellulaires de la Biologie

Dirigé par le Pr. Isabelle Fournier,

co-encadré par le Dr. Gwendal Josse

Soutenu publiquement à Villeneuve d'Ascq, le 07 Juillet 2021.

Composition du jury :

Rapporteur	Directeur de Recherche	Philippe DUGOURD	UMR5306 Université Claude Bernard Lyon 1
Rapporteure	Assistante Professeure	Livia EBERLIN	University of Texas at Austin
Examinateur	Professeur	Marcq-Emmanuel DUMAS	Imperial College of London
Présidente du jury	Professeure	Anne MUHR-TAILLEUX	UMR1011 Université de Lille
Examinateur	Docteur	Daniel REDOULES	Pierre Fabre Dermocosmétique, Toulouse
Directrice de thèse	Professeure	Isabelle FOURNIER	Inserm U1192 Université de Lille
Co-encadrant	Docteur	Gwendal JOSSE	Pierre Fabre Dermocosmétique, Toulouse
Invité	Professeur	Michel SALZET	Inserm U1192 Université de Lille

Université de Lille

École Doctorale Biologie Santé Lille

Laboratoire PRISM Inserm U1192 | Pierre Fabre Dermocosmétique

In vivo lipidomic and metabolomic analysis of dermatosis by real-time mass spectrometry using the SpiderMass technology

A PhD thesis submitted by Philippe Saudemont

To obtain the degree of *Doctor Philosophiæ* in Molecular and cellular aspects of biology from the university of Lille

Under the direction of Pr. Isabelle Fournier

And co-supervision of Dr. Gwendal Josse

Public Defence: July the 7th, 2021 in the University of Lille

Thesis defence committee:

Reporter	Research Director	Philippe DUGOURD	UMR5306 Université Claude Bernard Lyon 1
Reporter	Assistant Professor	Livia EBERLIN	University of Texas at Austin
Examinator	Professor	Marcq-Emmanuel DUMAS	Imperial College of London
Examinator	Professor	Anne MUHR-TAILLEUX	UMR1011 Université de Lille
Examinator	Doctor	Daniel REDOULES	Pierre Fabre Dermocosmétique, Toulouse
Supervisor	Professor	Isabelle FOURNIER	Inserm U1192 Université de Lille
Co-supervisor	Doctor	Gwendal JOSSE	Pierre Fabre Dermocosmétique, Toulouse
Invited Member	Professor	Michel SALZET	Inserm U1192 Université de Lille

I stand at the seashore, alone, and start to think.
There are the rushing waves
mountains of molecules
each stupidly minding its own business
trillions apart
yet forming white surf in unison.

Ages on ages,
before any eyes could see
year after year,
thunderously pounding the shore as now.
For whom? For what?
On a dead planet
with no life to entertain.

Deep in the sea
all molecules repeat
the patterns of one another
till complex new ones are formed.
They make others like themselves
and a new dance starts.

Out of the cradle
onto dry land
here it is
standing:
atoms with consciousness;
matter with curiosity.

Stands at the sea,
Wonders at wondering: I
a universe of atoms
an atom in the universe

Excerpt from an untitled poem written in 1955
by Richard Feynman

Illustration generated using MidJourney

Table of content

Table of content 2
CHAPTER I: General Introduction 9
CHAPTER II: State of the art 15
A. Ambient Ionisation Mass Spectrometry 15
1. Generalities 15
2. Classification of AIMS techniques 18
a) Liquid extraction and/or ionisation techniques 18
b) Plasma desorption and/or ionisation 23
c) Laser ablation/desorption and/or ionisation 24
d) Alternative methods 27
B. Chronic inflammatory dermatoses 29
1. Skin structure and functions 29
a) General organisation 29
b) Immune function 32
c) Exocrine and endocrine functions 34
2. Chronic inflammatory dermatoses and lipidomic aspects 35
a) Acne Vulgaris 35
b) Psoriasis 37
c) Atopic dermatitis 39
d) Seborrheic dermatitis 41
CHAPTER III: The SpiderMass Approach 45
A. Introduction 45
B. Conclusion 70
CHAPTER IV: Proof of Concept in the veterinary environment 72
A. Introduction 72
B. Conclusion 102
CHAPTER V: Technical developments and validation studies for dermo-cosmetic applications 104
A. Introduction 104
B. Experimental procedure 105
1. Instrumental developments 105
a) *In vivo* OCT imaging 105
b) Cholesteryl palmitate standards analysis 105
c) Lanosterol QC samples preparation 105

d) Validation experiment of the statistical approach 105
2. SpiderValid clinical validation study 106
a) Study design 106
b) Absorbent paper FTIR measurement 107
c) D-squam sampling 108
d) SpiderMass setups and acquisitions 108
3. SpiderCompar clinical study on skin aging 109
a) Study design 109
b) Sample collection and measurements description 110
c) Volunteer population profile 111
4. Data analysis 112
C. Results 113
1. Instrumental development et characterisation 113
a) Sampling automation 113
b) Laser ablation depth assessment 114
c) Characterisation of the ablated material using tapes 116
d) Interface development for material injection into the MS 118
e) Cholesteryl palmitate limit of detection assessment 122
f) Quality control and reproducibility assessment 123
g) Validation of the statistical approaches 125
2. "SpiderValid": First clinical validation study 129
3. Study of the intrinsic and extrinsic aging of the skin 132
a) Forehead sebum profile 133
b) In vivo forehead profile 136
c) In vivo forearm analysis 138
D. Conclusion and discussion 143
CHAPTER VI: Study of skin chronic inflammatory dermatosis by the SpiderMass 148
A. Introduction 148
B. Experimental procedure 149
1. Volunteer population profile 149
a) Acne and CTL subgroups 150
b) AD and CTL subgroups 151
c) Psoriasis and CTL subgroups 153
d) SD and CTL subgroups 154

2. Sample collection and measurements 154
a) Trans Epidermal Water Loss measurement 156
3. Data analysis 156
a) Biometrological criteria: 156
b) Biological criteria: 156
C. Results 157
1. Acne 157
2. Atopic dermatitis 164
3. Psoriasis 168
4. Seborrheic dermatitis 171
D. Conclusion and discussion 174
CHAPTER VII: General Conclusions and Outlooks 179
Appendices 184
A. General timeline of the significant MS ionisation developments 184
A. MOLO software screenshots 184
B. SMA software screenshots 186
C. SpiderCompar 189
1. Eligibility criteria 189
a) Inclusion criteria 189
b) Non-inclusion criteria 189
2. Table of SpiderCompar study positive ions tentative annotations 191
3. Table of SpiderCompar study negative ions tentative annotations 193
D. SMPatho study 195
1. Eligibility criteria 195
a) Inclusion criteria 195
b) Exclusion criteria 197
2. Acne supplementary results 200
Bibliography 202
List of publications 214
A. Publications in this thesis 214
B. Other publications 214
Acknowledgement 216
Summary 220
Résumé 221

Affaires

AD: Atopic Dermatitis 9
AIMS: Ambient Ionisation Mass Spectrometry 15, 16, 17
AML: Anti-microbial Lipid 32
AMP: Anti-Microbial Peptide 32
ANOVA: Analyse of Variance 151
AP: Atmospheric Pressure 16
APCI: Atmospheric Pressure Chemical Ionisation 16
APPI: Atmospheric Pressure Photo-Ionisation 29
CI: Chemical Ionisation 15
CNN: Convolutional neuronal network 181
CNN: Convolutional Neuronal Network 26
CTL: Control 148
CUSA: Cavitron Ultrasonic Surgical Aspirator 29
CV: Coefficient of Variation 124
DAII: Droplet Assisted Inlet Ionisation 29
DART: Direct Analysis in Real Time 16
DESI: Desorption Electrospray Ionisation 16
DG: DiacylGlycerol 34
DICE: Desorption ionisation by charge exchange 21
EAPPI: Extractive Atmospheric Pressure Photoionisation 29
EASI: Easy Ambient Sonic Spray Ionisation 19
EESI: Extractive ElectroSpray Ionisation 19
ESI: Electrospray ionisation 15
EtAc: Ethyl Acetate 110
FC_{abs}: Absolute Fold Change 128
FFA: Free Fatty Acid 31
FFPE: Formalin Fixed Paraffin-embedded 10
FLG: Filaggrin 30
FTIR: Fourier Transform InfraRed 107
GAE: Global Acne Evaluation 151
HI: Hydration Index 110
IGA: Investigator Global Assessment 153

IGR: InterQuartile Range 158
LAESI: Laser Ablation ElectroSpray Ionisation 25
Laser: Light Amplification by Stimulated Emission of Radiation 24
LCMS: Liquid Chromatography Mass Spectrometry 37
LDI: Laser Desorption Ionisation 24
LESA: Liquid Extraction Surface Analysis 21
LI: Lipid Index 110
LMJ-SSP: Liquid Micro-Junction Surface Sampling Probe 16
LTP: Low Temperature Plasma 24
LZ: Lesion Zone 154
m/z: mass to charge ratio 15
MAI: Matrix Assisted Ionisation 29
MALDI: Matrix Assisted Laser Desorption/Ionisation 15
MOLO: Motion Control Loop 108
MS: Mass Spectrometry 9
MSI: Mass Spectrometry Imaging 17, 21
nano-DESI: nano Desorption Electrospray Ionisation 21
Nd:YAG: Neodymium-doped Yttrium Aluminium Garnet 45
NEFA: Non-Esterified Fatty Acid 31
NMF: Natural Moisturising Factors 31
NPV: Negative Predictive Value 128
OCT: Optical Coherence Tomography 26
OPO: Optical Parametric Oscillator 45
PCA: Principal Component Analysis 113
PFDC: Pierre Fabre Dermo-Cosmetic 9
PGA: PyroGlutamic Acid 31
PIRL: Picosecond InfraRed Laser 26
PLZ: Peri Lesion Zone 154
PPV: Positive Predictive Value 128
PSI: Paper Spray Ionisation 17, 22
Pso: Psoriasis 9
PTFE: Polytetrafluoroethylene 22
QC: Quality Control 105
REIMS: Rapid Evaporative Ionisation Mass Spectrometry 10, 27

RIR-LA: Resonant InfraRed Laser Ablation 45
RZ: Reference Zone 154
SAI: Solvent Assisted Inlet Ionisation 22
SBR: Signal to Background Ratio 112
SC: *Stratum Corneum* 30
SCORAD: SCORing of AD Index 152
SD: Seborrheic Dermatitis 9
SESI: Secondary Electrospray Ionisation 21
SESI: Secondary ElectroSpray Ionization 19
SSL: Surface Skin Lipids 35
TENG: TriboElectric NanoGenerator 23
TEWL: Trans Epidermal Water Loss 40
TG: TriacylGlycerol 34
TIC: Total Ion Count 112
TLC: Thin Layer Chromatography 21
TNF: Tumor Necrotic Factor 33
UV: Ultraviolet 24
VOCs: Volatile Organic Compounds 21
WALDI: Water Assisted Laser Desorption / Ionisation 26
WE: Wax Ester 34
WHO: World Health Organisation 37

Chapter I

General Introduction

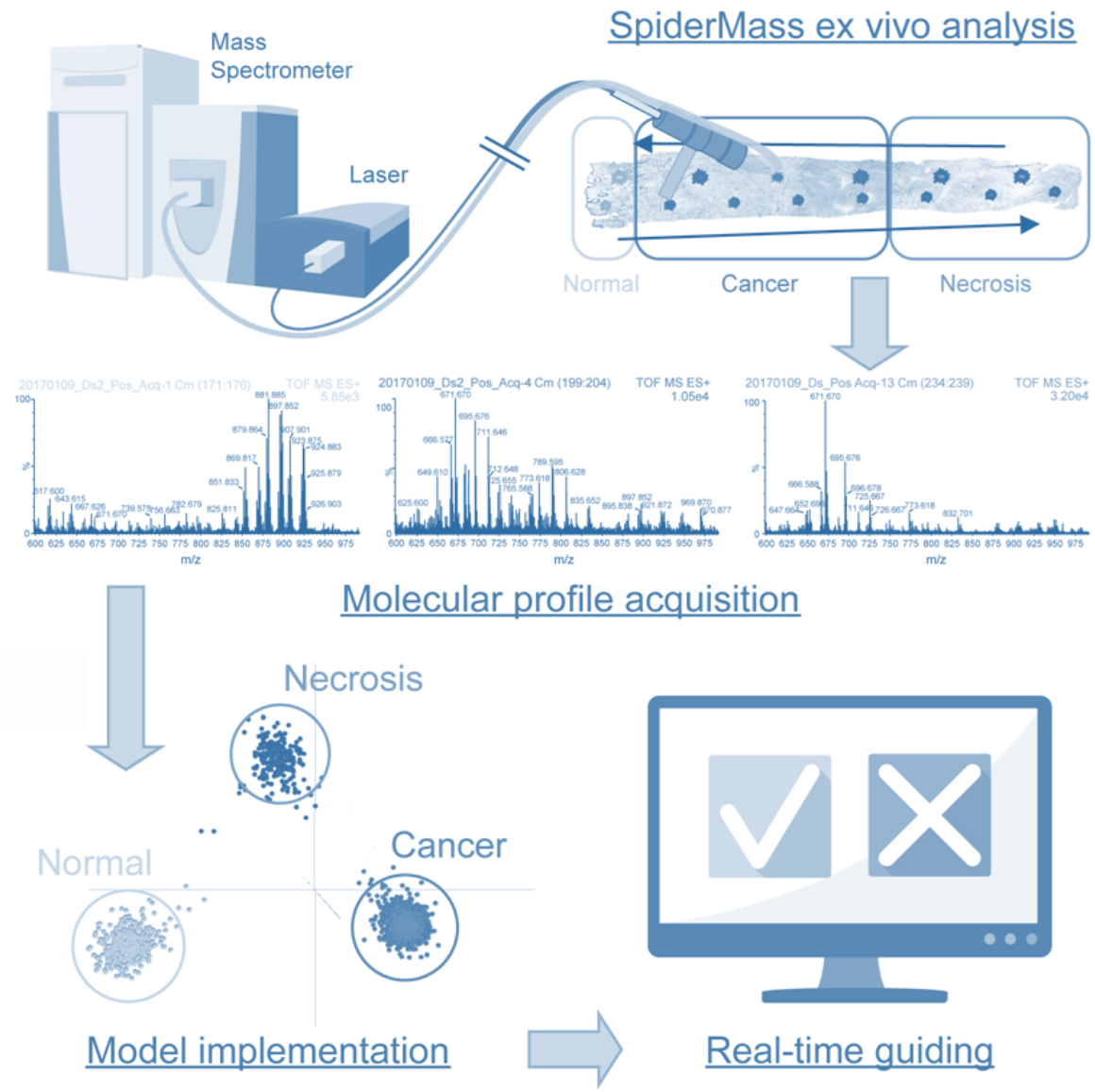

Graphical schematic showing the SpiderMass prototype and clinical analysis protocol. A series of samples are analysed *ex vivo* and used to generate a database of reference spectra, here for normal, cancerous, and necrotic tissues. These profiles are compiled to create a classification model that is used for real-time interrogation of tissues *in vivo*, reproduced with authorisation from Saudemont et al.[1]

CHAPTER I: General Introduction

Our skin is the interface between us and the surrounding, a supple barrier that has adapted for sensing, regulation, protection and immunity. First thought to be a still and inert organ, it is now seen as a dynamic and complex landscape where a lot of interactions takes place.

Acne, Atopic Dermatitis (**AD**), Psoriasis (**Pso**) and Seborrheic Dermatitis (**SD**) are chronic inflammatory skin conditions with a high incidence. According to the Global Burden of Disease 2010 study, the global prevalence of acne for all ages is of 9.38% and around 85% of young adults aged 12–25 year[2]. In France, approximately 6 million people were affected, 75% of whom were under 25 years old. On the other hand, 15-20 million people have symptoms representative of AD. It mainly targets infants (10-15%) and manifests itself from the age of 3 months[3]. Skin flora is one of the main pathophysiological factors of these two pathologies. Acne is, in fact, linked to bacterial colonisation and infection by *Cutibacterium acnes*[4] and the severity of AD is correlated with the presence of *Staphylococcus aureus*[5,6]. Psoriasis is a affects more than 60 million peoples worldwide[7]. It targets diverse area of the skin and can induce a significant decrease in the quality of life by an important psychological effect on crucial areas like the face, hands, feet, and external genitalia. Finally, SD is a chronic mycotic inflammatory dermatosis showing erythemato-squamous lesions in sebaceous areas such as the scalp, face, and some body folds. Ranked third behind AD and contact dermatitis for its potential to impair the quality of life, SD affect all ethnic groups with a prevalence evaluated around 70% in 3 month old babies, 5% in adults but increase throughout life toward 15% in older populations[8–10]. These dermatoses have an important physical and psychological impact on people explaining why it is so necessary to improve their treatment. It is one of the Pierre Fabre Dermo-Cosmetic (**PFDC**) company commitment to improve quality of life with the consumers through the development of dermo cosmetic products. The company combines pharmaceutical research and dermo-cosmetic research, with a particular expertise on plants and an expert knowledge on natural active ingredients.

Thus, PFDC is studying the physiopathological mechanisms of those dermatosis as close as possible to the pathological area to better understand their genesis and response to treatments. In a normal physiological context, the skin homeostasis is related to the balance of metabolic pathways. Natural physiological changes, such as a change in the hormonal cycle, or pathophysiological changes, cause significant molecular changes in proteins, lipids or metabolites[11–13]. It is possible to monitor such pristine physiological or pathophysiological changes in the skin by measuring variations in the associated molecular profiles. However, such monitoring requires the implementation of a technology that allows the collection of non-targeted molecular information in real time and *in vivo*.

Mass spectrometry (**MS**) has shown for many years, sensitivity, speed, versatility and reproducibility which have made it one of the most widely used technologies for the analysis of complex samples. However,

conventional MS is adapted to the analysis of extracted samples and does not allow for *in vivo* analysis. Over the last 20 years, the development of ambient sources has contributed to the rise of *in situ* analysis of unprocessed biological systems by extremely limited sampling and sample preparation, in real time, and in ambient conditions. These technical advances have made it possible to bring MS closer to *in situ* analysis by analysing living organisms, detecting pesticides on plants and fruit or detecting drug residues, gunpowder or smoke on the skin[14–18].

Classical ways to sample the skin for MS based studies are presented in **Figure 1**. The skin biopsies obtained by punching can be used for extraction or often fixed in formalin and paraffin embedded so they can be stained, imaged as a whole, or analysed more selectively by the use of laser capture microdissection. The analysis can also be conducted on skin layers obtained through suction blisters, squams collected by tape stripping or cells and subpopulations of cells can be purified by flow cytometry. But even if most of these sampling methods are interesting for routine analysis on the bench, they don't allow *in vivo* measurements.

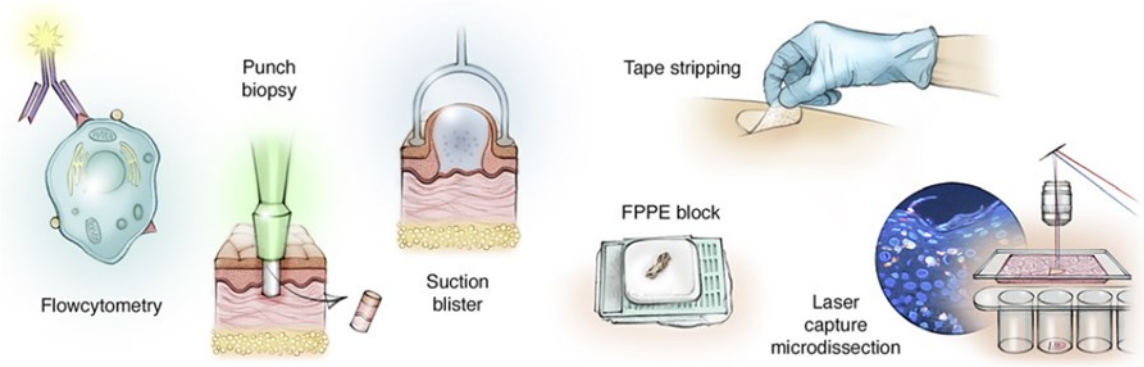

Figure 1: In dermatology, plural types of skin sampling techniques enable MS-based studies. The skin biopsies obtained by punching can be used for extraction or often fixed in formalin and paraffin embedded (**FFPE**) so they can be stained, imaged as a whole or analysed more selectively by the use of laser capture microdissection. The analysis can also be conducted on skin layers obtained through suction blisters, squams collected by tape stripping or cells and subpopulations of cells can be purified by flow cytometry. Reprinted from Fredman et al.[19] ©2021 The Authors. Published by S. Karger AG, Basel under CC BY-NC 4.0 licence

The same constraints applies to the MS techniques that are used to analyse these samples for various reasons such as safety problems caused by the use of solvents or electric currents, the invasiveness of the technique, the impossibility to analyse large 3D samples far from the MS.

The first system enabling *in vivo* patient analysis was introduced in 2009: the iKnife, which is based on the coupling of a surgical knife to MS. The iKnife uses an original ionisation mechanism termed Rapid Evaporative Ionisation Mass Spectrometry (**REIMS**)[20]. This method collects in real-time the fumes emitted by the electric scalpel used by the surgeon during an operation[20,21]. However, this technique is still very invasive, as the sample is completely destroyed during data acquisition, making cross-validation by conventional histological methods impossible[22]. Furthermore, detection is limited to metabolites and lipids in negative mode. More recently, another system named the MassSpec Pen, has been introduced by Eberlin and

colleagues[23]. This system is based on local extraction at the tissue surface by water. This is achieved by bringing a drop of water into contact with the sample for a few seconds, allowing the extraction of molecules of interest without any degradation of the sample. Then this drop content is analysed after aspiration through a tube for MS analysis.

The PRISM laboratory (Inserm U1192) has been developing an innovative tool called SpiderMass™ since 2014 to perform minimally invasive *in vivo* and real-time analyses[24]. This technology is based on biological tissues microsampling by an infrared laser (2940 nm) that does not penetrate deeply into the tissues due to the large amount of water molecules absorbing at that wavelength. The choice of this wavelength specifically excites the most intense absorption band (O-H bond stretching) of water molecules[25–27]. Thus, the endogenous water in the tissues becomes a matrix for a MALDI process. The desorption/ionisation process generated in this context has been called WALDI (Water Assisted Laser Desorption/Ionisation) to differentiate it from the traditional MALDI performed *ex vivo*. The description of the general workflow for SpiderMass analysis is described in **Figure 2**. As designed, the system offers the possibility to use the laser probe remotely, since the beam is injected into a fibre and the sampled material is sucked over several metres via a transfer line to the spectrometer. This system was initially developed to provide decision support for guided cancer surgery[24]. Indeed, the characteristic measured molecular profiles can be analysed *in vivo* and in real time by comparison with previously established classification models. They can be constructed from *ex vivo* from biopsies, in order to give an indication of the histological nature of the analysed cells[1]. Thus, it is possible to provide feedback to the practitioner on the presence or absence of remaining cancer cells at the margins after tumour removal.

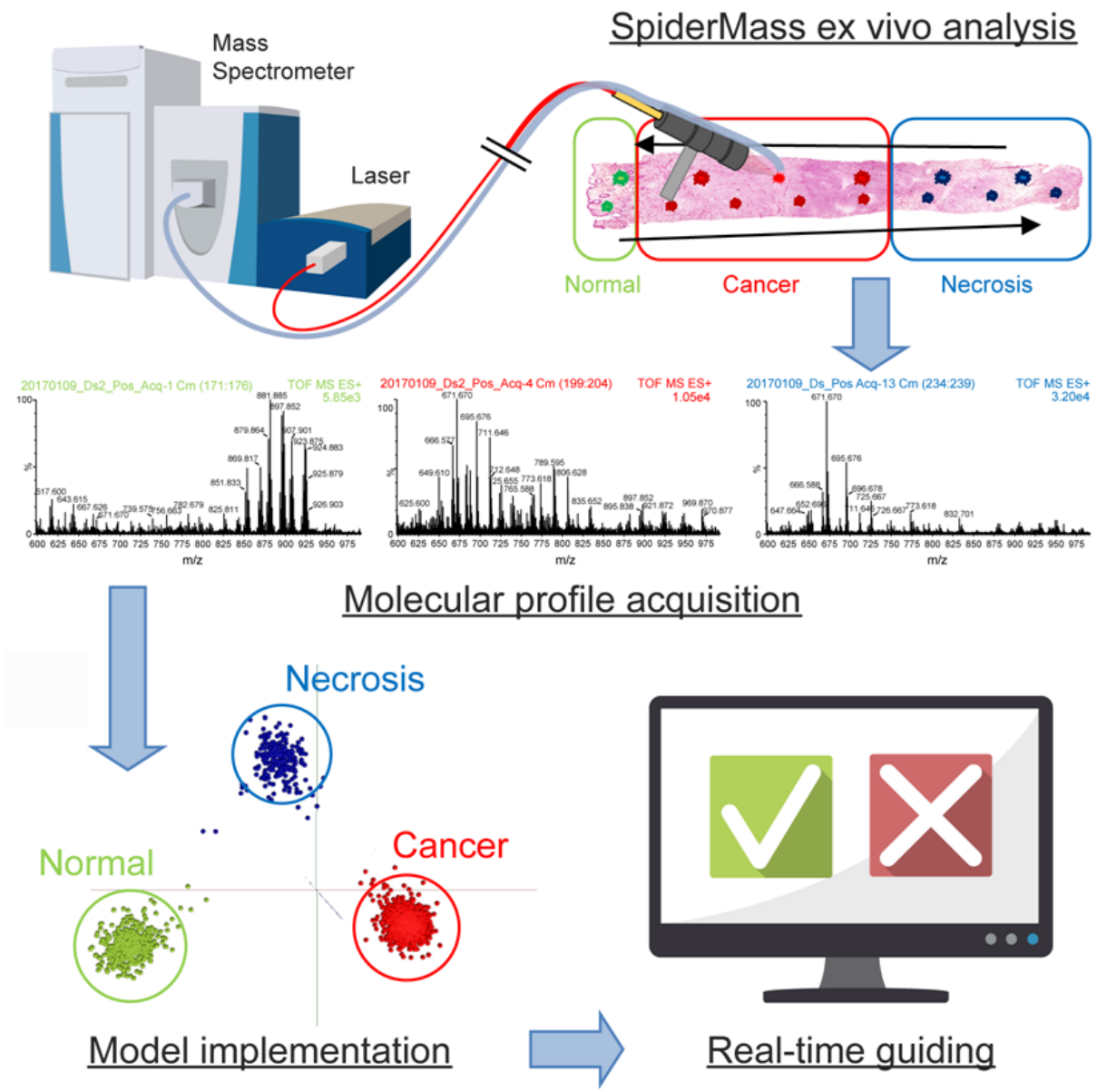

Figure 2: Graphical schematic showing the SpiderMass prototype and clinical analysis protocol. A series of samples are analysed *ex vivo* and used to generate a database of reference spectra, here for normal, cancerous, and necrotic tissues. These profiles are compiled to create a classification model that is used for real-time interrogation of tissues *in vivo*, reproduced with authorisation from Saudemont et al.[1]

The SpiderMass system is very versatile and is also of great interest for dermatology applications because of the possibilities offered by the system to conduct direct *in vivo* analysis of the human skin. Indeed, the instrument allows *in situ* characterisation without the need for biopsy or sample preparation and with a very limited invasiveness by a totally painless micro-sampling. The aim of my thesis project in collaboration with PFDC, is therefore to demonstrate the usefulness of SpiderMass in dermatology by characterising *in vivo* and in real time the physio-pathological states of the skin as well as the effect of products under development by the company.

Objectives of the thesis

The problematic of the thesis project was to provide new experimental and analytical strategies using the SpiderMass technology in the Pierre Fabre Skin Research Centre. The objectives were to characterise the skin physio-pathological states of patients suffering from Acne, AD, Pso, SD and Rosacea. This is done at a molecular level in the context of the search for biomarkers and the effectiveness evaluation of products developed by PFDC.

To this aim, the project has been divided into different specific objectives, with first a technical development phase to install and develop a dermatological compliant SpiderMass prototype, and a second phase dedicated to applications via clinical studies.

Instrumental development and technical performance of SpiderMass

The first objective of the thesis project was to further investigate the clinical potential of SpiderMass. In addition to the system's performance in oncology[1], we were able to demonstrate its interest in the study of the skin[28]. This first objective required to reproduce the SpiderMass prototype from the PRISM laboratory in PFDC Research Centre and then validating the performance of this prototype. In addition to assembling the prototype, this objective therefore included tests on known standards: sensitivity, fragmentation and effect of experimental conditions. One part also concerned the development of a data analysis workflow for quality control, as well as descriptive and differential analysis.

Bacterial typing and identification of compounds of interest by SpiderMass

A second objective was planned on the study of bacteria already known to compose the cutaneous flora as well as those playing a role in the physiopathology of acne (*Cutibacterium acnes*) and AD (*Staphylococcus aureus*). The results related to this objective have not been presented in this manuscript. Briefly, we conducted direct analysis of bacterial cultures on Petri dishes as well as on primary culture derived from skin sampling. We also started to identify commercial standard metabolite and lipid compounds using real-time fragmentation strategy.

Clinical studies

The final objective of my thesis was to test the new prototype in a clinical setup. In this phase of the project, our interest was focused on the identification of inflammatory biomarkers of Acne, AD, Pso and SD. It is indeed known in the literature that lipids such as ceramides, phospholipids, eicosanoids and arachidonic acid derivatives are bioactive compounds. They play an important role in inflammation and immunity in the skin[29–31]. These studies are closely linked to the search for active compounds from PFDC products for real-time DMPK analysis.

Chapter I

State of the Art

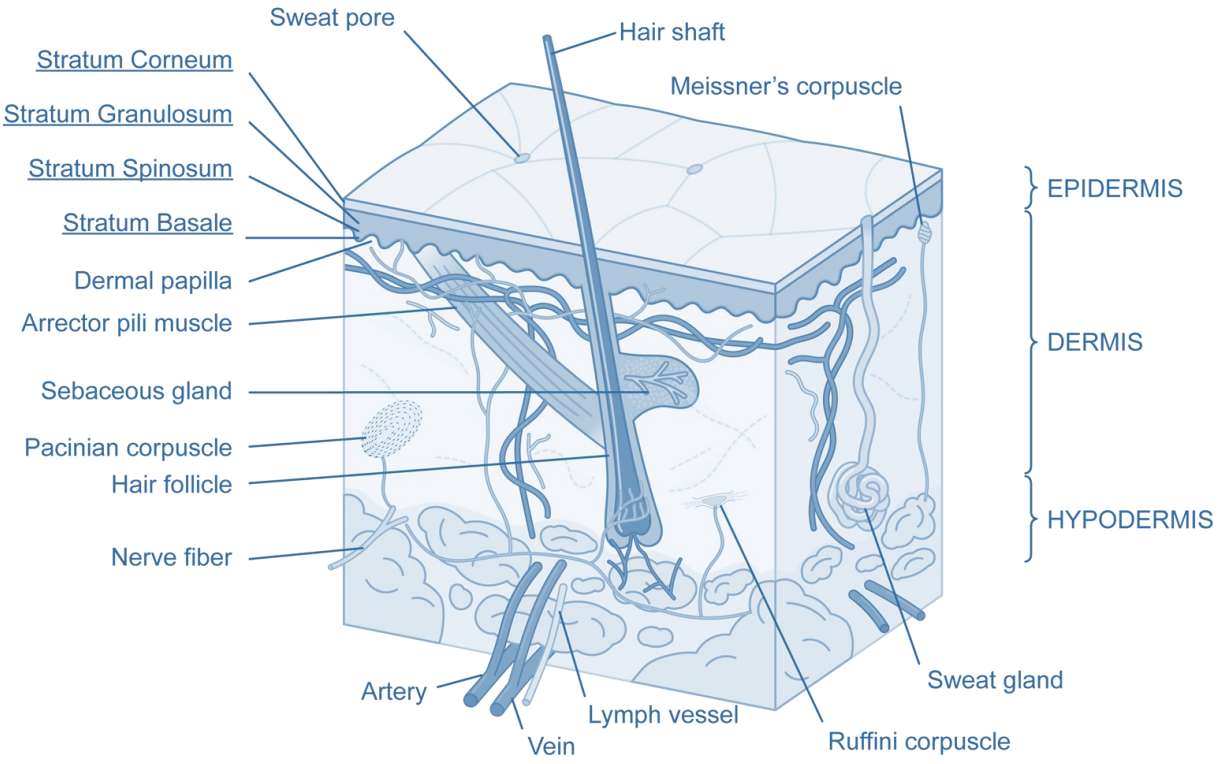

Human skin structure schematic. The most superficial layer, the epidermis is constituted by strata: the stratum corneum, granulosum, spinosum and basale as well as hairs and glands. The dermis right under contains the vessels and sensory corpuscules and is constituted by the papillary area above the reticular area. The hypodermis contains all the deep arteriovenous plexus and the subcutaneous fat. Adapted from "Human_Skin_Structure" by Tomáš Kebert, under CC BY SA 4.0.

CHAPTER II: State of the art

The state-of-the-art is divided in two main sections following the 2 main objectives of the PhD project which are 1/ related to the development of a novel ambient mass spectrometry solution and 2/ its applications to skin pathologies. Therefore, in the first part of this state of the art is dedicated to the ambient ionisation mass spectrometry (**AIMS**)) and the second part, is focused on skin pathologies with a special attention to lipidomic analysis of the skin.

A. Ambient Ionisation Mass Spectrometry

1. Generalities

MS is an analytical technique used to identify compounds of diverse origins (mineral or organic), complexity (pure or complex mixture) and sizes (ranging from single atoms to huge proteins complexes). The principle of MS is to separate gas phase ions according to their mass-to-charge (***m/z***) ratio. This is achieved in the core part of the mass spectrometer, the mass analyser, which operates under high vacuum, and uses electric or magnetic fields to separate ions. This results in a mass spectrum which reports the ion current as a function of the *m/z* ratio. The simpler configurations of the MS instrument is composed of 3 parts: the ions are created in the source, directed and separated in the mass analyser and are detected by the detector. The firsts instruments developed by Thomson and Aston in 1919 were first called mass spectrographs, measuring ions by a photographic plate or phosphor screens[32]. They are now called mass spectrometers since they measure ions by the means of electrical detectors.

As the creation of gas phase ions is required for the measurement, various developments were necessary to increase the variety of samples that could be analysed; the ionisation being a clear limiting step both in terms of analysable molecules and of sensitivity. Indeed, Electron Impact Ionisation or Chemical Ionisation (**CI**) which use collision between analytes and charged particles, respectively electrons and ions, are limited to the analysis of small molecular weight compounds (<500 u.) of limited polarity. Following methods such as plasma desorption (PDMS), Fast Atom Bombarment (FAB), or thermospray ionisation started to overcome these difficulties though they still required large concentration of rather small proteins and were presenting instrumental limitations (use of ^{252}Cf for the PDMS, large bombardment gun for the FAB).

This has been overcome by the almost simultaneous development of the Matrix Assisted Laser Desorption/Ionisation (**MALDI**) by Karas and Hillenkamp[33] and the ElectroSpray Ionisation (**ESI**) by Fenn[34]. Both MALDI and ESI provide a wide range of analysable molecules from small low polarity molecules to large and

polar ones (e.g., proteins) and have largely contributed to the general usability of MS[a]. They are nowadays the two most used technics and they have themselves been at the origin of other ion sources. For a general timeline of the major techniques developed in this part, see **Appendix 1**. One of the great advantages of ESI is the possibility to be coupled to liquid chromatography eluate allowing depth analysis of highly complex sample mixture but above all, being able to work under atmospheric pressure (**AP**). Indeed, the conventional MS analysis is at low pressure, requires the sample introduction into a confined space where high electrical fields are applied risking the sample (or instrument) to be damaged and requires sample preparation which are largely modifying the sample. For the APMS methods, like ESI or Atmospheric Pressure Chemical Ionisation (**APCI**) among others, the sample still needs to be extracted, processed, and injected in front of the MS explaining why there was a will and necessity to broaden the MS analysis to solid surfaces without extraction.

This is the exact characterisation of the AIMS field, defined by Prof. R. Graham Cooks as "the ionization of unprocessed or minimally modified samples in their native environment, and typically refers to the ionization of condensed phase samples in air"[36]. The originality comes from the possibility to conduct chemical investigations in both qualitative and quantitative ways from samples not directly suited to MS analysis. This ability has been put under general attention by the almost concomitant development of the two first AIMS methods: Desorption Electrospray Ionisation (**DESI**) developed by G. Cooks[37] and Direct Analysis in Real Time (**DART**) by Laramee, Cody and Durst[38] in 2004 not so long after the preliminary work conducted by Van Berkel and colleagues on Thin Layer Chromatography analysis by Liquid Micro-Junction Surface Sampling Probe analysis (**LMJ-SSP**) in 2002[39].

The development of these methods together with the improvement of their performance has been constant over the years. Many other AIMS techniques using different mechanisms of sampling and/or ionising the analytes have been developed since then. The main differences between the APMS and the AIMS fields are summarised in the **Table 1**.

[a] For a description of MS history focusing on the peoples making it, see « *A brief History of Mass spectrometry* », by Griffiths[35].

Table 1 : Main differences between Atmospheric Pressure and Ambient Ionisation methods. Adapted with permission from Smoluch et al.[40]

	APMS	AIMS
Ionisation space	Closed, inside the ion source	Open air
Sample state	Liquid, solid	Gas, liquid or solid
Type of analysis	Modified sample	*In situ, in vivo*
Sample preparation	Needed	Little to no
Time	Minutes to hours	Instantaneous to minutes

Indeed, for APMS the ionisation space is usually constrained inside the ion source when AIMS is done under open air, in some cases remotely from the MS. The sample state usually needs to be liquid for APMS but can be in all states for AIMS. The need to prepare the sample in APMS takes times when AIMS can run analysis *in situ* and sometimes *in vivo* with little to no sample preparation in a short to instantaneous manner.

The **Figure 3** highlights the level of interest drawn by this topic by summarizing bibliographic information on AIMS. The number of publications has increased constantly up to about 150 articles per year until 2016 and since then it reached a plateau (PubMed interrogation using "Ambient ionisation mass spectrometry" terms. Retrieved April 2nd, 2021). A publications terms network representation from Kuo et al.[41] showed the most frequently used keywords from 2592 works published between 2000 and 2019 using the search terms "Ambient Ionization Mass Spectrometry" visualized by VOSviewer. The node size varies with the frequency of usage. In this analysis, the top 4 highest frequency words were (number of occurrences in parentheses): DESI (91), MS Imaging (**MSI**, 87), DART (79), ESI (40), and Paper Spray Ionization (**PSI**, 34).

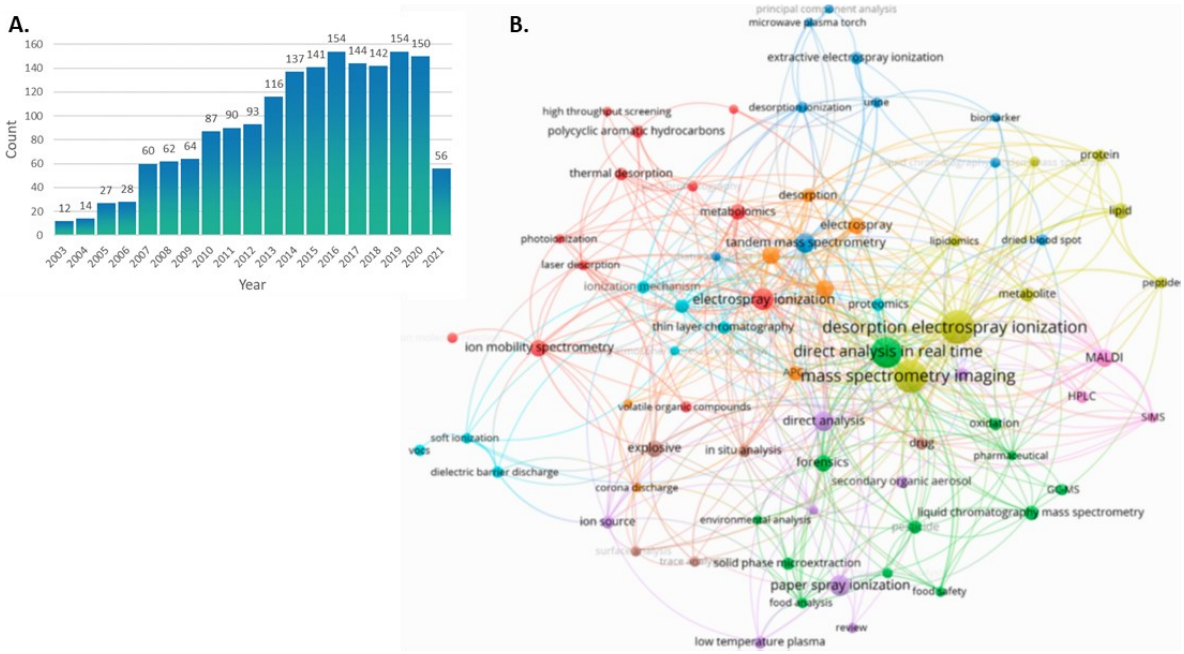

Figure 3 : Ambient ionisation mass spectrometry publications field. A. Number of publication evolution along the years since 2003 citing "Ambient Ionisation Mass Spectrometry" according to PubMed records (retrieved April 2nd, 2021). B. AIMS related publications network visualisation. The most frequently used keywords in works published from 2000 to 2019 using the search terms "Ambient Ionization Mass Spectrometry" (2592 publications, retrieved September 18, 2019) were visualized by VOSviewer. The node size varies with the frequency of usage. A minimum word frequency of 8 was required for inclusion. Reprinted with permission from "Ambient Ionization Mass Spectrometry Today and Tomorrow: Embracing Challenges and Opportunities" Ting-Hao Kuo, Ewelina P. Dutkiewicz, Jiying Pei, and Cheng-Chih Hsu. Analytical Chemistry 2020 92 (3), 2353-2363. DOI: 10.1021/acs.analchem.9b05454. Copyright 2020, American Chemical Society

2. Classification of AIMS techniques

The AIMS techniques can be classified according to the method by which the molecules are turned into the gas phase (e,g. desorption, extraction) and/or ionised. . In only a few methods the analytes are simultaneously transferred to the gas phase and ionized and most of the methods show a 2 steps approach; first extracting and then ionising[42]. In this way, three main categories of AIMS are identified: i) the Liquid extraction techniques, ii) the Plasma based techniques and (iii) the Laser related techniques. Every techniques that uses other modalities like thermal, vibrational or acoustic desorption/ionisation were grouped together as "Alternatives" according to a previous classification used by Feider et al.[43].

The following sections aim to describe the most known and used techniques for each of these groups and some of their applications. This is not intended to be a systematic review nor an exhaustive list but rather an overview giving a glimpse of the overall field and multiple ambient methods with a specific focus on AIMS that can be translated *in vivo* which was the application targeted in the project.

a) Liquid extraction and/or ionisation techniques

Derived from the ESI mechanism to obtain charged particles[34], in which a high voltage current is applied onto a liquid to create an aerosol of charged droplets leading to the transfer of those charges to the analytes,

these methods uses solvents to extract and or desorb analytes from the sample's surface. They are usually separated in 3 groups depending on the form of the solvent: 1) spray-based extraction, 2) direct liquid extraction, and 3) substrate spray. They are more suited to polar molecules even if some techniques showed a widder polarity of molecules that can be analysed.

i. Spray based methods

The main spray-based technique encompass DESI, Easy Ambient Sonic spray Ionisation (**EASI**), Extractive ESI (**EESI**) and Secondary ESI (**SESI**). With around 70 publications per year using DESI and its variations, this is the widely known and most used AIMS method. Its principle is illustrated in the **Figure 4A**: It uses an electrospray directed onto a surface to creates a thin liquid layer at the tissue surface enabling analyte extraction. Then, new colliding droplets causes secondary highly charged droplets carrying analytes to be ejected from the surface. Charged droplets travel through air into the atmospheric pressure interface corresponding to an extended ion transfer capillary toward the mass spectrometer.

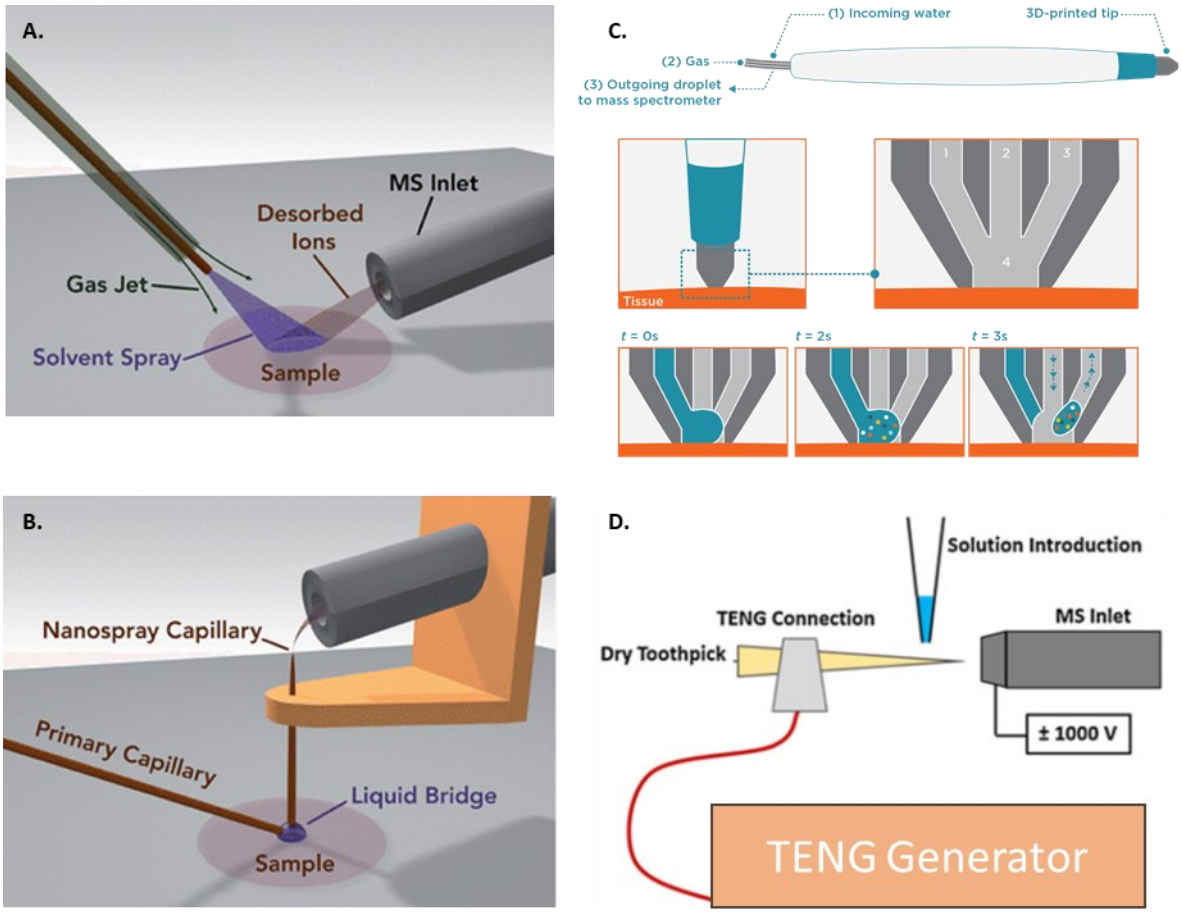

Figure 4: Liquid extraction and/or ionisation techniques. **A.** Traditional DESI: an electrospray is directed onto a surface to creates a thin liquid layer at the tissue surface enabling analyte extraction and removal from the surface. **B.** nano-DESI: a primary silicate capillary is used to bring a continuous flow of solvent onto the sample surface which is withdrawn by a nanospray needle in a liquid micro-junction manner. Adapted from Roach at al.[44] with permission from The Royal Society of Chemistry. **C.** MassPec Pen handeld probe. The pen-size device is composed of a PDMS 3D printed tip and 3 PTFE tubing: one for the incoming solvent (1), one for gas delivery (2) and one connected to the transfer tube toward the MS (3). The zoom shows the tip, its 3 channels and the dispensal of solvent, the extraction step and the aspiration to the MS. Reprinted with permission Owlstone Medical[45], adapted from Zhang et al.[23] **D.** TENG-MS: a liquid sample is loaded onto a toothpick and sprayed into the MS by applying a high current generated by a triboelectric nanogenerator. Adapted from Bernier et al.[46] under CC BY-4.0.

As in ESI, DESI seems to be relying on two distinct ionisation mechanism, depending on the molecular weight of the analytes: High molecular weight such as proteins and peptides are multiply charged indicating an evaporation mechanism during which multiple charges are transferred to the analyte during the inlet desolvation. For the smaller molecules, ionisation seems to occur by charge residue mechanism in which electron or proton charge are transferred between the solvent ions and the analytes whether each one is in gas phase or on the surface[17].

The pneumatic electrospray implies using gas, solvent and tensions each involving their own optimal parameters. The geometrical parameters between the spray, the sample and the MS are of the highest importance while running DESI experiments and induces a lot of intra-experiment, and inter-laboratory variation in the results[47]. This has largely been corrected with the introduction of commercial versions of such ion sources; initially by Prosolia (DESI 2D Omni Spray Ion Source; Prosolia, Indianapolis, IN. USA), and now by

Waters ("DESI XS", Milford, MA. USA), not forgetting the continuous improvements carried out by academic groups such as Pr. Graham Cooks laboratory at Purdue University.

Variations around DESI has led to several secondary methods such as Nanospray Desorption Electrospray Ionisation (**nano-DESI**), Reactive-DESI and Desorption ionisation by charge exchange (**DICE**). The nano-DESI principle is illustrated in **Figure 4B**: a silicate capillary brings a continuous flow of solvent onto the sample surface which is withdrawn by a nanospray needle in a liquid micro-junction manner[44]. This allows for precise surface sampling at high lateral resolution (and create molecular images i.e.). Unlike DESI the charged droplets are created without the use of a nebulizing gas. Reactive-DESI uses specific solvents or reagents, added in the spraying solution to enhance the sensitivity or to follow a reaction. A similar technique, the DICE has been developed to analyse less polar compounds in which organic solvent like toluene are used[48]. Both DESI and DICE can be coupled in the same experiment by using a tee union to mix both solvents and offer a broader range of polar compounds[49].

Alternatively, if no current or heating is applied, a neutral spray is obtained through the gas flow which can be directed against a surface. In this case, the technique is referred as EASI[50] and provides a more friendly environment for the sample on which is performed the study. Moreover, DESI is a versatile analysis modality that can be used in different contexts including *ex vivo* intraoperative analysis but it can also be used for DESI MS Imaging (DESI-**MSI**)[51].

EESI corresponds to two colliding ESI plumes. The first one with the analyte and the other one with the extractive solvent for re-extraction and post-ionisation[52]. The great feature about this method is its capability to analyse undiluted matrices like urine, milk, or polluted water for long periods of times without fooling the MS. Similar to EESI but in secondary electrospray (**SESI**), whether an ESI solvent plume or a nano spray is mixed with an incoming gas phase analyte. It has been extensively used to analyse Volatile Organic Compounds (**VOCs**) in the exhaled breath to evaluate differences in metabolic profiles of patients with cystic fibrosis compared to healthy controls[53]. This source is now commercialised as the "SuperSESI" by the Fossiliontech company (Fossil Ion Technology S.L. Albacete, Spain).

ii. Direct extraction methods

The direct extraction techniques use a direct contact to promote solid-liquid exchange from the sample surface to be analysed. First represented by LMJ-SSP[39], two coaxial capillaries were used to generate a continuous flow of solvent applied onto a Thin Layer Chromatography (**TLC**) plate. The solvent was directly sent to the MS inlet and ionised via a venturi ESI source. In Liquid Extraction Surface Analysis (**LESA**), droplets are dispensed by a pipette tip onto the tissue for discreet analysis[54]. It can be useful for spatially resolved micro extraction of samples directly sprayed in front of the MS by using an ESI nebulising chip. The extracts can be

also processed and go through liquid chromatography MS[55]. These methods were developed to enable spatially resolved analysis.

On the other hand, the MasSpec Pen developed in 2017 by Livia Eberlin's group is based on direct solid-liquid extraction performed remotely from the MS through an handled probe to allow the analysis of 3D and uneven sample surfaces[23]. An illustration of the probe is presented in **Figure 4C** and composed of three parts: a syringe pump delivering 4-10 µL of water to the sampling probe, a PolyTetraFluoroEthylene (**PTFE**) tubing integrated with valves to transport the water to and from the tissue after a 3s contact, and a pen-size device for probing the biological tissues. This system disposes a droplet of water on tissues in an extraction chamber located at the tip of the pen-like shaped hand tool. This tip has 3 channels, one for the solvent arrival, one for gas delivery and one connected to the transfer tube toward the MS. By pressing a foot pedal, the solvent is brought to the chamber, maintained in place and then sent directly into the ion transfer capillary where the solvent is vaporised in a process similar to Solvent Assisted Inlet Ionisation (**SAII**)[56] in which inlet ionisation mechanism occurs under the coincident action of pressure dropping and temperature increasing at the inlet of the mass spectrometer. The use of water as solvent allows damage-free extraction of hydrophilic and amphiphilic compounds but requires the probe to be placed in tight contact with the tissue.

The MasSpec Pen was used to analyse *ex vivo* human biopsies of breast, thyroid, ovary, lung cancer and healthy tissue or *in vivo* on mice model samples[23]. The performance of the system was evaluated for rapid diagnosis of high-grade serous carcinoma where it showed 96.7% clinical sensitivity and 95.7 % specificity[57]. Recently, the system has been coupled to a DaVinci surgical robot[58] and also used by 7 different surgeons *in vivo* and on *ex vivo* excised tissues during 100 surgeries[59].

iii. Substrate spray

In this category, the native sample or the support in which the sample is contained is used as a mean of producing the ionisation. In Paper Spray Ionisation (**PSI**) presented in 2010[60], the liquid sample is absorbed onto a triangular shaped filter paper and let to dry. At the time of analysis, a spraying solvent is pippeted, and a high tension is applied to create an electrospray between the tip of the paper and the MS inlet[60]. Interfering species from complex matrixes like salts can adhere to the paper while soluble analytes are released by the solvent and analysed, improving sensitivity and reproducibility without any sample preparation. This method has been of choice for Dried Blood Spot Analysis by MS[61] and allowed fast profiling and testing of blood biomarker. Due to the polar nature of the paper, analysis of hydrophilic compound has been challenging by PSI[62] as well as negative mode studies in which the current needed to be higher, created electrical discharges in the source at the origin of an increased instability like classical ESI[63]. Some modifications in the technique have been made for example by using a 3D printed paper holder with embedded electrodes between the paper and the MS and also creating sheath gases around the paper to better focalise and inject the ions[64].

Variation around the idea of PSI has led to the development of several methods like wooden-tip electrospray[65] presented in **Figure 4D**. Likely, a liquid sample is loaded, here onto a toothpick and sprayed into the MS by applying a high current. This has been originally coupled with TriboElectric NanoGenerator (**TENG**) in which high current can be generated by rubbing objects together (triboelectric effect), removing the necessity of a high voltage generator on the field for example[46].

b) Plasma desorption and/or ionisation

Plasma desorption and or ionisation techniques are derived from APCI, in which an electrical discharge interacts with and ionises gas molecules, which in turn ionizes gas phase analytes of interest through a series of ion–molecule reactions. Usually coupled to liquid chromatography, the gas-phase ions are often produced by the rapid vaporization of a pneumatically assisted analyte effluent going through a heating element. Plasma techniques uses the plasma discharge to desorb and ionize molecules but modified to allow the direct analysis of unprepared samples[b].

The DART was one of the first AIMS technique as explained before and is illustrated in **Figure 5.**

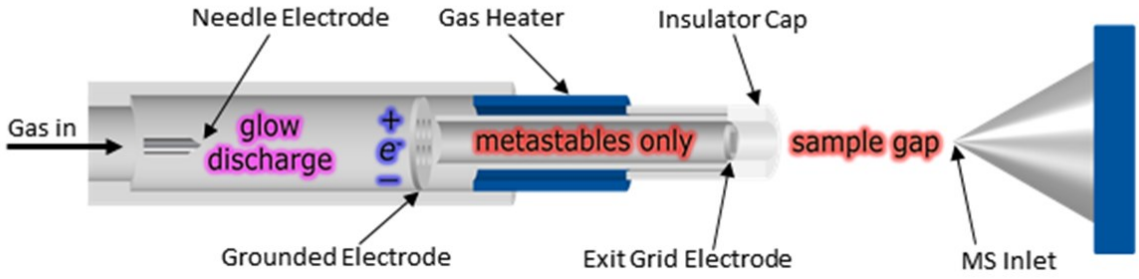

Figure 5: Schematic diagram of a DART ion source. A flux of heated gas goes through a corona needle electrical discharge and is excited into reagent ions. A grounded electrode is used to selects positive or negative species as well as metastable ions which are interacting with ambient air. The excited molecules beam is directed against the samples in front on the MS inlet, to desorb and ionize molecules from its surface. By Rbcody own work, under CC BY-SA 4.0 via Wikimedia Commons.

In these sources, a flux of heated gas like helium, argon or nitrogen goes through a corona needle electrical discharge and is excited into reagent ions. A grounded electrode is used to selects positive or negative species as well as metastable ions which are interacting with ambient air leading mostly to protonated water clusters in positive ion mode and anions radicals in negative mode through charge transfer. The beam of excited molecules is directed against the samples situated in front on the MS inlet, to desorb and ionize molecules from its surface in case of liquid and solid phase analytes. Gases and vapours are introduced directly through the source. Corona discharge techniques predominantly ionise volatile and semi-volatile molecules, for which they can be a more robust form of ionisation than SESI because does not suffer neither from solubility effects nor clogging. This source is commercialised as the "DART®" by IonSense (IonSense Inc, Saugus, MA) and

[b] For more information about the plasma based techniques, see the extensive review written by Smoluch et al.[40]

used in various situations such like forensic warfare agent and drug of abuse[66] but also microorganisms identification[67] and food safety and origin identification[68,69].

For *in vivo* measurements, some adjustments were necessary to remove the high temperature gas and plasma. To that aim Low Temperature Plasma (**LTP**)[70] was developed and allows for the plasma to be generated between two electrodes and extracted by the gas flow inside the probe. The samples are exposed to temperature around 30 °C, which prevents damage due to overheating. The plasma-based techniques allow the analysis of small molecules usually up to 1000 Da

c) Laser ablation/desorption and/or ionisation

The Light Amplification by Stimulated Emission of Radiation (**Laser**) consist of a beam of monochromatic, spatially, and temporally coherent photons named by Gordon Gould in 1959 and successfully developed by Theodore H. Maiman in 1960[71]. Laser ablation and MS have been extensively coupled for the study of condensed state matter since the very beginning of laser development by first experiments conducted as soon as the beginning of the 60s by Hönig & Woolston[72]. The great advantages of such approaches are the reduced need for sample preparation, the contactless sampling, the higher analysis rate and a controllable size of ablation with precise scanning capability of the sample surface.

When a beam of the light at the correct wavelength interact with matter, a portion of the bulk mass is removed in the form of electrons, ions, atoms, molecules clusters and particles; Each modality involving its own mechanism, separated in time and space on the ablation site[73]. In general, the three recognised steps can be described as first the laser-matter interaction, then the fast transition of the solid matter to the gas phase and finally the expansion of the ablation plume into the gas phase.[74].

Nonetheless, the first laser desorption and ionisation ("**LDI**") experiments for the direct analysis of large and fragile molecules has shown to be complex due to significant fragmentation and were challenging until MALDI was developed. It is with the introduction in 2000 of the first AP-MALDI ion sources that laser ionisation was first coupled with MS in AP conditions[75]. Using this method, the ions yield represents a clear limitation to analyse lower abundances compounds due to extensive loss of ions when working in AP conditions. There are also safety issues linked to the use of organic matrices and UltraViolet (**UV**)laser in open air. A great example of this APMS application comes from the SMALDI ion source developed by Sprengler and colleagues and commercialised by TransMIT GmbH which shows a 1.4µm lateral resolution[76].

When searching for higher ion production rate, alternative methods using post-ionisation have developed. In such technique the desorption is decoupled from the ionisation and the laser is exclusively used

to turn the molecules into the gas phase. Various configurations and ion sources have developed around this idea and a blowout of the number of different technical names[c].

However, among the most known are the Laser ablation ESI (**LAESI**) which uses a combination of laser-based technology and ESI illustrated in **Figure 6A**.

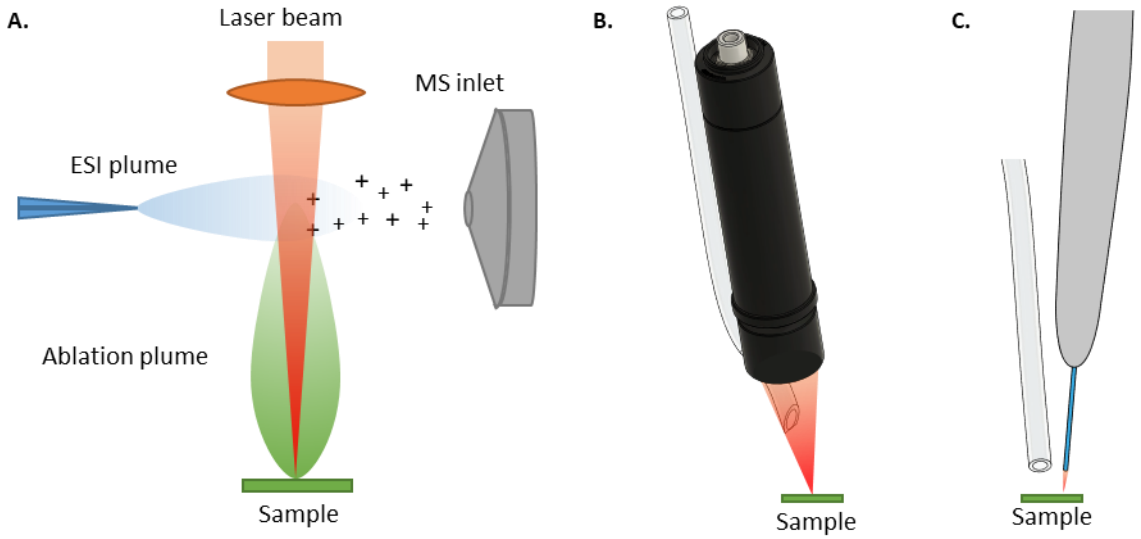

Figure 6: Schematic diagram of the discussed IR laser-based techniques. **A.** In LAESI, the laser is used to induce material ejection which is intercepted by an orthogonal electrospray. The created ions meet the neutral material and transfer the charges before entering the MS inlet. **B.** The SpiderMass handheld is focalising a ns IR laser toward the sample which is desorbed ablated/ionised and aspired toward the MS via the transfer tubing. **C.** PIRL-MS handheld probe containing the laser fibber and directed toward the sample. The same way, the ablated material is aspired toward the MS via an aspiration tubing.

In LAESI, a mid-IR laser is used to promote a soft ablation and the ablated the plume material is intercepted by a flow of charged droplets coming orthogonally which are submitted to desolvation to lead to naked analyte ions in the gas phase before entering the MS inlet[78]. In LAESI, the resolution is more limited than conventional UV-MALDI because of the diffraction limit. Nevertheless, down to 30 µm spatial resolution can be obtained by oversampling. Improvements has been done around LAESI to allow remote laser ablation in a closed ablation chamber[79] and implementation of several strategies to permits analysis of less polar compounds by using polar solvent with ESI[80] or more recently a combination of ESI and APCI[81]. A very close method is the MALDESI, in which a matrix is used to promote the absorption of the laser by the sample. Therefore, the methods were used both in the UV and IR range.

The matrix has a central role to ensure a high energy transfer by photon absorption while preventing the analytes of receiving too much energy and extensively fragmenting. However, the use of an organic matrix prevents the use of MALDI for *in vivo* applications. On the other hand, the simple LDI technique is known to have a limited analytical range and low sensitivity. Long ago in the mid-90's it was already shown that water could serve as a MALDI matrix using ice crystals as a matrix to analyze peptides[25]. Therefore, has been gradually

[c] At least 29 according to the non-exhaustive review from Ding et al.[77]

using IR-laser instead of UV and make more used of the possible resonant excitation of water molecule (most intense absorption band 2.94 µm, O-H stretching vibrational mode). Because water is present in any biological tissues (about 75%-80% in most tissues) it can be used as an endogenous matrix. This enables to avoid using organic ones which are not compatible with *in vivo* analysis. This is the concept that was exploited to develop the SpiderMass technology. By resonant excitation of water molecules, we think it is possible to recreate a MALDI process, that was coined Water Assisted Laser Desorption/Ionization (**WALDI**) to account for the differences with conventional MALDI-MS. The ionisation regime is reached above a certain laser energy with the SpiderMass for simultaneous desorption an ionisation. The WALDI bears very similar characteristics to the traditional UV-MALDI including collective effects observed when studying the variations of the laser wavelength on the signals. Indeed, we observe that in the specific 600-900 mass range, more than 90% of the signals observed in UV-MALDI MS are similar to those observed with the SpiderMass (unpublished results).

The SpiderMass has been developed in 2014 and is composed like all handheld AIMS techniques of a microsampling probe presented in the **Figure 6B**, a transfer line and a MS[24]. The laser beam is conducted to the sample by the mean of a laser fibre allowing scanning of *ex vivo* or *in vivo* complex shaped tissues. The SpiderMass system has been applied to the analysis of *ex vivo* ovarian cancer biopsies and *in vivo* human skin[24] as well as cultured cells without preparation[28]. On *ex vivo* dog sarcoma samples, the system obtained 97% correct classification rate on tumour typing and grading and was the occasion to test the system directly in a veterinary operating room[82]. These classification results has been recently processed through an innovative Convolutional Neuronal Network (**CNN**) and transfer learning approach to decrease the pre-processing steps and improve the classification results[83]. It has shown great interest in the analysis of unprepared FFPE samples (publication under review) and is now coupled to a small robotic arm with 6 degrees of freedom for 3D topographical imaging of tissues surfaces (publication under review). The current system limitation comes from technical aspects regarding the fibre brittleness, signal reproducibility, and evaluation on an important cohort sample.

More recently, Zarrine-Afsar and colleagues presented a shorter impulsion IR laser in the picosecond range named Picosecond InfraRed Laser (**PIRL**) are of interest because in the shorter impulsion regime (picosecond rather than nanosecond) thermic effects are decreased explaining why it was first used as a way to ablate biological matrices in a heatless manner[84] and then like an ultrafast way of atomizing samples and extracting proteins by Desorption by Impulsive Vibrational Excitation PIRL-DIVE[85]. It has been then used directly coupled to MS by the mean of an optical fibre in a handheld probe presented in the **Figure 6C**, a transfer tubing and a heated MS inlet for the analysis of human medulloblastoma murine xenograft[86] and intraoperative identification of medulloblastomas[87]. Developments have been done on the coupling of PIRL MS with polarimetric information[88], Optical Coherence Tomography (**OCT**)[89], and DESI-MSI[90] as well as displaying the MS classification information on a video feed of the analysed sample in an augmented reality manner[91].

However, picosecond lasers yet remain expensive and challenging regarding the fibering due to the peak energy for the injection into the fibre. It is known that the laser pulse duration influences the laser penetration and the material ablation threshold, as well as the thermal propagation in the tissue. Indeed the "colder" irradiation of PIRL-MS allows for less thermal damages on the tissue but also has the drawback to have less ion production yield[88]. During the ns laser ablation, the plasma is created during the pulse duration, and the pulse itself serves to reheat the plasma, thus decreasing the size of the ablated particles[92]. However, the yet used PIRL system uses a laser of a few hundred picoseconds which is only 10 times shorter than the SpiderMass picosecond laser. To date, it is not clear from the publish data if one of the lasers has better performances in terms of analytical sensitivity and how the thermal effect might affect the ionisation through the ion yields.

d) Alternative methods

Other ways to provide energy to a condensed phase material to vaporise it can be used such as vibrations or heat. The more represented method falling in this category is the Rapid Evaporative Ionisation Mass Spectrometry (**REIMS**) published for the first time in 2009 by Zoltán Takáts group[20]. The idea is to heat the tissues at a molecular evaporation rates comparable to the rate of decomposition, which leads to the creation of a huge quantity of gaseous molecules or molecular ions. The high electrical current induces dissection by Joule heating, and by its characteristic radiofrequency alternating current, intensive electrical discharges are created in the tissue creating ionized water molecules which raises the possibility of another ionisation mechanism involving neutral desorption and chemical ionisation in the gas phase[20]. The potential mechanism of tissue evaporation includes rapid boiling of the water followed by denaturation and precipitation of the proteins, membranes disintegration and formation of aqueous droplets loaded with cell debris. The most represented ions in REIMS are singly charged lipids, most abundant in the 600-1000 *m/z* mass range for eukaryotic tissue and additionally in the *m/z* 1100-1500 mass range in case of bacteria in form of lipid dimers or cardiolipins[93]. The use of electrical dissection surgery tool and MS has been called iKnife for intelligent knife and is presented in **Figure 7A**.

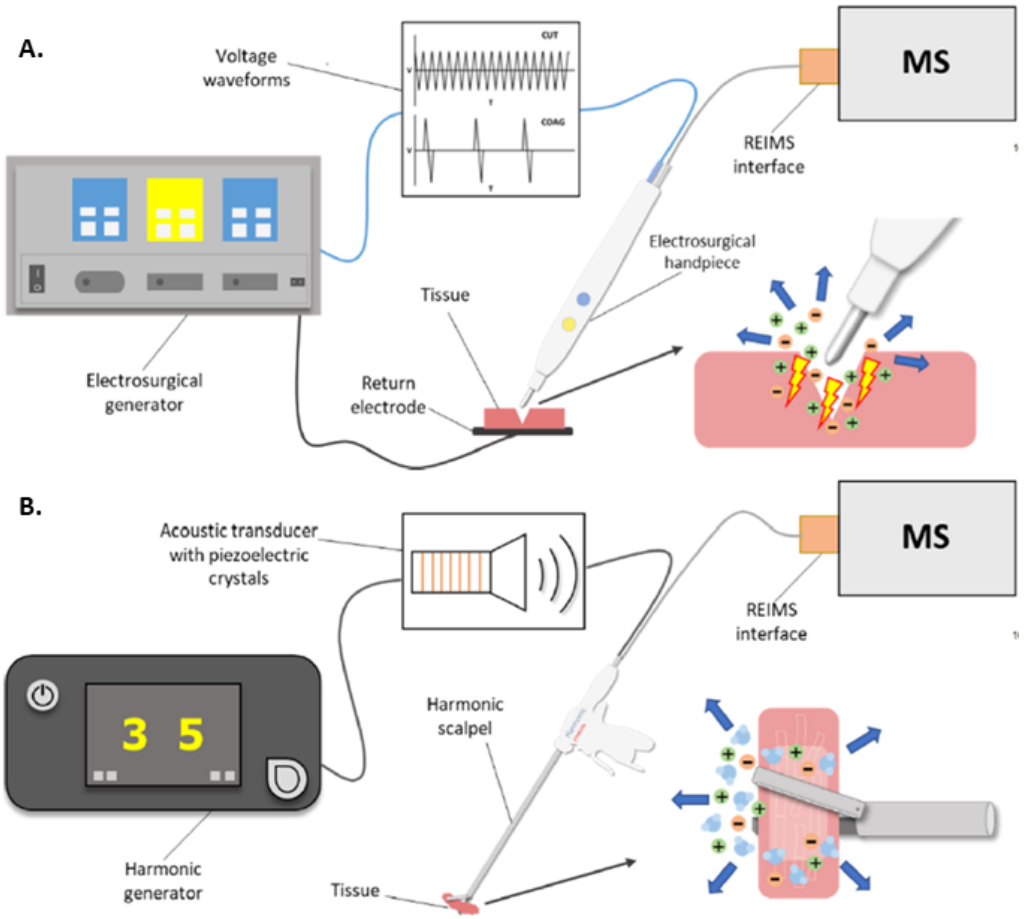

Figure 7: Alternative AIMS method using surgical tools. A. The iKnife uses a surgical scalpel also called electrosurgical handpiece already used for electrocauterization to generate fumes and creates ions that are aspired toward the MS through the REIMS interface. B. The newly presented harmonic scalpel uses ultrasounds to dissect and coagulate the tissues. Adapted from Manoli et al.[94] under CC BY-4.0

This tool was already routinely used for tissue cutting and electrocauterization of tissues, which is in fact the major disadvantage of this technique as several hundredth of microns are affected by thermal degradation around the site of sampling, making cross-validation of the results quite complex.

This technology has been successfully used in a wide number of applications from bacteria and cell line characterisation[93,95], food safety[96–99], to extensive tissue analysis in clinical or surgical situations[20,22,100–102]. Indeed, it has been effectively used *in vivo* on 198 patients and allowed for the identification of malignant, borderline and normal tissues derived from ovary[102] as well as in breast conserving surgery, on 72 patients distinguishing stromal tissues and tumour[103] or in 87 patients applied to cervical disease[104]

Last developments around the REIMS mechanism brought the implementation of an Ultrasonic Harmonic Scalpel coupled to MS illustrated in **Figure 7**. Interestingly, comparison with electrosurgical dissection, showed signal differences with the electrosurgical system notably in the phospholipid region of *m/z* 600–1000. Within the Harmonic REIMS spectra, diglycerides and triglycerides were abundant contrasting to the high abundances of glycerophospholipids previously observed[94].

Other vibrational processes have also been used as means to vaporize samples prior to post-ionisation and MS injection. For example, in extractive atmospheric pressure photoionisation (**EAPPI**), an ultrasonic wave is used to create an aerosol from a liquid phase sample, leading to gas-phase molecules production. The analytes are then drawn to the MS inlet and ionised by Atmospheric Pressure Photoionisation (**APPI**)[105]. In this modality, high energy UV photons are used to ionise gas-phase ions and is better suited for weakly polar and non-polar compounds. A hand-held probe for intraoperative MS analysis has been developed by using Cavitron Ultrasonic Surgical Aspirator (**CUSA**) has been used combined to EASI ion source on *post-mortem* and *ex vivo* human samples including astrocytomas, meningiomas, metastatic brain tumours, and healthy brain tissue[106].

Some other techniques rely on the post ionisation of analytes by direct introduction in the MS inlet. For example, in Matrix Assisted Ionisation, (**MAI**), the sample is mixed and co-crystallised with a matrix and placed in close vicinity to the MS vacuum region inducing the analyte/matrix sublimation and subsequent ionisation[107]. In SAII or Droplet Assisted Inlet Ionisation (**DAII**), the analytes are dissolved in a solvent and brought in the entrance of the MS respectively as a liquid flow[56,108], or droplets[109]. The simultaneous effect of temperature increasing and pressure dropping ease the sample vaporisation and ionisation. It is possible that all the previously described techniques rely to a certain extent, on such mechanisms of ionisation as soon as the analytes is still complexed with solvent or matrix when entering the MS.

The field of AIMS development and even more specifically, of clinically implementable techniques, is extremely active which shows its maturity to be translated[d].

B. Chronic inflammatory dermatoses

1. Skin structure and functions

a) General organisation

The skin is a multi-faceted organ with a wide variety of aspects and functions. As an interface with the outer world it maintains what's inside within and keep what's foreign outside. It is a barrier against microorganisms and viruses, UV light, chemicals, and mechanical injury but also a place of exchange with temperature and water releasing into the environment, essential to maintain homeostasis. Indeed, it is also a sensory organ allowing us to experience the world and communicate in reaction to environmental changes and emotions. The skin is the second largest organ in the body after the surface represented by the small

[d] For reviews of the MS technology aiming at being implemented in the clinic and during surgery, the reader is referred to the recent article from Zhang et al.[110] and Ogrinc et al.[111]

intestine: in adults, its surface area is between 1.5 and 2 m². Its total weight is between 2 and 3 kg. Its thickness can vary from 0.5 mm at the eyelids to 4/5 mm at the top of the back or palmoplantar areas.

The skin is constituted by three layers: the epidermis, the dermis, and the hypodermis. The general human skin structure is detailed in **Figure 8.**

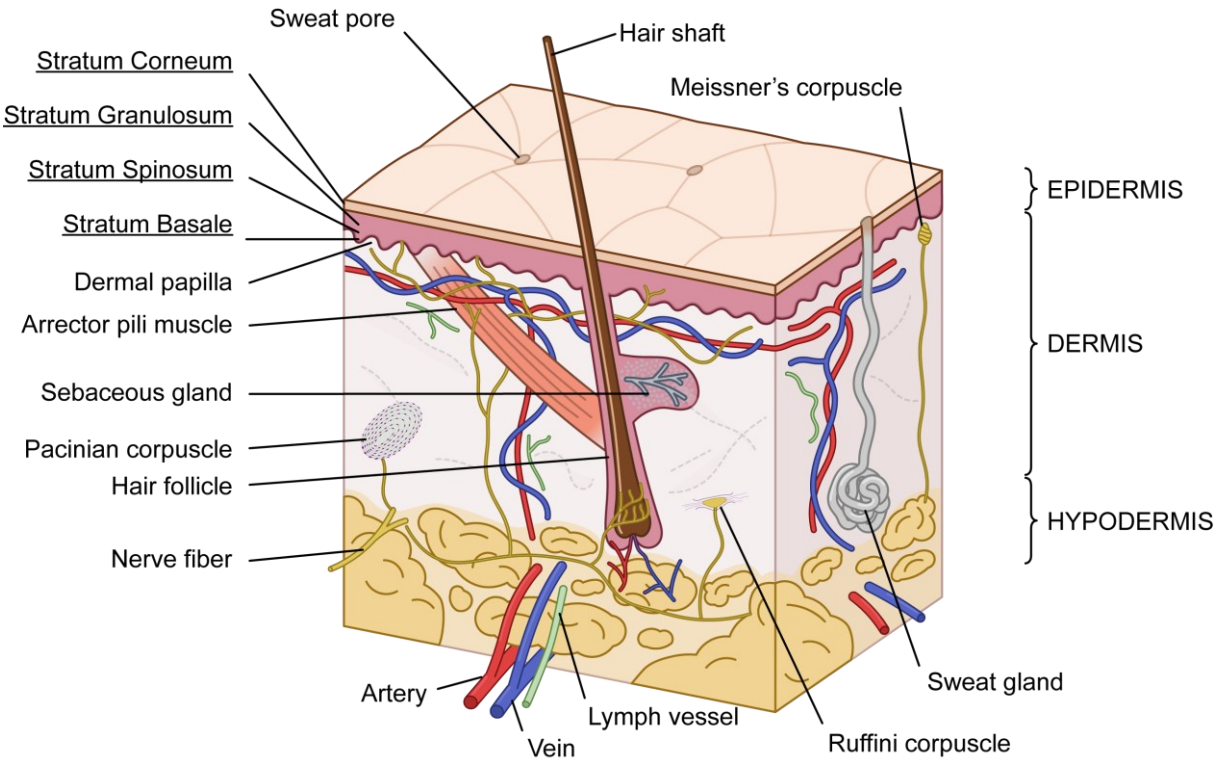

Figure 8: Human skin structure schematic. The most superficial layer, the epidermis is constituted by strata: the stratum corneum (**SC**, granulosum, spinosum and basale as well as hairs and glands. The dermis right under contains the vessels and sensory corpuscules and is constituted by the papillary area above the reticular area. The hypodermis contains all the deep arteriovenous plexus and the subcutaneous fat. Adapted from "Human_Skin_Structure" by Tomáš Kebert, under CC BY-SA 4.0.

i. Epidermis

The epidermis is the most superficial part of the skin leading to the creation of the horny/cornified layer. With a thickness around 100 µm, it varies greatly depending on the region of the body. It bears no blood vessels and cells as far as 400 µm in depth relies almost completely by the diffused oxygen from the surrounding air[112].

The cells making up the epidermis are keratinocytes, Merkel cells (sensory cells), melanocytes, and Langerhans cells (immune cells). The keratinocytes multiply at the *stratum basale* in contact with the dermis and are gradually pushed toward the surface, i) manufacturing proteins like keratin, and filaggrin (**FLG**), ii) collecting melanin from the melanocytes, and iii) secreting lipids by the form of lamellar vesicles.

Keratin is a fibrous structural protein arranged in filaments protecting epithelial cells from mechanical and non-mechanical stresses. FLG is one of the major intermediate filament-associated proteins aggregating

to keratin and then crosslinked to lipids contributing to the interwoven lipid/protein matrix, holding the cell bricks together in a brick and mortar manner[113]. In addition to its structural role, FLG is slowly degraded by proteases to release hygroscopic amino acids such as trans-urocanic acid and pyroglutamic acid ("**PGA**")[114]. They form the so-called Natural Moisturising Factors (**NMFs**) essential for epidermal barrier integrity, pH balance and help to keep the epidermis hydrated[115]. The keratinocytes finally lose their nucleus and die in the upper part, forming the desquamating horny layer. The hair follicles and skin glands are derived from the epidermis but are deeply embedded in the dermis.

The second constituent of the brick and mortar system are the lipids constituting the SC that are secreted by the keratinocytes through the lipid lamellae which are mainly constituted of ceramides, cholesterol, and Free Fatty Acids (**FFA**) also called Non-Esterified Fatty Acids (**NEFA**), of which ceramides represents approximately 50% by weight[116]. The latter are of critical importance as they are the lipids being bound to the **FLG**.

The general organisation of the epidermis is at the origin of several physiological gradients considered to be functionally important for the maintenance of an effective skin barrier. Indeed, as shown in the **Figure 9**, the water content of the skin is lowering (from 70% to 15%) at the SC junction because the proportion of lipids at that junction is increasing with retain water. At that location, the increased liberation of FFA is lowering the pH which helps in maintaining the immune functions. Finally, there is also a Ca^{2+} gradient which accumulates and induces the keratinocytes differentiation[117,118].

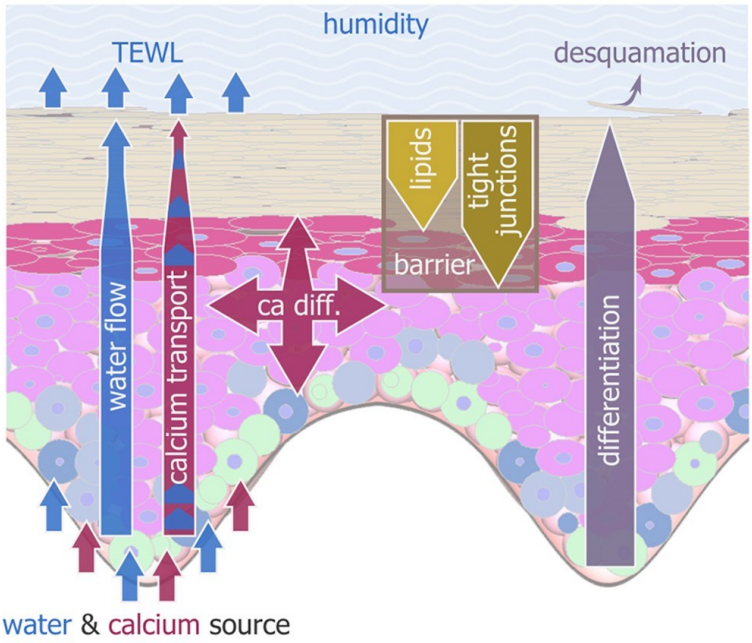

Figure 9: General organisation of the epidermidis and physiological gradients helping in preserving its functions. The epidermal barrier slows down the TEWL, calcium flow and water flow, leading to calcium accumulation and the corneocytes differentiation. Adapted from Sütterlin et al., under CC BY-SA 4.0.

ii. Dermis

The dermis is right under the epidermis and consists of two layers of connectives tissues: The papillary layer in close contact and composed of loosed connective tissue and the reticular layer thicker and composed by a dense connective tissue made mainly by collagen fibres. Running through the dermis, a huge quantity of blood capillaries can ensure more than needed for skin nutrition but can serve as a body temperature control system. In the dermis are located numerous mechanoreceptors allowing the skin to inform the brain continuously about pressure (Pacinian's and Meissner's corpuscle) and touch (Ruffini's corpuscles). These are mainly located in the superficial dermis, but free nerve endings extend through the epidermis to the surface of the skin to sense pain, heat, and cold.

iii. Hypodermis

The last layer to be descripted is the hypodermis constituted mainly by a layer of fat underlying the skin, responsible of attaching it to the muscles and bones as well as providing cushioning and thermal isolation.

b) Immune function

Although the main function of the epidermis is to synthetise the horny layer, it has a preponderant immunological function by innate and adaptive mechanisms.

i. Innate immune response

The innate response is driven by physicochemical parameters such as desquamation, sweating, the acidic pH, and a low abundance of nutrient at the skin surface. The natural pH at the surface of healthy skin ranges from 4.5 to 5.4[119] and it is known that In several skin conditions where the microbiome is altered, including acne, AD, and Pso, the surface pH of the skin is increased[120,121]. Moreover, it has been shown that a topical application of an acidic water in oil emulsion accelerated the barrier recovery and integrity in aged skin, confirming the role of skin pH in several situations[122]. On another hand, the innate immune response is also supported by the keratinocytes production of a wide range of compounds such as simple inorganic molecules (i.e peroxidase and nitric oxide), complement proteins, C-reactive proteins, antimicrobial peptides (**AMP**) including defensins and cathelicidins, and antimicrobial lipids (**AML**) including certain fatty acids and long-chain bases (sphingosine derivative)[123].

Most of the AMPs can directly kill pathogens, whereas some act indirectly by modulating the host system response. They have a great interest against the increasing development of antibiotic resistance and to access microorganisms directly inside biofilms. The keratinocytes can also synthetise cytokines and it has been recently demonstrated that there is a differential expression of AMP and cytokines across the different

epidermal layers: AMP such as human beta-defensin (hBD)-2 and -3 were more expressed in the outermost epidermal layers, and the main expression of pro-inflammatory cytokines like IL-1β and IL-6 occurred in the deepest parts of the epidermis[124]. The AMPs are positively charged and can interact with the negatively charged phospholipids & lipopolysaccharides or teichoic acids respectively from the Gram negative and Gram positive bacteria[125]. The most abundant AMP at the skin surface are β-defensins and cathelicidin LL-37. Another effective molecule is the lysozyme discovered by Alexander Fleming in 1922[126], found in the external parts of the epidermis in the keratinocytes secreted lamellar bodies and is able to kill Gram-positive bacteria by hydrolysing linkages between N-acetylglucosamine and N-acetylmuramic acid in the peptidoglycan in the cell wall[127]

Cytokines are mostly represented by Interleukins, tumour necrosis factor (**TNF**) and promote the recruitment and differentiations of local or circulating immune cells. After an acute barrier disruption there is an increase in the epidermal expression of TNF, IL-1 and IL-6[128,129]. The acute response seems to be crucial for skin barrier repair but if the disruption is prolonged a chronic increase in cytokine production occurs, potentially having an harmful effect conducting to inflammation and epidermal proliferation[130]. The permeability disruption, epidermal hyperproliferation and inflammation is well known in several diseases like AD and Pso and is thought to induce flares and increase the severity of the diseases.

The fact that lipids of the skin could have an antimicrobial activity has long been described[131] and after a long period of uninterest are now recognised as functioning along with antimicrobial peptides in innate immunity. AMLs comes from epidermal and sebaceous origins, showing activity against bacteria, viruses, fungi, and parasites[132]. The epidermal derived AMLs, the sphingoid bases are long chain amino alcohols synthesised in the epithelium made of a hydrocarbon chain, hydroxyl groups, and an amine group making them amphipathic molecules. Sphingoid bases (also called “long chain bases”) are represented by sphingosine, dihydrosphingosine, and 6-hydroxysphingosine. The host derived sebaceous AMLs are produced by the skin microbiota and consists of FFA between 7-22 carbon. Amongst them, sapienic acid (C16:1Δ6), lauric acid (C12:0), and oleic acid (C18:1Δ9), shows the strongest antibacterial and anti-inflammatory properties and strongly stimulate the innate antibacterial defence of the skin[133,134]. The FFAs generated within the epidermis are long 20-28 carbon with no described antimicrobial activity so they are not to be confused with the ones secreted in the sebum. These AML lipids are acting by the destabilisation and following disintegration of the bacterial membrane without affecting the host cell walls. Lipids may also accumulate in the cytoplasm and interact with protein components inhibiting enzymes, bacterial respiration, and synthesis[135]

ii. Adaptive immune response

Represented by the dendritic cells of the skin, the Langherans cells are very important in the process of antigen presentation and are a link between innate and adaptive immune systems. They are observed in all

layers of the epidermis but are more prominent in the stratum spinosum and in the papillary dermis. They serve as sentinels directly sensing microorganisms and pro-inflammatory cytokines, then engulfing pathogens and presenting antigens in the lymph nodes.

The organisms living on our skin such as mites, fungus, viruses, and bacteria have adapted to the harsh conditions found on the surface of the skin. Together with immune cells and keratinocytes, the skin bacteria are participating in the correct skin barrier[136]. They are mostly non-pathogenic and able to produce molecules inhibiting the colonisation of other microorganisms and their behaviour. The epidermal surface and outermost layers are hosting most of our normal flora which varies a lot based on the body regions. The human body can be divided in 3 microbiomes: dry (legs and arms), moist (axilla, perineum, feet), and oily (head, neck, trunk). The most represented bacteria are the S*taphylococci (S. epidermidis*, *S. aureus)*, *Cutibacteria (C. acnes)*, *Corynebacteria*, *Streptococci*, and *Candida*. There is a self-regulation of the human skin microorganisms creating a balanced microflora. For examples*, C. acnes* produce lipases that hydrolyse the sebum lipids, releasing FFAs and DiacylGlycerol (**DG**). Along with propionic acid, which is a fermentation product, they acidify the skin surface creating conditions not favourable for colonisation by pathogens[137].

When this balance is modified, overgrowth and dysbiosis can be seen leading to infection and dermatosis. For example, there is a known effect of antibiotics on the intestinal and skin microbiota, leading to an overgrowth in some yeasts. This can lead to anogenital or inguinal candidosis by secondary colonisation[e].

c) Exocrine and endocrine functions

The skin has an endocrine role as it is producing hormones which are released in the circulation and are important for functions in the entire organism. A large proportion of sex hormones are produced in the peripheral tissues like the skin dermis and hypodermis while the epidermis is the only site for cholecalciferol production by the keratinocytes which transforms the cholesterols precursors into vitamin D under the action of heat and UV-B[140].

The exocrine function of the skin is represented by the sweat and sebum productions respectively by the sweat and sebaceous glands. The sweat is used as a key thermoregulatory component but present also antimicrobial compounds like cathelicidins[141].

The human sebum is produced by the sebaceous glands mostly attached to the hair follicles which makes it unevenly distributed across the body, to the “oily” regions. It is composed of a mixture of lipids mainly triglycerides (45%), wax esters (**WE**, 25%), squalene (12%), FFAs (10%), cholesterol and esters (4%), and DG (2%)[142,143]. The triglycerides (**TG**) are extensively hydrolysed by bacteria before reaching the skin surface, so

[e] For more information on the skin microbiota, the reader is referred to the excellent reviews of Byrd et al.[138], Cundell[136], and Flowers & Grice[139].

that about a third of the surface skin lipids (**SSL**) consists of FFAs. The WEs and squalene are compounds specifically found on the skin.

Squalene is a cholesterol precursor rapidly converted in most of the tissues, but not in the skin where it is highly accumulated. By getting peroxidised, it is able to neutralise the UV induced reactive oxygen species[144]. The modification of the squalene peroxide level has been described in several skin conditions in seborrheic dermatitis i.e[145].

The sebum flows around the hairs and covers the skin helping in lubrication but also delivers glycerol and vitamin E providing hydration, elasticity and antioxidant protection[146,147, f].

2. Chronic inflammatory dermatoses and lipidomic aspects

As our skin is an interface and a barrier, dermatosis are often the results of our interactions with the environment and mainly our microbiota. In a general manner, there are predisposition factors, triggering events and biological responses leading to the clinical observations but also significant molecular changes in the immune response and epidermal and sebum composition[149].

a) Acne Vulgaris

Commonly named “acne”, this dermatosis is linked to a disorder of the pilosebaceous apparatus and takes the form of lesions at the surface of the oiliest regions of the body and is characterised by a sebum hypersecretion. The onset of acne correlates with the adolescence arrival, when sebum production increases at puberty and decrease at the beginning of adulthood[150]. A recent meta-analysis by Heng & Chew on 35 recent review evaluated a strong association between acne and several factors like family history, age, sexes, BMI and skin type but less associated and inconsistent results for other factors like smoking and dietary factors[151]. It has been proposed that in acne predisposed skin, there could be a subclinical inflammation level related to modification of the pH skin surface leading to microorganisms stimulated production of pro-inflammatory cytokines which conduct to inflammation and lesions[120].

The different lesions states are presented in the **Figure 10** and are caused by an increased and altered sebaceous production associated with an hormonal microenvironment dysregulation, aberrant differentiation and hyperkeratinisation of the follicular epithelium leading to inflammation and dysfunction of the innate and adaptive immunity. The pilosebaceous unit is impaired and clogs leading to the transition from a normal follicular canal to micro-comedones, comedones and finally inflammatory lesion namely papule and pustules[152].

[f] For more information on the skin lipids in health and diseases, the reader is referred to the recent review of Knox & O’Boyle[148].

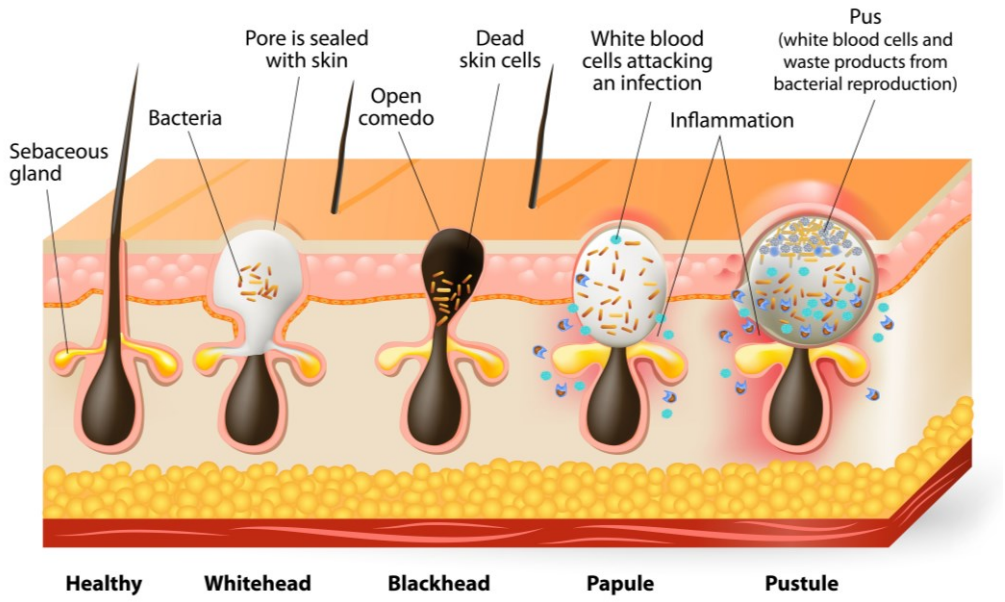

Figure 10: Illustration showing the different types and / or stage of acne lesions. The blackhead is an open air comedo consisting of a plug of dead skin cells and sebum. The whitehead is a small and sealed lesion which becomes a papule and a pustule depending on the lesion invasion by immune cells. From "Type of acne pimples" by Designua[153].

The **Figure 11** displays photographs obtained during the SMPatho study of two different acne profiles. In panel **A.** we can see a patient with an inflammatory profile and papule lesions showed by white arrows and in panel **B.** there is another patient presenting a highly retentional profile with mostly blackheads showed by black arrows.

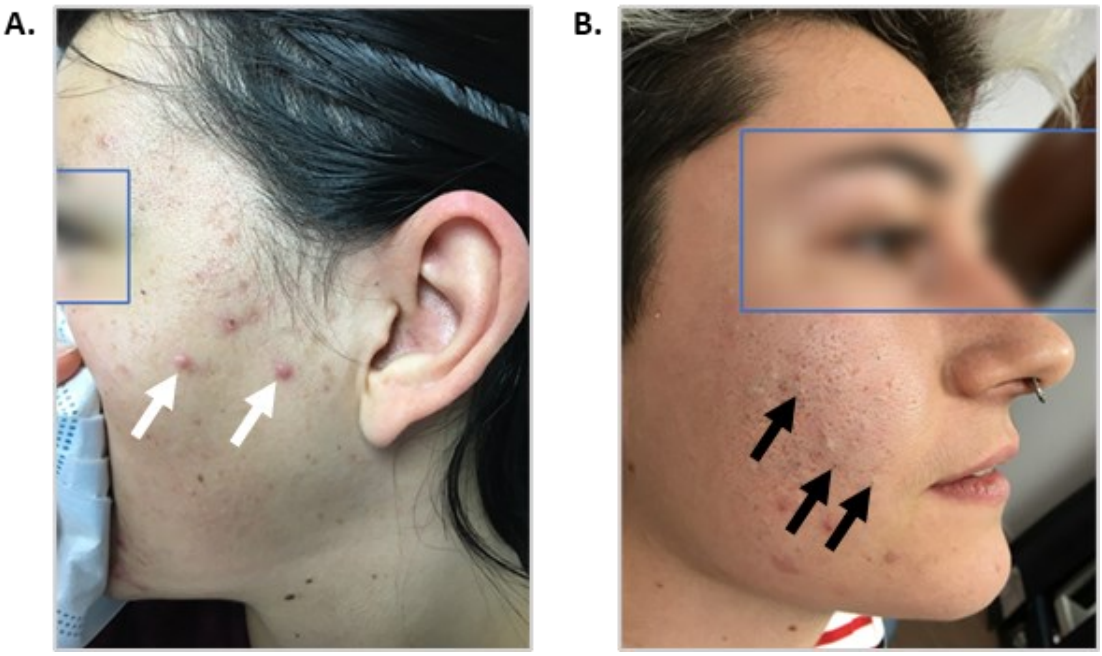

Figure 11: Photographs showing acne lesions. **A.** Acne of the face with an inflammatory profile and papule lesions (showed by white arrows). **B.** Acne of the face with a highly retentional profile showing mostly blackheads (black arrows). Photographs obtained during the SMPatho study. The volunteer's consent has been obtained for illustrative purposes.

The sebum composition is affected by the onset of acne in adolescents compared to healthy subjects. By Liquid Chromatography MS (**LCMS**) analysis, DGs were described to be more abundant in acne, with 16 of 17 DGs showing elevated levels, as well as squalene and FFAs[142,154]. Facial sebum had significantly higher levels of phosphatidylserines, a reduced average chain length of ceramides, an increase in unsaturated FFAs and a decrease in saturated FFAs[155]. It has been recently proven that there is a correlation between the acne severity and the relative content of TGs, DGs, FFAs, and ceramides which is significantly increased from mild to moderate forms[156]. Interestingly Zhou et collaborators found an increase of long chain bases AMLs between healthy and mild form of acne which decrease going to moderate forms.

The role of *Cutibacterium acnes* in pathogenesis is major and antibiotics have a direct antimicrobial, as well as an anti-inflammatory effect, leading to lesion decrease even on resistant bacteria[150]. The main acne treatment strategies focus on reducing inflammation, lowering *C. acnes* levels, reducing skin cell shedding and sebum production to prevent blockage. Recommended treatments use topic drugs like local antibiotics in association with benzoyl peroxide, and / or retinoids. When not enough, systemic treatments such as antibiotics, hormonal agents, and oral retinoids are used[157]. New instrumental treatments are arising from the use of LED light[158,g].

b) Psoriasis

Psoriasis is defined by the World Health Organisation ("**WHO**") as a "chronic, non-communicable, painful, disfiguring, and disabling disease for which there is no cure" that affects more than 60 million peoples worldwide[7]. It affects diverse area of the skin and can induce a significant decrease in the quality of life by an important psychological effect on crucial areas like the face, hands, feet, and external genitalia.

There are several clinical forms of this autoimmune disease with the most prevalent being the plaque psoriasis also names psoriasis vulgaris which is the form treated in this thesis. It corresponds to well defined pink or red inflammatory lesions, indurated (oedema) and covered by pale scales in white skin and grey plaque with silver scales on black skin, see **Figure 12**.

[g] For more information on Acne vulgaris, the reader is referred to the extensive and excellent review of Zouboulis[152]

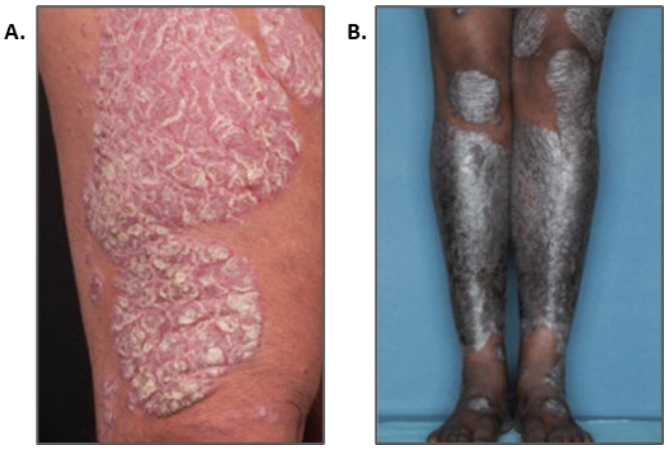

Figure 12: Photographs showing well demarcated psoriasis vulgaris plaque. A. Pink plaque with white scales on white skin. B. Grey scales on darker plaques on black skin. Reproduced partially, with permissions respectively from Griffiths et al.[159] and Elsevier

Each individual plaque lesion is dynamic, with its edges moving outward and corresponding to the most active area. The diagnosis is usually posed based on lesion morphology and distribution as well as family history of psoriasis (linked to genetic predisposition factors).

In normal skin there is a fine balance between production and loss of cells completely dysregulated in the case of psoriasis leading to thickened epidermis. There is an elevated infiltration of T cells in the dermis and epidermis highlighting a preponderant immunological role in the pathology, using IL-17 and IL-23 adaptive immune system pathways. It has been shown that autoantigens implicated in psoriasis pathogenesis include melanocyte antigens but also the keratinocyte cathelicidin LL-37. AMPs are thought to complexes with DNA, activating the immune system and causing inflammation[160]. Nonetheless, the AMP levels are increased in psoriasis lesions explaining why bacterial infection is not usual in this dermatosis despite the significant barrier disruption.

The lipidomic analysis conducted on psoriasis has shown a significant increase in serum circulating sphingomyelins and ceramides observed in the lesioned skin as well[161]. There were noted differences in serum circulating polyunsaturated fatty acids, α-linolenic (C18:3, n-3) and arachidic acid (FA 20:0)[162]. There were also an higher expression of the C12:0, C16:0, C18:0, C18:1, C24:0 and C24:1 ceramides associated with changes in the ceramide synthase mRNA levels in the skin[161]. FFAs abundance is also modified: in arthritic psoriasis, the serum concentrations of 10 out of 14 FFA from psoriasis patients were lower than the healthy controls. A correlation was found between the increased levels phospholipids and cholesterol in the epidermis and the severity of psoriasis[163,164].

The treatment strategies against psoriasis include prophylactic education of the patient, topical agents (emollients, corticosteroids, keratolytics, etc.), phototherapy, and systemic agents (methotrexate, ciclosporin, retinoids and more recently biologics)[165,h].

[h] For more information on psoriasis, the reader is referred to the extensive review of Griffiths et al.[159]

c) Atopic dermatitis

AD is a chronic inflammatory skin disease and the leading cause of global burden from dermatosis affecting up to 20% of children and 10% of adults in developed countries[166]. The first signs are usually seen during childhood even if this condition can appear at any time. The affected area pattern varies with the age as shown in **Figure 13**: Infants show poorly defined erythema widely distributed but typically affecting the trunk, cheeks, and face. Childs show more localised lesions affecting moist and flexor surfaces. The inflammatory flares of the disease are more commons in infants and early childhood. In teenagers and adults, the lesions are more diffuse across the body but tend to affect hands, eyelids, and scalp. Common features observed in AD patients are generalised skin xerosis[i], with very chronic erythematous[j], lichenified[k], swollen, wet (vesicles), and pruritic[l] patches of skin. In adults, the flares tend to be predominated by xerosis and lichenifications. The pruritus and sleep disturbance for patients and their families represent a large part of the burden.

[i] Dryness

[j] Red

[k] The lichenification is a thickening of the skin with hyperpigmentation that occurs in response to repeated and prolonged scratching.

[l] Itchy

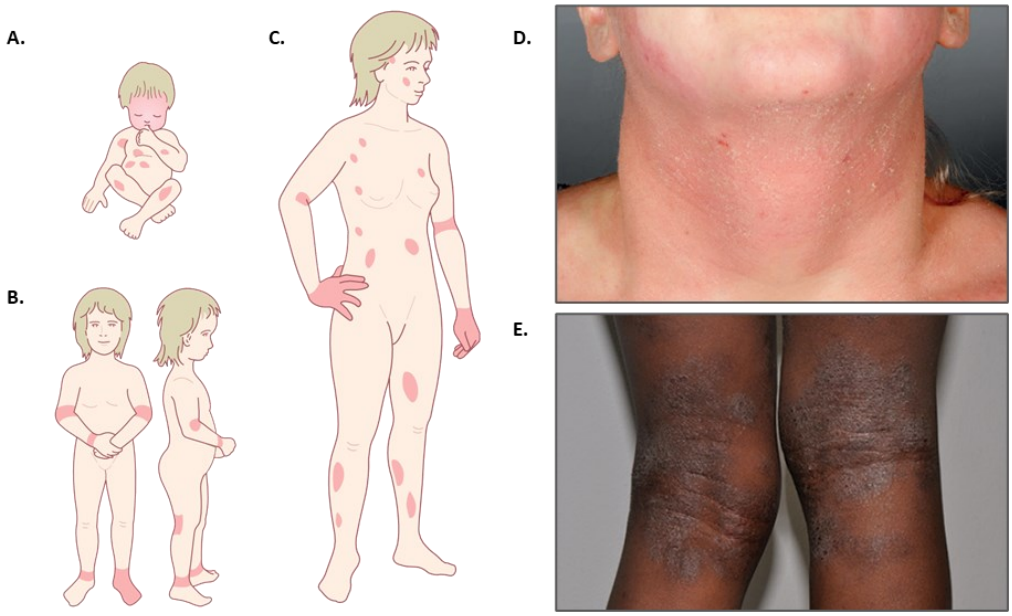

Figure 13: Illustration and photographs depicting the clinical signs of AD. **A.** Infants shows poorly defined erythema widely distributed but typically affecting the trunk, cheeks, and face. **B.** Childs show more localised lesions affecting moist and flexor surfaces. **C.** In teenagers and adults the lesions are more diffuse and tend to affect hands, eyelids, and scalp. **D.** & **E.** Photographs of adults affected by AD respectively on a white and black skin. Adapted from "*Pattern_of_atopic_eczema_varies_with_age*" by Madhero88, under CC BY-SA 3.0 via Wikimedia Commons and from "*Atopic dermatitis*" by Langan et al.[166] with permission from Elsevier.

The disease is strongly linked to family history of atopic diseases like asthma and allergic rhinitis. There is a part of AD patients which doesn't shows specific IgE sensitivity and henceforth are not technically atopic, leading to the proposition of using the term eczema for both atopic and non-atopic forms of AD.

The physiopathology of AD is complex and involves predisposition factors such as epidermal barrier dysfunction, immune system dysregulation and microbiota dysbiosis and triggering factors like stress, allergens, sweating. The skin barrier deficiency is linked to several factor and notably genetic predispositions. Indeed, there is approximately 75% of heritability in AD and more than 30 genetic loci have been linked to the pathology[167]. The loss of function of the FLG gene is the first and more described leading to a disturbed skin barrier and an increased Trans Epidermal Water Loss (**TEWL**)[168].

Extensive studies have confirmed the important implication in the skin SC lipids in AD patients. For example, there is a significant reduction in the total amount of ceramides compared to healthy patients modifying the ordered lipid lamellae[169]. Another modification comes from the higher abundance of short-chain lipids and a lower abundance of longer-chain lipids affecting FFA, sphingomyelins, lysophosphatidylcholines, and ceramides[170]. As smaller chain lipids are less hydrophobic, this size reduction is thought to contribute to the disrupted barrier organisation and therefore, the increase TEWL during disease[171]. In these cases, there is an altered expression of key biosynthesis enzymes such as the stearoyl-CoA desaturase (SCD) and the elongase 1 (ELOVL1), which partially contribute to these changes in composition[172].

These perturbations of endogenous lipid levels can promote pathogenesis by lowering the microbial development control. For example, the decreased levels of sphingosine[173] and the deficient sapienic acid

production[174] - which as previously described, are AML - are associated with AD and contribute to increased *S. aureus* skin colonisation in otherwise healthy individuals. In AD patients, the sphingomyelin deacylase has shown to be three-to-five times more actives than in healthy subjects explaining the relative lack of sphingosine[175]. In addition, this hydrolysis activity on sphingomyelin produces sphingosylphosphorylcholine instead of ceramides which contributes to the global reduction in ceramide in these patients[176].

Other lipid mediators, like prostanoids and leukotrienes, are also elevated in AD patients and can participate in the inflammatory reactions[177]. It is quite difficult to precisely analyse the role of these mediators with classical approaches since those molecules are metabolically and chemically unstable and tend to function only locally.

The barrier dysfunction and the immune system dysregulation leads to unbalanced skin microbiota. Indeed, a higher abundance of pathogenic *S. aureus* has been highly correlated with AD patient, along with a lower abundance of commensal *S. epidermidis*. This later species is known to produce lipoteichoic acid, a TLR2 ligand that plays an important role in reducing skin inflammation[178].

The therapeutic strategies encompass several levels starting by education of the patients on how the pathology can be regulated (reducing the stress for example). It means learning how to avoid the trigger factors and how to conduct basic wound care. This starts by following personal daily skin care with emollients or moisturising products. When these are not enough, topical antipruritic and immunomodulator agents can be used as well as phototherapy. Potential therapies not yet approved make use of JAK-STAT pathways inhibitors or IL receptor antibodies[179].

As it can be perceived, the highly complex physio-pathological aspects in AD leads to a high heterogeneity of patients' immunological responses or patient endotypes. It makes the "one-size-fits-all" therapeutic approach less effective for AD patients[180].

d) Seborrheic dermatitis

SD is a chronic mycotic inflammatory dermatosis showing erythemato-squamous lesions in sebaceous areas such as the scalp, face, and some body folds. There is a bimodal occurrence of this pathology with an infantile (ISD) form also called cradle cap and an adult (ASD) form.

Ranked third behind AD and contact dermatitis for its potential to impair the quality of life, SD affect all ethnic groups with a prevalence evaluated around 70% in 3 month old babies, 5% in adults but increase throughout life toward 15% in older populations[8–10]. Females have less probability to get SD and otherwise present more intense symptoms and HIV-AIDS positives patients as well as Parkinson patients tends to have a higher rate of SD[9].

On ISD, the infant scalp is covered by greasy and yellowish scales (see **Figure 14**) that doesn't seem to affect the baby. In ASD, Dandruff is the most common form of SD corresponding to scales without visible

inflammations. The presentation of SD needing medical care corresponds to erythematous patches covered by flaky and greasy scales with additional hypopigmentation on darker skinned adults[181].

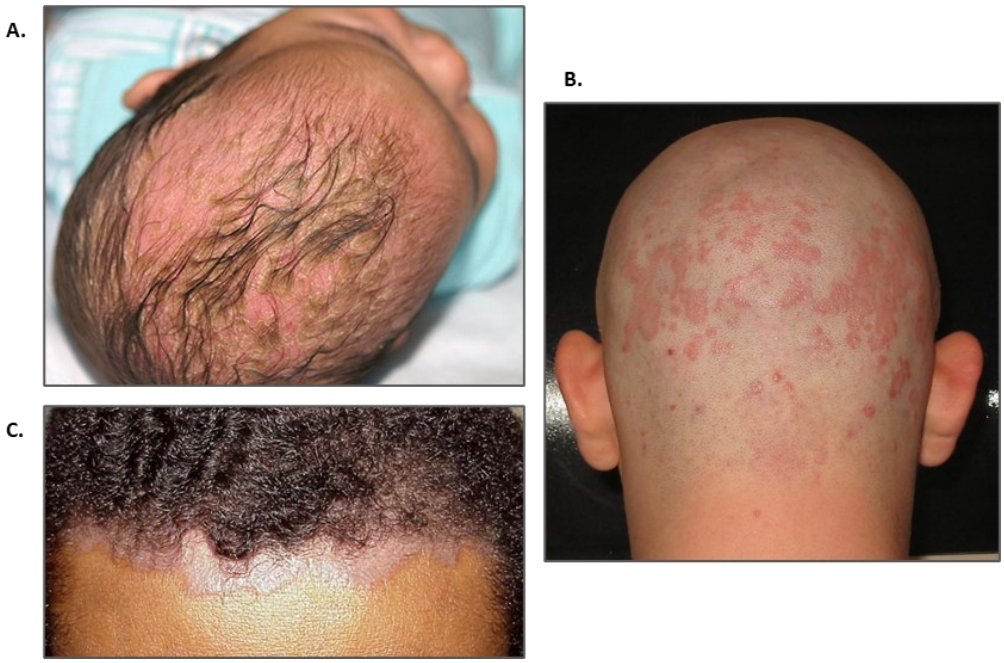

Figure 14: Seborrheic dermatitis pictures. **A.** Infant seborrheic dermatitis (ISD) also called cradle cap. **B.** Classical adult seborrheic dermatitis (ASD) erythematous lesions of the scalp. **C.** ASD lesions on Darker coloured skin at the border of the hairs depicted by lighter areas. Photos **A.** & **C.** obtained from Samuel Freire Da Silva and contributors, Free access via Atlas dermatologico. Photo **B.** By Amras666 - Own work, under CC BY-SA 3.0, via WikiMedia Commons.

The SD physiopathology is complex but major scientific progresses has been made recently. There are some prerequisites leading to SD: i) an increased and/or modified sebum production, ii) a dysbiosis in skin's microbiota involving *Malassezia*. which iii) trigger the immune system. The inflammatory state induces keratinocytes proliferation and differentiation which result in a disrupted skin barrier, erythema, pruritus, and scaling[182].

The increased hydrolysation of skin lipids produce FFA and lower the relative quantity of TGs. Then *Malassezia* uses the saturated FFA, leaving behind irritating and unsaturated FFA such as oleic acid and lipid peroxides[183]. The individual sensitivity to these FFA will determine the inflammation response and may affect the susceptibility for SD[184]. Contrary to AD, little genetic predisposition has been described in SD except for a certain susceptibility toward some HLA alleles.

The patient education to limit the exogenic factors leading to an acute response is essential in managing the disease. Further proofs for the implication of Malassezia (main species: *M. furfur, M. globosa, M. restricta*) includes their isolation from lesions sites and the resolution of SD with antifungal treatment such

as Hydroxypyridones, Selenium Zinc, or Tea tree oil. The first lines of treatments aim at reducing the inflammation and erythema using topical immunomodulators (corticosteroids) or phototherapy associated with antifungal therapy. Systemic medication is used only in case of widespread lesions.

Chapter III

The SpiderMass Approach

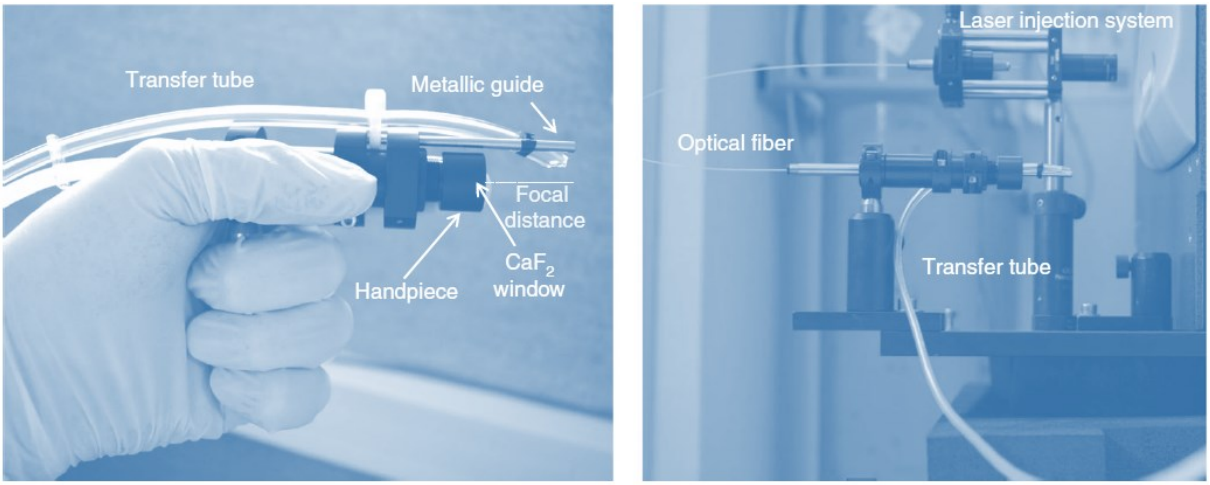

Close-up of view of the microsampling probe. Left, Configuration of the microsampling handpiece. Right, Picture of the whole microsampling probe, showing the injection system, connection to the optical fibre and the handpiece

Nina Ogrinc & Philippe Saudemont, Julia Balog, Yves-Marie Robin, Jean-Pascal Gimeno, Quentin Pascal, Dominique Tierny, Zoltan Takats, Michel Salzet and Isabelle Fournier

Nature Protocole, 2019

CHAPTER III: The SpiderMass Approach

A. Introduction

After a patent was filled in 2014[185], the SpiderMass was first officially presented at the ASMS Conference in 2015 and then in 2016 with the princeps publication of Fatou et al. presenting the first prototype of the technology[24]. In this initial work, we showed the possibility to use an infrared laser to induce a Resonant InfraRed Laser Ablation (**RIR-LA**) based on the excitation of the most intense vibration mode of the water molecules endogenous to the tissues. Because the process was developed to get a MALDI-like process using endogenous water as a matrix, we decided to coin the process WALDI. Water is highly abundant in various biological tissue and in average above 70% in organs. The advantage of using a matrix is to enable a similar desorption/ionisation process for all tissues which would not be that obvious by targeting resonant excitation of analytes. Moreover, the matrix prevents the analyte from receiving too much energy and therefore from extensive fragmentation as observed in conventional LDI. Water is highly abundant, and it solvate the analytes within the tissues; thus, it presents all the characteristics of a MALDI matrix absorbing at 2.94µm. Because of the *in vivo* need, we had to work in the IR domain because the UV photons are highly energetic and create irreversible damages to DNA. The penetration depth of such lasers has been shown proportional to the wavelength which means IR lasers get more deeply into the tissues than UV[186]. Nonetheless, using the specific wavelength of water make the beam intensely absorbed limiting the invasiveness. Moreover, we decided to go for nanosecond duration range of the impulsion. This choice was made for several reason. First, it has been shown that for longer impulsion (e.g., milliseconds) more thermic effects are observed and tissues are burnt by the irradiation making the process much more invasive[92]. On the other hand, ns range is typical for MALDI, and shorter impulsion lasers like pico- and femto- regimes are less produced, more expensive and generally bigger in size. Also, the importance of the thermic effects in the MALDI process and the impact on the analytical performance are still not really elucidated[187]. In this configuration, the invasiveness is limited and about 2-3 µm depth material is removed by every laser shot. The irradiation, thus, principally leave a white trace of dehydration on the skin and the process is painless. Most common lasers emitting at 2.94 µm are Erbium-doped yttrium aluminium garnet lasers (Er:YAG) though they are only available for the ms impulsion range. Nanosecond 2.94 µm can only be obtained using an Optical Parametric Oscillator (**OPO**). These are generally pumped by Neodymium-doped Yttrium Aluminium Garnet (**Nd:YAG**) emitting at 1064 nm. The advantages of the OPO is to modify the laser pump wavelength within a certain range due to non-linear interactions inside of a crystal cavity. This was important in the first experiments to check the optimum absorbing wavelength from tissues, and this gave us the opportunity to study the effect on the wavelength on the ion yields[188]. In the initial experiments, we used an open laser which beam was focused onto the sample using a series of

appropriated mirrors and lens. One of the technological locks to be lifted was then to get a fibered version of the laser, enabling to freely scan any surface. Because we had shown that we need at least 4 mJ/pulse to get sufficient ion yields, the fibering was tricky. The short impulsion time makes the peak energy very high and the injection not trivial at all because if the beam shape is not well controlled and the beam not well injected in the fibber, the fibbers are burning. However, we were able to produce a laser prototype which has led us to a second version prototype of the SpiderMass that could be moved in a relevant environment for testing. Also, it is very important to note that the laser is installed remotely from the mass spectrometer and the ablated material is transferred to the instrument by a simple tubing, the vacuum inside the mass spectrometer being enough to create an aspiration and an extremely fast transfer of the aerosol. From the mass spectrometer side, the conventional source is removed to the benefit of an interface which helps to break aggregates (decluster) liberating the ions and leading to improved sensitivity. The interface is also very important to limit the fouling of the instrument and extensive cleaning.

In this configuration, the SpiderMass allows the easy analysis of various kind of samples e.g., cells, plants, fresh frozen tissue section or *in vivo* organs. The novelty comes from the possibility to conduct the analysis on the sample in its native state and environment, with no to little sample preparation, characteristic of the AIMS technologies This prototype, which detailed operation was published in Nature Protocols in 2019, has served as model for the prototype which was setup at PFDC.

In the following, the general description and operation of the SpiderMass system is conducted under the form of a steps by steps protocol detailing how to conduct experiments with the technology.

nature protocols

PROTOCOL

https://doi.org/10.1038/s41596-019-0217-8

Water-assisted laser desorption/ionization mass spectrometry for minimally invasive in vivo and real-time surface analysis using SpiderMass

Nina Ogrinc[1,6], Philippe Saudemont[1,2,6], Julia Balog[3], Yves-Marie Robin[1,4], Jean-Pascal Gimeno[1], Quentin Pascal[1,5], Dominique Tierny[1,5], Zoltan Takats[3], Michel Salzet[1*] and Isabelle Fournier[1*]

Rapid, sensitive, precise and accurate analysis of samples in their native in vivo environment is critical to better decipher physiological and physiopathological mechanisms. SpiderMass is an ambient mass spectrometry (MS) system designed for mobile in vivo and real-time surface analyses of biological tissues. The system uses a fibered laser, which is tuned to excite the most intense vibrational band of water, resulting in a process termed water-assisted laser desorption/ionization (WALDI). The water molecules act as an endogenous matrix in a matrix-assisted laser desorption ionization (MALDI)-like scenario, leading to the desorption/ionization of biomolecules (lipids, metabolites and proteins). The ejected material is transferred to the mass spectrometer through an atmospheric interface and a transfer line that is several meters long. Here, we formulate a three-stage procedure that includes (i) a laser system setup coupled to a Waters Q-TOF or Thermo Fisher Q Exactive mass analyzer, (ii) analysis of specimens and (iii) data processing. We also describe the optimal setup for the analysis of cell cultures, fresh-frozen tissue sections and in vivo experiments on skin. With proper optimization, the system can be used for a variety of different targets and applications. The entire procedure takes 1–2 d for complex samples.

Introduction

Rapid, sensitive, precise and accurate analysis of samples in their native environment in in vivo conditions has become a critical part of routine analysis. By preserving samples in their original state, without the need for sample preparation, we can better decipher the underlying biological mechanisms. For example, the improvement of cancer treatment and prognosis relies heavily on the development of technologies that enable rapid molecular diagnostics in an intraoperative context of cancer surgery. Therefore, there is a growing need for the development of MS techniques that work under ambient conditions and enable in vivo/in situ analysis in real time[1–4]. The development and use of ambient ionization MS (AIMS) techniques[5,6] have become widespread, because they require minimal sample preparation for analysis, contrary to traditional vacuum-based MS approaches. Under ambient conditions, the formation of analyte ions from the sample is usually promoted by surface bombardment. This is achieved with charged solvent droplets (desorption electrospray ionization (DESI))[7], with photons (as in atmospheric pressure–MALDI[8,9], laser-ablation electrospray ionization[10,11] and matrix-assisted laser DESI (MALDESI))[12], or even through excitation of species from an inert gas and low-temperature plasma[13]. All these technological advancements have brought MS closer to in situ analysis by examination of living organisms, detection of pesticides in plants, and even the direct detection of drugs, smoke or gunpowder residues from skin samples[14–17]. In clinical practice, the first advances of AIMS were made with the development of probe electrospray analysis[18–20], needle biopsy and spray ionization[21] and direct analysis in real time[22,23] by directly analyzing patient material. The methods showed great potential and are ideal for routine bench-top analysis of patient samples. However, they cannot be used intraoperatively due to safety and invasiveness issues or incompatibility with the sample size. The next big challenge is to adapt the AIMS methodology for

[1]Université de Lille, Inserm U1192, Laboratoire Protéomique, Réponse Inflammatoire et Spectrométrie de Masse (PRISM), Villeneuve d'Ascq, France. [2]SATT-Nord, Immeuble Central Gare, Lille, France. [3]Department of Surgery and Cancer, St Mary's Hospital, Imperial College London, London, UK. [4]Unité de Pathologie Morphologique et Moléculaire, Centre Oscar Lambret, Lille, France. [5]OCR (Oncovet Clinical Research), Eurasanté, Loos, France. [6]These authors contributed equally: Nina Ogrinc, Philippe Saudemont. *e-mail: michel.salzet@univ-lille.fr; isabelle.fournier@univ-lille.fr

in vivo analysis, which requires rapid, sensitive, precise and accurate measurements. Recently, several MS-based systems have been developed in translational research for in vivo analysis and real-time diagnostics. The first system, the intelligent surgical knife (iKnife), based on rapid evaporative ionization MS (REIMS), was developed in 2009. The iKnife produces gas-phase ions of evaporated tissue after contact with the surgical tool[4,24]. The gas-phase ions are then transmitted to the mass spectrometer through a Teflon tube of >1 m length using a Venturi gas jet pump[24]. The analyzed molecular signatures are then subjected to classification using multivariate classifiers[4]. The system has been tested in vivo and has provided confident identification of normal, borderline and malignant tissues derived from patients with ovary cancer[25] or breast cancer[26], as well as endoscopic classification of intestinal wall, cancer and polyp tissues[27]. The technique is compatible with commonly used surgical devices (for example, electrosurgical electrodes, surgical diathermy instruments, bipolar forceps and cavitron ultrasonic surgical aspirators) but is highly invasive: the iKnife technique utilizes the surgical aerosols (or smokes) formed during normal surgical interventions and provides molecular information while tissue excision is performed. Because the analyzed tissue is physically cut, it makes it difficult to use it for histological cross-validation[26]. In addition, the detection of analytes is limited to metabolites and lipids in the negative ion polarity. The more recent MasSpec Pen system consists of a syringe pump delivering a defined water volume to the sampling probe, polytetrafluoroethylene (PTFE) tubing integrated with valves to transport the water to and from the tissue, and a pen-size device for probing biological specimens[2]. During the experiment, a water droplet is deposited on the tissue for a 3-s period, allowing the extraction of analytes. The droplet is vacuum-extracted to the mass spectrometer and analyzed. The system is based on non-destructive liquid–solid extraction and can be applied during in vivo tissue analysis[2]. The use of water as a solvent, however, limits the analyte extraction to hydrophilic species and suffers from contamination due to the presence of interstitial fluid and blood on surgically exposed tissue surfaces. The tip is placed in tight contact with the tissue, and after each use it must be replaced or washed with automated flushing. The MasSpec Pen was demonstrated for ex vivo analysis of ovarian cancer samples[28] and in vivo analysis of samples from mouse models[2].

In vivo real-time analysis using SpiderMass

We introduced the SpiderMass system for in vivo and real-time analysis using a laser in the IR wavelength in 2014 (refs. [3,29]). In contrast to its first applications for the direct excitation of analytes and laser ablation[30], the SpiderMass is tuned to excite the most intense vibrational band (O–H) of water molecules (2.94 μm) in a process called WALDI. Similar to MALDI, WALDI uses water as an endogenous MALDI matrix to produce gas-phase ions. Water has previously been reported to be a possible MALDI matrix and has been used to analyze proteins trapped in ice crystals[31], peptides in aqueous solution[9] and oligosaccharides[32]. Here, the water content of the tissues is submitted to resonant excitation to generate a MALDI-like mechanism, except that the matrix is already within the system to be analyzed. Organisms, on average, consist of 70–80% water. The resulting ions are then aspirated via a transfer line and detected in a mass spectrometer. The acquired MS spectra show characteristics similar to those observed during the MALDI process with, such as the collective effect, low fragmentation (if the laser energy used is just above the threshold energy for ion production) and the capacity to detect both positive and negative ions and to analyze large polar molecules such as proteins[33]. An optical parametric oscillator (OPO) system coupled to a neodymium-doped yttrium aluminum garnet (Nd:YAG) pump with an accordable wavelength providing a 6-ns pulse duration is used as a source. At the set 2.94-μm wavelength, the OPO system provides the necessary laser energy output (>3–4 mJ/pulse, but preferentially <9–10 mJ/pulse to limit fragmentation). The OPO can be coupled to a laser fiber ending in a handpiece, which enables the user to freely screen any surface ex vivo or in vivo. After the fired laser shot, the resulting plume is aspirated via a polymer-based tube of up to 5 m in length and positioned immediately above the analyzed tissue. The collected aerosols are then delivered to the mass analyzer, without the need of a post-ionization device. The laser source can thus be placed remotely from the MS instrument and is rendered mobile by the use of a fibered laser system with a fiber up to 2 m long. The system can be coupled to different MS analyzers, such as Waters Q-TOF technology (XEVO, Synapt G2-S) equipped with a custom-made REIMS interface or a Thermo Fisher Q Orbitrap (Q Exactive) instrument equipped with an in-house-built inlet interface (Fig. 1). The resulting molecular profiles can be further processed and compared with spectral libraries or databanks. In this protocol, we provide detailed instructions on how to correctly operate the SpiderMass system and acquire molecular profiles from several biological entities. In addition, a

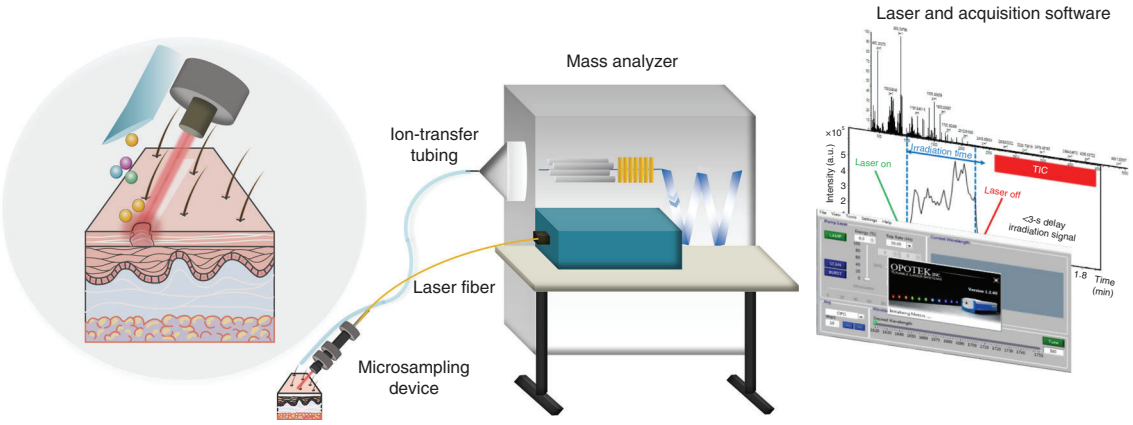

Fig. 1 | A schematic representation of the SpiderMass setup for in vivo experiments. The SpiderMass setup is equipped with the fiber laser microsampling device, an ion transfer tube and a mass spectrometer. Leftmost image adapted from Servier Medical Art (https://smart.servier.com/) under a Creative Commons Attribution 3.0 license (https://creativecommons.org/licenses/by/3.0/legalcode).

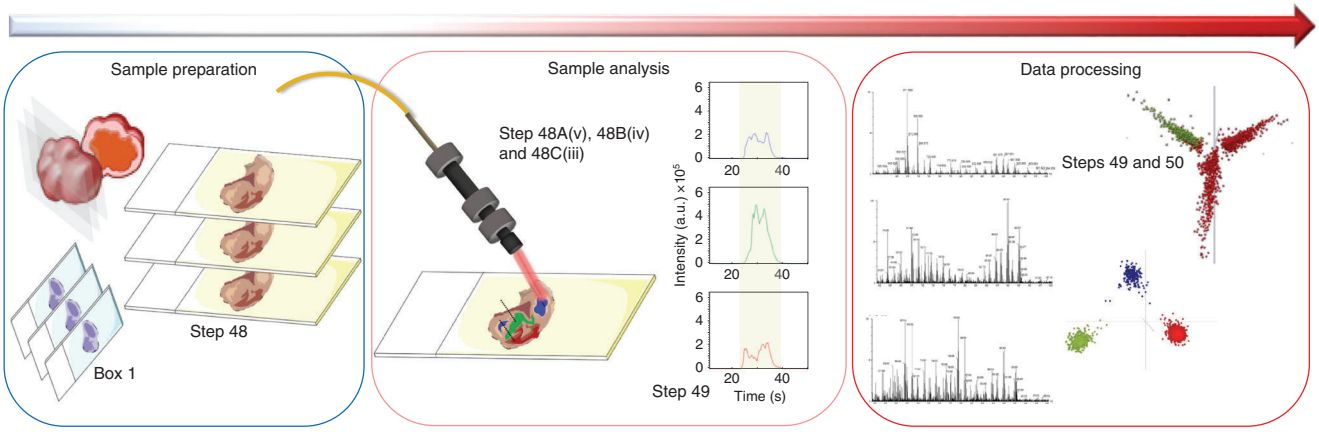

Fig. 2 | A flowchart of a standard SpiderMass experiment. The procedure contains step-by-step instructions from sample preparation to data processing and building classification models from biopsy samples. Samples are first carefully prepared before analysis by cutting tissues into halves; the first half is used for SpiderMass analysis and the second for control histological annotation of the associated tissue. The SpiderMass half is generally sectioned to spare tissue sections. SpiderMass analysis is generally performed over a 10-s irradiation period in triplicate for each of the tissue areas of interest. Recorded MS spectra are then assigned a histological class according to the pathologist's annotation of the tissue associated with the analyzed SpiderMass sample. Classed spectra are then submitted to unsupervised (for example, PCA) or supervised (for example, LDA) multivariate analysis to study the data separation and build classification models. After multivariate analysis, univariate analysis is performed to retrieve the *m/z* values associated with the highest variance between classes. These can be further studied by tandem MS for identification of markers associated with a specific class. Images of slides adapted from Servier Medical Art (https://smart.servier.com/) and images of cancer tissue adapted from http://www.aboutcancer.com/bre2d.htm under Creative Commons Attribution 3.0 licenses (https://creativecommons.org/licenses/by/3.0/legalcode).

schematic workflow (Fig. 2) from sample preparation to data processing is provided to ensure correct application of the system.

Applications of the method

Although the SpiderMass system has predominantly been developed for in vivo and real-time applications in oncology, it can be applied to a variety of different research areas, such as dermatology, food safety and drug pharmacokinetics[3,34,35]. To date, the SpiderMass system has been successfully applied to analyze ex vivo ovarian cancer samples and in vivo human skin, genetically modified macrophage cell lines, bacterial biotyping and intact proteins in solution[3,33,35,36]. Moreover, the recent ex vivo applications of the described protocol enabled analysis of dog sarcoma samples, and multivariate statistical analysis allowed for the correct classification (97% specificity) of tumor type and grading[34]. We also demonstrated the method's applicability in vivo during surgery of dogs in an Oncovet clinic[34].

Comparison with other methods

SpiderMass has several advantages over other ambient ionization techniques for in vivo and real-time analysis. One of the major advantages is the low invasiveness or low penetration depth of the microsampling probe in comparison to the iKnife[4,25]. Only ~0.025–0.05 mm^3 of tissue is sampled in one experiment for a total of 100 laser shots and a laser spot size of 400 μm, which means material with a depth of 2–4 μm is removed per laser shot[3]. On skin, the laser leaves a white trace due to tissue dehydration, which disappears within minutes after moistening the skin. Owing to this low invasiveness, SpiderMass analysis can be performed even on thin tissue sections when the availability of the biological material is limited. Although the recorded molecular profiles do not change if the tissue is sectioned or analyzed as whole pieces, it does affect the penetration depth. The laser marks are more visible when analyzing tissue sections because they are much drier than tissue pieces. Interestingly, hardly any tissue damage was observed even during in vivo experiments in dogs. Another method that is very similar to SpiderMass and was introduced by the Zarrine-Afsar laboratory in 2017 is called picosecond infrared laser desorption mass spectrometry (PIRL-MS)[37]. In PIRL-MS, the nanosecond laser is replaced by a handheld picosecond laser. The picosecond impulsion reduces the thermal effects and is expected to result in slightly smaller amounts of damage to the ablated tissue[37–39]. However, the picosecond range does not allow for a MALDI-like desorption/ionization mechanism and, therefore, results in lower ionization yields. Another advantage of the SpiderMass system is the positioning of the handpiece. The laser is positioned far enough from the sample and avoids cross-contamination of consecutively analyzed tissue areas, as opposed to the MasSpec Pen, the tip of which needs to be washed or removed after each use[2]. In addition, because of the nature of IR laser desorption/ionization (in WALDI), the system routinely provides good-quality and high-intensity spectra for a large variety of biomolecules, from lipids to proteins, in both positive and negative ion modalities; such spectra have been limited or not reported in the aforementioned techniques. Finally, the laser's optical fibers (fibers up to 2 m in length were shown to provide sufficient laser energy) and the system's transfer tubes of several meters render the use of the laser microprobe flexible and versatile.

Limitations and potential improvements of the protocol

One of the major limitations of the SpiderMass system is the lack of robustness of the microsampling device. The optical fiber is still very delicate and prone to breakage, when constantly moving the handpiece and operating the device in a real clinical environment (that is, the surgical theater). This, however, does not pose a great issue when performing routine research analyses in a stationary environment. In the future, we intend to replace the optical fibers with more-robust jacketed fibers or to place the fiber within a small-bore stainless-steel flexible conduit to avoid extensive breakage (especially for >1–m-long fibers) while maintaining flexibility. In the current setting, the microprobe device gives a laser spot diameter of 400 μm, but we wish to decrease the diameter to 100 μm for more accurate analysis of smaller margins or to enlarge it to >1 mm for screening of bigger areas. Another limitation for application in the clinic is the portability of the whole instrumentation platform. Owing to the size of the SpiderMass platform, it cannot be moved from one room to another as with other devices used in hospitals (for example, ultrasound devices). It must be installed at a dedicated location in the surgical theater or in pathology laboratories. Development of a more miniaturized platform for clinical or in-the-field applications is an important goal to strive for in the future to ensure better mobility of the system. An additional disadvantage as compared to other AIMS techniques is that the current SpiderMass system does not provide spatial resolution for morphology-based tissue analysis. This is currently performed with complementary techniques such as MALDI[34] for cross-validation. Although, techniques such as IR-MALDESI provide additional 2D information for ex vivo/in situ analysis, they cannot be used for fast screening or in vivo, limiting their use for cancer diagnostics. Their current setup also limits their use in the surgical theater. However, we plan to decrease the laser beam diameter (by changing the focal lens of the handpiece) to 100 μm and intend to add an imaging dimension to the SpiderMass system by automated acquisition through a motorized (*x*,*y*) plate.

Experimental design

Sample preparation

To ensure the proper performance of the sample analysis, it is important to properly design the sample preparation. Analysis of standards and cell cultures is straightforward and requires only a few microliters of the desired sample to be spotted onto a glass slide, followed by drying under vacuum.

Box 1 | Histopathological examination ● Timing 10 min

This box describes a staining procedure for the histopathological annotation of the second half of the fresh-frozen tissue sections. The staining should be performed while analyzing the tissue and before the analysis in Step 48B. The annotations should be performed by a trained pathologist.

Additional reagents

- Mayer's hematoxylin solution (Sigma-Aldrich, cat. no. MHS32-1L)
- Eosin–phloxine solution (Merck; VWR, cat. no. 1.02480.1000)
- Ethanol extract of saffron (10 mg/ml; VWR, cat. no. 10047028)
- Xylenes (reagent grade; Sigma-Aldrich, cat. no. 214736-1L)
- Histological mounting medium (EUKITT, Sigma-Aldrich, cat. no. 03989)

Additional equipment

- Conical centrifuge tubes (50 ml; Falcon; Thermo Fisher Scientific, cat. no. 14-432-22)
- Vertical staining jar with cover (Ted Pella, cat. no. 432-1)
- Ventana iScan HT (Roche)

Reagent setup

Preparation of 70% (vol/vol) ethanol. Pipette 35 ml of ethyl alcohol (HPLC grade) into a 50-ml Falcon tube. Add 25 ml of LC/MS-grade water. Mix well. The solution can be stored at RT for a week and used for staining.

Procedure

1 Section the second half of the tissue into 5-µm sections according to the 'Preparation of fresh-frozen tissue sections' section.
2 Prepare the solutions in the vertical staining jars in order of the staining procedure.
3 Submerge the slide in the hematoxylin solution for 1 min.
4 Rinse with tap water (10 s).
5 Put the slides in the phloxine solution for 1 min.
6 Rinse with tap water (10 s).
7 Dehydrate in 70% (vol/vol) ethanol and then in 100% (vol/vol) ethanol for a few seconds.
8 Immerse the slide in saffron extract for 5–10 s.
9 Rinse the slide in a 100% (vol/vol) ethanol bath.
10 Dip the slides in xylene to unsaturate the staining.
11 Mount the slide with a coverslip and histological mounting medium.
12 Digitalize the slides with the Ventana iScan HT. The nuclei are observed in dark blue, the cytoplasm is pink and the connective tissue is orange.
13 The samples can be further investigated with CaseViewer.

PAUSE POINT The stained slides can be stored at RT for up to 10 years.

The surgically removed tissues (obtained during biopsies) are processed following our preferred protocol (see 'Reagent setup' section). Immediately after removal, the tissue should be snap-frozen in liquid nitrogen and stored at −80 °C before further analysis. Before sectioning, the tissue should be warmed to −20 °C in the cryo-microtome (the sectioning temperature (*T*) varies, depending on the tissue analyzed, from −10 to −30 °C). The tissues are halved using a metallic tissue-cutting tool. The first half of the tissue is sectioned into 10- to 20-µm-thick sections and thaw-mounted on a glass slide for SpiderMass analysis. The second half is preserved for histopathological examination using hematoxylin, phloxine and saffron staining as described in Box 1. In this way, we obtain a direct correlation between the tissue areas analyzed with SpiderMass and the pathological annotations. This is vital in order to assign the MS spectra to the right morphological and pathological classes. The staining is evaluated by a trained pathologist, who provides the delineation of the different regions of interest (Box 1). This control must be incorporated into any SpiderMass analysis.

SpiderMass System setup

The SpiderMass setup consists of three main parts: (i) a microsampling probe, (ii) a transfer line and (iii) a MS analyzer. Each of the parts must be carefully set up and optimized for operation. The microsampling probe is composed of a tunable-wavelength OPO (between 2.8 and 3.1 µm) pumped by a Nd:YAG laser (pulse duration 5 ns, $\lambda = 1{,}064$). A biocompatible laser fiber is connected to the laser output and handpiece. The system includes a 4-cm focusing lens attached to the end of the fiber behind a CaF_2 window (Fig. 3). The proper setup of the microsampling probe is described in Steps 1–5 of the Procedure. The handpiece with the 4-cm focusing lens ensures proper holding and

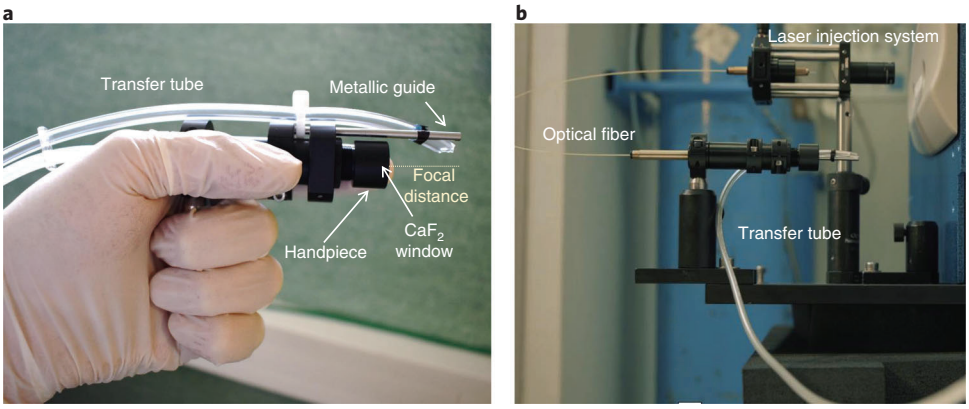

Fig. 3 | Close-up of the microsampling probe. a, Configuration of the microsampling handpiece, consisting of the handpiece itself with the CaF_2 window, the metallic guide and the attached transfer tube. **b**, Picture of the whole mobile microsampling probe, showing the injection system, connection to the optical fiber (here a short optical fiber of 30–50 cm) and connection of the laser fiber to the handpiece with focal lens included.

Box 2 | Preparation and polishing of the optical fiber ● Timing 1–2 h

This box describes the procedure to properly polish the optical fiber after damage or breakage. Breakage and damage to the fiber can occur at any time throughout the protocol.

Additional reagents

- 1-Methyl-2-pyrrolidinone (100 ml, Sigma-Aldrich, cat. no. 328634-100ML)

! CAUTION 1-Methyl-2-pyrrolidinone is highly toxic; handle with great care and use in a fume hood.

Additional equipment

- Glass beaker (50 ml)
- Clear glass screw-neck vial (10 ml; Waters, cat. no. 186001420)
- Fiber Optic Termination Kit (ThorLabs, dB Electronic Instruments, cat. no. CK05). Kit includes rubber polishing pad, polishing disk, fiber microscope inspector and polishing sheets using the rougher paper (5, 3, 1 and 0.3 μm)
- Ruby DualScribe Fiber Optic Scribe (ThorLabs, cat. no. S90R)

Procedure

▲ **CRITICAL** The instructions for stripping the fiber (steps 1–7) are available from Infrared Fiber Systems (http://www.infraredfibersystems.com/).

1. Heat a vial of 1-methyl-2-pyrrolidinone in a small beaker under the fume hood to 130–150 °C.
2. Dip the fiber in the solvent for ~1 min or until the coating softens and starts to peel.
3. Remove the fiber from the solvent and dip it in isopropanol or methanol for 1 min, and then wipe off any remaining coating, using tissue.
   ▲ **CRITICAL STEP** The end of the fiber should be clean and not have any remaining coating.
4. Strip the remaining swollen coating with your fingernails and a Kimtech wipe.
5. Put the fiber on a paper towel and hold it with your index finger.
6. Use a ruby fiber optic scribe with your other hand to slightly score the surface of the fiber.
   ▲ **CRITICAL STEP** You must touch the fiber surface perpendicularly or the fiber will break with an angle.
   ▲ **CRITICAL STEP** The fiber should not break during scoring or you will get a jagged edge.
7. Hold the fiber at each side of the score mark between your two thumbs and index fingers and tear the fiber apart. If the fiber does not cleave easily, rotate the fiber 180° and rescore it.
8. During normal operation, the fiber will be damaged by the high level of energy going through it; this will appear as a deterioration of the input and output faces. When you struggle to reach 4 mJ/pulse at the exit of the handpiece, and you are already at >95% of the laser's maximum energy, you need to polish the fiber's ends. To do so, first remove the fiber from the handpiece and the injection system by untightening the two holders.
9. Prepare the rubber polishing pad, the polishing disk, the fiber microscope inspector and the polishing sheets using the rougher paper (5 μm).
   ▲ **CRITICAL STEP** Avoid letting air bubbles to form between the rubber pad and the sheet. This can be done by putting a small amount of water on the pad before placing the paper.
10. Mount the fiber in the bare fiber temporary terminator and the polishing disk.
11. Start polishing by drawing figure eights with the disk.
    ! CAUTION Do not apply too much pressure or you will scratch the surface of the fiber.
12. Remove the fiber terminator from the disk and observe the fiber's end with the microscope; this first cycle of polishing allows you to correct big scratches or chips from the outside edge of the fiber and obtain a nice round shape with neat borders.
13. Repeat steps 9–12 using a finer-grit paper for each successive polishing cycle to finish with the 0.3-μm one.
    ▲ **CRITICAL STEP** At the last stage, very few marks should still be observable on the surfaces. Scratches that are larger than 1/10th of the wavelength should not be ignored because they will cause diffraction.

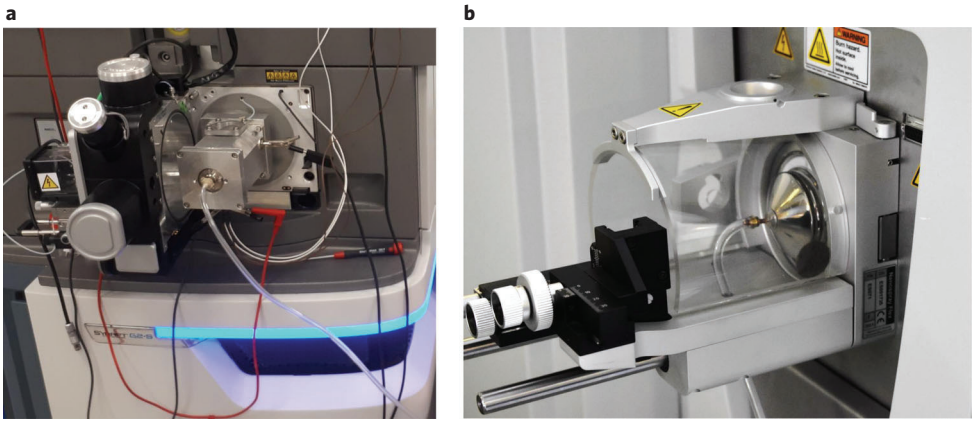

Fig. 4 | Interface. a,**b**, Transfer tube connections to the custom REIMS interface on the Synapt G2-S Q-TOF MS instrument (**a**) and interface to the Q Exactive Orbitrap instrument (**b**). For **a**, the connection used is direct and does not require an extra Venturi system. For **b**, a direct connection is also set up using an ion transfer capillary with a longer extension on the outside.

focusing of the beam diameter to 500 µm. Before analysis, the laser setup must be conducted as described in Steps 6–28 (note that the optical fiber is prone to damage; if damaged, see Box 2). The 3-m ion transfer line can be composed of different polymer materials with reduced polymer release, for example, PTFE. For in vivo analysis, the tubing should be composed of biocompatible polymers such as Tygon ND 100-65. One side of the transfer line is connected to the laser handpiece and the other side of the transfer line is connected directly to the inlet of the selected MS analyzer (Step 29). For example, on the Waters Synapt G2-S, the tube is connected to the REIMS atmospheric pressure interface, which is placed at the inlet of the MS instrument after removing the conventional ESI source (Step 29A). The transfer line is attached directly to the custom-made REIMS interface capillary. This interface is not created using the usual Venturi-assisted aspiration, because the vacuum of the mass spectrometer is sufficient to draw the molecules back for analysis and avoid vapor dilution (Fig. 4).

SpiderMass sample analysis

After the microprobe and transfer line system has been set up, the laser system should be properly optimized (such as the laser energy, number of laser shots, and distance between the sample and handpiece). Our laboratory practice is to use fresh-frozen 10- to 20-µm tissue sections of bovine liver thaw-mounted on a regular glass slide to optimize the necessary parameters (Steps 30–32). It is important to evaluate the influence of laser energy, irradiation time and laser shots, and check ion detection by monitoring the total ion current (TIC). To perform high-quality analyses, the energy should be set to 4–5 mJ (Steps 33–40). Routine systematic analysis should be performed every day to check the system stability and reproducibility. As an important consideration, the selected mass analyzer must be calibrated before use. After selecting the appropriate ion mode and mass range, external calibration is performed. Standards are selected on the basis of the molecules and mass range of interest. The external calibration will ensure high mass accuracy and confidence for further identification. For calibration on the Waters Synapt G2-S instrument, follow Steps 41–47. The calibration for the Q Exactive should be performed according to the standard Thermo Fisher protocol (Step 40). Before sample analysis, the fresh-frozen tissue sections must be removed from the −80 °C freezer and thawed to room temperature (RT; 20–25 °C) for 1 min. The different sampling regions can be selected on the basis of prior histopathological examination and annotation of the same specimen. The irradiation time of the microsampling probe is dependent of the samples under investigation. The irradiation times are shown for different examples. Finally, we describe the parameters for analysis of cell pellets (Step 48A), fresh-frozen tissue sections (Step 48B) and in vivo skin (Step 48C).

Data analysis

Data analysis is strongly dependent on the research question and the mass spectrometer used in the setup. On the basis of the quality of the spectra, several pre-processing steps must be considered. Background subtraction, noise removal, binning and peak-picking algorithms should be applied

Box 3 | OMB classification ● Timing 30–45 min

This box describes the use of the supervised classification software after Step 49. The software can be used for any type of analytes after sample acquisition on the Waters Q-TOF mass spectrometer. The Offline Model Builder v.1.1.773.0 is provided non-commercially by Waters Research Center for the analysis of Waters Synapt G2-S data. The software is capable of handling MS .raw files; it is used for pre-processing the data, for the calculation and cross-validation of multivariate classifiers, and for real-time feedback on samples at the time of sampling. The usual data analysis process consists of the steps below.

Procedure

1 Load the .raw files into the software using the 'Add sample files' button.
2 Assign a class label for each file by typing it into the 'Classification' column on the 'Sample List' page. If necessary, assign a class label for each spectrum separately by typing the label into the 'Classification' box under the spectral view. In this case, a warning sign will appear next to the file name in the list, showing that there are multiple classifications assigned within that .raw file.
3 Select the regions of interest (burns) on the TIC view.
4 Assign the patient code or group number in the 'Group' column. The cross-validation is based on the assigned group names. Each group or a batch of groups can be selected as a validation set.
5 Move to the 'Model Properties' page, select the model type (only PCA or PCA followed by LDA), and adjust the model and pre-processing parameters (number of components to calculate, binning mode and width, used mass range, and all necessary pre-processing steps, including background subtraction, normalization and lockmass correction). If lockmass correction is necessary, an internal or external lockmass compound must be selected. This can be adjusted in the 'lockmass database'. The color of each class can also be selected on this page.
6 After adjusting the parameters, build the classifier by selecting the 'Build the model' button on the 'Model Builder' page.
7 Open the model for visualization by moving over to the 'Visualisation' tab. Both PCA and LDA views can be selected, rotated and saved.
8 Run a cross-validation on the model by selecting all groups and checking the 'Full group out' checkbox. Adjust the outlier calculation parameters and start the cross-validation. Once the cross-validation is finished, it can be viewed and saved under the 'Reports' tab.
9 Navigate to the 'Loading Plot' tab and select the loading plots of interest. The coefficients can be exported with the 'Export Loading' function. The valid mass/charge candidates with highest absolute value coefficients are selected for tandem MS analysis.
10 Navigate to the 'Home' tab and select the 'Export for Recognition' button. This will export the classifier into the real-time identification module.
11 Open the 'Recognition' software and select the previously exported model.
12 Adjust the intensity limit on the 'Settings' tab above the background TIC level of your acquired file. Adjust the outlier parameters (standard deviation–based, $n = 25$ by default) and select the number of scans to combine for each feedback. For quasi-real-time feedback, select 1.
13 Navigate to the 'Recognition tab'. First start the MS acquisition using the MS software, then select the file under acquisition from here and select 'play'. This will start the real-time identification of the currently acquired signal.

(Steps 49–51). The data analysis software is provided by the MS instrument vendors. The MassLynx software and Xcalibur have the ability to pre-process the acquired molecular profiles. The spectra pre-processing and peak list can also be created using the mMass open source MS tool[40,41]. To perform intra-sample and inter-sample comparisons, the peak lists are extracted to realize additional statistical analysis. Unsupervised or supervised computational statistical analysis such as principal components analysis (PCA), linear discriminant analysis (LDA) and classification models can be processed using additional software packages such as the Offline Model Builder (OMB) v.1.1.773.0.

Building a classification model

Sample cohorts comprising many samples can be classified using the OMB software package according to Box 3. The raw data files acquired on the Waters Q-TOF mass spectrometer are directly imported into the OMB software. The previously described pre-processing of the spectra can also be performed within the software. All of the imported spectra are then used to build PCA- and LDA-based classification models. The PCA is used to decrease the dimensionality of the datasets and generate a list of features showing the largest variance within the dataset. Subsequently, the features are subjected to supervised LDA through user-assigned classes. These classes are usually defined on the basis of tissue phenotypes. The LDA is used for a second space transformation, in which it minimizes the intra- (within) class variance and maximizes the inter- (between) class variance. By the nature of LDA, the more classes the user assigns, the more dimensions are necessary for the separation of these classes in the LDA space. Once a transformation matrix is calculated, any novel spectrum can be transformed to the LDA space, and Mahalanobis distances are calculated from each previously assigned class average. The algorithm will classify the novel spectrum into the closest class,

Box 4 | MS/MS analysis for molecular identification

This box describes the proper procedure for performing MS/MS analysis of selected precursor ions in either the Synapt or Q Exactive configuration. The analysis should be performed after the regular acquisitions in Step 48 and after identifying *m/z* values of interest. The ions in question should have an intensity sufficient to perform MS/MS analysis. In the case of the analysis in the Waters Q-TOF configuration, the intensity of the precursor ions should not be $<10^4$.

Procedure

1 For MS/MS analysis on the Synapt G2-S, follow option A; for analysis on the Q Exactive, follow option B (see 'Experimental design' section for details).

(A) **MS/MS analysis on Synapt G2-S** ● **Timing 10–15 min**

(i) During sample measurement acquisition, select MS/MS scan mode.

(ii) In the software, select the desired precursor ion mass ±0.5.

(iii) Tune the parameters to achieve an ~1 *m/z* isolation window. Note: In our preferred setting, the LM (low mass) and HM (high mass) parameters are set to 15.

(iv) Select a collision energy between 30 and 50 eV.

(v) Acquire MS/MS spectrum.

? TROUBLESHOOTING

(B) **MS/MS analysis on Q Exactive** ● **Timing 10–15 min**

(i) Acquire a full scan at 70,000 full width at half maximum resolving power (cantered at $m/z = 400$) and 1-s scan.

(ii) Switch to MS/MS 'on the fly'.

(iii) Use HCD with an isolation window of 0.8 *m/z*.

(iv) Acquire spectrum during the 30-s irradiation.

? TROUBLESHOOTING

unless the distance is larger than a user-defined n^* s.d. of that class. In this case, the spectrum will be marked as an outlier. The performance of LDA can be assessed by cross-validation. Cross-validation is performed by removing a part of the cohort and building the model again. To avoid bias in the data, usually a full group of samples (patients) is removed from the cohort before the PCA and LDA are recalculated. This step is iteratively and randomly performed for at least one-third of the total cohort. Each time, the model is built again, and the remaining samples are classified against the built model.

Evaluation and identification of molecular species

Statistically significant discriminative molecular species are further identified using MS/MS analysis according to Box 4. Tandem MS (MS/MS) analysis using low- or high-energy collision-induced dissociation ensures the creation of specific fragmentation patterns of selected precursor ions. MS/MS analysis can be performed on either of the selected mass analyzers. For higher mass accuracy, it is preferable to use the Q Exactive mass spectrometer because of the higher collision dissociation provided by the high-energy collision dissociation (HCD) fragmentation cell of the Q Orbitrap instrument. Identification of selected ions is performed directly from the tissue sections in real time by switching the mass analyzer between 'full-scan' and MS/MS modes. The resulting fragmentation spectra are then compared with the available online spectral databases, such as the LIPID MAPS Lipidomics Gateway and METLIN ('Equipment'). Additional confirmation can be performed by MS/MS analysis of a standard solution.

Materials

Biological materials

- *Cell lines of interest*. In the example described in this protocol, we use wild-type rat alveolar NR8383 macrophages (ATCC, cat. no. CRL-2192), NR8383 PC1/3 knockdown (KD) and NR8383 non-target (NT) shRNA cell lines. The NR8383 PC1/3 NT and KD lines were produced in-house[42]. We anticipate that our approach will be compatible with any cell type **! CAUTION** The cell lines used in your research should be regularly checked to ensure they are authentic and are not infected with mycoplasma.
- *Frozen animal tissue sections*. In the example described in this protocol, we use frozen (−80 °C) dog sarcoma tissue samples (from dog patients). We collected tumor material from 25 animals with different pathologies. Normal, healthy material was obtained from the same animal when possible during surgeries. Fresh tissues removed during the biopsy should immediately be snap-frozen and stored at −80 °C. Fresh-frozen tissue sections can be prepared by following our preferred protocol, described in the 'Reagent setup' section **! CAUTION** All experiments performed on animals must follow the '3 Rs' policy of refinement, reduction and replacement according to international, European and

national ethical standards for experimental research. All dog sarcoma samples used in this protocol were collected after signed consent from the owners and were in accordance with French ethical guidelines.

- Patient donors for in vivo human skin analysis **! CAUTION** All study participants must give their written, informed consent, which should be submitted to the appropriate ethics committee before participation in the study. In France, all work involving the use of biological samples from patients and databases must follow the 'Loi relative aux droits des malades', 4 March 2002; law 2002-303, modified in February 2010; European directive 95/46 CE; and law 78-17 from 6 January 1978 (modified law 94-548, modified on1 July 1994, decree 78-774, from 17 July 1978, modified decree 95-682 from 9 May 1995) ('Loi informatique et Liberté') (http://www.cnil.fr).

Reagents

- Methyl alcohol (≥99.8%; Sigma-Aldrich, cat. no. 320390) **! CAUTION** Methyl alcohol is a volatile, highly flammable solvent that is harmful upon skin contact and inhalation and toxic when swallowed. Use in a fume hood.
- Ethyl alcohol (dehydrated, HPLC grade; Biosolve) **! CAUTION** Ethyl alcohol is a flammable liquid and vapor. Use in a fume hood.
- 2-Propanol (LC–MS grade; Sigma-Aldrich) **! CAUTION** 2-Propanol is a flammable liquid and vapor. Use in a fume hood.
- Water (HPLC grade; Acros Organics, cat. no. 268300025)
- Ham's F-12K (Kaighn's) medium (Thermo Fisher Scientific, cat. no. 21127022)
- FBS (Thermo Fisher Scientific, cat. no. 16140-071)
- Paclitaxel (Taxol, 58 mM; Sigma-Aldrich, cat. no. T7191)
- Puromycin dihydrochloride (Thermo Fisher Scientific, cat. no. A11138-03)
- Bovine liver (100 g; Auchan) for system calibration
- Acetone, HPLC grade (VWR, cat. no. 01030602)
- Sodium formate solution (Sigma-Aldrich, cat. no. 51197-100ML)
- Liquid nitrogen for preparing tissue sections **! CAUTION** Liquid nitrogen causes severe burns. Handle with cold-resistant gloves and wear safety goggles.

Equipment

- Personalized protective equipment (PPE)
- Kimtech wipes (Kimberly–Clark)
- Volumetric flask (100 ml)
- Micropipettes (1,000, 200, 20 µl; Eppendorf)
- Poly-L-lysine-coated glass slides (Thermo Fisher, cat. no. 6776215) and British Standard Microscope slides (Thermo Fisher, cat. no. 10144633CF)
- Wheaton dry seal vacuum desiccator (Sigma-Aldrich, cat. no. Z74816)
- PTFE tube (3 m with 2.5-mm i.d.; Automation Direct, cat. no. PT4MNAT100)
- Tygon ND 100-65 tube (3 m with 2.4-mm i.d., 4-mm o.d.; VWR, cat. no. VERNADF00004 or Thermo Fisher Scientific, cat. no. 14-171-296.)
- OPO laser (tunable between 2.8 and 3.1 µm; Radiant v.1.0.1, Opotek) pumped by a pulsed Nd:YAG laser (pulse duration 5 ns, λ = 1,064 nm; Quantel)
- Biocompatible laser fiber (450-µm core diameter; 1 m; Infrared Fiber Systems)
- PM100D power meter (ThorLabs, dB Electronic Instruments)
- Microtome blades (Microtech, cat. no. MM35)
- Cryo-microtome (Leica, cat. no. CM 1510S)
- Mass analyzer (Q-TOF Synapt G2-S, Waters; Q-TOF Xevo, Waters; Q Exactive Orbitrap mass spectrometer, Thermo Fisher Scientific)
- CaF_2 window, 1/2" wedged, uncoated (ThorLabs, cat. no. WW50530)
- Computer (64-bit operating system, 64 GB RAM, Windows 10)
- Laser Viewing Cards (ThorLabs, cat. no. VRC6S)
- PEEK adapter 1/4"-28 male (Interchim, cat. no. 871233)
- REIMS interface (prototype, Waters)
- Paper towel, Bobine 450 FT Blanc (Ultracut, cat. no. 280121)
- Coverslip, thickness 0, 15 × 15 mm (Thermo Fisher Scientific, cat. no. BB01500150A0D3MNT0)
- Aluminum foil 100 m × 0.326 (Alupal)

Software and databases

- Offline Model Builder v.1.1.773.0 (Waters Research Center, Hungary)
- OMB Recognition v.1.1.857.0 (Waters Research Center, Hungary)
- CaseViewer v.1.15 (3DHistech, https://www.3dhistech.com/caseviewer)
- mMass open source MS tool (http://www.mmass.org/)
- Lipid identification database (LIPID MAPS Lipidomic Gateway, https://www.lipidmaps.org/)
- METLIN MS/MS metabolite database (Scripps Research, https://metlin.scripps.edu/)

Reagent setup

5 mM NaF solution

Pipette 40.5 ml of 2-propanol and 4.5 ml of LC/MS-grade water into a 100-ml volumetric flask. Cap and invert to mix. This produces a 90:10 (vol/vol) solution. Pipette 56 µl of 4 M sodium formate into the 90:10 (vol/vol) solution. Cap and invert to mix. Store up to 4 weeks at 2–8 °C.

Preparation of cells

Cell lines are cultured according to established protocols for the studied cell line. For example, culture wild-type NR8383 macrophages in Ham's F-12K medium supplemented with 15% (vol/vol) FBS. NR8383 PC1/3 KD[43] and NR8383 NT shRNA cell lines should be cultured in Ham's F-12K medium supplemented with 15% (vol/vol) FBS and 12 µg/ml puromycin. Culture cells in an incubator at 37 °C and 5% CO_2. In our example, cell lines are pre-activated with paclitaxel or not after 24-h incubation of the cell lines with the treatment[44]. After culture, centrifuge the cells for 15 min at 5,000*g* at RT. After centrifugation, remove the supernatant and aspirate 10 µl of the cell pellet. Place the 10 µl of cell pellet onto a glass slide and dry it using a vacuum dryer before analysis. The samples should be prepared and analyzed fresh.

Preparation of fresh-frozen tissue sections

Follow the procedure below to prepare fresh-frozen tissue sections.

1 After surgical removal, put the fresh tissues into cryogenic tubes and snap-freeze them in liquid nitrogen **! CAUTION** When handling liquid nitrogen, wear PPE.
2 When the tissues are thoroughly frozen, label and store them in a −80 °C freezer until use.
3 Before sectioning, place the tube containing the tissue in the cryo-microtome at −20 °C. **▲ CRITICAL** The cryo-sectioning temperature may vary depending on the tissue type. It should be set between −10 and −30 °C. Stabilize the tissue for 20 min. Cut the tissue into two halves.
4 Section the first half of the tissue into 10–20-µm-thick sections **! CAUTION** When sectioning the tissue sections, wear protective cutting gloves.
5 Thaw-mount an individual tissue section on a glass slide.
6 Section one slice of the second half of the tissue for histopathological examination (Box 1).
7 Store the samples at −80 °C until further use.
■ PAUSE POINT The fresh-frozen tissue sections can be stored up to 2 years in the −80 °C freezer.

Equipment setup

MS parameters

Use the following MS parameters for the Q Exactive instrument.

Instrument parameter	Setting
Scan type	Full MS
Scan range	200–1,800
Resolution	70,000
Microscans	1
AGC target	5.00×10^6
Maximum injection time	1,000 ms
Run time	0.2 min
Scan rate	3.7 scan/s
NSI source	
Capillary temperature	350 °C
S-lens RF level	50.0

Use the following MS parameters for the Waters Synapt G2 instrument.

Instrument parameter	Setting
LM (low mass) resolution	4.7
HM (high mass) resolution	15.0
Source temperature (°C)	80.0
Sampling cone	40.0
Source offset	50.0
Desolvation temperature (°C)	150.0
Pressure	**Setting**
Backing	6.79×10^{-1}
Source	1.37×10^{-3}
Sample plate	1.00×10^{-6}
Trap	6.64×10^{-3}
Helium cell	7.88×10^{-5}
IMS	1.28×10^{-4}
Transfer	6.40×10^{-3}
TOF	4.82×10^{-7}
Function parameter	**Setting**
Scan time (s)	1.0
Interscan time (s)	0.015
Start mass	100
End mass	1,600
Start time (min)	0
End time (min)	0.4
Data format	Continuum
Analyzer	Sensitivity mode

Procedure

Setup of the microsampling probe ● Timing 20 min

1 Check that the CaF_2 window (piece of the handpiece) is free of particles or tissue debris. To clean the window, first unscrew the ring holding the window. Remove the window from the funnel and place the window on a wet Kimtech wipe rinsed with methanol or acetone. Rub the window gently with the Kimtech wipe to avoid scratching. When the window is clean, place it back inside the funnel and screw it into the O-ring.

! CAUTION Gently clean the window to avoid scratching the surface.

2 Check that the metallic guide end is still 4 cm away from the lens (preliminary setting) so that it is within the range of the focal distance. This is confirmed when the spot of the red guide diode is focused.

3 Prepare a 3-m PTFE or Tygon tube.

4 Cut its end at a 45° angle.

5 Place and attach the beveled end immediately under the tip of the metallic guide, right above the site of ablation (Fig. 3).

Setup of the laser ● Timing 30–45 min

6 Switch on the cooling system and wait for 5–10 min.

7 Switch on the computer and then plug in the USB cable connecting the laser.

8 Switch on the Opotek system, using the switch at the rear.

▲ CRITICAL STEP Make sure the switch is turned in the right direction before switching on the laser in Step 10.

9 Start the Opotek control software.

? TROUBLESHOOTING

10 Switch on the flash lamp with the 'LAMP' button from the software. Wait for 5–10 min for the laser to produce stable energy (cooling *T* should reach 37 °C).

11 Place the optical fiber in the injection support 17 mm away from the exit of the injection lens.
▲ CRITICAL STEP Tighten it slightly to stabilize the fiber and make sure it is in a fixed position.
12 Place the second end of the fiber into the second output fiber holder. Leave ~2 cm from the exit.
! CAUTION Be careful when handling the optical fiber, because it is prone to breakage. In the case of breakage, see Box 2.
▲ CRITICAL STEP Tighten slowly.
13 On the Opotek software, switch on the red diode by clicking on the 'AD' checkbox.
14 Open the OPO shutter using the white rotating button at the top.
15 Check the fiber alignment in the injection system.
16 Adjust the position of the fiber with the *x* and *y* micro-adjustment screws.
▲ CRITICAL STEP Visually inspect the fiber entrance surface to check whether the laser beam is properly injected into the fiber. Observation of the red diode beam on the edge of the fiber indicates that the injection is not optimized. Upon optimized injection, the red light partially disappears.
17 Plug in the power meter and then set it to 2,940 nm and a 6–10 mJ maximum value (depending on your power meter sensor).
18 Place the sensor at the end of the microprobe, 1 cm after the focal point, to avoid burning the sensor.
19 On the Opotek software panel, set the energy to ~50%.
20 Switch on the Q-switch to make the laser shoot by pressing the 'LASER' button.
21 Examine the laser energy values on the power meter and adjust the laser position (coordinates *x*, *y* and *z*). The energy should be as high as possible.
22 Adjust the laser energy percentage to obtain 4–5 mJ.
23 Run an acquisition on the power meter for at least 1,000 shots.
▲ CRITICAL STEP The standard deviation of the energy should not be >20% of the laser energy; a higher value indicates that there is a problem with the laser.
24 Switch off the Q-switch by pressing the 'LASER' button and remove the power meter.
25 Examine the aspect of the beam at the focal point using thermal reactive paper. The red diode should be focused and neat in the following steps.
26 Using the '1 SHOT' button, the diameter of the impact on the thermal paper should be ~500 µm.
27 Verify that the diode is right under the Tygon ion guide.
▲ CRITICAL STEP The tube should be placed just above the focal point to ensure the proper aspiration and guiding of the ions to the mass spectrometer.
28 Attach the back end of the tube to the source interface of the desired mass analyzer.

Connection of the transfer line to an MS instrument

29 Connect the transfer line to a Waters Q-TOF instrument (option A) or a Q Exactive instrument (option B).

(A) **Connection of the transfer line to a Waters Q-TOF instrument** ● Timing **2 min**
(i) Connect the DC power supply to the bottom of the REIMS interface.
(ii) Switch on the DC power supply to heat up the collision surface inside the interface. The value should be set to 2.4 A, 3 V.
(iii) Connect the transfer tube to the transfer capillary. The o.d. of the capillary is 1.55 mm; thus the classic PEEK fitting is necessary to connect the 2.44-mm-i.d. Tygon tube tightly to it.
? TROUBLESHOOTING

(B) **Connection of the transfer line to a Q Exactive instrument** ● Timing **2 min**
(i) Place the extended transfer capillary on the ion block of the mass spectrometer.
(ii) Add the metal junction to this transfer capillary.
(iii) Connect the transfer tube to the extension.
? TROUBLESHOOTING

System optimization ● Timing 30–45 min

▲ CRITICAL We recommend performing routine analyses on bovine liver each day to check the reproducibility and stability of the results.

Preparation of a bovine tissue section (Steps 30–32)

30 Cut the bovine liver into small (~1 cm^3) pieces. Wrap them in aluminum foil and snap-freeze the pieces in liquid nitrogen.

! CAUTION Wear appropriate equipment when handling liquid nitrogen.
! CAUTION Wear protective gloves when handling the samples in the freezer.
■ PAUSE POINT The samples can be stored in a −80 °C freezer for up to 2 years before thaw-mounting.

31 Prepare 10- to 20-µm-thick tissue sections in a cryo-microtome.
! CAUTION Be careful when cleaning the cryo-microtome and sectioning the samples. The blades are very prone to causing cuts.

32 Thaw-mount the section onto poly-L-lysine-coated or regular glass slides.
■ PAUSE POINT The mounted sections can be stored at −80 °C for up to 2 years before analysis.

Evaluation of laser parameters (Steps 33–40)

33 Place the mounted section from Step 32 under the sampling probe.

34 Take the handpiece with the microprobe into your hands or stabilize it in a fixed position.
▲ CRITICAL STEP The sampling probe should be 2–3 mm from the sample. This way, the beveled side of the Tygon tube should be right above the sample surface for optimal collection of the expanding plume.

35 Start acquisition on the mass spectrometer software.
▲ CRITICAL STEP Ensure that the mass spectrometer is calibrated and ready for use before starting acquisition ('Equipment setup' section).

36 On the Opotek software, use the 'BURST' button to go to the dedicated window. Activate the laser with ten 4-mJ, 10-Hz bursts and move the sample during and between each burst.
! CAUTION Analysis performed on biological materials, or volatile or toxic compounds, should be performed under a certified fume/biological hood.
▲ CRITICAL STEP A suggested scheme of analysis is to begin and end the acquisition with a 10-s blank and fire three bursts separated by 10 s to let the TIC go back to its initial background level.

37 Stop the acquisition.

38 Evaluate the different parameters for substantial ion signal detection. This is done by looking at (i) the TIC mean value during firing, (ii) the intensity of the highest peak on the 10-s averaged MS spectrum and (iii) the qualitative aspect of the signal.
▲ CRITICAL STEP The evaluation must be performed in positive and negative ion mode polarity.
? TROUBLESHOOTING

39 Build a model of the bovine liver. It is convenient to build a model of the bovine liver in the OMB software. This way, you can directly upload the freshly analyzed sample and have a visual look at where it is situated in regard to the other samples.

40 Select the parameters for analysis on the basis of the evaluation in Steps 35–38.
▲ CRITICAL STEP For calibration of the Waters Synapt G2-S instrument, proceed to Steps 41–47. The calibration of the Q Exactive instrument should be performed according to the standard Thermo Fisher protocol (https://assets.thermofisher.com/TFS-Assets/CMD/Reference-Materials/WS-MS-Q-Exactive-Calibration-Maintenance-iQuan2016-EN.pdf).

(Optional) External calibration when using the REIMS interface ● Timing 15 min

41 When using the Waters Synapt G2-S instrument, tune the mass analyzer to the appropriate ion polarity and set the desired mass range.

42 Use a 5 mM NaF calibration solution ('Reagent setup' section) infused into the mass spectrometer REIMS interface at a flow rate of 0.2 ml/min.

43 Once the TIC is stable, run the NaF solution into the instrument for 2 min and record the file.

44 Open the recorded TIC and select all scans to combine for a spectrum.

45 Change the MS spectrum to centroid mode with the MassLynx 'Automatic Peak Detection' feature and save the centroid spectrum.

46 Use the 'save centroid spectrum' option to calibrate the instrument on the 'Tune Page': 'Setup' > 'Calibration' > 'Calibrate TOF window'.

47 A calibration can be accepted if both the RMS residual mass and the 95% confidence interval are <1 p.p.m. Save both the tuning parameters and system settings.

Sample analysis

48 Analyze the samples. For cell pellets, follow option A. For fresh-frozen tissue sections, follow option B. For in vivo analysis of skin, follow option C.

(A) **Analysis of cell pellets** ● Timing **10 min**

▲ CRITICAL For option A, cell cultures should be prepared according to the 'Reagent setup' section.

(i) Collect the cell pellets and pipette 10 µl onto a poly-L-lysine-coated or regular glass slide.
▲ CRITICAL STEP For replicates, spot three times, 10 µl per cell condition, on three zones.

(ii) Dry the samples in a vacuum desiccator for 10 min.

(iii) Place the glass slide under the laser sampling probe.
? TROUBLESHOOTING

(iv) For cell analysis, set the laser energy to 2 mJ/pulse.

(v) Start the acquisition on the mass spectrometer software with a scan time of 1 s for the Synapt G2-S and 200 ms for the Q Exactive instrument. Use the laser in burst mode. Usually, 50 shots are enough to ablate an entire deposition spot. For MS/MS analysis for molecular identification, see Box 4.

(vi) Repeat Step 48A(v) on three different cell depositions for each cell condition.
? TROUBLESHOOTING

(B) **Analysis of fresh-frozen tissue sections** ● Timing **20 min**

▲ CRITICAL For option B, fresh-frozen tissue sections should be prepared according to the 'Reagent setup' section. The second half of the tissue should be prepared for the histopathological examination according to Box 1. We recommend having the histopathological annotations ready before analysis of fresh-frozen tissue.

(i) Take the frozen tissue section 'Reagent setup' section) samples from the −80 °C freezer, place them at RT and let them warm for 1 min.

(ii) Place the sample under the sampling probe.
? TROUBLESHOOTING

(iii) Select tissue regions on the basis of external histopathological examination.

(iv) Acquire at least three molecular profiles of each selected region using 10-s irradiation steps in positive ion mode. For MS/MS analysis for molecular identification, see Box 4.

(v) Repeat Step 48B(iv) for each heterogeneous pre-selected region on the basis of the histopathological evaluation.

(vi) Repeat Step 48B(ii–v) on several slides.

(vii) Repeat Step 48B(ii–vi) for negative ion mode.
? TROUBLESHOOTING

■ PAUSE POINT Samples can be stored in a −80 °C freezer for up to 2 years for further MS/MS analysis, but avoid taking samples in and out of the freezer multiple times to limit sample degradation.

(C) **In vivo analysis of skin** ● Timing **5 min**

(i) Place the finger or skin underneath the sampling probe at a distance roughly corresponding to the focal distance.
? TROUBLESHOOTING

(ii) Start acquisition on the mass analyzer software and turn on the laser. For MS/MS analysis for molecular identification, see Box 4.

(iii) Move the finger or skin slowly under the irradiation for 30 s.
! CAUTION Do not ablate the skin for longer than five shots on the same spot to avoid too much skin damage and irritation.
▲ CRITICAL STEP Moving the skin allows the laser to ablate only the outermost part of the skin without going deep into the epidermis. One shot per location ensures that only the stratum corneum is ablated.

(iv) Switch off the laser.

(v) Average the spectra over the 30-s irradiation time of each measurement. Extract the TIC from the averaged spectra.
? TROUBLESHOOTING

Computational analysis ● Timing 30 min–1 h

49 Load the acquired spectra into the appropriate software.
▲ CRITICAL STEP The software selection will depend on the vendor of the mass spectrometer. In our laboratory, all the data collected on the Waters Q-TOF instruments are processed by the OMB v.1.1.773.0 classification software; see Box 3.

50 Depending on the quality of the spectra, apply pre-processing of the spectra, such as noise removal, baseline subtraction, binning and peak picking.
51 Select peaks that show statistical and significant differences in the discriminative analysis.
? TROUBLESHOOTING

Troubleshooting

Troubleshooting advice can be found in Table 1.

Table 1 | Troubleshooting table

Step	Problem	Possible reason	Solution
Any step	Breakage of the optical fiber	Mechanical damage or high force applied to the fiber	Polish the optical fiber. See Box 2 for further instructions
9	Software cannot find the laser	Communication problem between the laser and the computer	Restart the software and turn off and on the pump and OPO laser
29A(iii), 29B(iii)	No aspiration at the end of the tube	The connection between the transfer line and transfer capillary is not tight enough or the transfer capillary is blocked	Make sure there are no possible leaks at the connection or clean the transfer capillary
38, 48A(iii), 48B(ii), 48C(i)	Low signal intensity	The sample is not positioned at the focal point	Adjust the height of the sample or handpiece
38, 48A(vi), 48B(vii), 48C(v)	Decreasing signal intensity during acquisition	Unclean transfer tube or source interface	Replace or clean the transfer tube or clean the source interface according to standard laboratory practice. The tube can be cleaned with methanol
	Very low signal intensity	Problem with the coil heating	Replace the coil in the interface; make sure the wiring is correct
Box 4, step 1A(v) and 1B(iv)	No fragment ions when performing MS/MS analysis	Low collision energy	Increase the collision energy until you see fragmented ions

Timing

Steps 1–5, setup of microsampling probe: 20 min
Steps 6–28, setup of laser: 30–45 min
Step 29A, connection of transfer line to a Waters Q-TOF instrument: 2 min
Step 29B, connection of transfer line to a Q Exactive instrument: 2 min
Steps 30–40, system optimization: 30–45 min
Steps 41–47, external calibration when using the REIMS interface: 15 min
Step 48A, analysis of cell pellets: 10 min
Step 48B, analysis of fresh-frozen tissue sections: 20 min
Step 48C, in vivo analysis of skin: 5 min
Steps 49–51, computational analysis: 30 min–1 h
Box 1, histopathological examination: 10 min
Box 2, preparation and polishing of optical fiber: 1–2 h
Box 3, OMB classification: 30–45 min
Box 4, MS/MS analysis: 10–15 min

Anticipated results

In this protocol, we describe the correct setup of the microsampling probe to perform SpiderMass analysis. The SpiderMass system is an MS-based system with a broad range of applications depending on the research question at hand. Here, we discuss the anticipated results when analysis is performed under optimized conditions using the described setup in our laboratory.

Molecular profiles

The mass spectra acquired directly, from pieces of tissue, tissue sections (such as bovine liver samples), cell lines or skin, lie within the 200–1,200 mass range in both positive and negative ion mode. In a single acquisition, we are able to detect hundreds of molecular species. These molecules have been

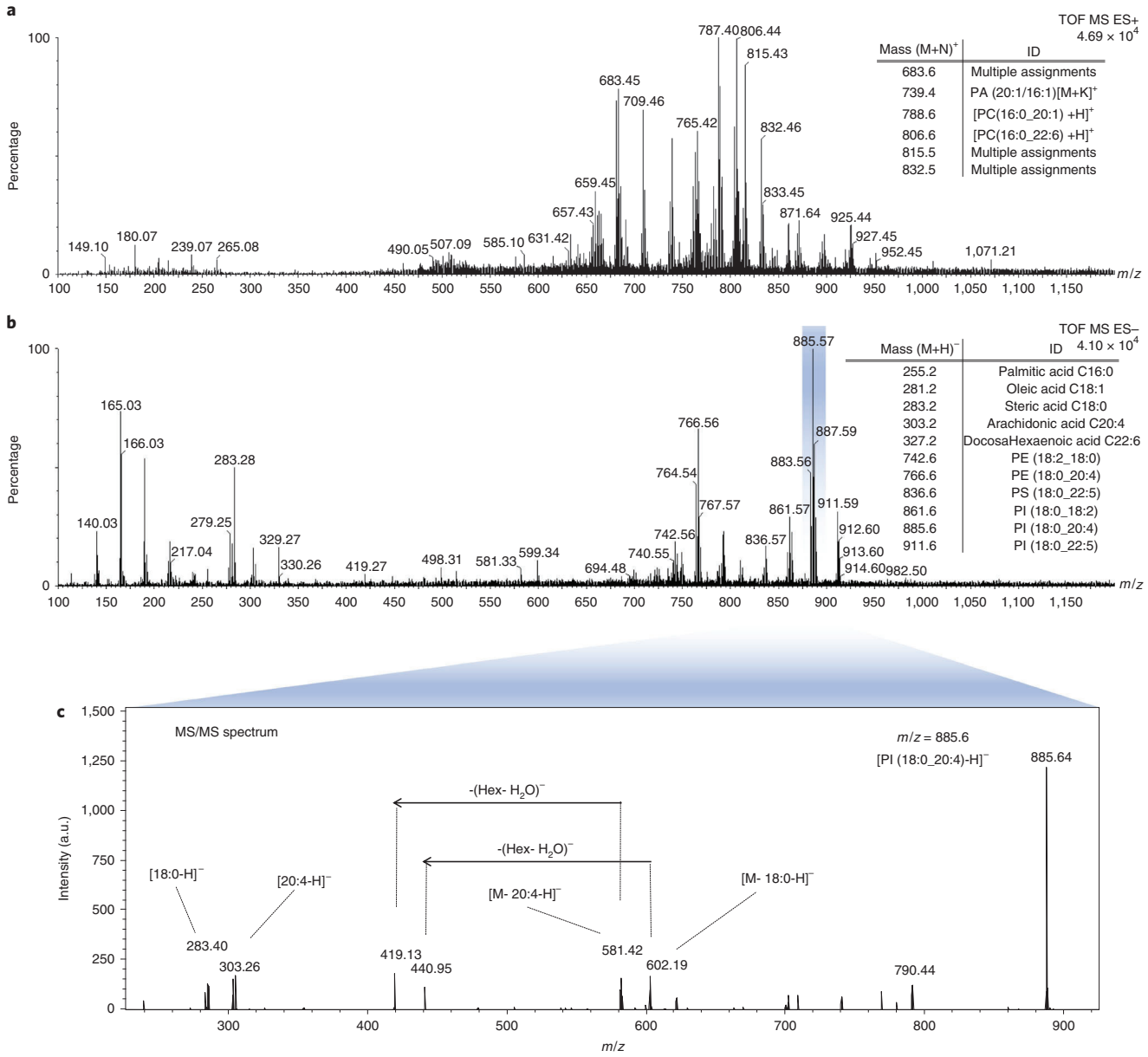

Fig. 5 | Typical MS spectra of bovine liver. a,**b**, SpiderMass-acquired positive (**a**) and negative (**b**) ion mode MS spectra of bovine liver with the Waters Synapt G2-S configuration. In the negative ion MS spectrum (**b**), a precursor ion is selected with an ~1-Da isolation window (*m/z* 885.6 ± 1 Da) and fragmented with 20–30 eV. **c**, Resulting MS/MS spectrum of *m/z* 885.6 parent ion acquired with 30 s of continuous irradiation with annotated resulting fragments. PI, phosphatidylinositol; PS phosphatidylserine; PE phosphatidylethanolamine; -(Hex- H_2O)$^-$ indicates loss of inositol; [M- 20:4-H]$^-$ indicates loss of arachidonic acid; [M- 18:0-H]$^-$ indicates loss of steric acid; [18:0-H]$^-$ steric acid; [20:4-H]$^-$ indicates loss of arachidonic acid; [PI (18:0_20:4-H]$^-$ is the phosphatidylinositol lipid with arachidonic and steric acid as fatty acid chains.

confirmed by MS/MS analysis and belong to different lipid and metabolite species, such as phospholipids (PC, phosphatidylcholine; PA, phosphatidic acid; PE, phosphatidylethanolamine; PG, phosphatidylglycerol; and PI, phosphatidylinositol), fatty acids, diacylglycerols and triacylglycerols[3,34]. In the negative ion mode, the lipid species are predominately detected as intact [M − H]$^-$ ions. The resulting MS/MS fragmentation patterns are deciphered manually and compared to available libraries, such as LIPID MAPS and METLIN, as well as to previous publications. An additional confirmation can be achieved with the MS/MS analysis of the external standard solutions. An example of the MS and MS/MS spectra (positive and negative ion modes) acquired from the 10-µm bovine liver sample using 10-s irradiation at 5-mJ laser energy coupled to the Synapt G2 mass analyzer is shown in Fig. 5. The MS/MS of the selected $m/z = 885.5$ was performed using 30-V collision energy. The fragmentation pattern was manually annotated and compared to spectral libraries.

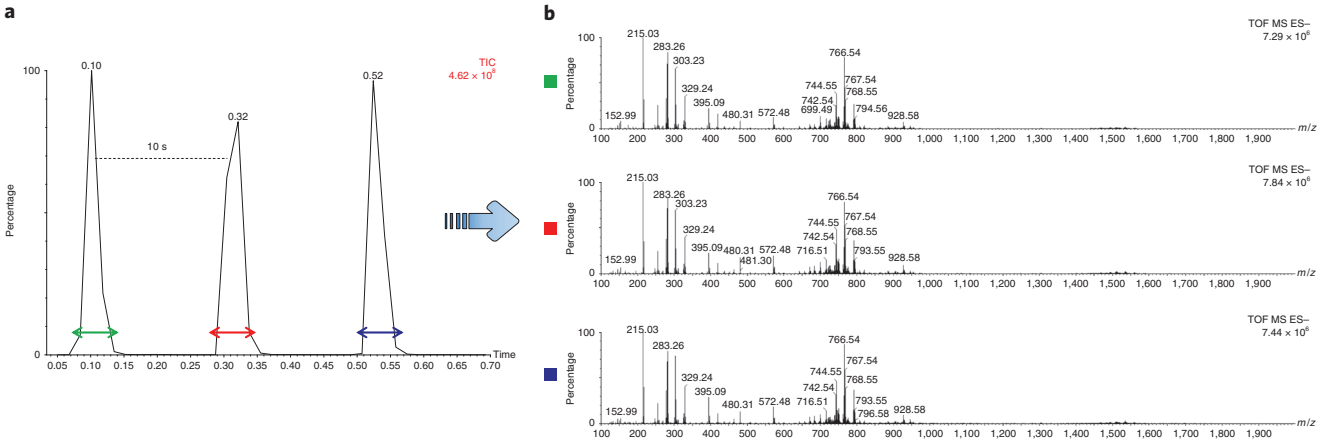

c

Single acquisition (n = 3)		Mean	σ	CV
Negative ion mode	TIC	7.55×10^6	2.87×10^5	0.04
	m/z = 283.2 (a.i.)	1.19×10^5	7.73×10^4	0.07
	m/z = 766.6 (a.i.)	7.58×10^5	4.65×10^4	0.06
	No. of peaks detected	860	9.17	0.01

Systematic analysis (n = 50)		Mean	σ	CV
Positive ion mode	TIC	9.27×10^6	8.90×10^6	0.97
	m/z = 683.5 (a.i.)	1.03×10^4	3.14×10^3	0.30
	m/z = 788.6 (a.i.)	2.84×10^4	2.30×10^4	0.81
	No. of peaks detected	916	45.00	0.05
Negative ion mode	TIC	6.53×10^6	3.08×10^6	0.47
	m/z = 283.2 (a.i.)	4.01×10^5	3.00×10^5	0.74
	m/z = 766.6 (a.i.)	6.46×10^5	3.47×10^5	0.54
	No. of peaks detected	813	77.04	0.09

Fig. 6 | Reproducibility experiment. SpiderMass acquisitions of bovine liver in positive and negative ion mode using the Q-TOF configuration. **a**, Chromatogram of a single acquisition using three repetitions of ten bursts with a 10-s pause in negative ion mode. The arrows indicate the TIC regions for extraction of the molecular profiles. **b**, Extracted molecular profiles of the individual chromatographic peaks. **c**, Tables of calculated mean, σ and CV values for a single acquisition and systematic analysis (n = 50).

Reproducibility

The molecular profiles obtained in both positive and negative ion modes are highly reproducible. With daily systematic analysis of bovine liver tissue pieces or 10- to 20-µm sections, we obtain the same molecular profiles with similar relative intensities between the different ions. With respect to absolute intensities, these are dependent on the mass analyzer used. On average, these are between 10^4 and 10^6 for the most intense peaks. There is no variability in molecular profile when analyzing dried, thawed tissue sections or small pieces of tissue. The reproducibility was tested using 20-µm bovine liver sections on the Q-TOF configuration by calculating the similarity of spectra (mean, standard deviation (σ) and coefficient of variance (CV)). The data were acquired by following Steps 33–39. The raw spectra were extracted and processed using mMass. The similarity was calculated for the TIC, selected ion intensities and number of peaks after applying the peak picking. The peak picking was performed using a signal-to-noise ratio of 3 as a threshold, with applied baseline subtraction and smoothing. In the first instance, we evaluated the single-acquisition reproducibility. Each acquisition comprises three molecular profiles during ten bursts (Fig. 6a). The extracted molecular profiles are shown in Fig. 6b. The calculated mean, σ and CV are shown in Fig. 6c. The CV values are all <0.1, which shows very low variance within a single acquisition. In the second instance, the reproducibility was tested on a larger cohort acquired at different time points. The mean, σ and CV were calculated for n = 50, using the same parameters as for the single acquisition (Fig. 6c). All the calculated values are CV < 1, which indicates good reproducibility and stability of the system.

Classification model

Through the OMB software, it is possible to build a classification model for any type of analyte. Figure 7 shows an example of how the OMB software classifies dog sarcoma samples in a two-class model discriminating healthy from cancerous tissue types (Fig. 7a) from positive ion mode spectra. Cancerous and healthy tissue molecular profiles were manually determined on the basis of histology. Within each distinct histopathological area, we observed a specific molecular profile and intra-sample

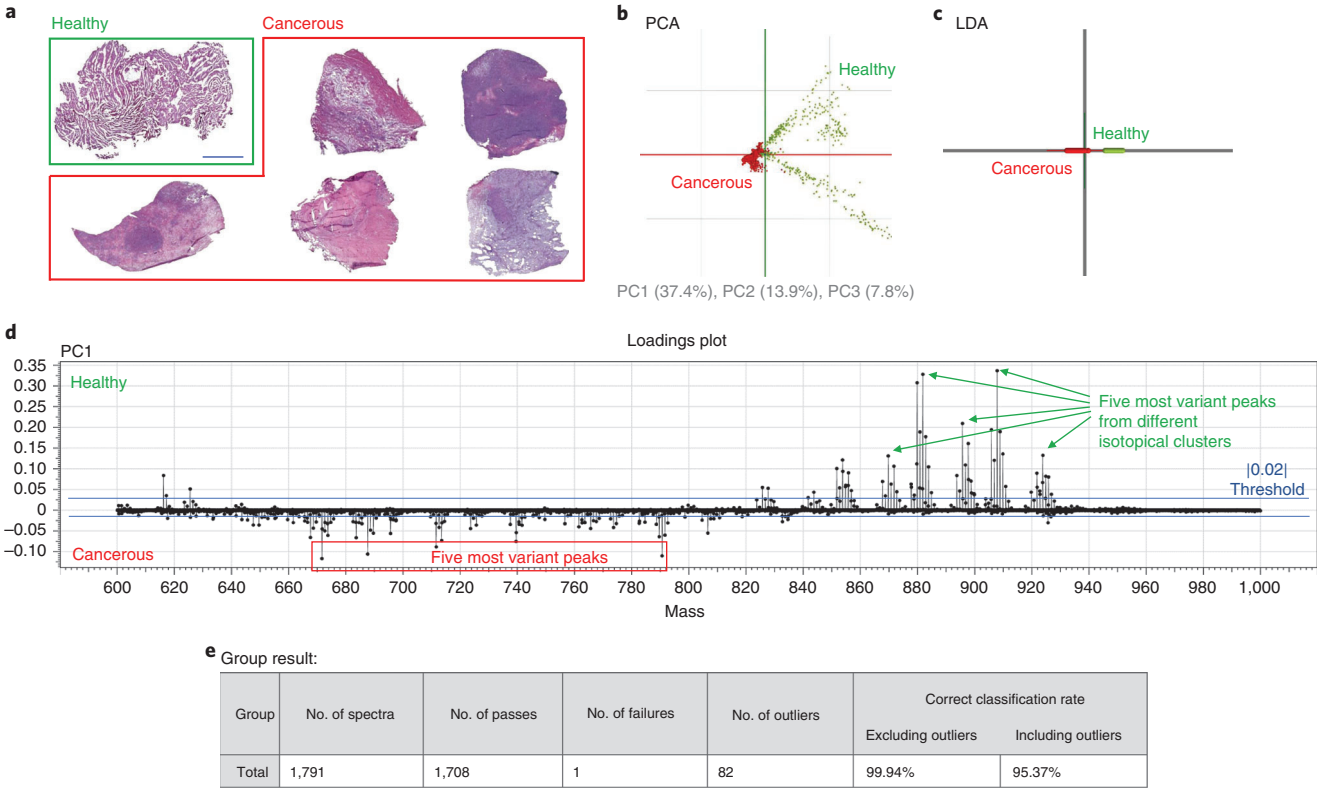

e Group result:

Group	No. of spectra	No. of passes	No. of failures	No. of outliers	Correct classification rate	
					Excluding outliers	Including outliers
Total	1,791	1,708	1	82	99.94%	95.37%

Fig. 7 | Two-class classification of 33 dog sarcoma samples. a, Examples of histopathological stains of healthy (green) and cancerous (red) tissue obtained during biopsies. Scale bar, 2,000 µm. **b**, Resulting two-class PCA using OMB software with same color scheme as in **a**. **c**, Resulting two-class linear discriminant analysis. **d**, Loadings plot from PC1 showing the most variant peaks (those best discriminating between healthy and cancerous tissues) with a 0.02 threshold. **e**, Cross-validation table from the leave-one-out method in the OMB software. Appropriate institutional review board permission was obtained for handling the material.

heterogeneity. We then used 33 samples (1,791 spectra) to build the PCA (Fig. 7b) and LDA (Fig. 7c) classification model. The first principal component (PC1) describes 37.4% variance, whereas PC2 and PC3describe 13.9% and 7.8% variance, respectively. Extraction of the top five loadings shows that the most discriminative ions are those at *m*/*z* 671.6, 687.6, 711.6, 739.6, 790.6 for cancerous tissue and those at *m*/*z* 870.8, 881.8, 895.8, 907.9, 923.9 for healthy tissue (Fig. 6d). The cross-validation method using leave-one-out for the two-class model showed a correct classification rate of 99.94% excluding outliers and 95.37% including outliers (Fig. 6e). The results show that the obtained molecular profiles for healthy and cancerous tissues are in fact reproducible and can be properly classified with the built model. Further data processing and a detailed explanation of the results can be found elsewhere[34].

Reporting Summary

Further information on research design is available in the Nature Research Reporting Summary linked to this article.

Data availability

All published data presented here are publicly available and can be found in the PRIDE Archive (https://www.ebi.ac.uk/pride/archive/). The dog sarcoma data are available from the ProteomeXchange Consortium (PXD010990), Real-time molecular diagnosis of tumors using water-assisted laser desorption/ionization mass spectrometry technology.

References

1. Takats, Z., Strittmatter, N. & McKenzie, J. S. Ambient mass spectrometry in cancer research. *Adv. Cancer Res.* **134**, 231–256 (2017).
2. Zhang, J. et al. Nondestructive tissue analysis for ex vivo and in vivo cancer diagnosis using a handheld mass spectrometry system. *Sci. Transl. Med.* **9**, eaan3968 (2017).

3. Fatou, B. et al. In vivo real-time mass spectrometry for guided surgery application. *Sci. Rep.* **6**, 25919 (2016).
4. Balog, J. et al. Intraoperative tissue identification using rapid evaporative ionization mass spectrometry. *Sci. Transl. Med.* **5**, 194ra93 (2013).
5. Huang, M.-Z., Cheng, S.-C., Cho, Y.-T. & Shiea, J. Ambient ionization mass spectrometry: a tutorial. *Anal. Chim. Acta* **702**, 1–15 (2011).
6. Alberici, R. M. et al. Ambient mass spectrometry: bringing MS into the "real world". *Anal. Bioanal. Chem.* **398**, 265–294 (2010).
7. Takáts, Z., Wiseman, J. M., Gologan, B. & Cooks, R. G. Mass spectrometry sampling under ambient conditions with desorption electrospray ionization. *Science* **306**, 471–473 (2004).
8. Laiko, V. V., Baldwin, M. A. & Burlingame, A. L. Atmospheric pressure matrix-assisted laser desorption/ionization mass spectrometry. *Anal. Chem.* **72**, 652–657 (2000).
9. Laiko, V. V. et al. Desorption/ionization of biomolecules from aqueous solutions at atmospheric pressure using an infrared laser at 3 μm. *J. Am. Soc. Mass Spectrom.* **13**, 354–361 (2002).
10. Nemes, P. & Vertes, A. Laser ablation electrospray ionization for atmospheric pressure molecular imaging mass spectrometry. *Methods Mol. Biol.* **656**, 159–171 (2010).
11. Nemes, P., Woods, A. S. & Vertes, A. Simultaneous imaging of small metabolites and lipids in rat brain tissues at atmospheric pressure by laser ablation electrospray ionization mass spectrometry. *Anal. Chem.* **82**, 982–988 (2010).
12. Sampson, J. S., Hawkridge, A. M. & Muddiman, D. C. Generation and detection of multiply-charged peptides and proteins by matrix-assisted laser desorption electrospray ionization (MALDESI) Fourier transform ion cyclotron resonance mass spectrometry. *J. Am. Soc. Mass Spectrom.* **17**, 1712–1716 (2006).
13. Wu, C., Dill, A. L., Eberlin, L. S., Cooks, R. G. & Ifa, D. R. Mass spectrometry imaging under ambient conditions. *Mass Spectrom. Rev.* **32**, 218–243 (2013).
14. Chen, H., Talaty, N. N., Takáts, Z. & Cooks, R. G. Desorption electrospray ionization mass spectrometry for high-throughput analysis of pharmaceutical samples in the ambient environment. *Anal. Chem.* **77**, 6915–6927 (2005).
15. Talaty, N., Takáts, Z. & Cooks, R. G. Rapid in situ detection of alkaloids in plant tissue under ambient conditions using desorption electrospray ionization. *Analyst* **130**, 1624–1633 (2005).
16. Takáts, Z., Wiseman, J. M. & Cooks, R. G. Ambient mass spectrometry using desorption electrospray ionization (DESI): instrumentation, mechanisms and applications in forensics, chemistry, and biology. *J. Mass Spectrom.* **40**, 1261–1275 (2005).
17. Katona, M., Dénes, J., Skoumal, R., Tóth, M. & Takáts, Z. Intact skin analysis by desorption electrospray ionization mass spectrometry. *Analyst* **136**, 835–840 (2011).
18. Hayashi, Y. et al. Intact metabolite profiling of mouse brain by probe electrospray ionization/triple quadrupole tandem mass spectrometry (PESI/MS/MS) and its potential use for local distribution analysis of the brain. *Anal. Chim. Acta* **983**, 160–165 (2017).
19. Zaitsu, K. et al. Intact endogenous metabolite analysis of mice liver by probe electrospray ionization/triple quadrupole tandem mass spectrometry and its preliminary application to in vivo real-time analysis. *Anal. Chem.* **88**, 3556–3561 (2016).
20. Zaitsu, K. et al. In vivo real-time monitoring system using probe electrospray ionization/tandem mass spectrometry for metabolites in mouse brain. *Anal. Chem.* **90**, 4695–4701 (2018).
21. Liu, J., Cooks, R. G. & Ouyang, Z. Biological tissue diagnostics using needle biopsy and spray ionization mass spectrometry. *Anal. Chem.* **83**, 9221–9225 (2011).
22. Song, Y., Liao, J., Zha, C., Wang, B. & Liu, C. C. A novel approach to determine the tyrosine concentration in human plasma by DART-MS/MS. *Anal. Methods* **7**, 1600–1605 (2015).
23. Zhou, M., McDonald, J. F. & Fernández, F. M. Optimization of a direct analysis in real time/time-of-flight mass spectrometry method for rapid serum metabolomic fingerprinting. *J. Am. Soc. Mass Spectrom* **21**, 68–75 (2010).
24. Schäfer, K.-C. et al. In vivo, in situ tissue analysis using rapid evaporative ionization mass spectrometry. *Angew. Chem. Int. Edn* **48**, 8240–8242 (2009).
25. Phelps, D. L. et al. The surgical intelligent knife distinguishes normal, borderline and malignant gynaecological tissues using rapid evaporative ionisation mass spectrometry (REIMS). *Br. J. Cancer* **118**, 1349–1358 (2018).
26. St John, E. R. et al. Rapid evaporative ionisation mass spectrometry of electrosurgical vapours for the identification of breast pathology: towards an intelligent knife for breast cancer surgery. *Breast Cancer Res.* **19**, 59 (2017).
27. Balog, J. et al. In vivo endoscopic tissue identification by rapid evaporative ionization mass spectrometry (REIMS). *Angew. Chem. Int. Edn* **54**, 11059–11062 (2015).
28. Sans, M. et al. Performance of the MasSpec Pen for rapid diagnosis of ovarian cancer. *Clin. Chem.* **65**, 674–683 (2019).
29. Fournier, I. et al. Device for real-time in vivo molecular analysis. WO2016046748 (A1) (2014).
30. Schäfer, K.-C. et al. In situ, real-time identification of biological tissues by ultraviolet and infrared laser desorption ionization mass spectrometry. *Anal. Chem.* **83**, 1632–1640 (2011).
31. Berkenkamp, S., Karas, M. & Hillenkamp, F. Ice as a matrix for IR-matrix-assisted laser desorption/ionization: mass spectra from a protein single crystal. *Proc. Natl Acad. Sci. USA* **93**, 7003–7007 (1996).
32. Pirkl, A., Soltwisch, J., Draude, F. & Dreisewerd, K. Infrared matrix-assisted laser desorption/ionization orthogonal-time-of-flight mass spectrometry employing a cooling stage and water ice as a matrix. *Anal. Chem.* **84**, 5669–5676 (2012).

33. Fatou, B. et al. Remote atmospheric pressure infrared matrix-assisted laser desorption-ionization mass spectrometry (remote IR-MALDI MS) of proteins. *Mol. Cell. Proteomics* **17**, 1637–1649 (2018).
34. Saudemont, P. et al. Real-time molecular diagnosis of tumors using water-assisted laser desorption/ionization mass spectrometry technology. *Cancer Cell* **34**, 840–851 (2018).
35. Fatou, B. et al. Real time and in vivo pharmaceutical and environmental studies with SpiderMass instrument. *J. Biotechnol.* **281**, 61–66 (2018).
36. Fatou, B., Salzet, M. & Fournier, I. Real time human micro-organisms biotyping based on water-assisted laser desorption/ionization. *EuroBiotech J.* **3**, 97–104 (2019).
37. Woolman, M. et al. Rapid determination of medulloblastoma subgroup affiliation with mass spectrometry using a handheld picosecond infrared laser desorption. *Chem. Sci.* **8**, 6508–6519 (2017).
38. Zou, J. et al. Ambient mass spectrometry imaging with picosecond infrared laser ablation electrospray ionization (PIR-LAESI). *Anal. Chem.* **87**, 12071–12079 (2015).
39. Woolman, M. et al. Optimized mass spectrometry analysis workflow with polarimetric guidance for ex vivo and in situ sampling of biological tissues. *Sci. Rep.* **7**, 468 (2017).
40. Strohalm, M., Hassman, M., Košata, B. & Kodíček, M. mMass data miner: an open source alternative for mass spectrometric data analysis. *Rapid Commun. Mass Spectrom.* **22**, 905–908 (2008).
41. Strohalm, M., Kavan, D., Novák, P., Volný, M. & Havlíček, V. mMass 3: a cross-platform software environment for precise analysis of mass spectrometric data. *Anal. Chem.* **82**, 4648–4651 (2010).
42. Gagnon, H. et al. Proprotein convertase 1/3 (PC1/3) in the rat alveolar macrophage cell line NR8383: localization, trafficking and effects on cytokine secretion. *PLoS ONE* **8**, e61557 (2013).
43. Duhamel, M. et al. Molecular consequences of proprotein convertase 1/3 (PC1/3) inhibition in macrophages for application to cancer immunotherapy: a proteomic study. *Mol. Cell. Proteomics* **14**, 2857–2877 (2015).
44. Duhamel, M. et al. Paclitaxel treatment and proprotein convertase 1/3 (PC1/3) knockdown in macrophages is a promising antiglioma strategy as revealed by proteomics and cytotoxicity studies. *Mol. Cell. Proteomics* **17**, 1126–1143 (2018).

Acknowledgements

We thank all members of SATT-Nord involved in SpiderMass and, in particular, E. Rollet and F.-X. Denimal for their support of the project. This work was funded by the Ministère de l'Enseignement Supérieur, de la Recherche et de l'Innovation, Université de Lille and Inserm. The project was also funded by ANR-14-CE17-0021 REALITY'MS (I.F.), Inserm Programme PhysiCancer SPIDERMASS (M.S.), Région Hauts de France-EU FEDER O'DREAMS (D.T., I.F. and M.S.) and SIRIC ONCOLille grant INCa-DGOS-Inserm 6041aa (D.T., I.F. and M.S.). SpiderMass was awarded Best Breakthrough Innovation Prize by the MATWIN 2015 international board.

Author contributions

N.O., P.S. and J.B. wrote the original draft of the manuscript. P.S., N.O. and J.-P.G. carried out the experiments. P.S. and I.F. developed the technique. Q.P. collected the samples and performed the histology. Y.-M.R. did histology and validated diagnostics. P.S., J.B. and I.F. analyzed the data. I.F., M.S. and D.T. designed the study. I.F., M.S. and Z.T. corrected the manuscript. I.F. and M.S. supervised the project and provided the funding.

Competing interests

J.B. is an employee of Waters Research Center. M.S. and I.F. are inventors on a patent (priority no. WO2015IB57301 20150922) related to part of the described protocol. Q.P. is an employee of OCR. D.T. is founder and CEO of OCR. Z.T. is a consultant for Waters Corporation. The system is under protection by patent CA2961491 A1 (29). The remaining authors declare no competing interests.

Additional information

Supplementary information is available for this paper at https://doi.org/10.1038/s41596-019-0217-8.

Reprints and permissions information is available at www.nature.com/reprints.

Correspondence and requests for materials should be addressed to M.S. or I.F.

Publisher's note Springer Nature remains neutral with regard to jurisdictional claims in published maps and institutional affiliations.

Received: 26 December 2018; Accepted: 14 June 2019;
Published online: 9 October 2019

Related links
Key references using this protocol
Fatou, B. et al. *Sci. Rep.* **6**, 25919 (2016): https://www.nature.com/articles/srep25919
Fatou, B. et al. *J. Biotechnol.* **281**, 61–66 (2018): https://www.sciencedirect.com/science/article/pii/S0168165618305169
Saudemont, P. et al. *Cancer Cell* **34**, 840–851.E4 (2018): https://www.cell.com/cancer-cell/fulltext/S1535-6108(18)30423-9

nature research

Corresponding author(s): Isabelle Fournier and Michel Salzet

Last updated by author(s): May 28, 2019

Reporting Summary

Nature Research wishes to improve the reproducibility of the work that we publish. This form provides structure for consistency and transparency in reporting. For further information on Nature Research policies, see Authors & Referees and the Editorial Policy Checklist.

Statistics

For all statistical analyses, confirm that the following items are present in the figure legend, table legend, main text, or Methods section.

n/a	Confirmed
☐	☒ The exact sample size (*n*) for each experimental group/condition, given as a discrete number and unit of measurement
☐	☒ A statement on whether measurements were taken from distinct samples or whether the same sample was measured repeatedly
☐	☒ The statistical test(s) used AND whether they are one- or two-sided *Only common tests should be described solely by name; describe more complex techniques in the Methods section.*
☒	☐ A description of all covariates tested
☒	☐ A description of any assumptions or corrections, such as tests of normality and adjustment for multiple comparisons
☒	☐ A full description of the statistical parameters including central tendency (e.g. means) or other basic estimates (e.g. regression coefficient) AND variation (e.g. standard deviation) or associated estimates of uncertainty (e.g. confidence intervals)
☒	☐ For null hypothesis testing, the test statistic (e.g. *F*, *t*, *r*) with confidence intervals, effect sizes, degrees of freedom and *P* value noted *Give P values as exact values whenever suitable.*
☒	☐ For Bayesian analysis, information on the choice of priors and Markov chain Monte Carlo settings
☐	☒ For hierarchical and complex designs, identification of the appropriate level for tests and full reporting of outcomes
☒	☐ Estimates of effect sizes (e.g. Cohen's *d*, Pearson's *r*), indicating how they were calculated

Our web collection on statistics for biologists contains articles on many of the points above.

Software and code

Policy information about availability of computer code

Data collection	MassLynxV4.1 software (Waters) Synapt G2S experiments, Xcalibur Software v4.0 or QExactive measurements
Data analysis	MassLynxV4.1 software (Waters) Synapt G2S experiments;Xcalibur Software v4.0 or QExactive measurements; Offline Model Builder, v1.1.773.0 (Waters research centre); OMB Recognition,v.1.1.857.0 (Waters research centre)

For manuscripts utilizing custom algorithms or software that are central to the research but not yet described in published literature, software must be made available to editors/reviewers. We strongly encourage code deposition in a community repository (e.g. GitHub). See the Nature Research guidelines for submitting code & software for further information.

Data

Policy information about availability of data

All manuscripts must include a data availability statement. This statement should provide the following information, where applicable:

- Accession codes, unique identifiers, or web links for publicly available datasets
- A list of figures that have associated raw data
- A description of any restrictions on data availability

The raw data sets have been deposited on the local server. Data collected to build the classification models have been deposited to the ProteomeXchange: consortium: PXD010990

Field-specific reporting

Please select the one below that is the best fit for your research. If you are not sure, read the appropriate sections before making your selection.

☒ Life sciences ☐ Behavioural & social sciences ☐ Ecological, evolutionary & environmental sciences

For a reference copy of the document with all sections, see nature.com/documents/nr-reporting-summary-flat.pdf

Life sciences study design

All studies must disclose on these points even when the disclosure is negative.

Sample size	The size of the sample biopsies was dependent on the veterinarian recruitment after sarcoma surgeries and all sarcoma samples were included, regardless of the origin.
Data exclusions	No patients or generated data were excluded from the study and outliers were defined per se when their value was more than 5 times the SD of the mean.
Replication	The samples included 25 different patient material. Samples were differentiated by histology between tumour (n=25) and healthy (n=6) tissue. All samples were analyzed at 5 different locations to replicate the measurements.
Randomization	Samples were not randomized by analyzed along inclusion in blind.
Blinding	The data was collected and processed in blind after keeping the anonymity of the patients using internal laboratory labeling

Reporting for specific materials, systems and methods

We require information from authors about some types of materials, experimental systems and methods used in many studies. Here, indicate whether each material, system or method listed is relevant to your study. If you are not sure if a list item applies to your research, read the appropriate section before selecting a response.

Materials & experimental systems

n/a	Involved in the study
☒	☐ Antibodies
☒	☐ Eukaryotic cell lines
☒	☐ Palaeontology
☐	☒ Animals and other organisms
☒	☐ Human research participants
☒	☐ Clinical data

Methods

n/a	Involved in the study
☒	☐ ChIP-seq
☒	☐ Flow cytometry
☒	☐ MRI-based neuroimaging

Animals and other organisms

Policy information about studies involving animals; ARRIVE guidelines recommended for reporting animal research

Laboratory animals	No laboratory animals were used in the study
Wild animals	No wild animals were used in the study
Field-collected samples	Immediately after removal the tissues were snap frozen in liquid nitrogen and stored in the -80°C before further analysis. Prior to sectioning the tissue should be thawed at -20°C in the cryo-microtome. The tissues are halved using a metallic tissue cutting matrix. The first half of the tissue is sectioned into 10µm thin sections and thaw-mounted on the glass slide. The samples are than stored in the -80°C prior to analysis.
Ethics oversight	For dog patients, all sarcoma samples were collected after the signed consent from the owners and within the respect of French ethical guidelines. This means that no tissue was collected for the only purpose of the research and that analyzed tissues were obtained from the biopsies performed for the normal diagnostic.

Note that full information on the approval of the study protocol must also be provided in the manuscript.

B. Conclusion

In this article, we extensively presented the SpiderMass experimental approach, and everything needed to reproduce the experiments. We took care of detailing the sample preparation, whether it consist of analysing cell cultures, samples slice or pieces of tissues. The system maintenance and some troubleshooting scenarios have been detailed. It shows that the system is easy to operate for MS profiling but also identification by real time fragmentation (MSMS). The statistical approaches are conducted using a proven and reliable software. One of the main limitations of the system come from the low robustness of the microsampling probe. Indeed, the laser fibre is still very brittle and prone to breakage. Also, we observe some variations coming from the laser that could induce an increased need for polishing. Still, in our routine practise, we tend to move the sample under the fixed laser handprobe wo this is not an issue. Work is being done to come up with a new generation of lasers, smaller and more robust including an easier “plug-and-play” system to replace the laser fibre. This new generation is also planned to have variable focusing elements to narrow or widden the beam size as well. The first case will be used when higher lateral resolution is needed and the second for large area screening. Another aspect is the automation of the acquistion to enable MS imaging with the SpiderMass system. This is currently under development both for 2D imaging uwith a controled (x,y) plate moving under the laser beam or for 3D topographical imaging mounting the laser probe of the SpiderMass on a stiff robotic arm[189]. Finally the interface is also an aspect that will need further developments. Yet, a well operational interface has been setup for the Waters instruments but robust dedicated intefraces have to be developed for other instruments such a orbitraps or Q-TOF from Bruker. The last but not the least is to look for further instrument of the mass analyzer itself in order to get a system that would be easily transportable and fully filling the requirements of the real-environnement whether it is a dermatological office or an operating room. Looking in this direction, the last Orbitrap generations which are only 534 × 763 × 703 mm (w, d, h) helds great promises.

Chapter IV

Proof of Concept in the Veterinary Environment

SpiderMass Prototype inside the Oncovet surgery room. Left, General arrangement of the surgery room at the veterinary clinic with the SpiderMass prototype installed beside the surgical table. B. Picture of surgeon with the handled laser microprobe ready to be used during the surgery. Reprinted from Saudemont et al.[1]

Philippe Saudemont & Jusal Quanico, Yves-Marie Robin, Anna Baud, Julia Balog, Benoit Fatou, Dominique Tierny, Quentin Pascal, Kevin Minier, Mélissa Pottier, Cristian Focsa, Michael Ziskind, Zoltan Takats, Michel Salzet and Isabelle Fournier

Cancer Cell, 2018

CHAPTER IV: Proof of Concept in the veterinary environment

A. Introduction

Progressing from a lab prototype to a medical device is not a quick and easy journey. The first published prototype needed to be improved on both the laser and the MS system leading to the second generation that has been presented in the previous chapter. To proof the concept, we decided to conduct a first clinical study where we could assess the performances of the system for tissue classification and the adequation of the system for its use directly during surgeries. We worked within the context of a close collaboration with a specialised veterinary clinic "Oncovet". Very interestingly, Oncovet which is a unique model in Europe for treating pets with cancer is on the same campus as our lab.

In agreement with the veterinarians, we mounted a cohort of dog patients with sarcoma. Sarcomas, or soft tissue tumours are a class of extremely heterogeneous lesions arising from mesenchymal tissues like fat, connective tissues, muscles, etc. Their morphological differentiation is complex and assessed by histological staining, immunostaining or *in situ* hybridisation i.e. In human, the first diagnosis is obtained by imaging means combined with blood marker assays. However, the final diagnosis is established on the gold standard histological examination of the anatomic pieces obtained from biopsy or during surgeries. In this last condition, the extemporaneous examination can be challenging to provide rapid, accurate or precise diagnosis. Although these tests provide precise information, they do not guaranty a known clinical evolution of the tumour between benign and malignant. For example pleomorphic lipoma and pleomorphic liposarcoma are morphologically almost identical but the first is benign and the second highly malignant[190,191]. These considerations outline the need of a validated molecular *in vivo* techniques for rapid and accurate classification to improve the diagnosis accuracy and give preliminary information instantaneously.

Sarcoma was chosen because of i) its indication on excision margin delineation, being a real issue in sarcoma during the surgery, ii) the recruitment capacity at the clinic and iii) the very high heterogeneity of sarcoma, making it a model of interest for further testing of the SpiderMass performances.

In this paper our goal was to evaluate the performance of a SpiderMass protype in the generation of molecular profiles on *ex vivo* sarcoma biopsies as well as describing its implementation in a relevant surgical environment.

Article

Cancer Cell

Real-Time Molecular Diagnosis of Tumors Using Water-Assisted Laser Desorption/Ionization Mass Spectrometry Technology

Graphical Abstract

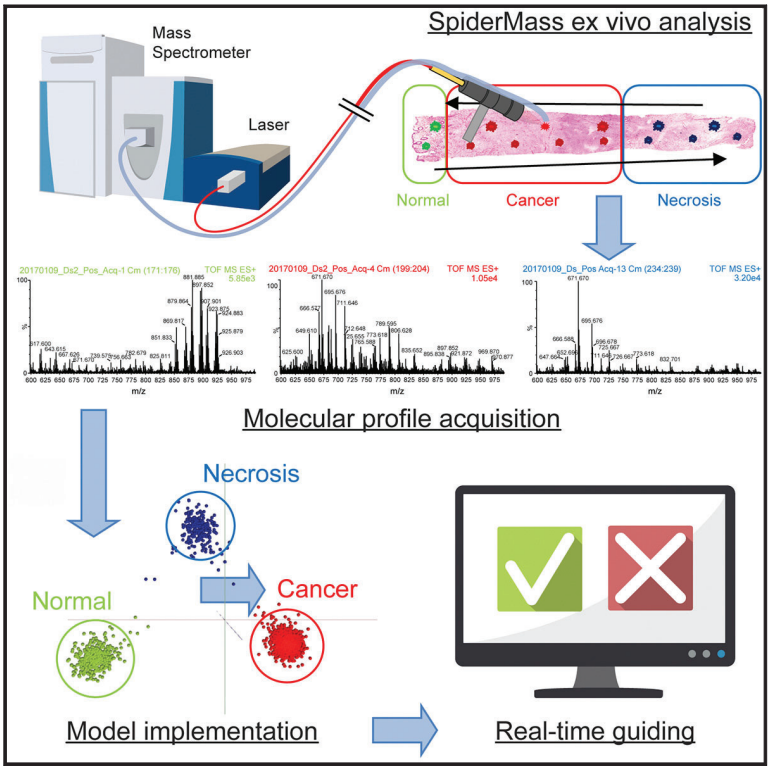

Highlights

- SpiderMass technology collects molecular information *ex vivo* and *in vivo*
- Tumor classification by typing and grading is obtained by the technology
- Found markers are cross-validated with mass spectrometry imaging
- The technology was assessed *ex vivo* at the vet surgery room

Authors

Philippe Saudemont, Jusal Quanico, Yves-Marie Robin, ..., Zoltan Takats, Michel Salzet, Isabelle Fournier

Correspondence

z.takats@imperial.ac.uk (Z.T.),
michel.salzet@univ-lille.fr (M.S.),
isabelle.fournier@univ-lille.fr (I.F.)

In Brief

Using dog tissue samples, Saudemont et al. evaluate the performance of a mass spectrometry-based analysis of lipids for fast *ex vivo* diagnosis of sarcomas. This approach may improve the clinical management of sarcomas by facilitating histopathological diagnosis of biopsy samples and surgical margin assessment.

Saudemont et al., 2018, Cancer Cell *34*, 1–12
November 12, 2018
https://doi.org/10.1016/j.ccell.2018.09.009

CellPress

Please cite this article in press as: Saudemont et al., Real-Time Molecular Diagnosis of Tumors Using Water-Assisted Laser Desorption/Ionization Mass Spectrometry Technology, Cancer Cell (2018), https://doi.org/10.1016/j.ccell.2018.09.009

Cancer Cell
Article

Real-Time Molecular Diagnosis of Tumors Using Water-Assisted Laser Desorption/Ionization Mass Spectrometry Technology

Philippe Saudemont,[1,2,3,9] Jusal Quanico,[1,2,4,9] Yves-Marie Robin,[1,5] Anna Baud,[1,2] Julia Balog,[2,8] Benoit Fatou,[1,2] Dominique Tierny,[1,6] Quentin Pascal,[1,6] Kevin Minier,[7] Mélissa Pottier,[7] Cristian Focsa,[4] Michael Ziskind,[4] Zoltan Takats,[2,8,*] Michel Salzet,[1,2,*] and Isabelle Fournier[1,2,10,*]

[1]Université de Lille, Inserm U1192, Laboratoire Protéomique, Réponse Inflammatoire et Spectrométrie de Masse (PRISM), Faculté des Sciences, Campus Cité Scientifique, Bât SN3, 1er étage, 59655 Villeneuve d'Ascq Cedex, France
[2]European Associated Laboratory Inserm-Imperial College of London, LANCET, 59655 Villeneuve d'Ascq Cedex, France
[3]SATT-Nord, Immeuble Central Gare, 4ème étage, 25 Avenue Charles St Venant, 59800 Lille, France
[4]Université de Lille, CNRS UMR 8523, Physique des Lasers Atomes et Molécules (PhLAM), 59655 Villeneuve d'Ascq Cedex, France
[5]Unité de Pathologie Morphologique et Moléculaire, Centre Oscar Lambret, 3 Rue Frédéric Combemale, 59020 Lille Cedex, France
[6]OCR (Oncovet Clinical Research), Parc Eurasanté Lille Métropole, 80 Rue du Dr Yersin, 59120 Loos, France
[7]Oncovet, Avenue Paul Langevin, 59650 Villeneuve d'Ascq, France
[8]Department of Surgery and Cancer, Imperial College London, St. Mary's Hospital, Praed Street, London, NW1 1SQ, UK
[9]These authors contributed equally
[10]Lead Contact
*Correspondence: z.takats@imperial.ac.uk (Z.T.), michel.salzet@univ-lille.fr (M.S.), isabelle.fournier@univ-lille.fr (I.F.)
https://doi.org/10.1016/j.ccell.2018.09.009

SUMMARY

Histopathological diagnosis of biopsy samples and margin assessment of surgical specimens are challenging aspects in sarcoma. Using dog patient tissues, we assessed the performance of a recently developed technology for fast *ex vivo* molecular lipid-based diagnosis of sarcomas. The instrument is based on mass spectrometry (MS) molecular analysis through a laser microprobe operating under ambient conditions using excitation of endogenous water molecules. Classification models based on cancer/normal/necrotic, tumor grade, and subtypes showed a minimum of 97.63% correct classification. Specific markers of normal, cancer, and necrotic regions were identified by tandem MS and validated by MS imaging. Real-time detection capabilities were demonstrated by *ex vivo* analysis with direct interrogation of classification models.

INTRODUCTION

Accurate cancer diagnosis plays a pivotal role in choosing optimal treatment and in consequence is crucial for cancer prognosis. Currently, the presence of the tumor can be detected by means of non-invasive tools such as X-ray scans, positron emission tomography scans, and computed tomography or MRI, which are regularly combined with blood marker assays. However, final diagnosis is established based on the histological examination of a tissue specimen, which is obtained via core biopsy, endoscopic punch biopsy, or surgical biopsy using laparoscopy or laparotomy. In most instances such as sarcoma management, surgical specimens are also subjected to pathological examination to support initial diagnosis and margin status assessment. Histological examination of core needle biopsies remains the gold standard for the diagnosis of sarcomas and related tumors. In these lesions rapid, accurate, or precise diagnosis based on morphology and routine ancillary techniques can be challenging. There is, thus, an ample need for a molecular technique that could ameliorate and expedite diagnostic decisions.

Significance

We validate, using the sarcoma biopsies *ex vivo*, the performance of a technology allowing the collection of tissue molecular profiles without *a priori* knowledge. This approach enables sarcoma grading and typing after statistical analysis of the collected data. All the results confirm the high accuracy of the technology in differentiating between histological areas or sarcoma subtypes in real time. Because this approach is designed to operate *in vivo* with low invasiveness, we envision the future implementation of this technology in clinical practice as a useful adjunct to existing techniques not only for biopsy-based diagnosis but also for *in vivo* real-time intraoperative surgical margin assessment, notably in malignant soft tissue tumors that is the focus of this paper.

Soft tissue tumors form a class of highly heterogeneous mesenchymal lesions, arising from tissues such as fat, muscle, cartilage, fibrous connective tissue, and the pericytes of small blood vessels in the subcutis and from skin. They cover an extensive range of morphological differentiation patterns. Current diagnostic methods include basic analytical processes such as standard histological staining, as well as more elaborate techniques such as immunostaining and molecular genetics, which include fluorescent *in situ* hybridization for the detection of gene amplification and rearrangements and RT-PCR for the detection of characteristic or specific gene fusions (Antonescu, 2006; Jaber and Kirby, 2015). Although these tests are limited by the fact that they cannot be multiplexed, they are adapted to and widely used in routine clinical practice especially for sarcomas presenting a specific line of differentiation. But this differentiation may be lacking in a substantial number of cases, rendering classification difficult. In addition, a morphologically bland-looking tumor may not necessarily follow a clinically benign course such as low-grade fibro-myxoid sarcoma or low-grade myxofibrosarcoma, both of which are classified as malignant tumors (Fletcher et al., 2013). Further, some rare tumors previously considered to be potentially malignant have been re-classified as benign. For example, the previously reported well-differentiated spindle cell liposarcoma (Mentzel et al., 2010) no longer belongs to the spectrum of atypical lipomatous tumor, but has a close relationship with spindle cell lipoma, now being termed fibrosarcoma-like lipomatous neoplasm (Deyrup et al., 2013). This illustrates the uncomfortable situation where, because of equivocal phenotypic overlap and imprecise prognostic correlation, the morphological distinction between benignity and malignancy in tumors not showing characteristic genetic alterations is not easy. This ambiguous setting is commonly encountered in benign myofibroblastic lesions versus low-grade spindle cell sarcoma, cellular schwannoma, or atypical neurofibroma versus low-grade malignant peripheral nerve sheath tumor, and cellular or atypical fibrous histiocytoma versus true sarcoma. The case of pleomorphic lipoma versus pleomorphic liposarcoma may represent an especially challenging diagnostic pitfall: they are morphologically almost identical but the former is benign, whereas the latter is highly malignant (Azzopardi et al., 1983).

These considerations underline the necessity to develop validated molecular techniques for rapid and accurate classification to improve diagnostic accuracy of tumor subtypes in human sarcomas. Emerging techniques with promising applications such as mass spectrometry (MS) may be of great value as an adjunct to existing tests. Microbiopsy-based diagnosis is currently considered to be the standard protocol prior to treatment, so that diagnostic precision is crucial for clinical management. Another challenge for sarcoma management is molecular assessment of surgical margin status, which plays a key role in prognosis. The best patient care possible is to establish a correct and precise initial diagnosis followed by the excision of the tumor with documented clear margins to avoid surgical and oncological complications, such as local or distant relapse and wound healing complications (Aerts et al., 2014; Liu et al., 2011; Pena et al., 2014).

MS has long been in the focus of interest for the direct analysis for discriminating cells of different phenotypes using tissue sections of patient biopsies (Le Rhun et al., 2015, 2016; Vaysse et al., 2017). But in the context of intraoperative tissue analysis, the main challenge remains to develop an MS instrument compatible with *in vivo* analysis working in a surgical environment. The Intelligent Knife (iKnife) system (Balog et al., 2013; Schafer et al., 2009) allows monitoring during surgery by the real-time mass spectrometric analysis of the aerosol liberated during electrosurgical tissue dissection. The *in vivo* and *ex vivo* application of the iKnife technique has successfully been demonstrated for breast and ovarian cancers (Phelps et al., 2018; St John et al., 2017). More recently another system, called MasSpec Pen, was described (Zhang et al., 2017), where sampling of tissues is achieved by aqueous extraction and the aqueous extract is analyzed by MS. However, this device must be placed in tight contact with the tissue for analysis, hence limiting its use for cancer research due to possible contamination of the device with tissue debris. So far, the MasSpec Pen was only demonstrated *ex vivo* for laboratory model samples.

Veterinary canine patients—similarly to humans—develop spontaneous tumors that share many features similar to the human disease (Takashima-Uebelhoer et al., 2012). Moreover, oncological surgery is a frontline treatment for both human (Abramson, 2010; Carpenter et al., 1991; Diamond et al., 1999; Greenfield et al., 1995; Lewis, 1995; Misdorp and Hart, 1976; Pluhar et al., 2000; Schneider, 1970; Schwyn et al., 1998) and veterinary patients (Caceres et al., 2016; Liu et al., 2011; Pena et al., 2014). Specifically, soft tissue sarcomas and osteosarcoma in dogs have similar morphological appearances, clinicopathological presentation, and phenotypes as in humans and have been shown to be an excellent comparative model. In current practice, canine sarcomas are diagnosed using human guidelines hence the diagnostic procedures face similar challenges. MS imaging (MSI) has already been demonstrated to provide excellent prognostic information on this group of diseases (Lou et al., 2017).

In the present work, we evaluate the potential of a recently developed MS technology called SpiderMass (Fatou et al., 2016, 2018a, 2018b; Salzet et al., 2017) in addressing the needs for sarcoma management.

RESULTS

SpiderMass Instrument

The SpiderMass technology has been designed for minimal invasiveness, allowing information to be obtained without causing in-depth tissue damage. The technology is based on a unique micro-sampling probe, built in-house, that uses laser desorption. The system performs MALDI-MS under ambient conditions, several meters away from the mass analyzer. This is achieved by resonantly exciting the endogenous water of biological tissues. Because water is in large excess within biological tissues (>50%) solvating practically all molecular species present, it can act as a MALDI matrix. Resonant excitation is obtained by tuning an optical parametric oscillator (OPO) laser system to the most intense absorption band of water at $\lambda = 2.94$ μm (Berkenkamp et al., 1996; Laiko et al., 2002). The high absorption coefficient ($\alpha \approx 3 \times 10^{-4}$ cm^{-1}) of the water O-H stretching band and the relatively low laser energy used (3–5 mJ/pulse) ensure that only a very low amount of material is ablated (penetration

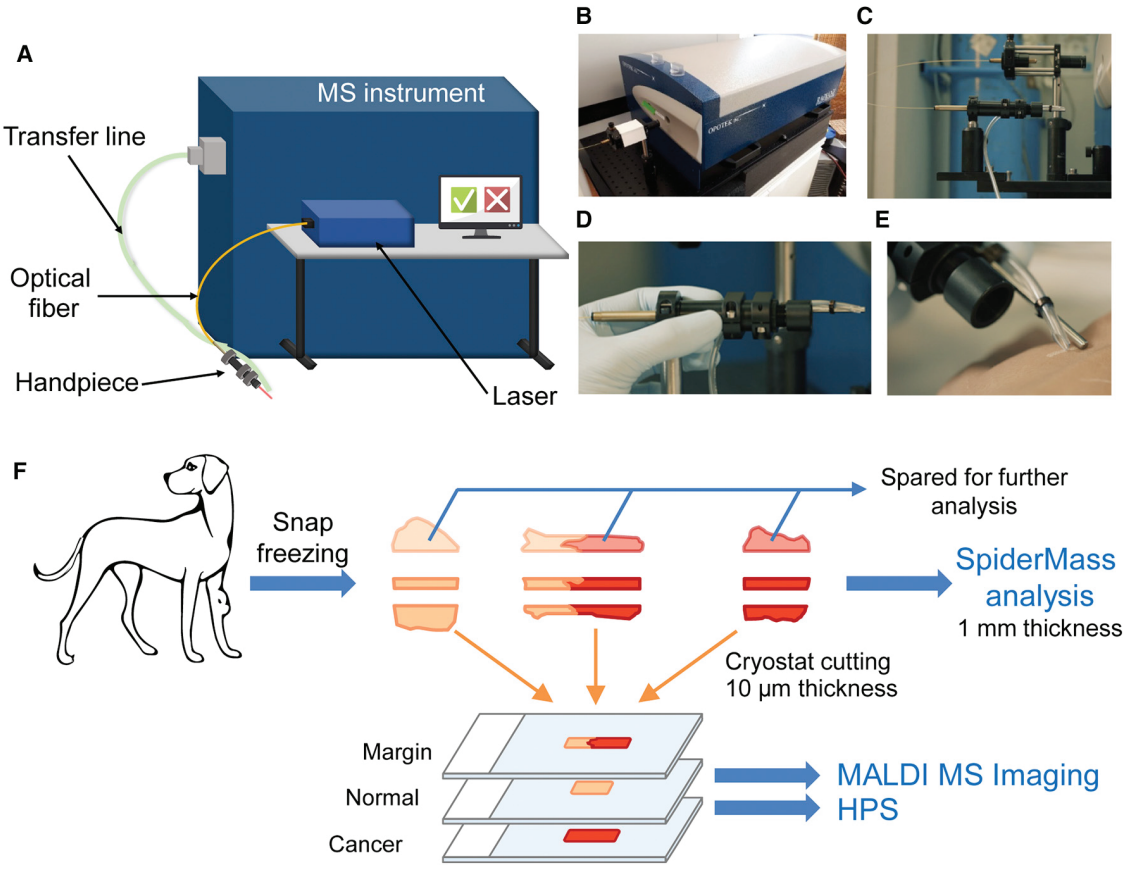

Figure 1. SpiderMass Prototype and Workflow Used in the Study

(A) Illustration presenting the water-assisted laser desorption/ionization mass spectrometry technology including the fiber laser microprobe equipped with its handpiece, the transfer line, and the mass spectrometer.

(B–D) Picture of the OPO fibered laser system with detailed views of the injection system (B), laser fiber (C), and handpiece (D). The optical fiber is inserted on the metal support at the back of the probe handpiece, while the transfer tube is tied to the probe guide.

(E) Picture of the system when in use for *in vivo* real-time skin analysis.

(F) Experimental workflow showing tissue processing after surgery and the analytical sequence.

depth: few µm/laser shot). Since the system is based on the MALDI principle, ion yields are sufficient to provide good sensitivity without post-ionization. As expected, only intact molecular ion signals are observed with the water matrix, preventing the analyte molecules from receiving an excessive amount of internal energy and undergo unwanted fragmentation.

Figure 1A shows a schematic representation of the SpiderMass instrument illustrating the modifications of the setup described previously (Fatou et al., 2016). This version of the prototype includes an infrared (IR) OPO pumped by a nanosecond Nd:YAG laser and connected to a Q-TOF instrument. The entire system is equipped with wheels allowing for easy transportation and deployment. At the exit of the OPO source the laser beam is injected inside the fiber (Figures 1B and 1C). The distal end of the fiber is directly connected to a handpiece equipped with a focusing lens to create a laser spot size of 500 µm in diameter at the focal point (Figures 1C and 1D). In this prototype, the optical fiber advantageously replaces the set of reflecting mirrors used to direct the incident laser beam to the sample surface and avoids incorporating the entire laser system into the handpiece. The optical fiber and handpiece now permit maneuverability over the sample and makes it suitable for analyzing surfaces of variable geometries especially when using a long optical fiber (>1 m). The ion transfer tubing is likewise attached to the handpiece (Figures 1D and 1E) to collect the ablated material (Figure 1E). The proximal end of the transfer tubing is connected to the ion source inlet of the mass spectrometer. This prototype operates both for *ex vivo* and *in vivo* analysis of surfaces by scanning the tissues, enabling real-time molecular signature acquisition under minimally invasive conditions. Figure 1E shows the laser beam leaving only a white trace on the tissue during real-time analysis of the user's skin which can be simply wiped off. In the current work, the instrument was used for building an *ex vivo* classification model by screening biopsies collected from canine subjects in a veterinary oncology practice. Figure 1F shows the workflow used to acquire spectra for classification. The obtained biopsies were divided into two parts. The first half was saved and stored at −80°C for further analyses. The second half was sectioned into: (1) a 1-mm-thick slice for SpiderMass analysis, and (2) several 10-µm sections for

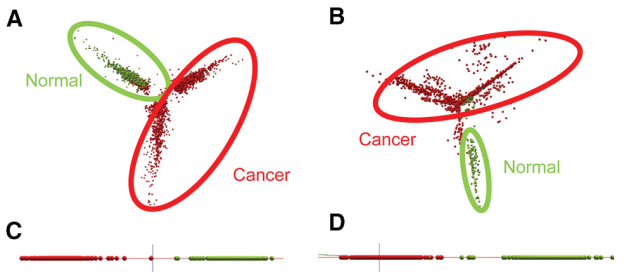

Figure 2. Classification of the Cohort Using PC-LDA Model Using a Two-Class Scheme (Normal and Cancer) Using all the Single MS Spectra Recorded

PCA representation of the model (A and B) and LDA models generated from the PCA (C and D) using positive ion mode (A and C) or negative ion mode (B and D) analysis. Each dot represents a single MS spectrum recorded with the SpiderMass instrument during the 10-s irradiation period, thus corresponding to a single MS scan.
See also Table S1.

MALDI-MSI and hemalun-phloxine-saffron staining (HPS). The optical images of the stained sections served as morphological controls and were used to define the normal, cancer, and necrotic zones.

Classification Models for Sarcoma Tumors

Sarcoma is a uniquely complex cancer type because it has more than 50 histological subtypes and is thus probably the most diverse and heterogeneous of all cancers (Bleloch et al., 2017; Skubitz et al., 2008; Stiller et al., 2013). We developed a classification model for a collection of canine sarcomas using lipidomic molecular signatures collected by the MS analysis of histologically annotated biopsy specimens (Table S1). In brief, the median age of the animals was 9 years, and 32 were pure breeds of various types, while one was a crossbreed. The majority of the biopsies fell into the three main categories including: fibrosarcoma (6 biopsies), osteosarcoma (5 biopsies), and undifferentiated sarcoma (6 biopsies); the osteosarcomas were further subtyped as osteoblastic (4 biopsies) or osteoblastic and chondroblastic (1 biopsy) sarcomas. Of the biopsies that have been graded (17 biopsies), 4 were grade I, 7 were grade II, and 6 were grade III; the latter is comprised mostly of undifferentiated pleomorphic sarcoma.

Following the acquisition of the MS spectra in both positive and negative ion modes, we were first interested in the possible differentiation between cancer and normal tissues. Results of the multivariate analysis using principal-component analysis (PCA) from the generated spectra acquired from the 33 biopsies are summarized in Figure 2A for the positive ionization mode and Figure 2B for the negative ionization mode. The first three principal components (PCs) explain 30.4% of the variance for the positive mode acquisition and 31.4% for the negative mode acquisition. Good separation is observed among the scores for the normal and cancer groups as shown in in the data plane defined by the first two PCs. The features extracted using PCA were subjected to supervised analysis using linear discriminant analysis (LDA) (Balog et al., 2013; Schaefer et al., 2009), with the spectra grouped into two classes for cancer and normal tissues. It can be observed from LDA that better discrimination was obtained for data taken in positive ion mode (Figure 2C) than in negative ion mode (Figure 2D). Excellent cross-validation results were obtained using the "leave one patient out" method with 99.94% and 95.37% correct classification rates with and without outliers in the positive mode and 97.63% and 94.54% in the negative mode (Table 1). PCA results reflect the heterogeneity of the cancer group, which is more spread than the normal tissues. We suspect that the subset of spectra can be attributed to the necrotic zones which are indicative of higher-grade sarcoma.

We tested this hypothesis on a fibrosarcoma biopsy (sample Ds2) sample of grade III, which contains normal, cancer, and necrotic zones as confirmed by HPS staining (Figure 3A). Using SpiderMass, a 1.7-min acquisition was done on the Ds2 sample, performing discrete micro-sampling using 10-s then 5-s laser irradiation periods per point with one spectrum generated per second to analyze the three different regions of the tissue. The total ion count for the 5-s irradiations (7–14) with the individual acquisitions colored according to the corresponding region is shown in Figure 3A, bottom, and sample spectra (averaged from the 5-s irradiations) recorded per region are shown in Figure 3B. The MS spectra of each of the analyzed regions clearly demonstrates that necrosis itself possesses a specific molecular signature when compared with viable cancer tissues.

Considering these results, the PC-LDA classification model shown in Figure 2 was reconstructed taking necrosis into account as a distinct group in the classification system. The LDA result of the classification model from positive ion mode data shows the separation of the necrotic zone group (blue) from the normal (green) and cancer (red) groups, when using individual spectra to generate the model (Figure 3C). From PCA, we can observe that necrosis explains a part of the heterogeneity of the cancer group but not all, which is not surprising considering the numerous subtypes that exist in sarcoma (Figure S1). Leave one patient out cross-validation based on the normal/cancer/necrosis classification shows 99.06% and 81.89% correct classification rates (Table 1).

Modeling of a Real-Time Tissue Analysis and Classification

To demonstrate the utility of our model in a surgical setting by classifying tissues in real time we simulated an *in vivo* application by analyzing *ex vivo* a fibrosarcoma biopsy (labeled Ds2) containing different histological regions. The model generated by PC-LDA for normal/cancer/necrosis classification was loaded into the OMB-Recognition software and tested on this sample. An animation, including a video of the real-time classification, is shown in Video S1. This depicts the acquisition of individual spectra as the laser probe samples over the entire tissue along its longitudinal axis, as well as the automated comparison with the model as a function of the input spectrum. The readout is a prediction of the cancer, normal, and necrotic classes, which is displayed with less than a 1-s time delay compared with spectral acquisition. Readout is given by a color code according to the class in the classification model (Figure 3C), i.e., green for normal tissues, red for cancer, and blue for necrosis. As the laser beam progressively passes over the tissue, it will come across normal, then cancer, and finally necrotic areas. The real-time classification readout did not show any failure in classification, with class similarity values always above 91%.

Table 1. Cross-Validation Results Using the "Leave One Patient Out" Methods

Model Type	Acquisition Methods	n Classes	n Tested Spectra	n Passes	n Failures	n Outliers	Correct Classification Rate (%)	
							Excluding Outliers	Including Outliers
Tissue typing	positive mode	2	1,791	1,708	1	82	99.94	95.37
		3	1,938	1,589	15	334	99.06	81.89
		3	180	166	0	14	100.00	92.22
	negative mode	2	1,779	1,692	41	46	97.63	94.54
Tissue grading	positive mode	4	139	98	19	22	83.75	70.50

Classification Models for Sarcoma Grading

Interestingly the normal versus tumor versus necrosis classification (Figures 4A and 4B) gives an easy access to the discrimination of grade III tumors. Since necrosis is more predominant at grade III and is one of the criteria taken into account in grading, this shows good correlation with histological standards (Trojani et al., 1984). Examination of the PCA features verify the presence of different PC loadings contributing to the variance observed for each group, notably for the first component, which explains 42.8% of the variance (16.9% and 13.7% for the PC2 and PC3 scores, respectively, for a total of 73.4% of variance explained by the first three components).

To assess the classification strength of our method, we explored the possibility of generating a classification model based on tumor grade. Figures 4C and 4D show the model after re-classifying the averaged spectra based on tumor grade assigned by the pathologist. The PCA plot (Figure 4C) shows good separation of the normal and grade III classes from each other and from grades I and II. In contrast, grades I and II are only partially separated from each other. Osteosarcomas are not graded but assigned to a separate class by the veterinary pathologist, named N/A (not assigned). The spectra recorded for these samples group with the grade I and II samples in the PCA representation. The LDA score plot (Figure 4D) shows good intergroup separation, suggesting distinct molecular signatures for each grade. In this plot, interestingly, the N/A group clusters closer to the grade II class, highlighting that these groups share similar molecular signatures. For three of the biopsies, namely Ds6, Ds18, and Ds22, the PCA plot shows that they cluster with the grade III class, rather than grade II or N/A as attributed by the pathologist. Ds18 is an osteosarcoma (usually graded N/A); but the presence of massive osteolysis could explain its similarity to necrosis and grade III. Similarly, Ds22 is an undifferentiated sarcoma that was not graded by the pathologist but was noted to bear major necro-hemorrhagic changes. Finally, for Ds6, the diagnosis was difficult but suggested a grade II fibrosarcoma, and it shows a molecular profile closer to grade III. Thus, the models based on SpiderMass molecular signatures could serve as an aid for the pathologist in such ambiguous cases. Cross-validation using a four-class model considering normal, grade I, grade II, and grade III (Table 1) shows correct classification rate of 83.76% and 70.50% excluding and including outliers, respectively.

To determine which lipids are discriminative of the normal, cancer, and necrotic classes, we extracted the top five loadings that significantly contributed to the variance observed in the scores of the first PC of the three-class PC-LDA model (Figure S2A). A few examples of these discriminative markers are presented together with the boxplots of the normalized intensities recorded for the different tissues (Figure 5). Figure S2B shows the complete boxplots for the top five loadings of each group, and Data S1 shows the statistical results used to generate the boxplots. Some of them, such as *m/z* 869.75, *m/z* 881.75, *m/z* 895.75, *m/z* 907.85, and *m/z* 923.85 are more abundant in the normal tissues, while the others are specific to the cancer regions (*m/z* 683.65, *m/z* 687.65, *m/z* 713.55, *m/z* 739.55, and *m/z* 790.65) or necrotic regions (*m/z* 647.65, *m/z* 671.65, *m/z* 687.65, *m/z* 695.65, and *m/z* 711.65).

Biomarker Identification and Cross-Validation by MALDI-MSI

The biomarkers we found to be discriminant in the normal/cancer/necrosis areas with SpiderMass were identified by tandem MS (MS/MS) and validated by conventional UV-MALDI-MSI approach. Structural elucidation was performed by on-tissue MS/MS analysis using SpiderMass connected to a high-resolution Orbitrap mass spectrometer. The identification was performed by interrogation of the LIPID MAPS database using accurate *m/z* measurement of parent followed by a manual assignments of MS/MS fragment ions to confirm identification. Figure S3 shows an example MS/MS assignment obtained for *m/z* 739.55, which was specific to the cancer area. A zoom of the MS/MS spectrum shows that the precursor ion mass at *m/z* 739.4667 was the most intense peak isolated in this experiment. The MS/MS spectrum shows potassiated cyclophosphate ion (*m/z* 162.9556) as the most dominant fragment, as well as peaks arising from the neutral loss of cyclophosphate (*m/z* 615.4745) and its potassiated adduct (*m/z* 577.5186), which confirm the potential assignment as PA(36:2) obtained by library search. *m/z* 485.3025 corresponds to the neutral loss of the C16:1 fatty acid, thus confirms this lipid as the potassiated phosphatidic acid PA (20:1/16:1). Other MS/MS assignments can be found in Data S2 and they are also summarized in Table S2. Lipids contributing to the discrimination between normal/cancer/necrosis tissue regions belong to different lipid classes, mainly triacylglycerols (TGs), phosphatidylglycerols (PGs), phosphoethanolamine (PE), and sphingomyelins (SMs). Many TGs are specific to the normal regions, whereas glycerophospholipids such as PG, PE, and PA are found more often in the cancer area and SM in the necrotic part of the tissues. Of note, the assignments enable determination of fatty-acid chain length and unsaturation number; however, the position of the double bonds in the fatty acyl moieties could not be identified. The presence of PA in the cancer region is in line with data showing that PA is involved in regulating the

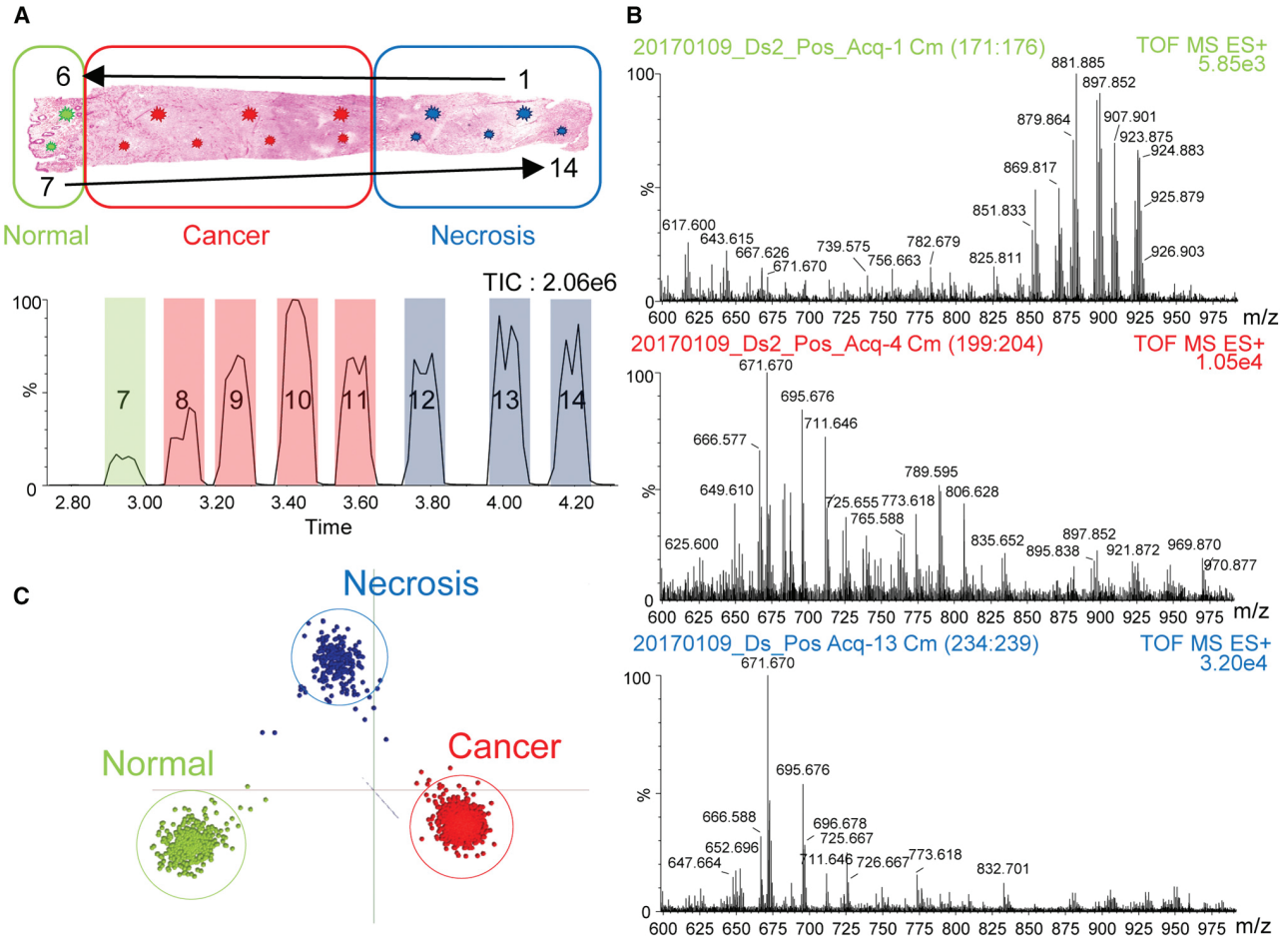

Figure 3. PC-LDA Models Using a Three-Class Scheme (Normal, Cancer, and Necrosis)

(A) Examination of the HPS-stained section of Ds2 fibrosarcoma shows three distinct regions identified as necrotic, cancer, and normal by the pathologist. The mirror tissue to this annotated section was analyzed with SpiderMass. Spots indicate where analyses were conducted (1–14), while the arrows indicate direction of acquisition starting at 1. Graph below the HPS image shows the total ion count for 5-s acquisitions (7–14).

(B) Sample averaged MS spectra corresponding to one zone of each of the normal, cancer, and necrosis regions.

(C) LDA representation of the PC-LDA model using a three-class scheme (normal, cancer, and necrosis). This model was built from the individual spectra recorded in the MS-positive ion mode.

See also Figure S1 and Video S1.

mammalian target of rapamycin (mTOR)-mediated signaling, which promotes cancer cell survival (Dancey, 2010; Foster, 2009), and that SMs are implicated in cancer metabolism and apoptosis pathways (Ogretmen, 2018).

Nine biopsies representing the different types of sarcoma analyzed with SpiderMass were also examined using conventional vacuum UV-MALDI-MSI for validation purposes on 10-μm tissue sections of the respective specimens. MALDI-MSI is a molecular imaging technique (also called molecular histology) and is now recognized as the gold standard for molecular imaging. It has been shown to enable the localization of several biomarkers, including marker lipids in oncology applications (Arafah et al., 2014; Carter et al., 2011; Walch et al., 2008). After MALDI imaging, data collected from the nine biopsies were subjected to spatial segmentation to identify the different molecular areas of the tissues (Figure S4). This led to principal discrimination of three areas which were attributed to normal, cancer, and necrosis areas as assigned from the HPS staining of adjacent sections (Figure S4A). PCA of the regions of interest defined from these clusters grouped according to normal, cancer, and necrosis groups are shown in Figure S4B. Very interestingly, a subclassification between the different subtypes of sarcoma was shown by plotting the scores of the first PCs. Discriminatory *m/z* values observed in these datasets were compared with the discriminatory *m/z* obtained using SpiderMass data. The cancer-specific peaks identified from the MALDI-MS images, namely *m/z* 713.46 and *m/z* 739.47, were also identified as cancer markers in the model generated from the SpiderMass dataset (Table S2). Examples of ion images of peaks identified by the SpiderMass and the MALDI-MSI data are depicted in Figure 5; the complete set can be found in Figures S5 and S6. This gives a cross-validation of the data obtained by the classification model built from SpiderMass data.

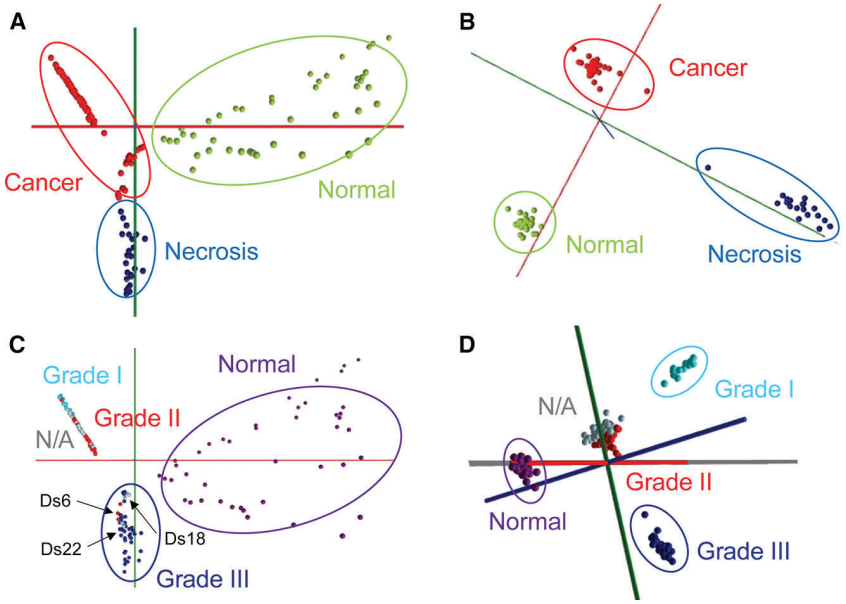

Figure 4. Classification of Samples Using the PC-LDA Model According to Tumor Grade

Three-class (normal, cancer, and necrosis) (A and B) and five-class (C and D) scheme PCA (A and C) and LDA (B and D) models of the samples for tumor grading. The three-class scheme model in (A and B) is the PCA result of the classification model depicted in Figure 3 when using averaged MS spectra recorded in positive mode. The same model with samples classified according to tumor grade (C), showing distribution of three samples (Ds 6; Ds 18; and Ds 22) with ambiguous diagnoses. In (D) the distinct separation of all grades from the normal group is observed. N/A represents osteosarcomas where grading is not applicable based on pathologist criteria, or biopsies without grade. Axis represents the first three dimensions of the PCA (A and C) and of the LDA (B and D), which are the dimensions that explain most of the variance. Each dot represents an averaged MS spectrum recorded with the SpiderMass instrument over a 10-s irradiation period, thus corresponding to the average of 10 individual spectra.

Subtyping of Sarcoma Tissues Using SpiderMass

To further assess the classification performance of SpiderMass, we looked at establishing a classification model using the different sarcoma subtypes plus normal tissues from the patient cohort (Table S1). LDA representation resulting from the classification models using the MS spectra recorded in positive mode and negative mode according to sarcoma subtypes from the four most represented classes (osteosarcoma, fibrosarcoma, undifferentiated, and normal) are shown Figure 6. Normal tissue is represented by common connective fibro-vascular and adipose tissue. Very good separation of these groups is observed in both positive (Figure 6A) and negative (Figure 6B) ion modes, although slightly better group separation is again observed for the positive ion mode. Since fibrosarcoma is a tumor derived from connective tissues, the differentiation between classes is to be attributed to the carcinogenesis process rather than the tissue origin. In some cases, the classification for sarcoma subtypes was not possible, due to the low number of samples in certain classes. Even though this was the case, specific molecular signatures were observed for different subtypes of sarcoma, as demonstrated by the distinct spectral profiles from *m/z* 600–1,000. This is demonstrated by example spectra acquired for each subtype in the positive mode (Figure S7A) and in the negative mode (Figure S7B). Although certain signals are shared between different groups, neither their intensity nor their global molecular signature is conserved in all 11 classes. Thus, the models show that sarcoma subtyping at the level of osteosarcoma, fibrosarcoma, undifferentiated, and normal tissues is possible using spectra acquired by the SpiderMass technology. This is highly interesting since pathologists struggle to achieve this classification using conventional techniques. For the other subtypes of sarcoma, which are less common, we obtained encouraging results shown in Figure S8A for positive and in Figure S8B for negative ion mode. We are planning to validate these results in the future using a statistically well-powered number of subjects.

Implementation of SpiderMass in the Operating Room

Figures 7A and 7B show the implementation of SpiderMass prototype into an operating theater. The instrument was operated on dog patients *in vivo* to confirm the low invasiveness of the technology in the context of surgery. It was also assessed for extemporaneous analysis on the bench during the course of surgery. Video S2 shows the use of the SpiderMass system during an actual surgical operation. In the video, a skin biopsy and a sample body fluid were analyzed extemporaneously using the SpiderMass system. The video also demonstrates the *in vivo* application of the system, using a 1.5-m laser fiber that allows the probe to be handled remotely from the instrument.

DISCUSSION

Our study shows that SpiderMass technology enables the acquisition of histologically specific molecular signatures (or molecular barcoding) in different sarcoma-type tumors. On one hand, developments in molecular signatures aimed at being more and more specific to cell phenotypes. On the other hand, there is great need to easily distinguish cancerous tissue from benign ones as there is no single universal discriminant biomarker currently available for all such cases. Moreover, tumor types as well as tumor grades can be established. Indeed, using the MS molecular profiles, classification models are created and successfully cross-validated. Models based on cancer/normal, cancer/normal/necrotic, and tumor grade or cancer subtype classification schemes all showed better than 97% correct classification rates for negative mode and 99% for positive mode, excluding outliers. The specific markers of the normal, cancer, and necrotic regions found with SpiderMass were identified by MS/MS and then validated by MALDI-MSI. Finally, we demonstrated that the instrument allows for *in situ*, real-time diagnosis using the established classification models.

A close relationship exists between clinical outcome and the efficiency of cancer cytoreduction or complete tumor resection.

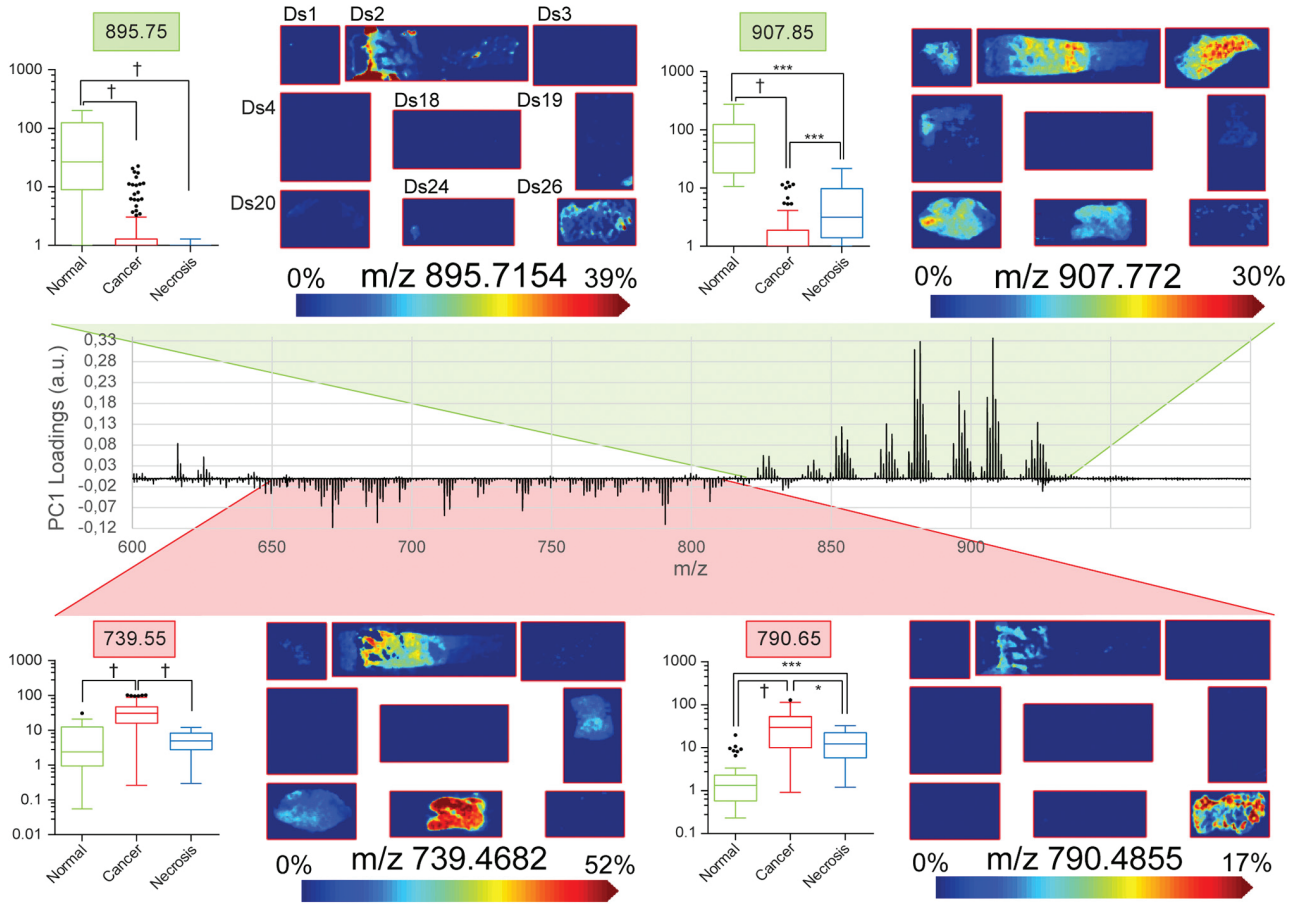

Figure 5. Normalized Intensities and MALDI-MS Ion Images of Selected PCA Loadings of the Classification Model

Shown are loadings with significantly different intensities for the normal (*m/z* 895.75 and *m/z* 907.85) and cancer zones (*m/z* 739.55 and *m/z* 790.65). For necrotic zones, see Figure S6B. Normalized against the total ion count, intensities are log10 transformed and represented with boxplots using the Tukey method for whiskers definition. The box extends from the 25th to 75th percentiles. The line in the middle of the box is plotted at the median. The up and down whiskers are represented at 1.5 times the distance between those 25th and 75th percentiles, and all points beyond the whiskers are represented as individual point dots and depict the outliers. *m/z* 687.65 was found to be significantly different for both cancer and necrosis zones compared against the normal zone. *$p \leq 0.05$, ***$p \leq 0.001$, †$p \leq 0.0001$. For the MALDI images, color bars indicate maximum intensities after normalization against TIC. Ds1, myosarcoma; Ds2, fibrosarcoma, containing normal and necrotic zones; Ds3, hemangiopericytoma; Ds4, MPNST; Ds18, osteosarcoma; Ds19, splenic sarcoma; Ds20, histiocytic sarcoma; Ds24, GIST; and Ds26, normal tissue. *$p \leq 0.05$, ***$p \leq 0.001$, †$p \leq 0.0001$.
See also Figures S2–S6, Table S2 and Data S1 and S2.

Despite the large panel of different technologies, it is still extremely difficult for surgeons to assess if they completely removed the tumor tissues. Due to this, in our Comprehensive Cancer Center, conventional intraoperative frozen section is not readily used for surgical margin evaluation in sarcomas, as this is far more reliably performed on the formalin-fixed paraffin-embedded surgical specimen. In the case of unexpected microscopically positive margins after primary resection, a second surgery can be planned to remove residual tumor tissue and ensure adequate local control. It is clear there is an unmet need for an instrument that allows the surgeon to characterize tumor margin status with optimal accuracy at the molecular level and in real time during the surgery avoiding all the risks associated with other resections. The desired features for this technology would include rapid analysis, high sensitivity and specificity, and low invasiveness. The recently introduced iKnife technology meets most of these criteria; however, as a combination of dissection tools with MS, it is highly invasive. Similarly, SpiderMass is capable of remote (several meters away) and *in situ* analysis, as the optical fiber allows for flexibility of the sampling probe. The handpiece format and extended transfer tube also provides maneuverability to permit sampling of uneven surfaces during intraoperative conditions. All these parts can be sterilized and do not have to be in contact with the surface to sample during analysis, thus minimizing possible contamination. In contrast to the iKnife, the technology is minimally invasive, allowing for the analysis of tissue surfaces before making any surgical decisions. In addition, because the laser energy per pulse is low and because the beam is mostly absorbed by ambient water, no special care needs to be taken when working with the IR laser. Similar wavelength lasers (Er:YAG lasers) are routinely used for eye surgery and cosmetic interventions. For these reasons,

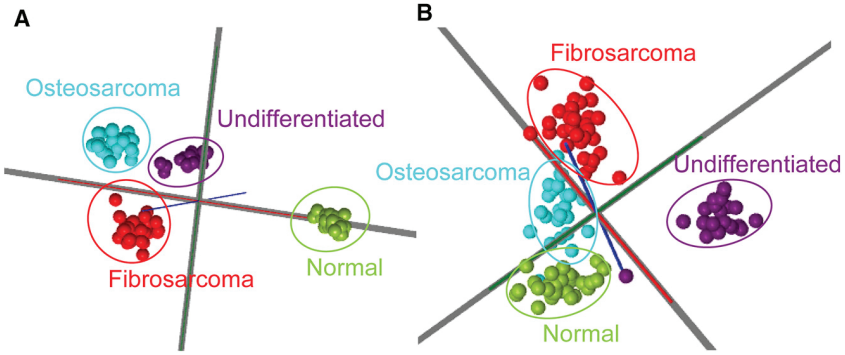

Figure 6. LDA Representation of the Classification Models for Sarcoma Subtyping

Models were established using the averaged MS spectra recorded both in positive (A) and negative (B) ion mode from the main classes of the cohort (osteosarcoma, fibrosarcoma, undifferentiated, and normal).

See also Figures S7 and S8.

surgeons could use the instrument to define excision margins with great accuracy before making their decision on the further removal of surrounding tumor tissue.

The animation shown in Video S1 demonstrates how the SpiderMass instrument could be used in the operating room while surgical procedures are being performed. Once the handpiece is positioned over the area of interest, the laser is activated and spectral acquisition is performed. The acquired spectra are then interrogated using the pre-constructed classification model and a readout identifying the analyzed region provides tissue classification in real time (<1 s time delay), similarly to the previously described algorithms (Balog et al., 2013). The feedback to the user is a traffic light system related to the class and the probability of correct classification. The handpiece is then moved progressively on the tissue until the entire area of interest has been analyzed with a continuous readout provided to the user. In the case of the presented example, a fibrosarcoma biopsy containing all three tissue types was analyzed. Screening of the biopsy was achieved within a few minutes (1.5 min) and the process was only limited by the speed of manual scanning, demonstrating the rapid information delivered by the SpiderMass instrument. The SpiderMass system can analyze directly the raw biopsy tissues and does not require any sample processing since it has been designed to operate under *in vivo* conditions and provides results within a few minutes of acquisition.

Finally, Video S1 illustrates the potential of SpiderMass for tumor margin definition. Even if the surgeon identifies the cancer/normal tissues, it is extremely difficult to define its excision margins with sufficient accuracy. This remains an important challenge in surgery because of the tight relation between clean excision margins and local recurrence and patient survival. If a proper classification model is defined with tumor/normal tissues, the real-time classification will allow to accurately define the tumor margins while avoiding removal of healthy tissues. We envision that future development of this technology will allow for automatic laser switch on the handpiece, allowing for easy tuning. In addition, we would like to add a camera for acquisition of images alongside the classification results.

The classification model was initially constructed for the instrument to distinguish cancer zones from benign or normal ones as this is the most important piece of information that surgeons need to make decisions. Such decisions are crucial as they can influence surgery time and removal of unaffected tissue, and consequently might affect patient comfort and surgical outcome. In addition, real-time diagnoses of tumor grade and cancer subtype are equally important. These parameters rely on the creation of strong models that should be built based on classifiers common to most or all sarcoma subtypes. They should also be independent of individual variability and/or the presence of histologic features shared with other pathologies, such as inflammation, immune cell infiltration, etc. In this regard, the cohort included 11 subtypes and 5 grades (3 tumor grades, normal, and N/A) of a cancer type. The database is expected to continuously develop as we constantly recruit more patients and gather more biopsies. The initial model was expanded considering necrotic zones, followed by grading and then subtyping to further improve the precision of the classification without sacrificing its good classification rate. As previously mentioned (Balog et al., 2013), increasing the number of classes in the supervised multivariate model compromises its identification efficiency. However, this problem can be mitigated by introducing multilevel, hierarchical classification models (Galea et al., 2017). Having such a classification system is extremely useful in clinical practice because it reduces the labor- and expertise-intensive procedures involved in grading and subtyping tumors. We thus explored this possibility by regrouping the acquired spectra based on their grades and subtypes according to histopathological data. Our preliminary results show the possibility to construct such models for even more classes (here 5 for grading and 11 for subtyping) using SpiderMass technology.

In this work, we built a canine sarcoma classification model based on lipid profiles. Lipids are a class of abundant biomolecules that are readily detected by MS and their use in the generation of tumor classification models has been demonstrated notably by MSI (Eberlin et al., 2012). Multiple studies have identified key lipids implicated in various pathobiochemical processes, including metabolic remodeling and altered signal transduction pathways. For instance, in myxoid liposarcomas, Willems et al. (2010) identified a significant decrease in PPARG regulated fatty-acid synthesis and triacylglycerols concentrations that increase with tumor grade (*m/z* 855.7436 assigned as TG[16:1/18:3/18:0]) *m/z* 881.7593 as TG[16:1/18:4/20:0], and *m/z* 907.7749 mis-assigned as TG[16:1/18:4/20:1] instead of 18:1/18:4/20:1). *m/z* 881.75 and *m/z* 907.77 were also detected in our study, but were instead associated with normal tissue since they contribute largely to the variance observed between the three groups, in accordance with previous findings where TGs decrease in high-grade sarcomas (Willems et al., 2010). Thus, the implication of these lipids in the shaping of our classification model corroborates with their potential role in cancer, as reported by other groups. This validates the efficiency of the multivariate approach used to generate the model based on the SpiderMass data.

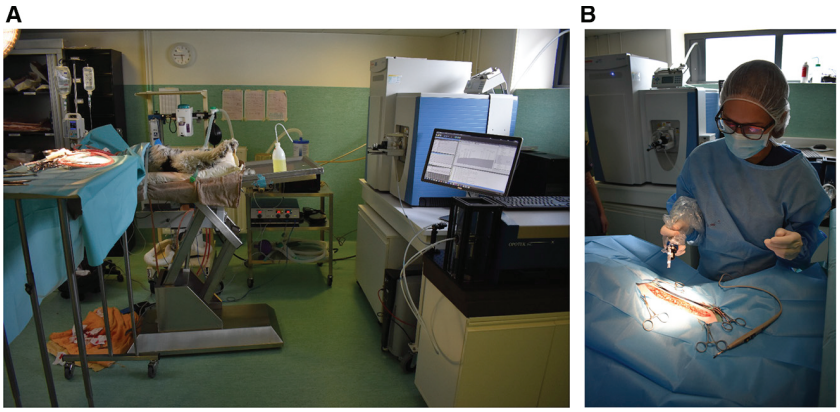

Figure 7. SpiderMass Prototype Inside the Surgery Room

(A) General arrangement of the surgery room at the Oncovet veterinary clinic with the SpiderMass prototype installed beside the surgical table.

(B) Picture of surgeon with the handled laser microprobe ready to be used during the surgery. Here the laser fiber is 1.80 m long to allow more freedom of movement.

See also Video S2.

In summary, we demonstrated that SpiderMass can generate a strong sarcoma classification model based on lipid MS molecular profiles acquired directly from canine tumor biopsies. We have presented the two potential advances supported by the technique, precise and rapid diagnostic classification of soft tissue tumors suspected of sarcoma on biopsy and accurate molecular intraoperative surgical assessment. Any clinical implementation of the technique in human sarcoma management requires beforehand validation on a great number of patients. A multi-center participation in a large-scale prospective trial seems to be the appropriate approach considering that sarcomas are a relatively rare entity. But this must be first supported by preliminary proof-of-concept validation studies on a small number of samples, such as the one presented here, whose results seem to be promising, and which are soon to include human tumors. Standardization of the method and validation of SpiderMass with existing techniques will be an important issue to resolve prior to its clinical use. Well-constituted databases also are paramount. We think that MS should ideally be integrated in pathology laboratories (in specialized centers at least) to achieve a uniform diagnostic workflow with existing methods and this would most probably prove to be a powerful incentive to pathologists and clinicians alike to focus on the extended range of diagnostic possibilities as well as on insights in disease mechanisms offered by the technique in cancer management.

STAR★METHODS

Detailed methods are provided in the online version of this paper and include the following:

- KEY RESOURCES TABLE
- CONTACT FOR REAGENT AND RESOURCE SHARING
- EXPERIMENTAL MODEL AND SUBJECT DETAILS
  - Patient Samples
  - Pathology Review and Histology Control
- METHOD DETAILS
  - Experimental Design
  - Tissue Preparation
  - SpiderMass Analysis
  - MALDI Mass Spectrometry Imaging
- QUANTIFICATION AND STATISTICAL ANALYSIS
  - Classification Model Construction
  - GraphPad Prism
  - Real-Time Analysis
  - Lipid Identification
  - *In Vivo* and Extemporaneous Analysis at the Surgery Room
- DATA AND SOFTWARE AVAILABILITY

SUPPLEMENTAL INFORMATION

Supplemental Information includes eight figures, two tables, two videos, and two data files and can be found with this article online at https://doi.org/10.1016/j.ccell.2018.09.009.

ACKNOWLEDGMENTS

The authors want to thank Eglantine Rollet and François-Xavier Denimal from SATT-Nord for their participation in this project. This research was supported by funding from the "Ministère de l'Enseignement Supérieur, de la Recherche et de l'Innovation," Université de Lille, and Inserm. The project was also supported by grants from ANR ANR-14-CE17-0021 REALITY'MS (to I.F.), Inserm Program PhysiCancer SPIDERMASS (to M.S.), Région Haut de France-EU FEDER (O'DREAMS (to D.T., I.F., and M.S.), SIRIC ONCOLille Grant INCa-DGOS-Inserm 6041aa (to D.T., I.F., and M.S.) and Bonus Qualité Recherche Université Lille 1 (to M.Z.).

AUTHOR CONTRIBUTIONS

Conceptualization, I.F. and M.S.; Methodology, A.B., B.F., C.F., I.F., J.Q., M.S., M.Z., and P.S.; Software, Z.T.; Validation, I.F., J.Q., M.S., A.B., P.S., Q.P., and Y.-M.R.; Formal Analysis, J.Q. and P.S.; Investigation, J.Q. and P.S.; Resources, D.T., I.F., K.M., M.P., M.S., and Z.T.; Data Curation, J.Q., P.S., and Z.T.; Writing – Original Draft, I.F., J.Q., M.S., and P.S.; Writing – Review & Editing, A.B., C.F., D.T., I.F., J.Q., M.S., M.Z., P.S., Q.P., Y.-M.R., and Z.T.; Visualization, I.F., J.Q., and P.S.; Supervision, I.F. and M.S.; Project Administration, I.F. and M.S.; Funding Acquisition, D.T., I.F., M.S., and M.Z.

DECLARATION OF INTERESTS

J.B. is an employee of Waters Research Center. K.M. and M.P. are employees of Oncovet. Q.P. is an employee of OCR. D.T. is a founder of Oncovet and OCR and a member of their scientific advisory boards. Z.T. is a consultant for Waters Corporation. System under protection by patent CA2961491 A1 (29).

Received: March 26, 2018
Revised: July 8, 2018
Accepted: September 21, 2018
Published: October 18, 2018

REFERENCES

Abramson, S. (2010). New views of modern medicine regarding treatment with stem cells, its practical and ethical consequences. Klin. Onkol. *23*, 10–13.

Aerts, H.J., Velazquez, E.R., Leijenaar, R.T., Parmar, C., Grossmann, P., Carvalho, S., Bussink, J., Monshouwer, R., Haibe-Kains, B., and Rietveld, D. (2014). Decoding tumour phenotype by noninvasive imaging using a quantitative radiomics approach. Nat. Commun. *5*, 4006.

Antonescu, C.R. (2006). The role of genetic testing in soft tissue sarcoma. Histopathology *48*, 13–21.

Arafah, K., Longuespee, R., Desmons, A., Kerdraon, O., Fournier, I., and Salzet, M. (2014). Lipidomics for clinical diagnosis: dye-assisted laser desorption/ionization (DALDI) method for lipids detection in MALDI mass spectrometry imaging. OMICS *18*, 487–498.

Azzopardi, J., Iocco, J., and Salm, R. (1983). Pleomorphic lipoma: a tumour simulating liposarcoma. Histopathology *7*, 511–523.

Balog, J., Sasi-Szabo, L., Kinross, J., Lewis, M.R., Muirhead, L.J., Veselkov, K., Mirnezami, R., Dezso, B., Damjanovich, L., Darzi, A., et al. (2013). Intraoperative tissue identification using rapid evaporative ionization mass spectrometry. Sci. Transl. Med. *5*, 194ra193.

Balog, J., Kumar, S., Alexander, J., Golf, O., Huang, J., Wiggins, T., Abbassi-Ghadi, N., Enyedi, A., Kacska, S., Kinross, J., et al. (2015). In vivo endoscopic tissue identification by rapid evaporative ionization mass spectrometry (REIMS). Angew. Chem. Int. Ed. *54*, 11059–11062.

Berkenkamp, S., Karas, M., and Hillenkamp, F. (1996). Ice as a matrix for IR-matrix-assisted laser desorption/ionization: mass spectra from a protein single crystal. Proc. Natl. Acad. Sci. U S A *93*, 7003–7007.

Bleloch, J.S., Ballim, R.D., Kimani, S., Parkes, J., Panieri, E., Willmer, T., and Prince, S. (2017). Managing sarcoma: where have we come from and where are we going? Ther. Adv. Med. Oncol. *9*, 637–659.

Caceres, S., Pena, L., Lacerda, L., Illera, M.J., de Andres, P.J., Larson, R.A., Gao, H., Debeb, B.G., Woodward, W.A., et al. (2016). Canine cell line, IPC-366, as a good model for the study of inflammatory breast cancer. Vet. Comp. Oncol. *15*, 980–995.

Carpenter, L.G., Piermattei, D.L., Salman, M.D., Orton, E.C., Nelson, A.W., Smeak, D.D., Jennings, P.B., Jr., and Taylor, R.A. (1991). A comparison of surgical training with live anesthetized dogs and cadavers. Vet. Surg. *20*, 373–378.

Carter, C.L., McLeod, C.W., and Bunch, J. (2011). Imaging of phospholipids in formalin fixed rat brain sections by matrix assisted laser desorption/ionization mass spectrometry. J. Am. Soc. Mass Spectrom. *22*, 1991–1998.

Dancey, J. (2010). mTOR signaling and drug development in cancer. Nat. Rev. Clin. Oncol. *7*, 209–219.

Deyrup, A.T., Chibon, F., Guillou, L., Lagarde, P., Coindre, J.-M., and Weiss, S.W. (2013). Fibrosarcoma-like lipomatous neoplasm: a reappraisal of so-called spindle cell liposarcoma defining a unique lipomatous tumor unrelated to other liposarcomas. Am. J. Surg. Pathol. *37*, 1373–1378.

Diamond, D.W., Besso, J., and Boudrieau, R.J. (1999). Evaluation of joint stabilization for treatment of shearing injuries of the tarsus in 20 dogs. J. Am. Anim. Hosp. Assoc. *35*, 147–153.

Eberlin, L.S., Norton, I., Dill, A.L., Golby, A.J., Ligon, K.L., Santagata, S., Cooks, R.G., and Agar, N.Y. (2012). Classifying human brain tumors by lipid imaging with mass spectrometry. Cancer Res. *72*, 645–654.

Fatou, B., Saudemont, P., Leblanc, E., Vinatier, D., Mesdag, V., Wisztorski, M., Focsa, C., Salzet, M., Ziskind, M., and Fournier, I. (2016). In vivo real-time mass spectrometry for guided surgery application. Sci. Rep. *6*, 25919.

Fatou, B., Saudemont, P., Duhamel, M., Ziskind, M., Focsa, C., Salzet, M., and Fournier, I. (2018a). Real time and in vivo pharmaceutical and environmental studies with SpiderMass instrument. J. Biotechnol. *281*, 61–66.

Fatou, B., Ziskind, M., Saudemont, P., Quanico, J., Focsa, C., Salzet, M., and Fournier, I. (2018b). Remote atmospheric pressure infrared matrix-assisted laser desorption-ionization mass spectrometry of proteins. Mol. Cell. Proteomics *7*, 1637–1649.

Fletcher, C., Bridge, J., Hogendoorn, P., and Mertens, F. (2013). World Health Organization Classification of Tumours of Soft Tissue and Bone, Fourth Edition (IARC Press).

Foster, D.A. (2009). Phosphatidic acid signaling to mTOR: signals for the survival of human cancer cells. Biochim. Biophys. Acta *1791*, 949–955.

Galea, D., Inglese, P., Cammack, L., Strittmatter, N., Rebec, M., Mirnezami, R., Laponogov, I., Kinross, J., Nicholson, J., Takats, Z., and Veselkov, K.A. (2017). Translational utility of a hierarchical classification strategy in biomolecular data analytics. Sci. Rep. *7*, 14981.

Greenfield, C.L., Johnson, A.L., Schaeffer, D.J., and Hungerford, L.L. (1995). Comparison of surgical skills of veterinary students trained using models or live animals. J. Am. Vet. Med. Assoc. *206*, 1840–1845.

Jaber, O.I., and Kirby, P.A. (2015). Alveolar soft part sarcoma. Arch. Pathol. Lab. Med. *139*, 1459–1462.

Laiko, V.V., Taranenko, N.I., Berkout, V.D., Yakshin, M.A., Prasad, C.R., Lee, H.S., and Doroshenko, V.M. (2002). Desorption/ionization of biomolecules from aqueous solutions at atmospheric pressure using an infrared laser at 3 microm. J. Am. Soc. Mass Spectrom. *13*, 354–361.

Lewis, D.D. (1995). Management of penetrating joint injuries. Vet. Clin. North Am. Equine Pract. *25*, 1197–1223.

Liu, W., Bennett, M., and Helm, T. (2011). Canine melanoma: a comparison with human pigmented epithelioid melanocytoma. Int. J. Dermatol. *50*, 1542–1545.

Lou, S., Balluff, B., Cleven, A.H.G., Bovee, J., and McDonnell, L.A. (2017). Prognostic metabolite biomarkers for soft tissue sarcomas discovered by mass spectrometry imaging. J. Am. Soc. Mass Spectrom. *28*, 376–383.

Mentzel, T., Palmedo, G., and Kuhnen, C. (2010). Well-differentiated spindle cell liposarcoma ('atypical spindle cell lipomatous tumor') does not belong to the spectrum of atypical lipomatous tumor but has a close relationship to spindle cell lipoma: clinicopathologic, immunohistochemical, and molecular analysis of six cases. Mod. Pathol. *23*, 729.

Misdorp, W., and Hart, A.A. (1976). Prognostic factors in canine mammary cancer. J. Natl. Cancer Inst. *56*, 779–786.

Ogretmen, B. (2018). Sphingolipid metabolism in cancer signalling and therapy. Nat. Rev. Cancer *18*, 33–50.

Pena, L., Gama, A., Goldschmidt, M.H., Abadie, J., Benazzi, C., Castagnaro, M., Diez, L., Gartner, F., Hellmen, E., Kiupel, M., et al. (2014). Canine mammary tumors: a review and consensus of standard guidelines on epithelial and myoepithelial phenotype markers, HER2, and hormone receptor assessment using immunohistochemistry. Vet. Pathol. *51*, 127–145.

Phelps, D.L., Balog, J., Gildea, L.F., Bodai, Z., Savage, A., El-Bahrawy, M.A., Speller, A.V., Rosini, F., Kudo, H., McKenzie, J.S., et al. (2018). The surgical intelligent knife distinguishes normal, borderline and malignant gynaecological tissues using rapid evaporative ionisation mass spectrometry (REIMS). Br. J. Cancer *118*, 1349–1358.

Pluhar, G.E., Heiner, J.P., Manley, P.A., Bogdanske, J.J., Vanderby, R., Jr., and Markel, M.D. (2000). Comparison of three methods of gluteal muscle attachment to an allograft/endoprosthetic composite in a canine model. J. Orthop. Res. *18*, 56–63.

Le Rhun, E., Duhamel, M., Wisztorski, M., Zairi, F., Maurage, C.A., Fournier, I., Reyns, N., and Salzet, M. (2015). METB-07 classification of high grade glioma using matrix-assisted laser desorption/ionization mass spectrometry imaging (MALDI MSI): interim results of the GLIOMIC study. Neuro Oncol. *17*, v136.

Le Rhun, E., Duhamel, M., Wisztorski, M., Gimeno, J.P., Zairi, F., Escande, F., Reyns, N., Kobeissy, F., Maurage, C.A., Salzet, M., and Fournier, I. (2016). Evaluation of non-supervised MALDI mass spectrometry imaging combined with microproteomics for glioma grade III classification. Biochim. Biophys. Acta *1865*, 875–890.

Salzet, M., Fournier, I., Focsa, C., Ziskind, M., Fatou, B., and Wisztorski, M. (2017). Device for real-time in vivo molecular analysis. In (US Patent App. 15/512,703).

Schaefer, K.-C., Denes, J., Albrecht, K., Szaniszlo, T., Balog, J., Skoumal, R., Katona, M., Toth, M., Balogh, L., and Takats, Z. (2009). In vivo, in situ tissue

analysis using rapid evaporative ionization mass spectrometry. Angew. Chem. Int. Ed. *48*, 8240–8242.

Schneider, R. (1970). Comparison of age, sex, and incidence rates in human and canine breast cancer. Cancer *26*, 419–426.

Schwyn, U., Crompton, N.E., Blattmann, H., Hauser, B., Klink, B., Parvis, A., Ruslander, D., and Kaser-Hotz, B. (1998). Potential tumour doubling time: determination of Tpot for various canine and feline tumours. Vet. Res. Commun. *22*, 233–247.

Skubitz, K.M., Pambuccian, S., Manivel, J.C., and Skubitz, A.P. (2008). Identification of heterogeneity among soft tissue sarcomas by gene expression profiles from different tumors. J. Transl. Med. *6*, 23.

St John, E.R., Balog, J., McKenzie, J.S., Rossi, M., Covington, A., Muirhead, L., Bodai, Z., Rosini, F., Speller, A.V.M., et al. (2017). Rapid evaporative ionisation mass spectrometry of electrosurgical vapours for the identification of breast pathology: towards an intelligent knife for breast cancer surgery. Breast Cancer Res. *19*, 59.

Stiller, C.A., Trama, A., Serraino, D., Rossi, S., Navarro, C., Chirlaque, M.D., Casali, P.G., and Group, R.W. (2013). Descriptive epidemiology of sarcomas in Europe: report from the RARECARE project. Eur. J. Cancer *49*, 684–695.

Takashima-Uebelhoer, B.B., Barber, L.G., Zagarins, S.E., Procter-Gray, E., Gollenberg, A.L., Moore, A.S., and Bertone-Johnson, E.R. (2012). Household chemical exposures and the risk of canine malignant lymphoma, a model for human non-Hodgkin's lymphoma. Environ. Res. *112*, 171–176.

Trojani, M., Contesso, G., Coindre, J., Rouesse, J., Bui, N., De Mascarel, A., Goussot, J., David, M., Bonichon, F., and Lagarde, C. (1984). Soft-tissue sarcomas of adults; study of pathological prognostic variables and definition of a histopathological grading system. Int. J. Cancer *33*, 37–42.

Vaysse, P.M., Heeren, R.M.A., Porta, T., and Balluff, B. (2017). Mass spectrometry imaging for clinical research - latest developments, applications, and current limitations. Analyst *142*, 2690–2712.

Walch, A., Rauser, S., Deininger, S.O., and Hofler, H. (2008). MALDI imaging mass spectrometry for direct tissue analysis: a new frontier for molecular histology. Histochem. Cell Biol. *130*, 421–434.

Willems, S.M., van Remoortere, A., van Zeijl, R., Deelder, A.M., McDonnell, L.A., and Hogendoorn, P.C. (2010). Imaging mass spectrometry of myxoid sarcomas identifies proteins and lipids specific to tumour type and grade, and reveals biochemical intratumour heterogeneity. J. Pathol. *222*, 400–409.

Zhang, J., Rector, J., Lin, J.Q., Young, J.H., Sans, M., Katta, N., Giese, N., Yu, W., Nagi, C., Suliburk, J., et al. (2017). Nondestructive tissue analysis for ex vivo and in vivo cancer diagnosis using a handheld mass spectrometry system. Sci. Transl. Med. *9*, 406.

STAR★METHODS

KEY RESOURCES TABLE

REAGENT or RESOURCE	SOURCE	IDENTIFIER
Biological Samples		
Healthy and Cancerous dog tissues	Oncovet	https://www.oncovet.net/
Chemicals, Peptides, and Recombinant Proteins		
2,5-dihydroxybenzoic acid (2,5-DHB)	Sigma-Aldrich	Cat#85707; CAS: 490-79-9
HPLC Water	Biosolve	Cat#232106; CAS:7732-18-5
Trifluoroacetic acid (TFA)	Biosolve	Cat#202306; CAS: 76-05-1
Ethanol (EtOH)	Biosolve	Cat#052506; CAS: 64-17-5
Isopropanol (IPA)	Biosolve	Cat#162606; CAS: 67-63-0
Xylene	Biosolve	Cat#242505; CAS: 1330-20-7
Mayer's Hemalun solution	VWR	Cat#1.09249.0500;
Phloxine B	RAL Diagnostics	Cat#350750
Saffron	Labonor	Cat#11507736
EUKITT slide mounting medium	Sigma-Aldrich	Cat#03989; CAS:25608-33-7
Deposited Data		
Raw Data (Spectral library used for classification models and MS images)	ProteomeXchange via PRIDE database	ProteomeXchange: PXD010990
Software and Algorithms		
Offline Model Builder, v1.1.773.0	Waters research center	z.takats@imperial.ac.uk
OMB Recognition, v1.1.857.0	Waters research center	z.takats@imperial.ac.uk
GraphPad Prism v6	GraphPad Software	https://www.graphpad.com/
ImageQuest v1.1.0 build 54	Thermo Fisher Scientific	http://www.thermofisher.com/order/catalog/product/10137985
SCiLS v2018a MVS Premium 3D	SCiLS GmbH	https://scils.de/
Pannoramic viewer v1.15	3DHISTECH	https://www.3dhistech.com/pannoramic_viewer
Other		
Lipids identification Database	The LIPID MAPS Lipidomics Gateway	http://www.lipidmaps.org

CONTACT FOR REAGENT AND RESOURCE SHARING

Further information and requests for resources and reagents should be directed to and will be fulfilled by the Lead contact, Isabelle Fournier (isabelle.fournier@univ-lille.fr).

EXPERIMENTAL MODEL AND SUBJECT DETAILS

Patient Samples

This prospective study was performed on *ex vivo* biopsies from dog patients with sarcoma. We purposely built a cohort including all breed types for our instrument to be applicable to all patients at the veterinary clinic. The cohort size depended on the veterinarian recruitment after sarcoma surgeries and all sarcomas were included, regardless of the origin, so that the cohort reflected the actual cases treated at the clinic.

All dog patient samples were collected after signed consent of their owner, and this clinical trial has been approved by the Oncovet ethical committee. Tumor material was available from 25 patients following this pathology distribution: Fibrosarcoma (n = 7), Osteosarcoma (n = 5), Undifferentiated (n = 5), Hemangiopericytoma (n = 2), Rhabdomyosarcoma (n = 1), Histiocytic sarcoma (n = 1), Gastro-Intestinal Stromal Tumor (GIST, n = 1), Malignant Peripheral Nerve Sheath Tumor (MPNST, n = 1) and Splenic sarcoma (n = 1). Normal material was obtained from the same patient when possible or during other surgeries. Complete details can be found in the Table S1.

Pathology Review and Histology Control

For histology, one veterinary pathologist (QP) read and annotated HPS stained tissues, and one human sarcoma board certified pathologist (Y-MR, Oscart Lambret Center) commented and validated these annotations. The pathologists were blind to any information about the acquisition from MS studies. The annotations were done on Hemalun/Phloxine/Saffron (HPS) stained tissues. For HPS staining, a 10-μm thick tissue slice consecutive to the SpiderMass-analyzed tissue was treated with hemalun solution for 1 min and rinsed with tap water. Then the tissue section was stained in phloxine 0.1% solution for 10 s and rinsed with tap water before dehydration in 70% and 100% ethanol baths. Finally, the sections were dipped in saffron for 5 s, rinsed twice in alcohol, cleaned in xylene, and mounted with cover slips and the EUKITT® slide mounting medium. After HPS staining, the nuclei were colored dark blue, the cytoplasm pink, and the conjunctive tissue orange. The stained slide was scanned for digital image acquisition using the Pannoramic MIDI slide scanner (3DHISTECH LTD. Budapest, Hungary) and the images were viewed and exported using Pannoramic viewer 1.15.

METHOD DETAILS

Experimental Design

The data were collected and processed in blind after keeping the anonymity of patients using an internal laboratory labeling. All samples of the cohort were analyzed and since sarcoma is a very heterogeneous class of cancer originating from various types of tissues, we took great care that features discriminating the different types of tissues contributed less weight to the classification model than the other features of interest such as grading or typing.

No patients or generated data were excluded from the study and outliers were defined per se when their value was more than 5 times the SD of the mean. All cross-validation results are shown with and without the outliers taken into account. The tissues were analyzed in 5 different locations to replicate the measurement and in both modes of analysis.

Tissue Preparation

After removal, the fresh biopsies were immediately snap-frozen in liquid nitrogen and stored at −80°C until use to avoid tissue degradation. When possible, distant healthy tissues and tumor margins were sampled as well. The tissues were warmed up to −20°C in a cryostat (Leica Microsystems, Nanterre, France) before preparation according to the workflow presented in Figure 1F. Using a metallic tissue cutting matrix (Ted Pella. Redding, California, USA) as a guide to obtain a neat surface, the tissues were cut in two halves and one was kept frozen in case further experiments would be needed. On the other half, a 1-mm thick slice was cut to be used for the SpiderMass analysis. Considering that we use resonant excitation of water molecules this thickness is needed to slow down the drying of the tissue during sampling. The remaining tissue was cut at 10 μm with the cryotome. Two sections were deposited onto polylysine-coated slides by finger-thawing. One was used for Mass Spectrometry Imaging (MSI) analysis while the other was stained with HPS and served as morphological control. This workflow was designed to ensure that the tissue used for MSI reflects the true composition of the tissue surface analyzed by SpiderMass and of the morphological control.

SpiderMass Analysis

The global design of the instrument setup is described in a previous study (Fatou et al., 2016). Briefly, the system is composed of three parts including a laser system for micro-sampling of tissues set remotely, a transfer line allowing for transfer of the micro-sampled material to the third part, which is the mass spectrometer itself. The first part is composed of a tunable wavelength OPO which is tunable between 2.8 μm to 3.1 μm (Radiant version 1.0.1, OPOTEK Inc., Carlsbad, USA) pumped by a pulsed Nd:YAG laser (pulse duration: 5 ns, λ=1064 nm, Quantel, Les Ulis, France). A biocompatible laser fiber (450 μm core diameter; length of 1 m, Infrared Fiber Systems, Silver Spring, USA) is connected to the laser system output and a handpiece including a 4 cm focusing lens is attached to the end of the laser fiber. The handpiece with a 4 cm focusing lens allows the user to hold the system and screen the surface of raw tissues at a resolution of 500 μm. In these experiments the irradiation time was fixed to 10 s at 4 mJ/pulse laser energy corresponding to a laser fluence of 2.03 J/cm^2. The laser energy was measured at the focal point of the focusing lens using a power meter (ThorLabs, Maisons-Laffitte, France). The second part of the system corresponds to a 3 m length transfer line made from a Tygon ND 100-65 tubing (2.4 mm inner diameter, 4 mm outer diameter, Akron, USA). The transfer line is attached on one side to the laser handpiece at the end of the laser fiber and on its other side directly connected to the mass spectrometer (Synapt G2-S, Waters, Wilmslow, United Kingdom) from which the conventional electrospray source was removed and replaced by an atmospheric pressure interface described elsewhere (Balog et al., 2015). The SpiderMass prototype system used for these experiments is presented in Figures 1A–1E. Spectral acquisition was performed both in positive and negative ion resolution mode with a scan time of 1 s. Prior to SpiderMass analysis, the samples were taken out of the −20°C freezer and thawed to RT for 1 min. The spectral acquisition sequence was composed of 5 acquisitions using 10-s irradiation periods. Taking into consideration that both positive and negative ion modes were recorded, a total of 10 acquisitions per biopsy were performed. Biopsy homogeneity was verified using the morphological control prior to each acquisition to ensure that each acquisition was performed on the same histological area or to take into account the variability caused by tissue heterogeneity when needed. SpiderMass data were validated by MALDI-MSI and significantly discriminant lipids were identified, where possible, using MS/MS experiments.

MALDI Mass Spectrometry Imaging

For MALDI-MSI experiments, slides were taken out of storage, immediately dehydrated under vacuum at room temperature for 30 min, and scanned using a slide scanner (Nikon, Tokyo, Japan). 2,5-Dihydrobenzoic acid (DHB) matrix (20 mg/mL in 7:3 (v/v) MeOH/0.1% TFA in water) was manually sprayed using a syringe pump connected to an electrospray nebulizer operating at a 300 μL/h flow rate with compressed nitrogen flow pressure maintained at 1.1 bar. The nebulizer was moved uniformly throughout the entire tissue for 10 to 12 min according to tissue size. The homogeneity of the crystals was examined under a light microscope after spraying. The tissues were then analyzed using a MALDI LTQ Orbitrap XL mass spectrometer (Thermo Fisher Scientific, Bremen, Germany) equipped with an N_2 laser (model MNL-100; LTB Lasertechnik, Berlin GmbH) which has a maximum repetition rate of 60 Hz. The maximum energy per pulse was set to 10 μJ and acquisition was performed in positive mode at 30,000 mass resolution (centered at *m/z* 200). Each spectrum was generated using one microscan at one microscan per step. The automatic gain control (AGC) feature was turned off and the number of laser shots was set to 10. The raster step size was set to 70 μm. The generated images were then converted to imzML format using the manufacturer software ImageQuest and exported to SCiLS. Spectral normalization was performed using the DHB peak at *m/z* 177. Medium edge-preserving spatial denoising, peak picking using orthogonal matching pursuit (OMP), and peak alignment by centroid matching to the mean spectrum were applied to generate the set of peaks used in subsequent analysis.

QUANTIFICATION AND STATISTICAL ANALYSIS

Classification Model Construction

For data analysis, all raw data files produced with the SpiderMass instrument were imported into the Offline Model Builder software. After importation, spectra were subjected to pre-processing steps including background subtraction, total ion count normalization, and re-binning to a 0.1 Da window. All of the processed MS spectra obtained from the 33 histologically validated samples were then used to build a principal component analysis and linear discriminant analysis (PC-LDA) classification model. The first step consisted of PCA to reduce data multidimensionality by generating features that explain most of the variance observed. These features were then subjected to supervised analysis using LDA by setting the classes that the model will be based upon. LDA attempts to classify the sample spectra and assess the model by cross validation. Cross validation was carried out by the ''leave one patient out'' method. In this method, the spectra are grouped by patient and left out one by one; at each step the model without the patient is interrogated against this model.

For tissue typing, the 2-class model (n = 2) corresponds to normal vs. cancer and the 3-class model (n = 3) to normal vs. cancer vs. necrosis. The tested spectra (n = 180) correspond to the model built using averaged MS spectra, while the others correspond to those generated using individual spectra. For tissue grading, the 4 classes correspond to normal vs. grade I vs. grade II vs. grade III. The tested spectra (n = 139) correspond to the model built using averaged MS spectra and removing the spectra from the samples for which grading was not given.

GraphPad Prism

m/z intervals corresponding to loading scores with the largest contribution to the first principal components (i.e., where ideally 80% of the variance is explained) were obtained and their normalized intensities across different classes were plotted using GraphPad Prism 6. To consider the imbalance in the numbers of sample per class we used non-parametrical two-sided ANOVA (Kruskal-Wallis) followed by Dunn's test and adjusted the p value to account for the multiple comparisons with a family-wise significance and confidence level of 0.05.

Real-Time Analysis

For real-time analysis, the built model was exported to a second software module called OMB Recognition. The parameters for this analysis were: a TIC threshold of $1E^{+4}$ count for irradiation detection, a normalized intensity threshold of $1E^{+6}$, and an outlier limit of 5 standard deviations. The software analyzes 1 scan per spectrum and has a 3 s timeout waiting for good spectrum. The cross-validated models are exported from the OMB software and then loaded in the OMB Recognition software module before any real-time piece of tissue analysis by the SpiderMass. The real-time acquired data are then directly interrogated, giving an immediate feedback using a color scale predefined from the specified classes.

Lipid Identification

m/z intervals corresponding to loadings with the largest contribution to the explained variance observed in the different groups were selected for MS/MS-based identification. For these experiments, the settings were exactly the same as described in the SpiderMass section, except that a Q-Exactive mass spectrometer (Thermo Fisher Scientific, Bremen, Germany) was used instead of the Synapt G2-S due to the high mass accuracy of the instrument. Full scans were acquired in the Orbitrap mass analyzer operated at 70,000 full width at half maximum (FWHM) resolving power (centered at *m/z* 400) and 1 s scan time in positive mode. The identifications were performed directly on the tissue by doing a full scan first to verify the presence of the targeted masses. Then after switching to MS/MS mode, the ions were selected ''on the fly'' for high-energy collision dissociation (HCD) with an isolation window of 0.8 *m/z* and with the normalized collision energy (NCE) ramp set according to the given mass. MS/MS spectra were acquired for a continuous irradiation

time of 30 s. The resulting spectra were annotated manually, and assignments were verified by interrogating the high accuracy mass measurements of the precursor ions using the LIPIDMAPS database.

In Vivo and Extemporaneous Analysis at the Surgery Room

For assessment in real conditions, the SpiderMass prototype was moved to the vet surgery room (Figure 7A). After installation, the different parts of the prototype including the MS instrument, laser system and laser probe were sterilized using gas. Additionally, the laser probe was sterilized in 70% ethanol immediately before the surgery and covered in sterile protection sleeve. The SpiderMass system was operated by a trained surgeon during a surgical operation using the same parameters both for the laser probe and the MS instrument as for the *ex vivo* experiments (Figure 7B). After analyzing canine tissues *in vivo*, the adjacent muscle was excised and extemporaneous analysis was conducted on the bench. Video S2 shows the use of SpiderMass in the operating theatre under sterile conditions. To demonstrate the low invasiveness of the system and its ability to produce tissue-specific molecular profiles *in vivo*, SpiderMass was assessed on a dog patient *in vivo* and for extemporaneous analysis on the bench in the course of surgery.

DATA AND SOFTWARE AVAILABILITY

The MS imaging files in imzML format and the spectral library used to construct the classification models have been deposited to the ProteomeXchange consortium: PXD010990.

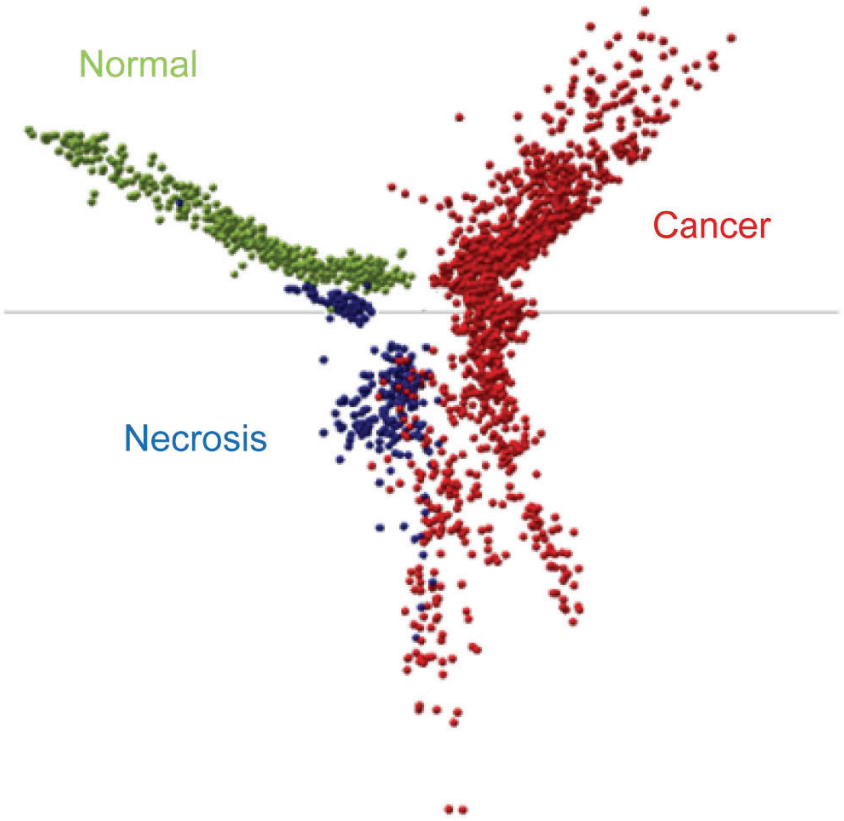

Figure S1. Related to Figure 3. PCA result of the 3-class model (normal vs. cancer vs. necrosis). Model was built using individual MS spectra acquired in positive mode. The necrotic group (blue) partially explains the heterogeneity of the spectra belonging to the cancer group (red).

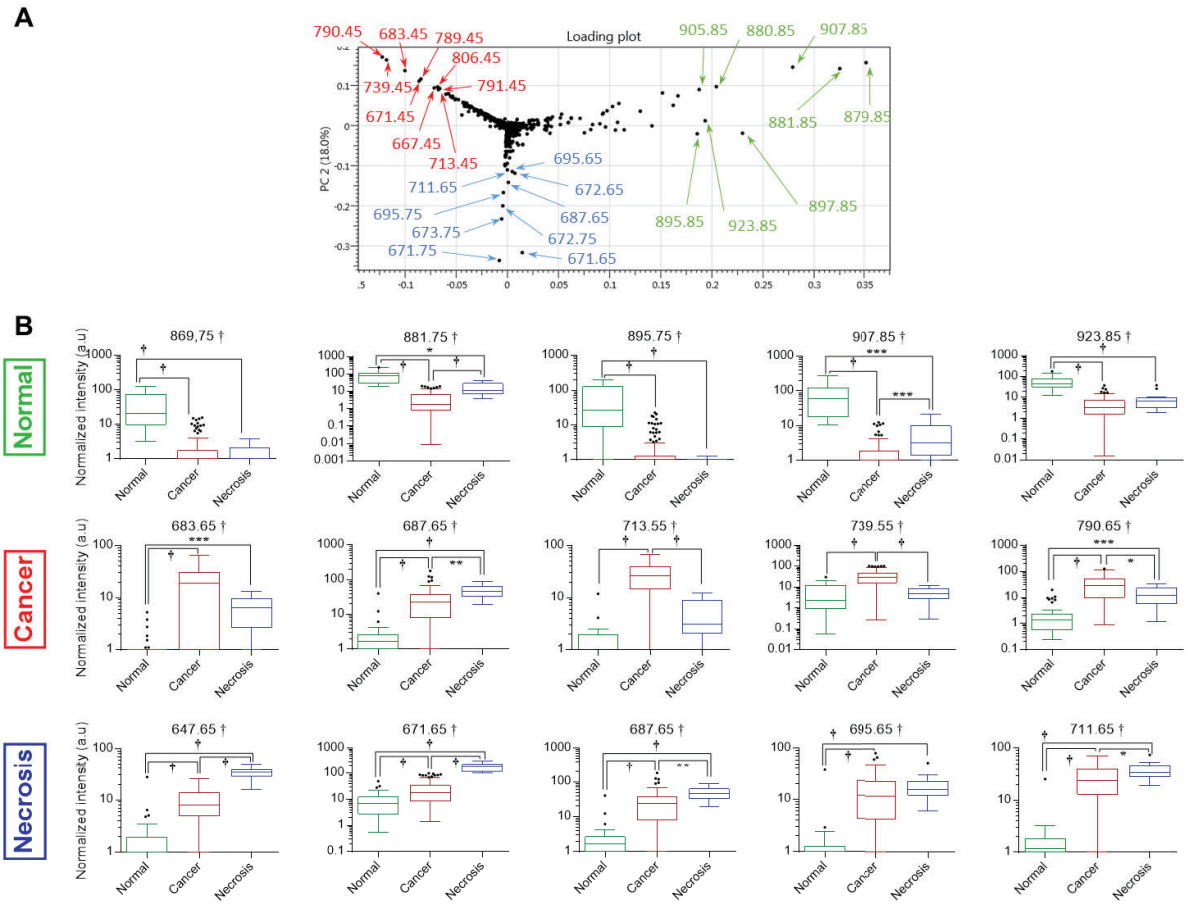

Figure S2. Related to Figure 5. Plots of the 3-class model (normal, cancer, and necrosis) and boxplot representation of some of the extracted *m/z* values explaining most of the variance between the groups. (**A**) Loading plots showing the *m/z* values that explain most of the variance between these classes. (**B**) Peaks significantly different for the normal, cancer, and necrosis classes, respectively. Normalized against the total ion count (TIC) intensities are Log10 transformed and represented with boxplots using the Tukey method for whiskers definition. The box extends from the 25th to 75th percentiles. The line in the middle of the box is plotted at the median. The upper and down whiskers are represented at 1.5 times the distance between those 25 and 75 percentiles and all points beyond the whiskers are represented as individual point dots and depict the outliers. *m/z* 687.65 was found to be significantly different for both cancer and necrosis zones compared against the normal zone. * = p value ≤ 0.05, **=p value ≤ 0.01, ***=p

value ≤ 0.001, †= p value ≤ 0.0001. All statistical results and experiments are presented in the **Data File S2**.

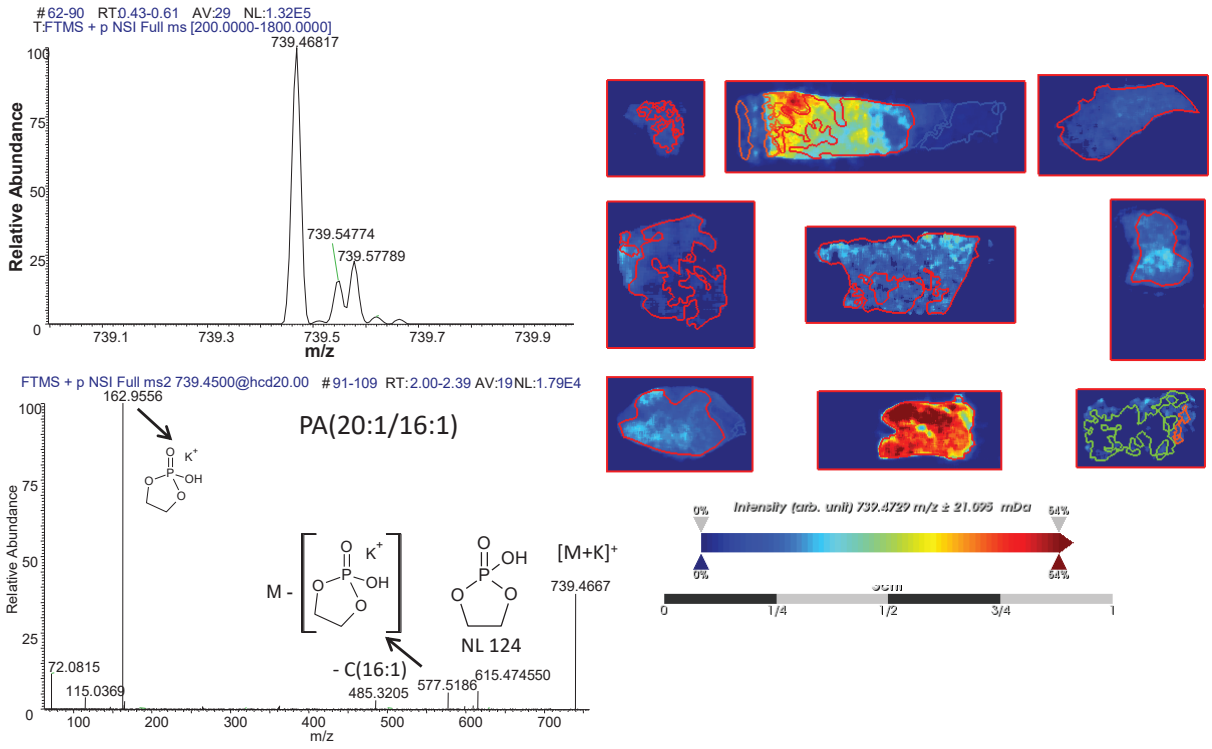

Figure S3. Related to Figure 5. MS/MS fragmentation of *m/z* 739.55. The full MS spectrum acquired at 70,000 resolution (at *m/z* 400) shows at least 3 peaks with very close nominal masses, each of which shows different distribution in MALDI-MSI. Two of these, *m/z* 739.46817 and *m/z* 739.54774 show distinct localizations in some cancer regions (ROIs outlined in red), while *m/z* 739.57789 particularly localized in the necrotic region. *m/z* 739.46817 is the most intense peak in this window, and fragments of its potassiated adduct dominate the MS/MS spectrum.

Table S2. Related to Figure 5. Lipid identifications based on SpiderMass high-resolution MS & MS/MS data, recorded in positive mode.

m/z			Assignment	
SpiderMass [1]Q-TOF	SpiderMass [2]HR-MS	[3]MSI	HR-MS/MS	[4]LIPIDMAPS (adduct, Δppm)
Normal				
869.75	869.6991	869.697		TG 50:2 ([M+K]$^+$, 0.46)
881.85	881.7584	881.761	TG (18:1/18:0/16:0) [M+Na]$^+$	TG 52:2 ([M+Na]$^+$, 1.70)
895.75	895.7154	895.705		TG 52:3 ([M+K]$^+$, 0.31)
907.85	907.7727	907.771	TG (18:1/18:0/18:2) [M+Na]$^+$	TG 54:3 ([M+Na]$^+$, 0.22)
923.85	923.7443	923.741		TG 54:2 ([M+K]$^+$, 2.30)
Cancer				
683.65	683.5012	683.472	PG (16:1/14:2) [M+Na]$^+$	[5]
687.65	687.5469	N/O		*18:2 cholesteryl ester ([M+K]$^+$, 1.24) or SM (d18:2/15:0) ([M+H]$^+$, 2.91) or PE-Cer ([M+H]$^+$, 2.91)
713.55	713.4524	713.448	PA	PA 34:1 ([M+K]$^+$, 0.90)*
739.55	739.4682	739.515	PA (20:1/16:1) [M+K]$^+$	PA 36:2 ([M+K]$^+$, 0.92)
790.65	790.4855	790.924	PE (37:5) [M+K]$^+$	PE 37:5 ([M+K]$^+$, 9.00)
Necrosis				
647.65	647.5591	647.506		DG ([M+Na]$^+$, 0.93)
671.65	671.5733	671.575		*20:5 cholesteryl ester ([M+H]$^+$, 4.31) or 18:2 cholesteryl ester ([M+Na]$^+$, 0.59)
687.65	687.5455	N/O[6]		*SM (d18:2/15:0) ([M+H]$^+$, 2.91) or PE-Cer* ([M+H]$^+$, 2.91) or 18:2 Cholesteryl ester ([M+K]$^+$, 3.20) *
695.65	695.5731	695.454		20:4 cholesteryl ester ([M+Na]$^+$, 0.85)
711.65	711.5439	711.437	PA	**

[1]QTOF indicates m/z values with significant contribution to the PC scores from the PC-LDA classification model acquired using a QTOF instrument.
[2]HR-MS indicates m/z obtained from high-resolution MS mass measurements using an orbitrap instrument
[3]MSI indicates m/z obtained by MALDI imaging
[4]MS^{2}LIPIDMAPS assignment disregarded because of conflicting evidence with MS/MS fragments observed in the HR-MS/MS experiments
[5]Multiple assignments possible
[6]N/O not observed

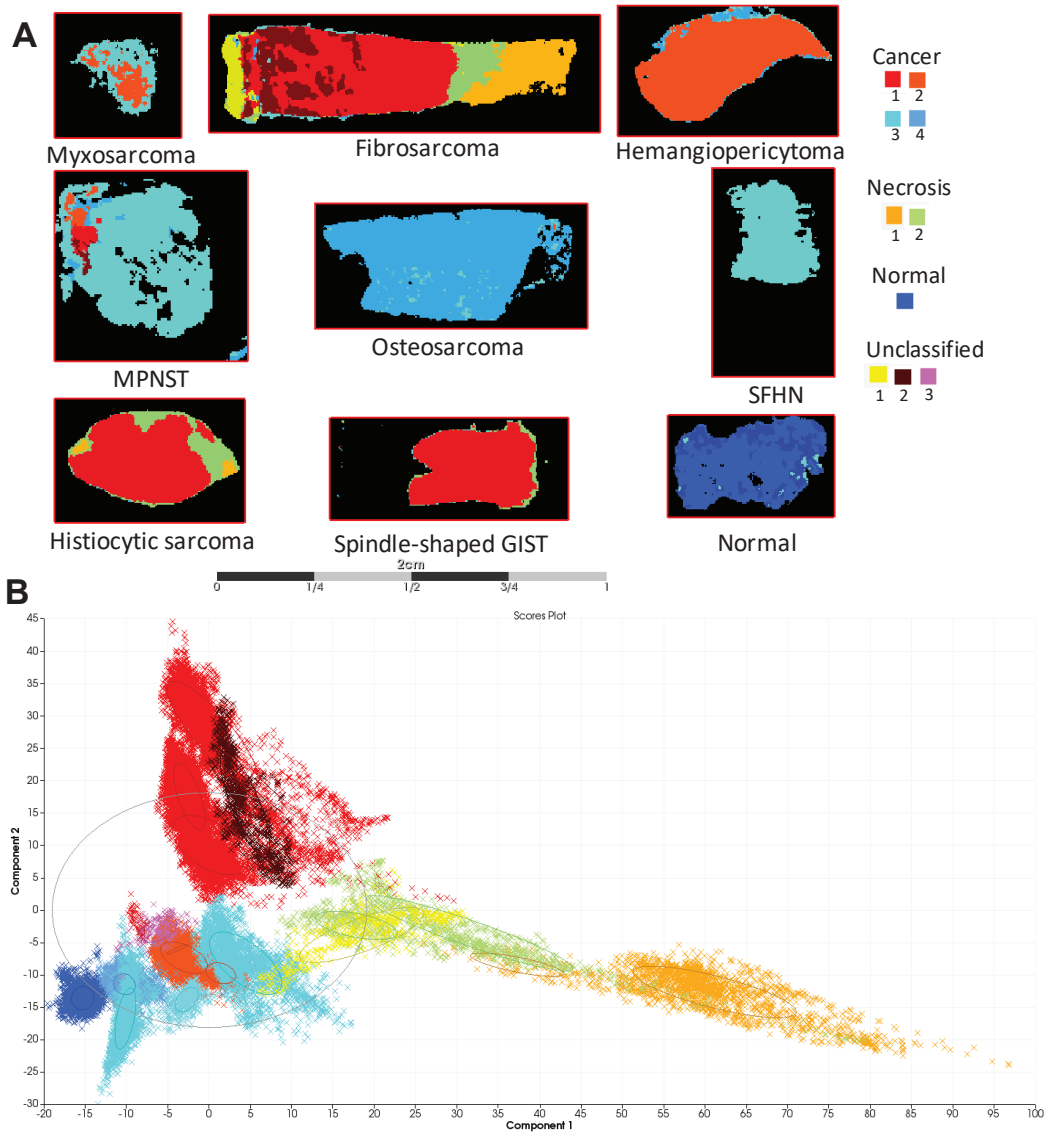

Figure S4. Related to Figure 5. MALDI-MSI analysis of sarcoma biopsies. (**A**) Spatial segmentation of spectra from the acquired MALDI MS images, using k-means clustering with Manhattan as the algorithm for distance measurement. (**B**) Regions of interest (ROIs) from each biopsy were extracted and subjected to principal component analysis; scores of the first two principal components are plotted, following the same color scheme used to distinguish the ROIs in spatial segmentation. MPNST = Malignant Peripheral Nerve Sheath Tumor, SFHN = Splenic Fibrohistiocytic Nodule, GIST = GastroIntestinal Stromal Tumor.

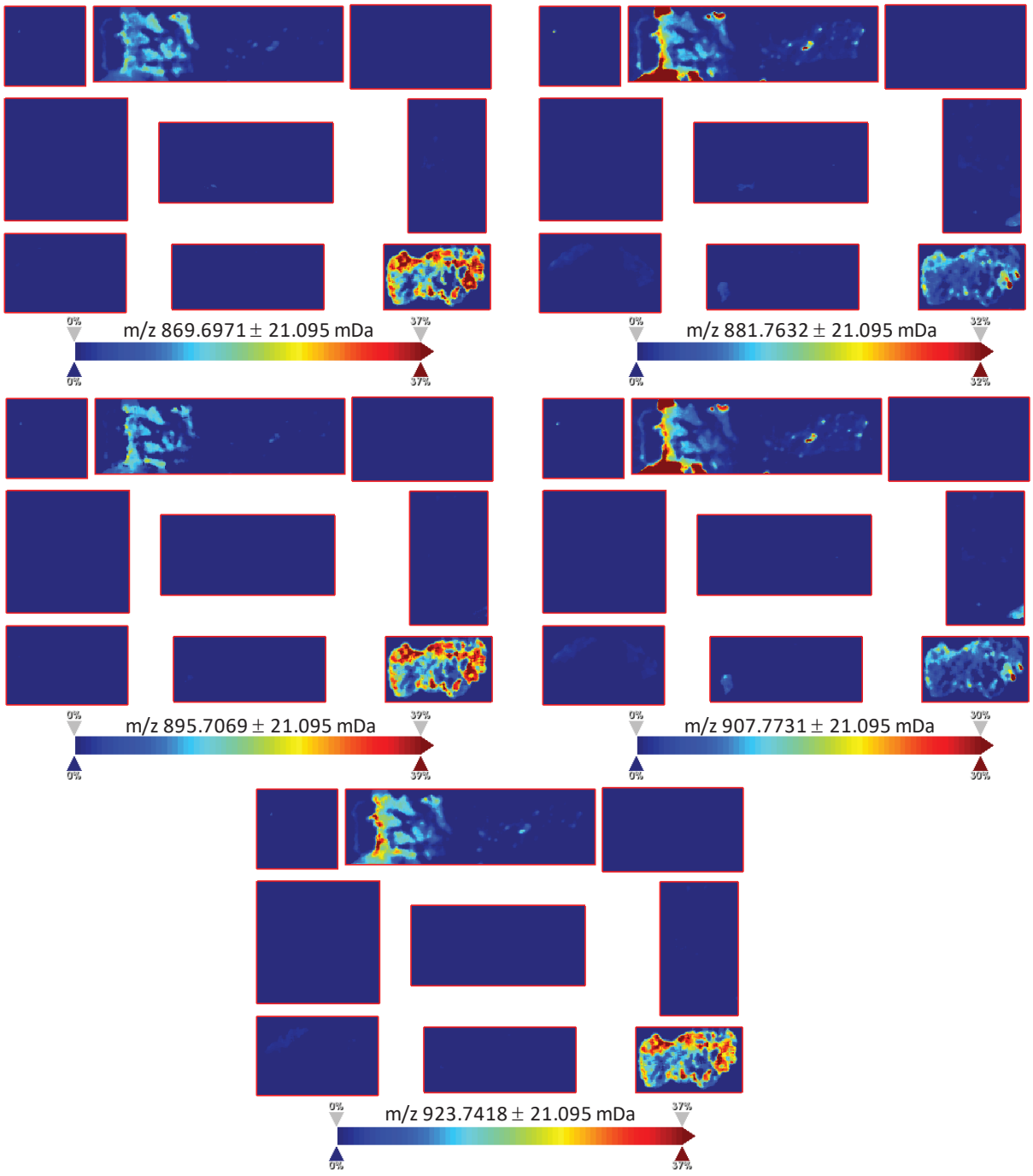

Figure S5. Related to Figure 5. MALDI MS ion images of *m/z* enriched in the normal areas of tissue.

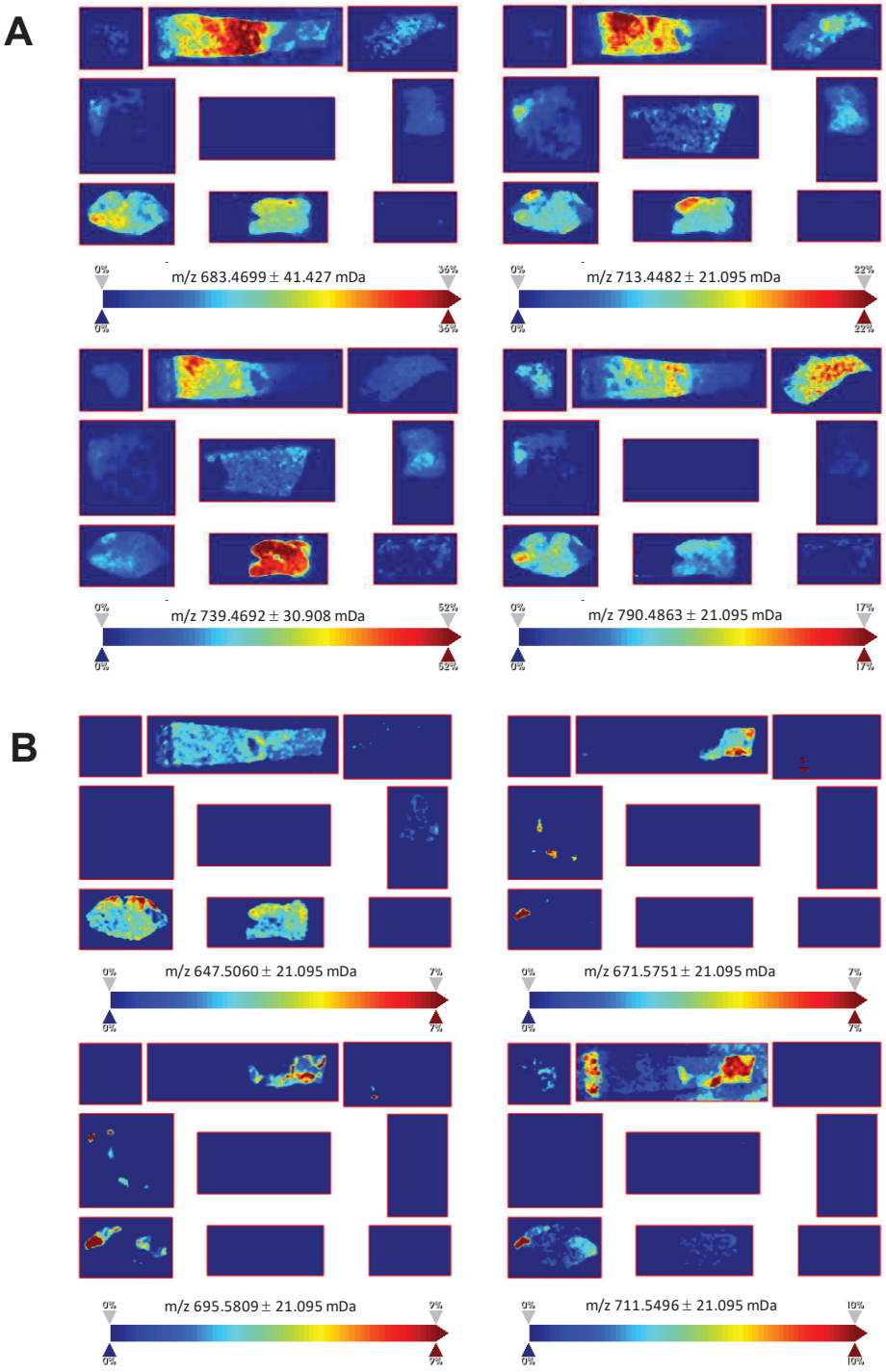

Figure S6. Related to Figure 5. (A) MALDI MS ion images of *m/z* enriched in the cancerous areas of tissues. **(B)** MALDI MS ion images of *m/z* enriched in the necrotic areas of tissue.

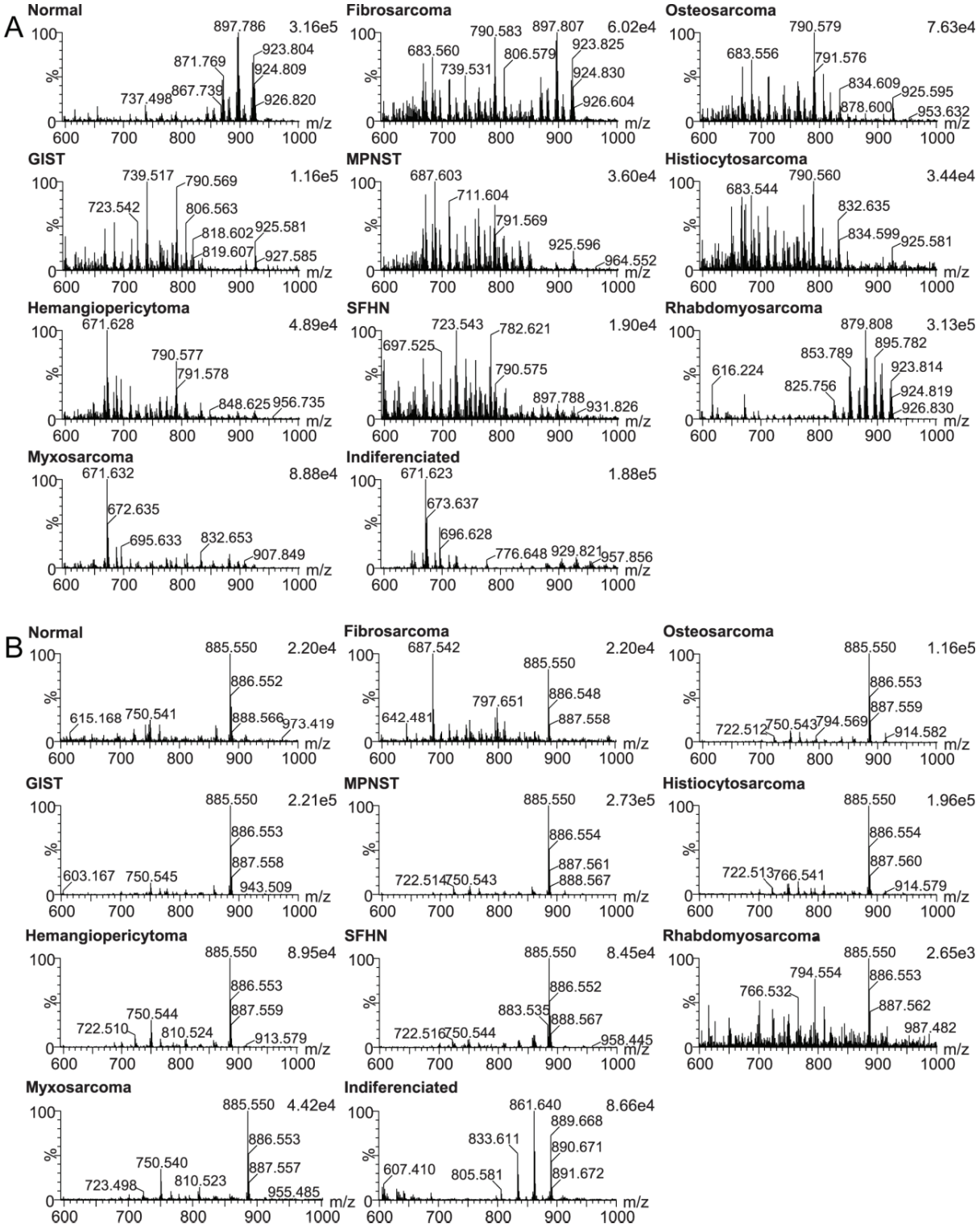

Figure S7. Related to Figure 6. (A) Typical MS spectra recorded in real-time from each subtype of sarcoma biopsies using the SpiderMass in positive mode. **(B)** Typical MS spectra recorded in

real-time using SpiderMass in negative mode from each subtype of sarcoma biopsies. After acquisition, all acquired MS spectra are loaded into their respective class and used for the establishment of the classification model shown in **Figure S8**.

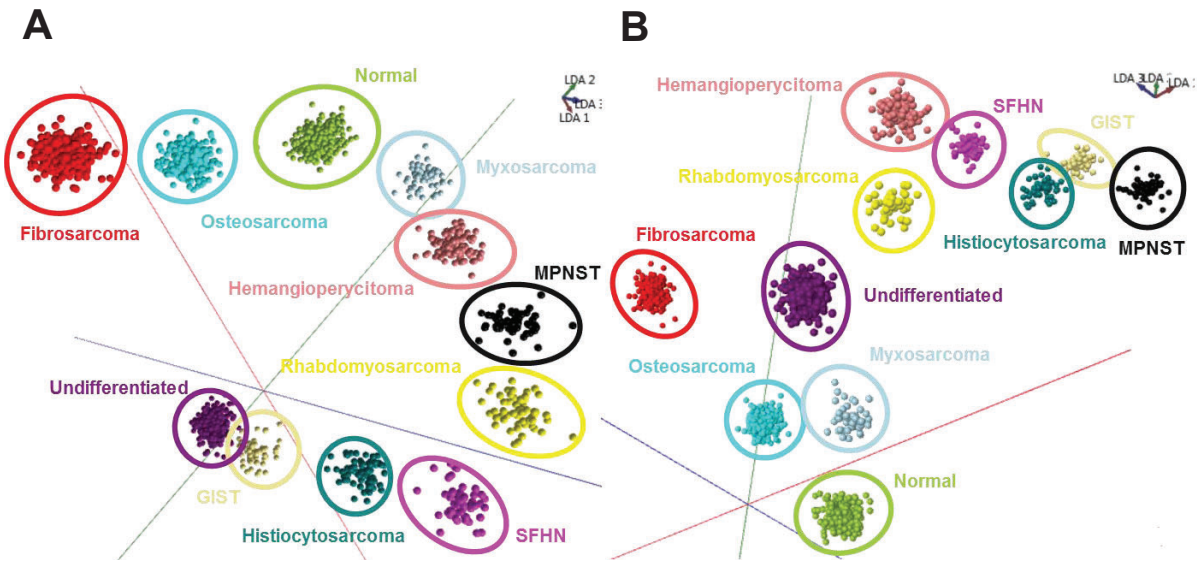

Figure S8. Related to Figure 6. LDA representation of the PC-LDA models for subtyping. These were established using MS spectra recorded in both positive **(A)** and negative **(B)** modes from all biopsies using their individual spectra.

Table S1, related to Figure 2. Complete description of the patients

Lab number	OCR number	Reception date	Tissue nature	Subtype	Pathological type	Classification	Adicap code			Breed	Age	Notes
Ds 1	H15-3523	12/05/2016	Articular capsule of the knee		Myxosarcoma	Grade I	OH	TZ	X7K0	Cavalier King charles	6	Right back limb
Ds 2	H15-3263	12/05/2016	Superficial dermis		Fibrosarcoma	Grade III	OH	TZ	X7K0	Cane Corso	8	Perianal mass, invading the sub-cutaneous tissues
Ds 3	H15-2015	12/05/2016	Subcutaneous tissue		Hemangiopericytoma	Grade I	OH	TZ	X7K0	Golder Retriever	10	
Ds 4	H15-1570	12/05/2016	Subcutaneous tissue		MPNST	Grade II	OH	TZ	X7K0	Crossbreed	10	Left axillary region. "Malignant Peripheral Nerve Sheath Tumor"
Ds 5	H15-1480	12/05/2016	Subcutaneous tissue		Fibrosarcoma	Grade II	OH	TZ	X7K0	Beagle	10	Right back limb
Ds 6	H15-1457	12/05/2016	Mucosal chorion		Fibrosarcoma	Grade II	OH	OT	X7K0	Golder Retriever	7	Labial mass, infiltrating the underneath musculous tissue
Ds 7	H15-1289	12/05/2016	N/A		Fibrosarcoma	Grade II	OH	OT	X7K0	Golder Retriever	12	Shoulder mass. Recurrence. May be a MPNST
Ds 8	H15-1234	12/05/2016	Bone	Osteoblastic	Osteosarcoma	N/A	BH	LO	Q7A0	Bouledogue Français	9	Mandibular bone. Infiltrating the mucosal chorion
Ds 9	H15-1048	12/05/2016	Lung		Indifferenciated	Grade III	OH	RP	X7K0	Shetland	8	90% Necrosis so difficult to diagnose
Ds 10	H15-0037	12/05/2016	Mesenchymal tissue		Fibrosarcoma	Grade II	OH	OT	X7K0	Berger Allemand	12	Recurrence. Infiltrating the surrounding soft tissues and bone
Ds 11	H15-2397	12/05/2016	Subcutaneous tissue		Indifferenciated	Grade III	OH	TZ	X7K0	Setter	12	Left anterior limb. Massively infiltrating. >50% necrosis
Ds 12	H15-2364	12/05/2016	Subcutaneous tissue		Rhabdomyosarcoma	Grade II	OH	TZ	X7K0	Fox Terrier	15	No subtype determined by IHC
Ds 13	H15-1767	12/05/2016	Bone	Osteoblastic and chondroblastic	Osteosarcoma	N/A	OH	LO	Q7A0	Bouledogue Américain	N/A	One of the back limbs. Loci of cartilagoid matrix
Ds 14	H15-1475	12/05/2016	Omentum		Indifferenciated	Grade III	OH	XA	X7K0	Labrador	11	No subtype determined by IHC. <50% Necrosis
Ds 15	H15-1184	12/05/2016	Bone	Osteoblastic	Osteosarcoma	N/A	OH	LO	Q7A0	Dogue Allemands	4	Presence of osteoïd matrix
Ds 16	H15-1130	12/05/2016	Bone	Osteoblastic	Osteosarcoma	N/A	OH	LO	Q7A0	Berger Belge Groenendael	2	Costal bone. Same amount of cartilagoid and osteoid matrices. Necrosis and hemorrhage
Ds 17	H15-1950	12/05/2016	Cutaneous and subcutaneous tissues		Hemangiopericytoma	Grade I	OH	TZ	X7K0	Braque Allemand	9	Right buttock
Ds 18	H15-1701	12/05/2016	Bone	Osteoblastic	Osteosarcoma	N/A	BH	LO	Q7A0	Dogue Argentin	7	Moderate osteoid matrix production
Ds 19	H14-0697	28/11/2016	Spleen	Fibrohistiocytic	splenic sarcoma	Grade III	OH	SR	X7K0	Cocker	10	Huge metastasis
Ds 20	H14-1242	28/11/2016	Lung		Histiocytic sarcoma	N/A	OH	RP	X7K2	Bouvier Bernois	10	
Ds 21	H15-1687	28/11/2016	Mucosal chorion		Fibrosarcoma	Grade II	OH	GG	X7K0	Rottweiler	9	Vaginal mass, infiltrating, Necrosis and hemorrhage changes
Ds 22	H16-0812	28/11/2016	Cutaneous tissue		Indifferenciated	N/A	OH	OT	X7K4	Border Collie	5	This tumor could be a : Giant cell anaplastic sarcoma, well-differentiated histiocytic sarcoma, low-differentiated subcutaneous hemangiosarcoma
Ds 23	H16-1124	28/11/2016	Subcutaneous tissue		Fibrosarcoma	Grade I	OH	OT	X7K0	Springer Anglais	5	
Ds 24	H16-1397	28/11/2016	Digestive tract	Spindle-shaped	GIST	N/A	OH	OT	X7K0	Bobtail	7	"GastroIntestinal Stromal Tumor"
Ds 25	H16-1707	28/11/2016	Subcutaneous tissue		Indifferenciated	Grade III	OH	OT	X7K0	Teckel	8	>50% necrotic changes
Ds 26		09/12/2016			Normal							Surgery : 20161201
Ds 27		09/12/2016			Normal							Surgery : 20161128
Ds 28		09/12/2016			Normal							Surgery : 20161201
Ds 29		09/12/2016			Normal							Surgery : 20161129
Ds 30		09/12/2016			Normal							Surgery : 20161206
Ds 31		09/12/2016			Normal							Surgery : 20161129
Ds 32		09/12/2016			Normal							Surgery : 20161201
Ds 33		09/12/2016			Normal							Surgery : 20161202

B. Conclusion

The goal of this study was to evaluate the performances of a SpiderMass prototype to acquire specific molecular signatures in different sarcoma type tumours and then test it in the veterinary operating room. Overall, we were able to demonstrate that we get discriminant molecular profiles of the different histological regions of the tissues (cancer, necrosis, normal) but that we had also discriminant profiles for the different sarcoma grades and even the different sarcoma sub-types. Interestingly, the SpiderMass has this particularity that we obtained good molecular profiles (in terms of number of signals and signals intensity) both in the positive and negative ion mode. We have shown here that either positive or negative MS spectra could be used to discriminates region, grades or sub-types. Therefore, from the molecular spectra we could build classification models which were successfully validated. Indeed, the cancer VS normal, cancer/normal/necrotic, and the tumour subtyping models all showed better than 97% correct classification rates for negative mode and 99% for positive mode, excluding outliers. These results are to be put in perspective as the patient cohort was small and there were no validation cohort used here, explaining why we haven't talk about sensitivity nor specificity and didn't calculated them. Different lipid markers were identified from these experiments and in particular several TGs were found to be over-expressed in the sarcoma which is in line with the previous already published findings from other groups. The last step of the study was dedicated to test the system in a relevant operating situation. This has demonstrated that the system, even if to be further improved, could be used. In particular, we have demonstrated during these experiments that the technology is not dangerous and really minimally invasive for the patients. We were as well obtaining feedbacks to improve the laser probes. Indeed, during the surgery the laser was equipped with a 1.5-2 m length laser fibber which demonstrated to be too fragile and prone to breakage.

For oncology, the system needs now to be tested in the human clinics from larger patient cohorts. Yet, we have an ongoing study on ovarian cancer and hopefully a demonstrator will be setup soon at Lille Comprehensive Cancer Center (Centre Oscar Lambret). Standardization of the method and comparison of the prototype with existing techniques will be an important issue to resolve prior to its clinical use. In particular, comparison to the gold standard histology is the next important step.

This study has paved the way of the application I made during my PhD by demonstrating the innocuity of the technology for its use *in vivo* in patients greatly facilitating the adoption by the dermatologist at PFDC and their will to test the system.

Chapter V

Technical Developments and Validation Studies for Dermo-Cosmetic Applications

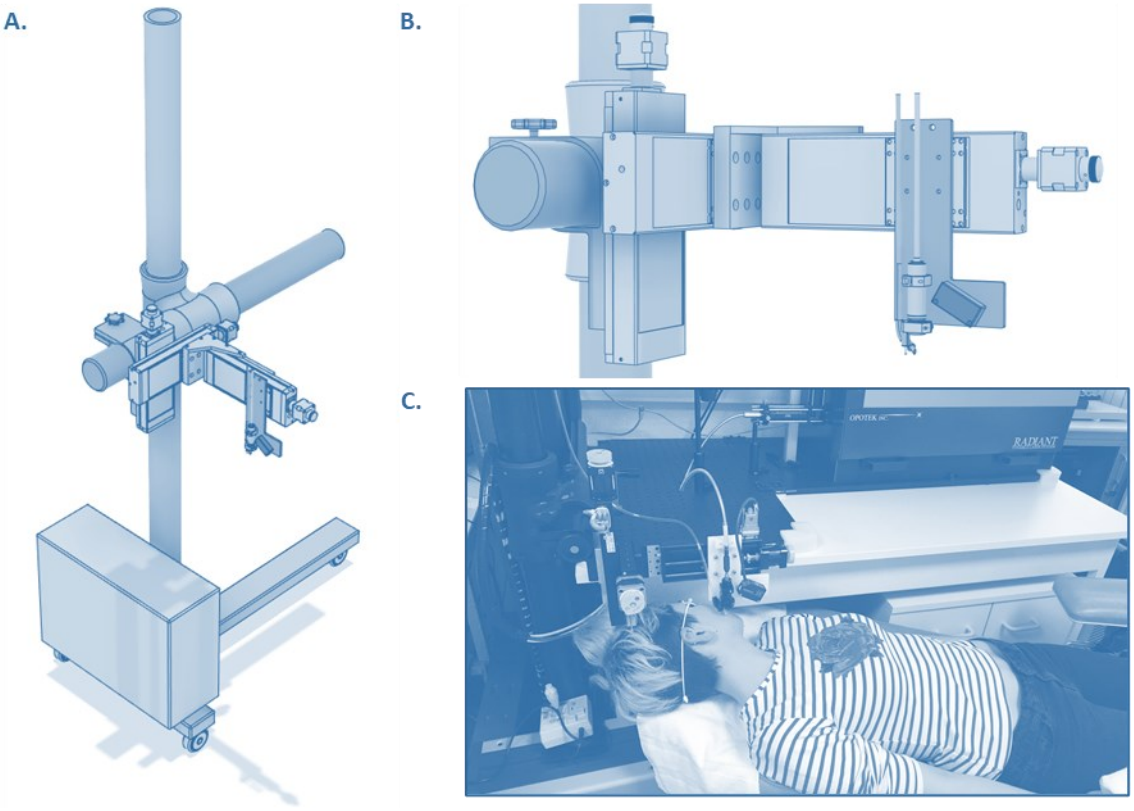

Motorised movement system on a trolley for automatic scanning of samples and volunteers. **A.** General 3D model of the system and **B.** zoom **C.** Photo of the device during a facial skin analysis with the volunteer lying on a sampling seat and wearing opaque protective glasses.

Philippe Saudemont, Célia Ipinazar, Jérôme Filiol, Éric Cros, Éléonore Gravier, Amaury Alves, Aurélie Villaret, Gwendal Josse & Isabelle Fournier

CHAPTER V: Technical developments and validation studies for dermo-cosmetic applications

A. Introduction

This chapter is dedicated to the development of the SpiderMass prototype developed at the Toulouse PFDC Skin Research Centre for dermatological application first discussing about the system itself, then addressing a proof-of-concept application to cosmetic product detection and finally, using the system to study skin aging.

The distinction of Toulouse's and Lille's prototypes comes from the sampling system coupled to the laser, and the MS. As previously described the system is based on a pump laser emitting at 1064nm which is then wavelength modulated to 2940nm using an **OPO**. The Laser+OPO assembly is produced by OPOTEK (Carlsbad, Ca. USA). To reproduce the Lille's system, we needed to come up with a sampling solution to analyse the volunteer's skin with the best reproducibility. We also needed to find a way to prepare and introduce the analytes inside the MS considering the specificity of the Q-TOF system available for the experiment.

The first half of this part will describe the instrumental developments conducting to the actual system and the "SpiderValid" study. It was aiming at validating the prototype, its robustness, and the analytical performances but as well the effect of the laser ablation on the patient skin, like erythema and eventual post-analysis inflammation. This was a mandatory step prior to launching the principal clinical trial presented in **CHAPTER IV**: Proof of Concept in the veterinary environment, and get it approved by the personal protection committee.

The second half of this part will present the results obtained during the "SpiderCompar" clinical study conducted on young and mature female subjects recruited during summer. The name comes from one question of this study aiming at comparing the Lille and Toulouse systems. Otherwise, the analyses were directed onto characteristically different areas of the body, the forehead and forearm, to have an oily and a dry skin area. On the forearm, two zones were analysed, one on the inner and the other on the outer side of the arm to compare UV-exposed and not exposed areas. The SpiderMass prototype has been used to study the molecular changes in the SC constituting lipids and the skin surface lipids by the mean of different sampling modalities for the study of UV-related or age-related skin aging.

B. Experimental procedure

1. Instrumental developments

a) *In vivo* OCT imaging

The Standard Imaging OCT System (Thorlabs, Ref OCP930SR) was used to image laser ablation depth on the Forearm skin. Little to no parameters needs to be adjusted to conduct the measurements. This OCT is working at 930nm central Wavelength and allows imaging at 8 frames/sec on a 6mm wide to 1.6 mm depth cross-sectional imaging. This OCT can be handled but, in our case, has been mounted on a scanning stand (Thorlabs, Ref: OCT-STAND). The integrated CCD camera Window allows to precisely position the sample under the probe before any measurement. Once correctly positioned, the B-scan windows can be saved as snapshots.

b) Cholesteryl palmitate standards analysis

20 mg of cholesteryl palmitate (Sigma Aldrich, Ref C6072) is weighted and dissolved in 10mL of pure $CHCl_3$ to obtain a mother solution at 2mg/mL. This solution is then diluted in EtAc to obtain solution with varying concentration at 200, 100, 75, 50, 25, 10 and 5 µg/mL. Then, 10µL of each solution is pipetted onto an absorbent paper spreading around a surface of 1cm diameter and allowed to dry. The SpiderMass analysis is done according to the specific paragraph described later.

c) Lanosterol QC samples preparation

For Quality Control (**QC**) preparation, Lanosterol (Sigma Aldrich, Ref L5768) is used and 0.62mg is dissolved in 4.2mL of pure $CHCl_3$ to obtain a mother solution at 0.15 mg/mL. 10mm Acuderm biopsy Punches (Fisher Scientific, Ref NC9236770) are used to punch 10mm discs from absorbent papers. Those punches are also dipped in the mother solution and allowed to dry before being placed in a small glass vial and under a gentle flow of nitrogen for inerting. Before every volunteer in any clinical setup, a QC is measured with the SpiderMass system.

d) Validation experiment of the statistical approach

The objective of this experiment is to evaluate and validate the statistical approaches with a validation dataset. Therefore, sebum was sampled on the same subject 15 times and then measured with the system. Then 10µL of a homemade dopant solution was deposited on the paper, allowed to dry and analysed again. Stock solutions were prepared out of the standard powders by dissolving 2mg/mL in Chlorofom/Methanol (1:1, v/v). The standard solution was constituted of 10 standards (**Table 2**) at different concentrations allowing observation of their signals in a similar intensity range. Standards that could not be detected were not included in the final mix (products with 'X' as volume).

Table 2: Description of the compounds constituting the dopant solution. The products volumes that are X were not prepared.

	Product name	CAS Number	MW (g/mol)	Volume (µL)
a	1,3 distearine	504-40-5	625.02	50
b	tribehenin	18641-57-1	1059.8	400
c	1,3 diarachidin	59925-28-9	681.12	100
d	1,3 dibehenin	32-2203-8	737.23	200
e	Ditetracosanoin	960594-30-3	789.3	X
f	1,3 dicaprin	17598-93-5	400.59	10
g	1,3 Dilauroylglycerol	539-93-5	456.7	10
h	Cholesteryl palmitate	601-34-3	625.06	30
i	Protoporphyrin IX dimethylester	5522-66-7	590.71	200
j	Coproporphyrin III Tetramethyl ester	5522-63-4	710.82	X

Then the spectra are processed by the homemade “SMA software” and submitted to our classical workflow of analysis (See **§I.B.4 Data analysis**) to find out which peaks were detected, and which ones were not.

2. SpiderValid clinical validation study

a) Study design

The first clinical study carried out with the system was on 23 volunteers with healthy skin on the forearms and mixed skin on the face. The volunteer’s forearms were treated with different PFDC products namely Avène Cold Cream, Ducray Melascreen Photo-Aging Night Cream and cosmetic grade glycerol. These were applied in a randomised latin square pattern to the forearms at a usual quantity of 43g/cm². After application, the zone was massaged until full penetration of the products and then wiped. Each of the application sites was divided into 6 areas of 1cm², 3 were used to perform a triplicate measurement, and the 3 others were used for tape sampling. The areas summary schematic is presented in the **Figure 15**.

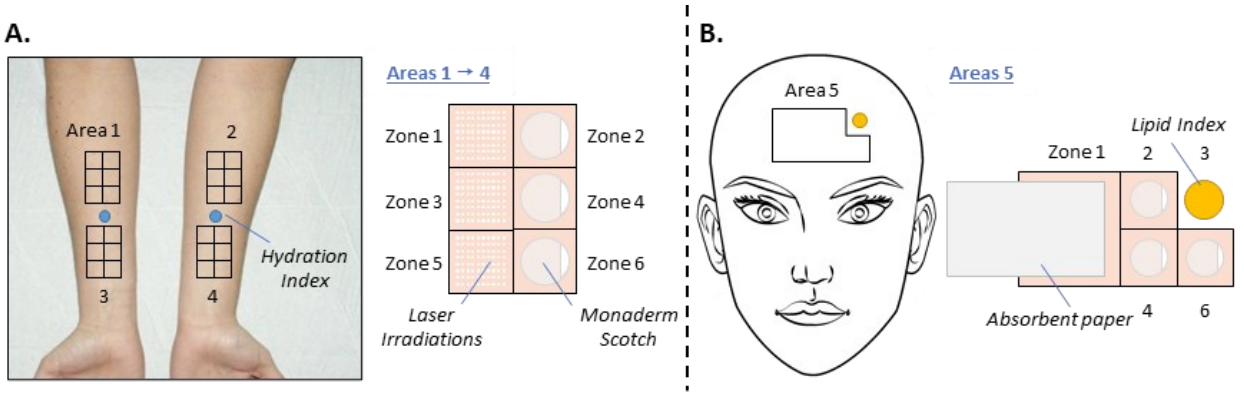

Figure 15: Schematic of the samplings and measurements sites on the SpiderValid Study. **A.** On the inner faces of the forearm the Hydration Index (Blue circles) were taken in the middle of the 4 studied areas. Each area comprises 6 zones, 3 used for SpiderMass measurements, 3 for D-Squam tape sampling. **B.** On the forehead, the D-Squam tape were sampled before taking the Lipid Index (Yellow circle) and sampling the surface sebum with the absorbent paper.

No products were applied on the forehead, absorbent paper were used to collect the sebum from the oily skin and squams were collected by D-squams tapes. On the absorbent paper, FTIR transmission measurement has been done before being analysed by the SpiderMass to evaluate the Pearson correlation between the FFA/TG ratio and some specific masses detected by the system. No acquisitions were conducted on the D-squams tape yet.

b) Absorbent paper FTIR measurement

The Fourier Transform InfraRed ("**FTIR**") transmission measurement we collected using a Frontier Spectrum 400 FT-IR (Perkin Elmer) equipped with a DTGS detector in transmittance mode through an absorbent paper. 8 spectra are acquired and averaged with a spectral resolution of 2 cm^{-1} on a wavelength range from 1200 to 3100 cm^{-1}.

The absorbent paper is a commercially available cigarette paper commonly used for sebum sampling in the PFRC (JOB 38bis, JOB. Perpignan France). This reference doesn't contain any gum or additives and has the advantage to bare low signal both in FTIR and SpiderMass analysis. On any paper that is used for sampling, the background is first measured. Then wearing gloves, half of the paper is slipped inside a plastic sleeve to protect it from contamination and the other half is applied on the skin. The finger is used to impregnate the paper with the sebum.

Then the FTIR acquisition is conducted, and the software automatically subtract the blank to obtain the sebum signal. Using a homemade "IR Analyse" software (v2017.10.0.11), the baseline is first corrected without normalisation[m]. The Free Fatty Acid to Triglycerides Ratio ("FFA/TG ratio") is obtained for each sample by computing the area under curve of free fatty acids (1710 cm−1) and triglycerides (1740 cm−1) peaks.

[m] An almost ubiquitous normalising signal is used usually on the FTIR which cannot be applied on the wavenumber range defined for lipid analysis.

c) D-squam sampling

The D-squam 14mm stripping discs (DS101, Monaderm. Monaco) used to sample the outermost layer of squams. With tweezers, the strip is removed from its storage plastic sheet, placed and maintained on the skin for 30 seconds. Then is taped upside down on a glass slide and box stored in -20°C until use.

d) SpiderMass setups and acquisitions

The prototype is equipped with a Radiant laser from OPOTEK (Carlsbad, Ca. USA) which operates at a 2.94 µm wavelength, 10Hz frequency, and a 6ns pulse duration. The laser fibres were purchased from Le Verre Fluoré (Bruz, France). They are made of ZBLAN, have a core diameter of 400 µm, cladding diameter of 460 µm and are 4m long to allow the analysis of the patient skin with more ease. They are half patches meaning they are connectorized with a SMA connector on the handpiece side and are naked on the injection side. They have a Kevlar protecting sleeve and a metallic coat making it less prone to breakage and helping the fibre to support its own weight. In these conditions, we can obtain an energy of 0.8mJ/pulse at the exit of the 400µ fibre.

To better control the laser deposition and reproducibility of the experiments, the previously described hand probe is coupled to a homebuilt XYZ motorised stage equipped with a distance sensor to ensure a correct positioning of the laser according to the patient skin or sample topology. This system is controlled by a specifically developed software program named Motion Control Loop (**MOLO**) for that uses Labview to control the laser as well as the linear motors and the distance sensor. It allows to define measurement schemes and to follow a controlled procedure for the SpiderMass acquisitions, screen prints of the MOLO software can be seen in **Appendix 2**.

The classical measurement procedure begins by letting the volunteer sit or lie down on the seat or put the sample onto a small wheeled table. Then the trolley on top of the area and proceeding to macro adjustment. The computer wireless keyboard is then used to place more precisely the probe and approach the zone. A visual display on the software allows to know the position of the probe regarding the motor's limits, and the distance from the surface. Then by a click of a button, the probe is automatically going at the right distance for analysis. At the next step, the probe scans the defined zone boundaries without firing the laser to precisely adjust the position of the subject/sample. When correctly adjusted, the mass spectrometer acquisition can be started: after a 30 s waiting time to let the system stabilise, the probe goes into place and the laser is triggered while moving. Once done, the laser head goes up and is homed. The waiting time at the beginning is used to create an averaged background signal spectrum during data analysis.

The sampling arm is set at a 2mm/sec speed, a step size of 0.5mm and a distance retro control at 40 mm from the analysed surface. For *in vivo* skin measurement, a circular surface of 10 mm diameter, representing about 80 shots is scanned in 20 s. For sebum analysis, the absorbent paper is placed in a homemade paper holder and analysed. The analysis movement is made of two zones: a 25mm² square on a

blank area and the same surface than the *in vivo* conditions described above for the sebum impregnated area. For D-squam analyses, the tape is placed upside down on the table and the movement scheme represents the tape shape (see **Figure 21A**) minus a 1mm margin around the borders. For QC analysis, the method is set to irradiate a disk shape of 8 mm diameter on the 10 mm diameter QC size.

Before the MS interface, the aspiration tubing is 4m long and connected to a modified APCI source under patenting. The mass spectrometer is a MicroTOF-QII, Bruker (Billerica, Massachusetts, USA). The source parameters are presented in the **Table 3**.

Table 3: Instrumental parameters that can be optimised and their current values in the APCI based MS interface developed for the new SpiderMass system.

Modified APCI source	
Solvent	
Composition	Water
Flow	150 µL/min
Dopant (acid / bases / salts / detergents)	No
Nebulising gas pressure	49 psi
Vaporisation temperature	400 °C
Corona needle tension	7 000 (+) / 9 000 (-) nA
Mass spectrometer	
Transmission element tensions	
Shield offset	+/-500 V
Transfer capillary	+/- 4500 V
Drying gas	
Flow	3 L/min
Temperature	200 °C

For the MS acquisition the mass spectrometer operates in 3 distinct methods: A low tuned positive method, a low tuned negative and a high tuned negative mode. The difference between those methods are the favourable transmission of low or high mass molecules. Data generated by the negative tune high methods won't be presented it this thesis. The m/z range is set between 100 and 1400 a scan time of 1Hz corresponding to the sum of 5k micro-scans

3. SpiderCompar clinical study on skin aging

a) Study design

The subjects were included in TLS city PFRC from the 23/07/2020 to 06/08/2020. The measurements were carried out under controlled experimental conditions: temperature of 20 ± 5°C, after the subject rested for 15/30 minutes in an air-conditioned room with uncovered measured areas.

Three areas are studied per subjects: the forehead for sebum analysis, the inner side of the right forearm for a UV underexposed area and the outer side of the right forearm for a UV exposed area. The samplings and measurements performed were distributed as described in **Figure 16**. On the forehead, the *in vivo* SpiderMass analysis is done in triplicates as well as an *in vivo* measurement of the global lipid content by infrared

spectroscopy (FTIR fibered probe). Then the lipid index (**LI**) is measured and the sebum is sampled at 2 different places using an absorbent paper. After FTIR transmission measurement, the paper is stored in -20°C before the SpiderMass analysis.

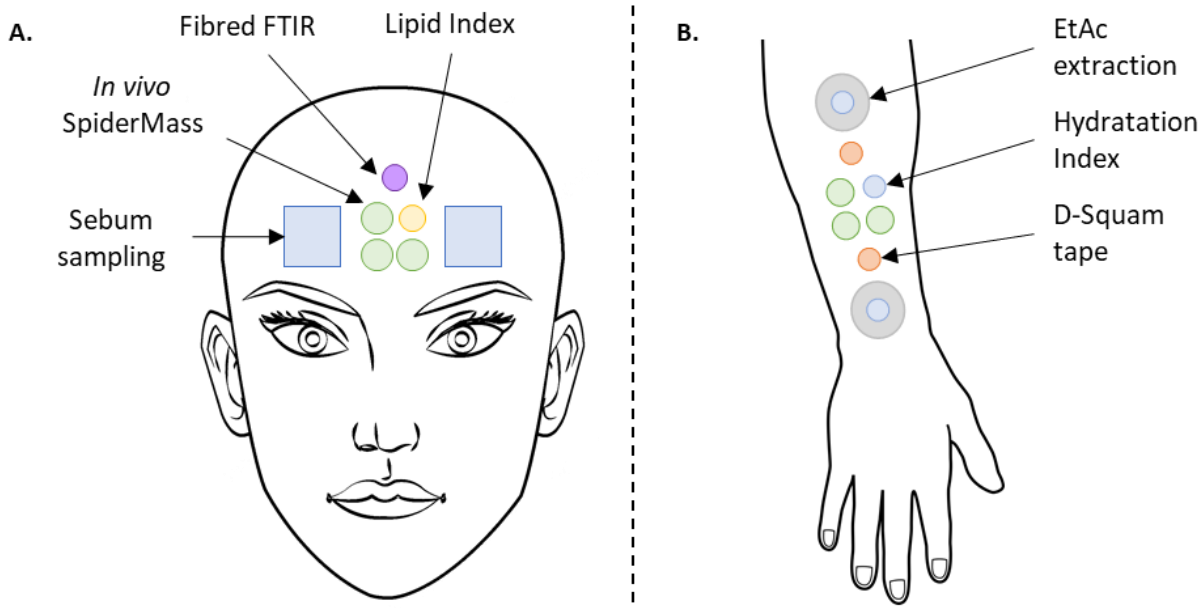

Figure 16: Drawing depicting the samplings and measurements sites for the SpiderCompar study. **A.** On the forehead, the surface sebum is sampled on two sites using an absorbent paper (blue squares), the Lipid Index (Yellow circle) is measured in the middle of the SpiderMass replicates (Green circles) and is closed to the *in vivo* FTIR measurement (Purple circle). **B.** On the inner and outer faces of the forearm the Hydration Index (Blue circles) were taken at three different locations to obtain an average value before the two Ethyl acetate extractions (Gray circles), D-Squam tape sampling (Light red circles) and SpiderMass analysis.

On the forearm, the samplings and measurements are the same for the photo-exposed area (external face of the right forearm) and under-photo-exposed area (inner side of the right forearm). The *in vivo* SpiderMass analysis is done in triplicates, then the Hydration Index is measured (**HI**), the D-Squam tape are used to sample the squams at the surface of the stratum corneum. Finally, surface lipids are extracted at 2 locations using ethyl acetate (**EtAc**) following the procedure described below.

b) Sample collection and measurements description

i. Ethyl-Acetate lipid extraction

The use of ethyl acetate for cosmetic purpose makes it a good biocompatible solvent for surface lipid extraction. Custom glass discs were specifically produced to have an inner surface of 10cm² (TechLab, Metz. France). They are pressed against the volunteer skin and 1mL of EtAc is added. A glass rod is used to stir the skin surface for 10 sec and the obtained liquid is aspired and placed in a closed glass vial. The extracts of the 2 zones are pooled and dried under a gentle flow of nitrogen, resuspended in 3mL of EtAc, partitioned in 3 different vials and dried again. One vial has been used for lipidomic LC-MS analysis, and the other two were

used for SpiderMass analysis: The dried extract are suspended in 100µL of EtAc, vortexed at 20Hz for 5min and 10µL is deposited on an absorbent paper before analysis.

ii. In vivo FTIR measurements

Two different FTIR measurements were conducted. On one hand, the *in vivo* ATR measurements were recorded using Harrick Scientific's MultiLoop-MIR probes (Harrick Scientific Products Inc. Pleasantville, NY, USA) with FiberMate™ fiber optic coupler installed on an FTIR spectrometer (Thermo Scientific™ Nicolet™ iS™5, Thermo Electron Scientific Instruments LL Madison, WI USA) with a DTGS detector (deuterated triglycine sulfate) and a beamsplitter: KBr/Ge mid-infrared optimized. The probe tips were pressed gently onto the subject's skin for data collection. Spectra were collected at 8 cm^{-1} resolution with 32 scans signal averaged. The Multiloop-MIR™ includes a chalcogenide fibre for operation from 6500 to 1700 cm^{-1}. On the other hand, the sebum paper transmission assessment has been conducted as described in **I.B.2.b): Absorbent paper FTIR measurement.**

iii. HI and LI measurements

The LI is measured by grease spot photometry using a Sebumeter® SM815 and a MPA6 multiprobe adapter (Courage + Khazaka electronic GmbH. Köln, Germany) giving a 0 to 350 units value approximated to µg/cm^2. The transmittivity of an opaque film is measured before sampling, and then applied onto the skin for 30 seconds before being measured again.

The HI is measured in triplicates using skin conductivity with a Corneometer® SM825 (Courage + Khazaka electronic GmbH. Köln, Germany) connected to a MPA6 multiprobe adapter. It allows to quantify the moisture content of the skin surface from 0 (no water at all) to 120 (liquid water). It is accepted that the skin is defined as very dry with HI value under 35, dry between 35 and 50 and normal above 50 a.u. In this study, the probe is applied onto 3 different sites of the forearm skin to obtain its average HI value.

c) Volunteer population profile

The Toulouse PFDC Skin Research Centre is dedicated to the clinical evaluation of Pierre Fabre product being developed. This study was carried out in compliance with the Declaration of Helsinki (1964) and its successive revisions, the Good Clinical Practices (EMA/CHMP/ICH/135/1995) and the current French regulations. The measures taken to protect their personal data and confidentiality are in accordance with the European Regulation 2016/679/EU of 27/04/2016 on the protection of individuals regarding the processing of personal data and the free movement of such data (GPDR). The subjects were included following inclusion and exclusion criteria that are described in the **Appendices I.C.1: SpiderCompar Eligibility Criteria**. They were separated in 2 groups of distinct age: the first between 18 and 25 years ("Groupe 1" or "Young"), and the

second between 55-65 years ("Groupe 2" or "Old"). The subject of the second group were asked for their menopausal status. The population details are summarised in the **Table 4**.

Table 4: Study population description with detail on the sexes, ages and phototypes distribution.

	Groupe 1 – "Young""	Groupe 2- "Old"
Sexes:		
Male	0	0
Female	20	20
Age:		
Average	23.1	58.7
Mean	23.5	57.8
Standard Deviation	1.3	2.7
Minimum	20.6	55.1
Maximum	24.5	63.6
Phototype:		
II	4	7
III	15	12
IV	1	1

4. Data analysis

Except for the SpiderValid study that was used to build up our workflow, the SpiderMass data were processed by a homebuilt web application named SMA for SpiderMass Analysis Software (v4.4) based on R (version 3.6.0) using the Shiny framework (v1.3.2). This application allows the conversion of Bruker (for the Toulouse's system) and Waters (for the Lille's system) related files to .mzXML by using the ProteoWizard (v3.0.19157) MSconvert tool[192] and screenshots can be seen in the **Appendix 5**. After conversion, the spectra were binned to reduce their size by summing all the intensities in the same window, usually 0.1 Da and giving a mass value corresponding to the middle of the bin. Then a dynamic display was used to detect the irradiation periods and retrieve the related MS spectra. This was achieved using in a semi-automatic function which looks at rising and decreasing of the Total Ion Count (**TIC**and then by adjusting the limits by hand when needed. At that stage we define the time window where the background signal is selected. Then for each detected period the spectra were averaged, and the background subtracted. After a TIC normalisation, *m/z* values and samples can be sorted out according specific criteria like Signal to Background Ratio (**SBR**) and the signals can be filtered out by using different kind of thresholds. Finally, the intensity values are transformed using a y=Log2(x+1) function.

Out of this pre-processing, an Excel file called the "clinical file" is generated that lists all the acquisitions, some metadata (i.e. the file generation date) and calculated parameter such as the SBR, the mean TIC etc. This file needs to be completed with other important parameter to be assessed like including the batch

number, laser energy, and class for example. All the gathered information were used for the data quality panel that allows to visualise its structure and potential experimental biases, outliers, groups of samples, etc… These first results were obtained via boxplots, correlation analysis, Principal Component Analysis (**PCA**), hierarchical clustering (dendrogram or heatmaps plots).

A number of .Rdata matrices were generated for differential analysis by using linear models. If necessary, these models can take into account factors considered relevant for the analysis such as the date of processing, the TIC value as adjustment factors. The obtained p-values are adjusted by Benjamini-Hochberg to account for multiple comparisons. The results are displayed as volcano plots, Venn diagrams and tables containing the fold change and adjusted p-values per masses. A new type of plot was generated that displays the averaged spectra on which is superimposed the significant peak state on every bin.

C. Results

1. Instrumental development et characterisation

a) Sampling automation

In contrast to the analysis of flat, immobile sample sections, volunteer analysis in clinical studies requires automation of sampling to better control the deposited dose of light and reproducibility. An automatic displacement system was set up first derived from a commercial Arduino based drawing machine adapted for our uses and shown in **Figure 17.**

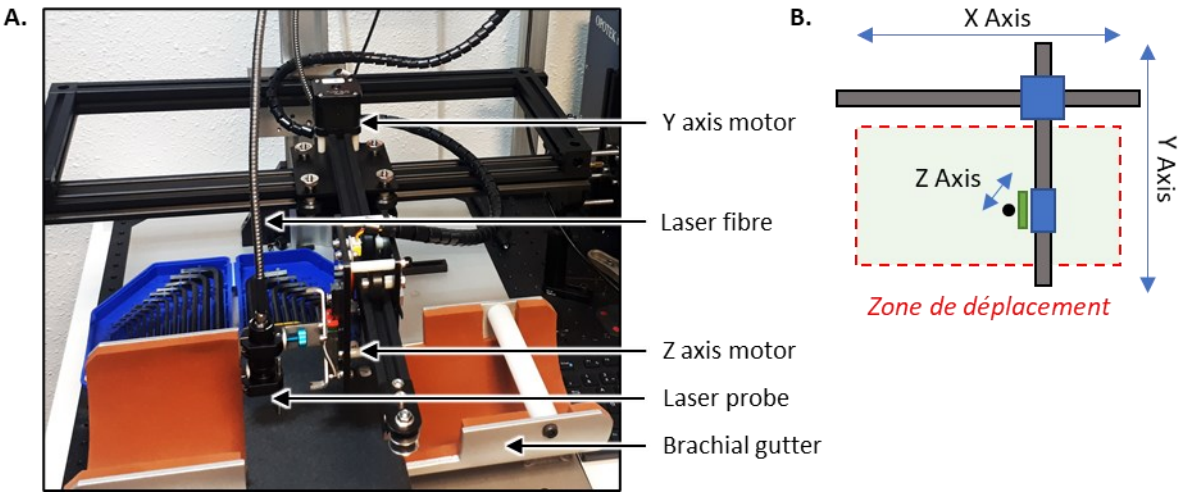

Figure 17: Motorised movement system for automatic sample scanning. **A.** Photo of the device showing the brachial gutter in which the volunteer places his forearm for analysis. Above, the laser probe at the end of the fibre is attached to the Z-axis motor. The X- and Y-axis rails allow the carriages to move. **B.** Simplified diagram of the system showing the area of possible laser movement. Black circle: laser probe; Green rectangle: Z motor; Blue rectangles: X and Y axis travel carriages

This motorised displacement system is positioned above a gutter into which the volunteer places his or her forearm for analysis. Above, the end of the laser fibre is attached to the Z-axis motor. The X- and Y-axis

rails allow the carriages to move. Simple rectangular shapes can be prepared through a small homemade script that generates a position matrix from the width and height of the displacement area, the steps, and the speed as input parameters. For more complex shapes, an export is possible from the drawing machine software. Processing steps are required before the export can be used by the machine. The commands are sent to the machine's Arduino board from the computer using the Grbl communication protocol.

This first system that was setup didn't allow to sample other parts of the body than the forearm because it was not self-adjusting on uneven surfaces. Thus, we have chosen to mount 3 linear motors for the X, Y and Z axes on a trolley bracket presented in **Figure 18**. The trolley also carries the communication modules and power supply and allows a quick macroscopic adjustment of the sampling probe around the volunteer. Adjacent to laser microprobe is now a distance sensor diode which allows the distance between the laser probe and the volunteer to be measured and the position of the laser to be adjusted accordingly.

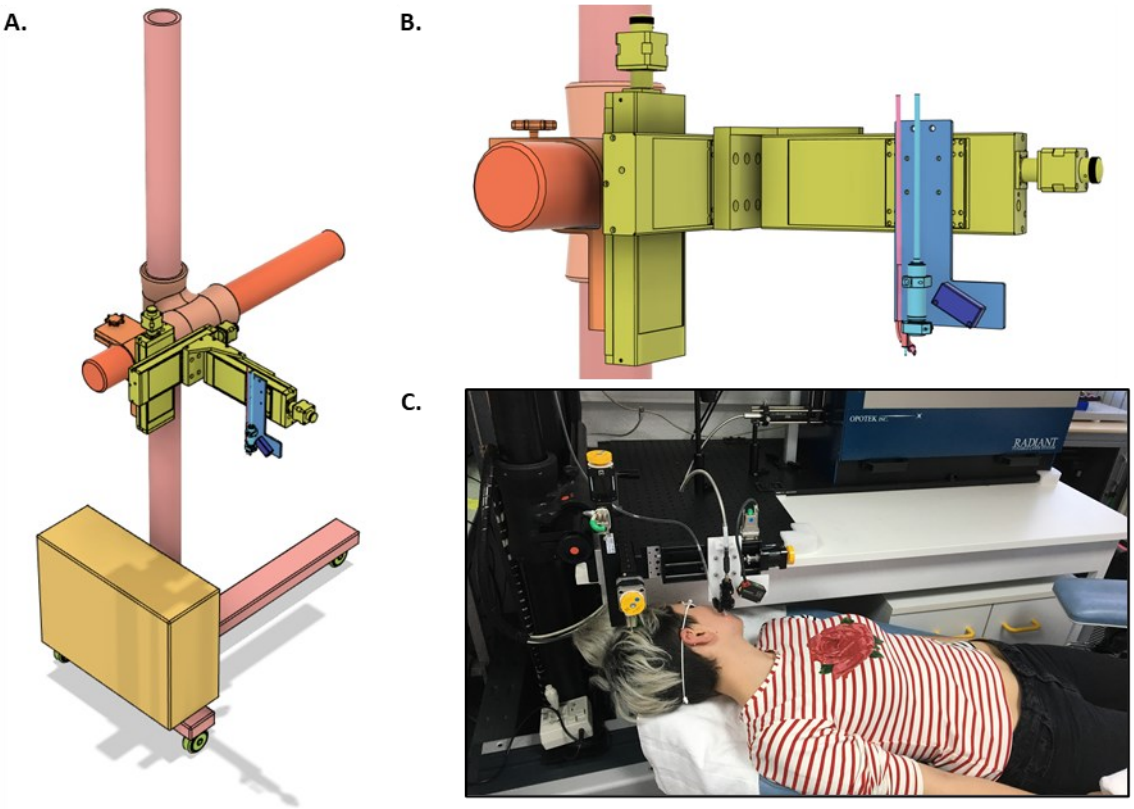

Figure 18: Motorised movement system on a trolley for automatic scanning of samples and volunteers. **A.** General 3D model of the system and **B.** zoom with the parts coloured from pink to orange corresponding to the wheeled system. Yellow box: power and communication enclosure. Green parts: X, Y and Z axis motors. Blue parts: micro-sampling probe attachment plate with laser fibre, distance sensor (dark blue). Pink pipe = molecule suction tube. **C.** Photo of the device during a facial skin analysis with the volunteer lying on a sampling seat and wearing opaque protective glasses.

b) Laser ablation depth assessment

Laser depth evaluation on the skin has been conducted a while ago for the Lille's system but not on skin or *in vivo*. It was essential to conduct this experiment before being able to expose volunteers to the

system. In dermo-cosmetic studies, a technic that is considered to be non-invasiveness describes techniques that don't go beyond the most superficial layer of the skin which is the SC which is described to be 15 to 20 µm thick. Thus, this is the depth limit that should never be exceeded during the analyses. We were therefore initially interested in evaluating the ablation depth as a function of the irradiation conditions. In preliminary experiments, commercial skin explants were used to measure the ablation depth by stereometry and fringe projection (DermaTOP-HE, EOTECH Marcoussis France). These measurements proved to be unreliable due to freezing artefacts on the skin patches but also because and informatically because of important corrections in the 3D surfaces applied by the commercial software during analysis which is made to compare the surfaces evolutions between timepoints but not single accurate measurements. A second series of experiments were performed directly *in vivo* on the forearm coupled by *in vivo* OCT measurements. **Figure 19** shows the *in vivo* forearm shot design and reaction of the skin after laser irradiation.

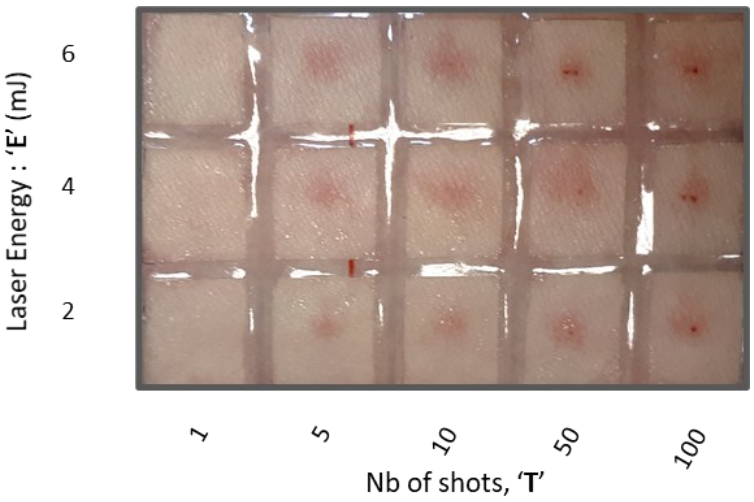

Figure 19: Photograph showing ablation spots on the skin forearm showing its reaction as a function of the number of shots and laser energy. "E4T50" correspond to the 4mJ/pulse condition and 50 laser shots.

The picture of the forearm shows the skin reaction for laser energies of 2, 4 and 6 mJ / pulse with a number of shots ranging from 1 to 100. It can be observed important reactions, with the appearance of an inflamed redness (even a little blood) for the highest energy and number of shots conditions (E6T50, E2T100, E4T100 and E6T100). These conditions are extreme for the purpose of this experiment and do not represent the energy used in conventional conditions which correspond to condition E4T1 and E4T5 in Lille (it is to be noted that for this experiment, the laser fibre has been removed to increase the energy). To compare each of the conditions it is necessary to speak in terms of fluence (J/cm²) rather than energy. The ablation spot was measured in the E4T1 condition by the white dehydration trace left on the skin immediately after the shot. This trace describes an ellipse of 1.4*0.6 mm, which represents an area of 0.006 cm². Thus, with an energy of 2, 4, and 6mJ/pulse, we have an equivalent fluence per shot of 0.3, 0.6 and 0.9 J/cm² respectively. OCT observations without and with laser ablation are shown in **Figure 20**.

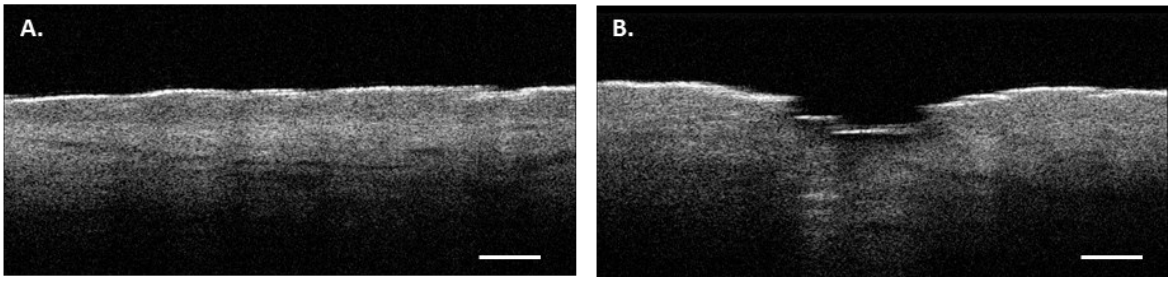

Figure 20: In vivo OCT imaging of the skin before and after ablation A. OCT profile of skin without ablation. The transition between the epidermis (dark grey) and the dermis (light grey) can be observed. B. OCT profile of skin after laser irradiation, condition E6T100, the depth of the ablated material is 350 µm. The white scale bars correspond to 500µm

The image in panel B shows the most extreme condition at E6T100. The depth is measured from the bottom of the crater to a line connecting the two crater rims and equals 350µm. Ablation starts to be visible from condition E6T1 with 10 µm and a fluence of 0.9 J/cm². Thus, at 0.6 J/cm², which is the classic condition of use, we approximated the ablation to be between 4 and 6 µm depth in total and therefore that we should not shoot more than twice per location to ensure that we do not exceed the SC and remain non-invasive.

c) Characterisation of the ablated material using tapes

When further analyses are required on dried skin areas or when SpiderMass measurement is not possible, indirect analysis is then carried out after sampling of the skin with a scotch tape traditionally used for the evaluation of skin desquamation. This sampling method allows the recovery of the most superficial layer of the SC by adhesion of only the last layer of corneocytes as well as any sebum and bacterial flora present at that site. **Figure 21** shows the appearance of a scotch tape and how the skin is ablated from its surface to a glass slide for further analysis.

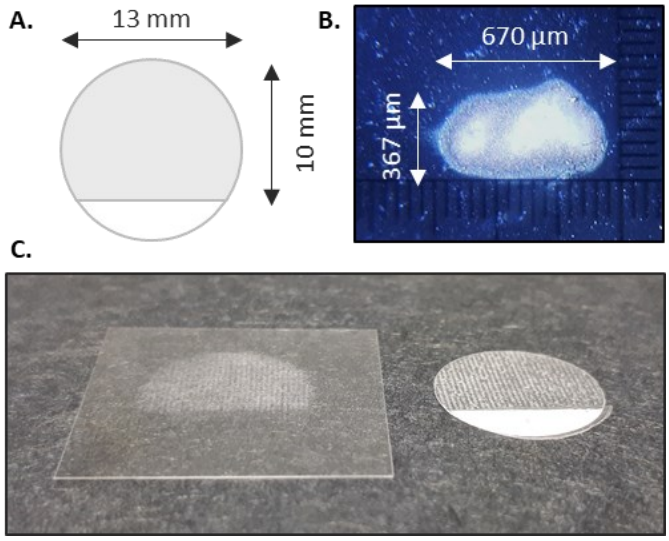

Figure 21: Monaderm peeling tape A. schematic of the tape and dimensions of sampled area. B. Size and appearance of the laser ablation spot in this experiment. C. Photo of a tape after removal and ablation of the material on a glass slide. It is to be noted that this experiment has been conducted before the OPO module modification and it is still possible to observe the 3 beams on the B. panel

On the 10*13mm useful area shown on the **Figure 21A,** the use of the first XY scanning system allowed the creation of a precise raster of points. The spacing of the rows and columns was chosen so that the 367*670 µm ablation spots depicted in **Figure 21B** could be adjacent without oversampling. A glass slide was positioned above the tape, in the path of the laser beam and spaced 1mm from the tape surface. Thus, as the material is projected mainly at the normal of the irradiated surface, the maximum

amount of material can be collected on the slide and is shown on **Figure 21C**. The **Figure 22** shows imaging of the material removed from the tape and projected onto the slide.

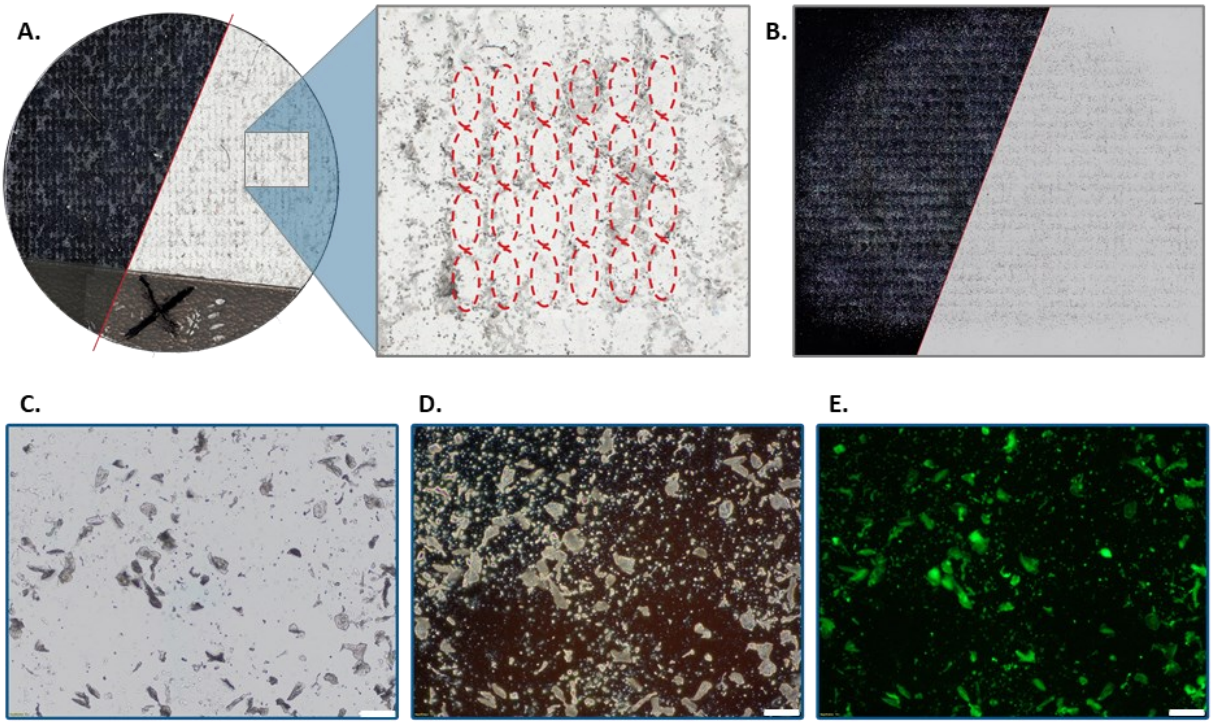

Figure 22: Light microscope images showing the ablation of material from a scotch tape and its projection onto a glass slide. A. 2.5X magnification photo in Dark field (DF, left half) and bright field (BF, right half) of a scotch tape after ablation with a zoom (10X) to visualise the ablation points. B. 2.5X magnification photo in Dark field (DF, left half) and bright field (BF, right half) of the glass slide after ablation. C.D.E. 40X image of the projected material on the glass slide in BF/DF and fluorescence (white bar = 50µm).

This figure shows that the spots are confluent, allowing approximately 50% of the total material to be ablated from the surface. Indeed, with a calculated fluence of 1.67J/cm² (done without any laser fibre), elliptic ablation zones can be seen in panel **A** as optically empty areas in the dotted red circles. In panel **Figure 22B**, we can see the projection of the material onto the coverslip has been correctly achieved. On the images **C.** to **E.** at 40X magnification shows corneocytes projected whole onto the coverslip, but also particles of disaggregated tissue, and projections of the scotch tape glue (projection resembling droplets in fluorescent light). This experiment was carried out 10 times consecutively; all the scotch tapes were weighed before and after skin sampling on a precision balance, which made it possible to evaluate the quantity of material recovered about 60µg. The lipids were extracted from the glass slides by a Chloroform/Methanol Folch extraction and their quantity measured by FTIR. The **Figure 23** shows the transmission spectrum centred on a spectral window from 2200 to 3600cm^{-1}. The bands of interest are those present at 2850 and 2924 cm^{-1} and correspond respectively to the symmetrical and asymmetrical vibrational band of the CH2 bonds. By measuring the air under these two peaks it is possible to quantify the total lipids present in the mixture.

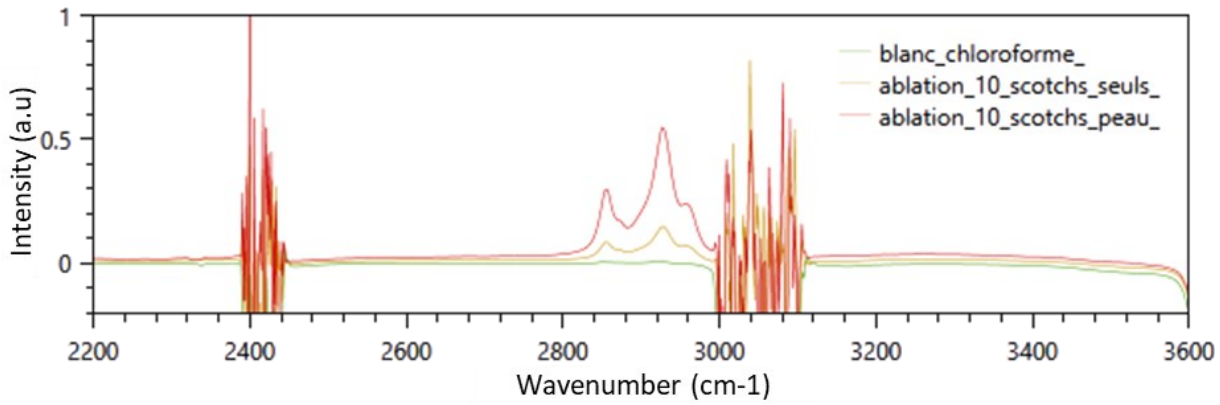

Figure 23: IR transmission spectrum of total lipid extracts. The peak at 2850 cm-1 represents the symmetric vibration of the CH_2 bonds of the lipids while the peak at 2924 cm-1 represents the asymmetric vibration of the CH_2 bonds.

The measurement on the blank shows that the signal without compounds is negligible in this spectral region (green curve), the adhesive tape generates a signal (orange curve). The signals from the skin is much stronger (red curve). After subtracting the glue signal and using a Cholesteryl palmitate calibration curve, the quantity of ablated glue was estimated to be 10µg per scotch. The ablated material represents 50% of the whole scotch surface and the amount of total lipid extracted at 30µg. This sampling method is therefore evaluated as effective for the study using skin samples when *in vivo* measurements are not possible.

d) Interface development for material injection into the MS

Once the laser system was set, the optimisation of the analysis system itself was carried out. Many versions of the interface were necessary before a functional solution could be found that would allow sufficient signal to be observed. Indeed, the interface between the transfer tube that brings the ions to the instrument and the interior of the spectrometer is a crucial part of the system to get a good signal.

This interface must meet the following 3 requirements:

- It should allow sufficient molecules and particles (clusters) to be drawn from the ablation site
- It should allow the particle clusters to be disaggregated and the ions to be released, or even to create charges and transmit them to the ablated neutral molecules that pass through it
- It must allow an efficient transmission limiting the losses to the mass spectrometer

In a preliminary attempt, a simple joint was set up between the transfer capillary of the device and the suction pipe. This configuration is not usable, because under these conditions the internal vacuum of the mass spectrometer is not high enough and the flow rate of the pumps doesn't create enough suction.

Subsequently, I modelled a part inspired by a heat engine injector, keeping in mind the classical precision machining methods used for the manufacturing of mass spectrometer parts. As the precise machining of this version was complex, it has been chosen to remodel the piece to make it 3D printable. The final result printed in titanium is shown in **Figure 24**. However, the tests carried out showed that this interface,

which allows the addition of an auxiliary suction, only fulfils the first and third conditions cited above. Indeed, although it is possible to heat this part using a nitrogen flow at 350°C passing through the part (see "heating conduct", **Figure 24B**), to promote the vaporisation and disaggregation of the clusters of molecules and results were obtained for standards, no signal was obtained from the skin.

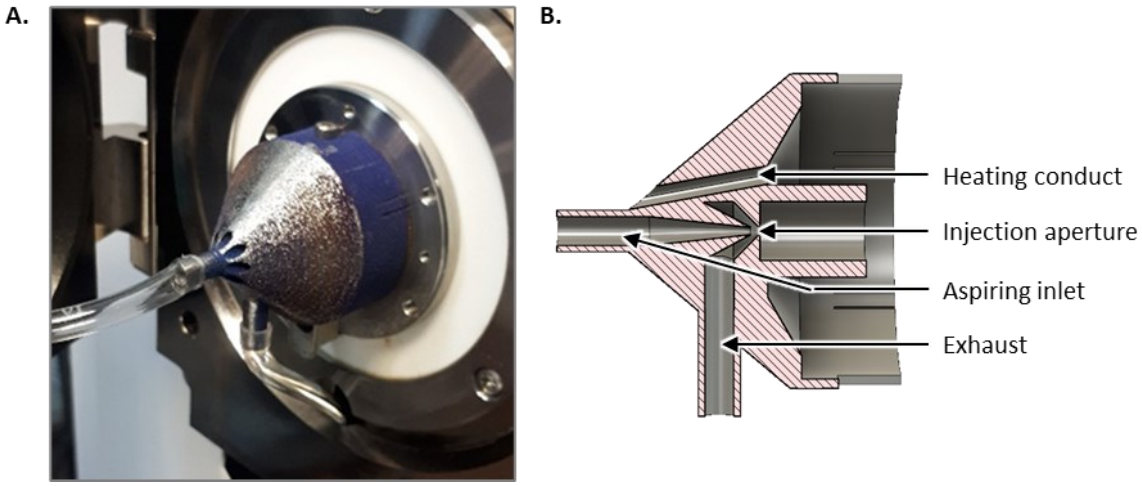

Figure 24: Titanium 3D printed injection interface. A. Photo of the part on the mass spectrometer. The pipe on the left is from the ablation site, the one below is for auxiliary aspiration. B. Cross-section schematic of this part revealing the injection chamber, and the heating gas circulation lines.

It was then decided to modify a commercial APCI source available with the instrument to suit the needs of the system (**Figure 25**). Briefly, the molecules to be analysed are nebulised in a sealed chamber and this spray is fully vaporised at 400°C. The molecules mixed with the solvent are then passed in front of a high voltage needle at the end of which an electrical discharge is generated. This ionises the solvent and transfers the charge to the analytes which are then drawn into the spectrometer by the electric fields around the transfer capillary. It was necessary to modify the APCI source to add an auxiliary suction system and a means of mixing the analytes with the solvent. The molecules arrive at the interface through the suction tube connected directly to a Venturi-type suction system. The gas creation the suction is nitrogen directly mixed with the solvent, in this case water, through the nebuliser. The particles are therefore mixed with this spray and then undergo chemical ionisation at atmospheric pressure.

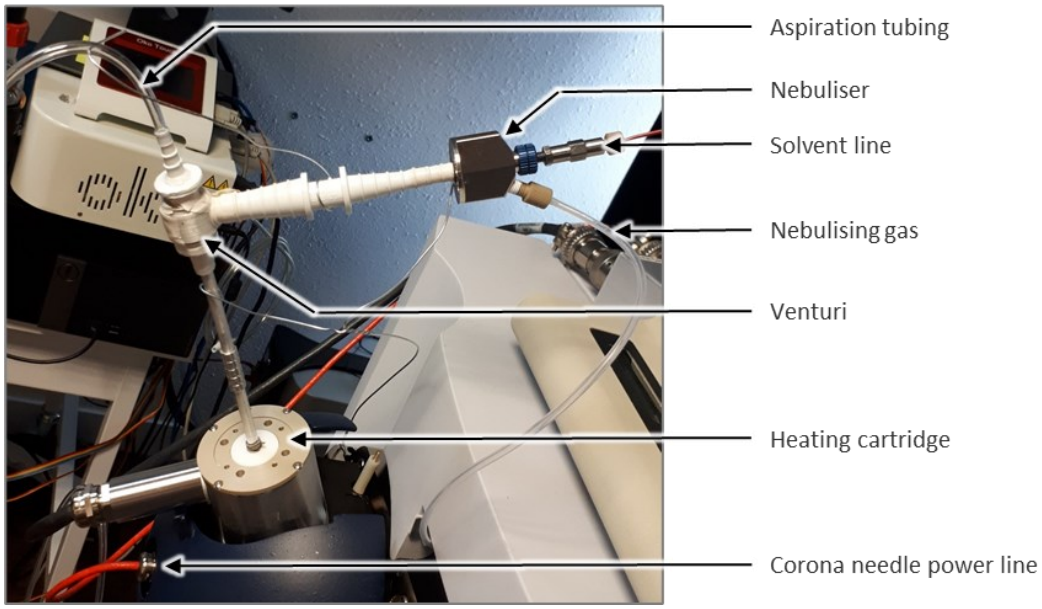

Figure 25: First prototype of the modified APCI interface for SpiderMass analysis. The molecules are aspired in through the suction tube and then mixed with a solvent spray. The mixture passes through the heating cartridge enter the source and cross the corona needle discharge.

This APCI source is the first one that allowed us to obtain signal from biological samples. The workable mass range in which we observe most of the peaks goes from 100 to 1kDa. **Figure 26** shows an acquisition file from the SpiderCompar study discussed later on in this part in which skin lipids have been extracted using EtAc on the forearm skin and deposited on absorbent paper. In panel **A.** we can see the typical noise level and TIC response when the laser is fired (periods between green Dashed lines). The coloured areas correspond to the 3 average spectra periods on panel **B.** and corresponding to first the signal background of the source, the blank zone of the absorbent paper and the zone of the paper which received the total lipid EtAc extract. We can see that the interface background shows a variety of signals mostly situated in the lower part of the mass range and corresponding to the constant transit of molecules through the source typical from APCI ionisation sources. Noticeably we can see peaks at *m/z* 177 and *m/z* 205 which could be assigned as terpenoids fragments. The *m/z* 257 and 283 assigned to FA16:0 and FA18:0 and *m/z* 371 / 445 identified as volatile small molecular weight silicones. These last peaks can become really intense and create signal suppression requiring their careful monitoring. Their evolution has been correlated to some activities in the research centre, i.e when the hairdresser is working. Indeed, a lot of cosmetic product contains silicones, and their high volatility, low polarity and mass makes them easily detectable with our system. On the last average spectra, a lot of different signals can be assigned to putative biomolecules like FFAs, DG, TG, WE, Squalene and Cholesterol/Cholesterol esters.

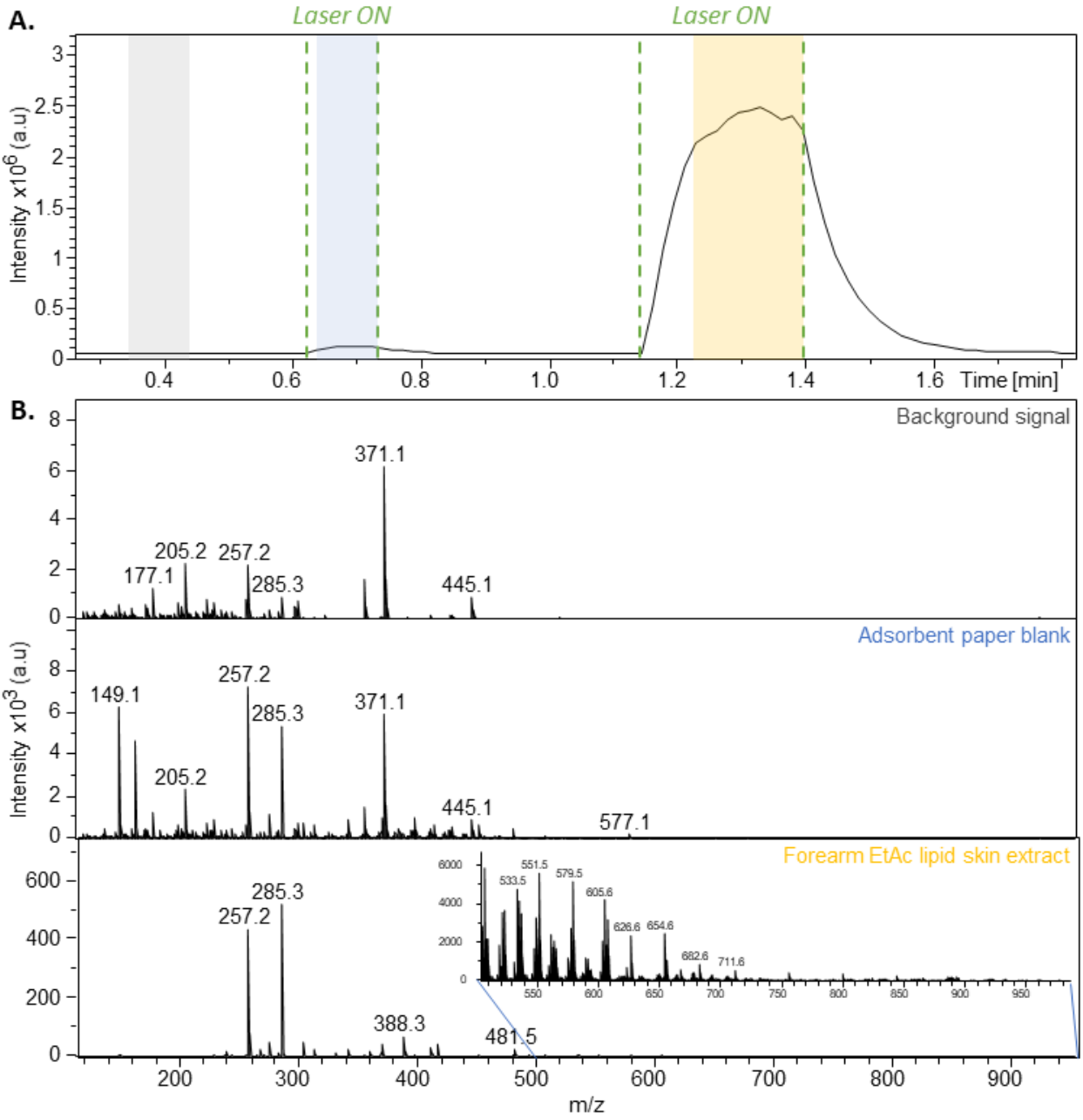

Figure 26: Mass spectrometric response obtained with the APCI prototype source on a skin EtAc lipid extract. **A.** The TIC shows response when the laser is turned on (between green Dashed lines) directed on blank and EtAc impregnated zones of the absorbent paper. The coloured areas correspond to the 3 average spectra periods on panel **B.** and corresponding to first the signal background of the source, the blank zone of the absorbent paper and the zone of the paper which received the total lipid EtAc extract.

Several source and spectrometer parameters had to be optimised to improve the APCI post-ionisation conditions and thus enhance the obtained molecular signals. The classical source parameters used during analysis are presented in **Table 3.** The most important parameters were quickly optimised before moving to the clinical feasibility study of the system on cosmetic products (SpiderValid). Unfortunately, due to the laser situation and mass spectrometer source development, we had accumulated too much delay and took little time to study the impact of source parameters on our analytical conditions. On preliminary tests conducted

on the version of this source presented here, variation of solvent type and flow rate showed little to no effect on the obtained spectra. We think that the origin of this phenomenon comes from the early prototype of the source itself which does not allow correct solvent flow conditions compatible with a real APCI ionisation mechanism but rather, for example, ionisation by the plasma produced by the corona needle. This part is being patented and meanwhile, improvements on the different source elements by more precise machining is underway to optimise and reinforce the device before being able to completely design a whole source.

e) Cholesteryl palmitate limit of detection assessment

One of the direct effects of improved source parameters could be a decrease in the detection limit of compounds and an increase in sensitivity. In order to determine the current detection limit and thus get an idea of its sensitivity, we performed an analysis on 10µL of cholesteryl palmitate (Mw 625.1) at different concentrations. **Figure 27** shows the mass spectra from 200 to 5 µg/mL (3.2mM to 8nM) as well as a graph describing the evolution of the intensity of the ion detected *m/z* = 369.35 as a function of the deposited quantity. The response is linear despite the measurement were carried out on a solution pipetted on absorbent paper which is more or less homogeneous. The detection limit is estimated at 50pg of deposited cholesteryl palmitate or 10µL of a 5µg/mL solution. At this concentration, the signal starts to blend into the background even though it is still easily possible to observe the signal at 369.35 Da.

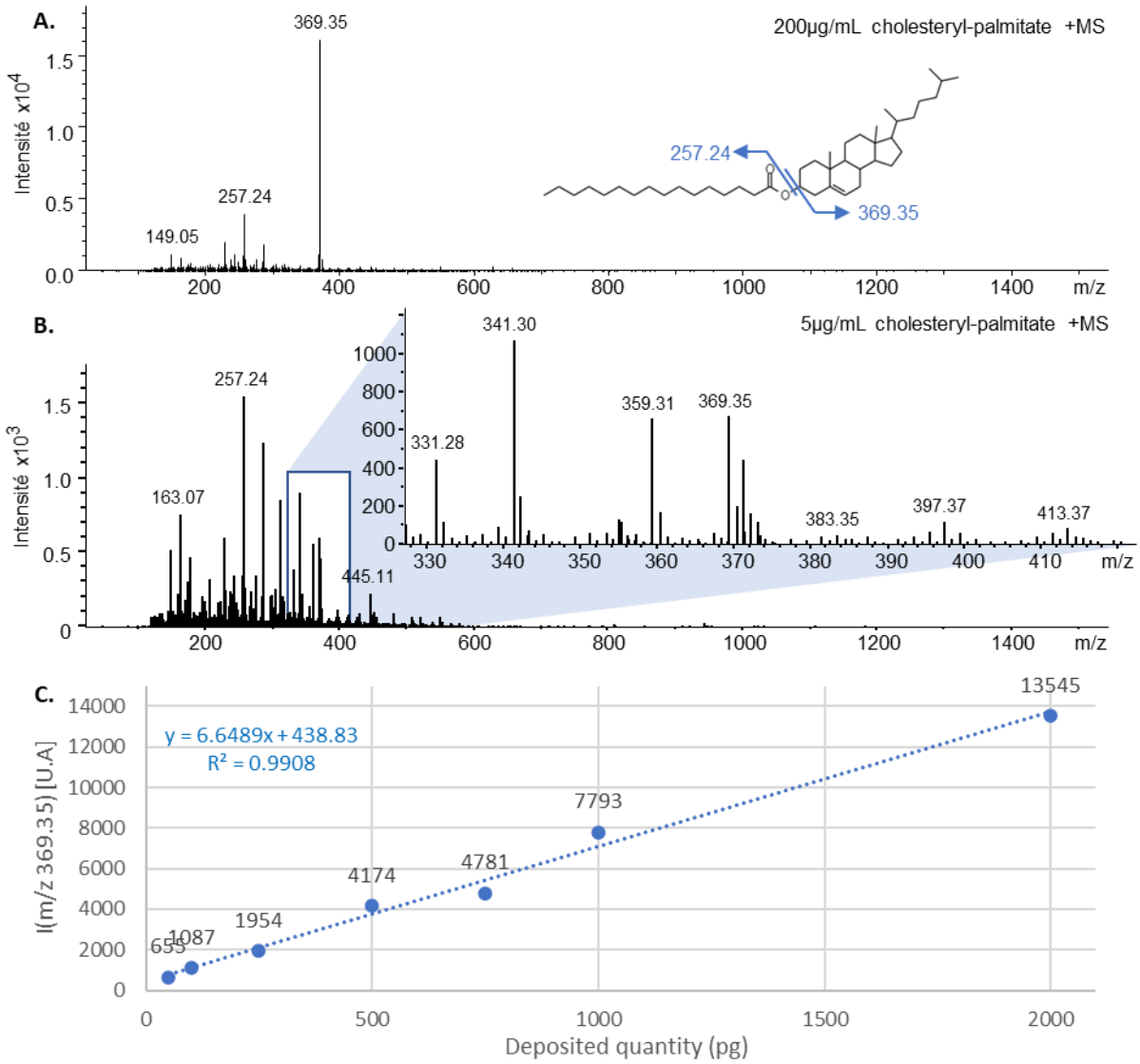

Figure 27: Searching for the detection limit of Cholesteryl Palmitate. **A.** and **B.** Mass spectra at 200 and 5µg/mL and the semi-developed formula of the investigated molecule. **C.** Graph describing the evolution of the intensity of ion 369.35 Da as a function of the quantity deposited.

f) Quality control and reproducibility assessment

Mass spectrometry measurements are known to present a certain variability along the time. This can lead to be substantial by batch effects especially in our experiments that had to be conducted over a long period of time of several months. In a classical research laboratory setup, these parameters can be limited by creating a good design of experiments. In the clinical setup, the analysis depends on the system state when the volunteers are coming for the measures and instrumental variations hinder the interpretation of the data, reduce the statistical power and limit the repeatability and reproducibility of the results. In order to observe these instrumental effects, it seemed necessary to set up a quality control system using a standard sample. Lanosterol, which is derived from squalene and is a precursor of cholesterol, was prepared at 150µg/mL in EtAc, and 1cm absorbent papers were soaked in this solution before left to dry.

Several hundred of these patches were prepared, dried in glass vials under nitrogen for inerting and stored at -20°C before analysis. In the context of clinical studies, before each patient a QC is analysed, and its spectrum kept for statistical analysis. **Figure 28** shows the typical mass spectrum obtained from a sample analysis and describes the loss of a water molecule by Lanosterol in its protonated form. A whole set of QCs was analysed and then pre-processed according to the SMA software and were analysed by PCA to evaluate the batch effect.

The major form observed after water loss is at *m/z*=409.37 Da, but there are also other signals on the spectrum that need to be identified. The PCA here groups 159 QC samples analysed throughout the study presented in **CHAPTER VI**: Study of skin chronic inflammatory dermatosis by the SpiderMass. We can see a strong effect with samples grouping together, especially in the bottom left of the 2D space where we find mainly the first QCs analysed (pink) and the last ones (purple). We must add here that an additional effect is added, linked to the use of two laser movement methods, which induces additional variability (data not shown). Variability analyses on 75 samples generated over several months with the continuous laser method indicate a Coefficient of Variation (**CV**") of 30 and 33% on the 409.37 and 427.38 Da peaks. With the point-by-point laser method the CV is equal to 23 and 45% respectively on the 409 and 427 Da peaks. There is a high correlation between those peaks' intensities and the QC TIC level but unfortunately, this relation is not as strong between the QC TIC and the following volunteers' measurements.

In the other conventional -omics techniques, it is usual to have a CV of less than 20%, though the analysis is generally lasting on a shorter time period. The QC preparation protocol is supposed to generate samples that are similar, but it is complicated to know to what extent they really are. To evaluate this effect, freshly prepared QC were measured by FTIR and SpiderMass. 6 consecutive FTIR measurements on 10 different QCs showed a total variability of about 25%, when 10 SpiderMass measures on 10 different QCs had an intensity variation of the *m/z* 409 signal of about 10% (data not shown). Thus, the FTIR measurement showed more experimental variability than the SpiderMass. This might be attributed to the measured area that is smaller on the FTIR than the SpiderMass making it more sensitive to an eventual heterogeneous coating of the paper.

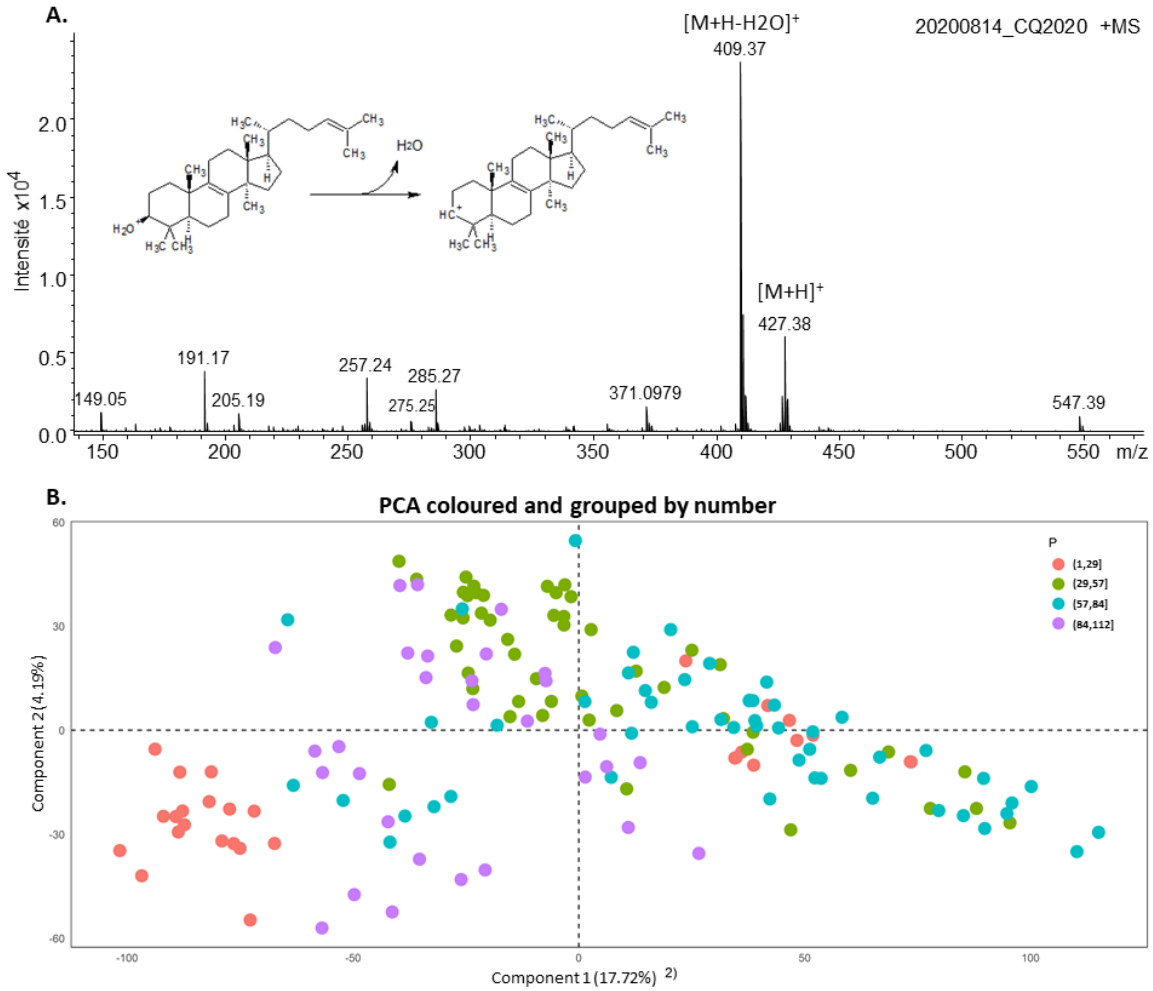

Figure 28: Mass spectrum obtained from an analysis of a Lanosterol control sample and whole cohort analyses of QCs for 2 years. **A.** The typical spectrum obtained for the standard shows mainly the shape of the molecule having lost a water molecule at *m/z*=409.37 Da. **B.** 2D PCA representation of 159 QCs analysed during the SMPatho study showing their variabilities. Each point represents a QC. QCs are coloured according to the patient number, processed in numerical order.

g) Validation of the statistical approaches

The objective of this experiment was to evaluate and validate the statistical approaches with a validation dataset. Sebum was sampled from the same subject 15 different times and then measured with the SpiderMass. Then 10µL of a homemade standard solution was deposited on the paper, allowed to dry and analysed again. The dopant solution was constituted by 10 standards described in **Table 2** at different concentrations allowing observation of their signals in a similar order of intensity. In the **Table 5** is summarised the composition of the standard solution and the signals detected by the SpiderMass analysis. Each compound is described with its specific Mw and observed signals. The greyed lines are compounds detected individually but not in the final standard mix.

Table 5: List of the dopant compounds and their detected signals. Each compound is described with it specific Mw and the signals observed with the SpiderMass. The greyed lines are compounds detected individually but not in the final composition of the dopant.

Nom produit		Mw (g/mol)	SPIDERMASS		
			m/z	Intensity	Identification
a	1,3 distearine	625.02	341.3	6.E+04	$[M-(FA\ 18:0)+H]^+$
			607.56	1.E+05	$[M+H-H_2O]^+$
b	tribehenin	1059.8	719.68	5.E+03	$[M-(FA\ 22:0)+H]^+$
c	1,3 diarachidin	681.12	369.33	3.E+04	$[M-(FA\ 20:0)+H]^+$
			663.62	5.E+04	$[M+H-H_2O]^+$
d	1,3 dibehenin	737.23	719.69	5.E+03	$[M+H-H_2O]^+$
			397.36	5.E+03	$[M-(FA\ 22:0)+H]^+$
e	Ditetracosanoin	789.3	423.37	2.E+04	$[M-(FA\ 24:0)+H]^+$
			771.71	1.E+04	$[M+H-H_2O]^+$
f	1,3 dicaprin	400.59	383.31	5.E+05	$[M+H-H_2O]^+$
g	1,3 Dilauroylglycerol	456.7	439.37	6.E+05	$[M+H-H_2O]^+$
h	Cholestéryl palmitate (cholestérol)	625.06	369.35	1.E+05	$[M-R+H-H_2O]^+$
i	protoporphyrine IX dimethylester	590.71	591.29	2.E+04	$[M+H]^+$
j	Coproporphyrine III Tetramethyl ester	710.82	711.33	3.E+03	$[M+H]^+$

The **Figure 29** shows exploratory elements representing this experiment with the obtained averaged spectra and the PCA representation.

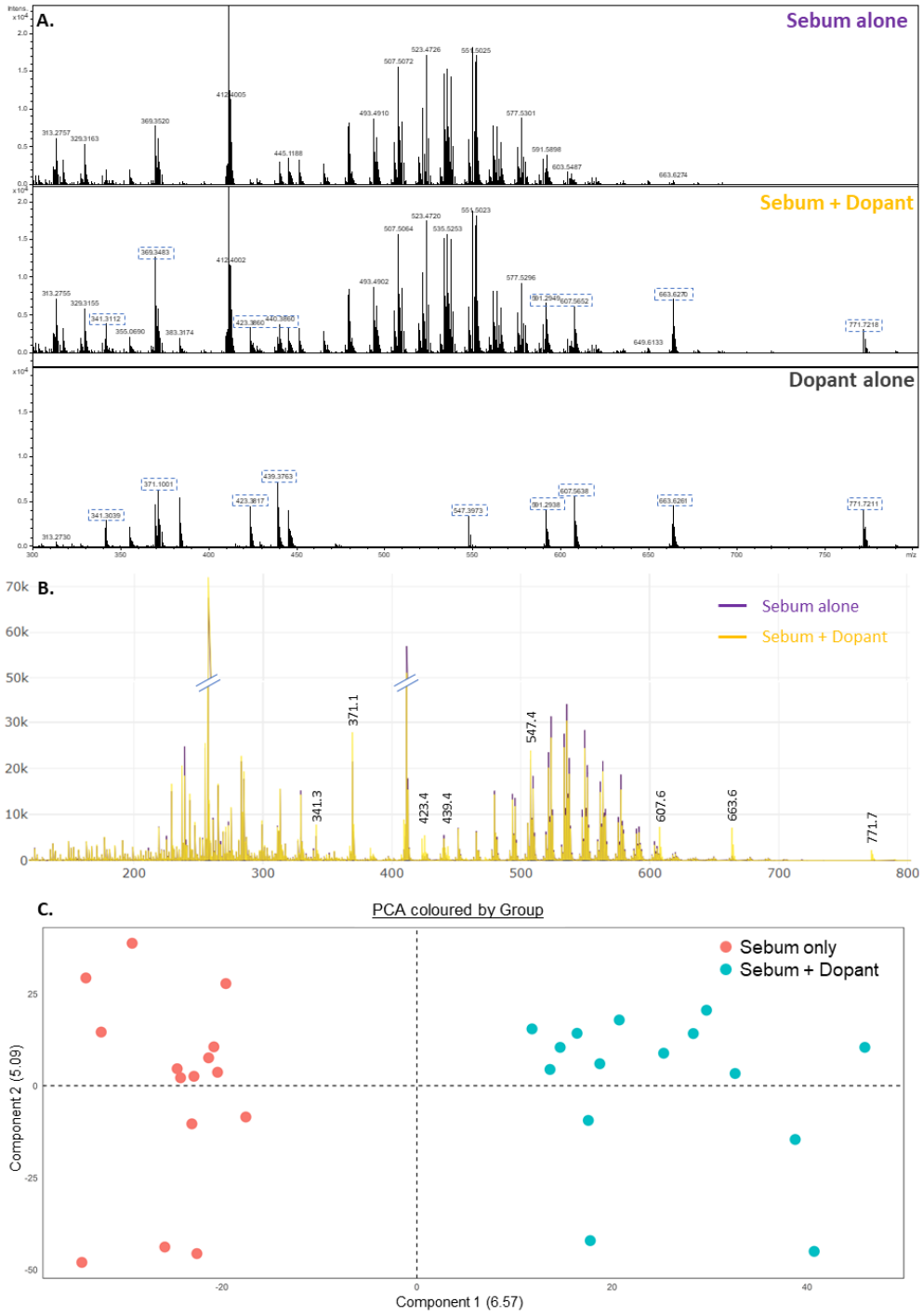

Figure 29: Exploratory elements representing the dopant experiment. A. The spectra observed from the Raw files allows to see the profile of the sebum alone, the dopant alone and the sebum + dopant together. The dashed squares highlight the dopants peaks. B. The average spectra obtained from SMA Software from all the samples in this experiment. In purple the sebum alone and in yellow the Sebum + Dopant. The written masses correspond to the dopant peaks. C. PCA representation of the dataset coloured by the condition (Red = Sebum and Blue = Sebum + dopant) shows a great separation between the two conditions.

In the panel **A.** of **Figure 29**, the raw files spectra allow to see the profile of the sebum alone, the dopant alone and the sebum + dopant together. The dashed squares highlight the dopants peaks. In the panel **B.** is presented the average spectra obtained by the SMA Software from all the samples in this experiment. In purple is the sebum alone and in yellow the Sebum + Dopant. The written *m/z* correspond to the dopant peaks.

In panel **C.**, the PCA 2D representation of the dataset is coloured by the condition (Red = Sebum and Blue = Sebum + dopant) and shows a great separation between the two conditions.

Then, using linear models explaining the intensity differences between the two conditions by taking the groups as fixed effect. The obtained p-values are adjusted by Benjamini-Hochberg to account for multiple comparisons. The results of this differential analysis are summarised in the **Table** 6.

Table 6: Summary of the differential analysis showing the number of peaks truly in the dopant found significantly expressed in the dopped sebum paper.

	In the dopant	**Not in the dopant**	Total:
Significant	23 (FC>0) 4 (FC<1.5)	21 (FC>1.5) 137 (FC<1.5)	185
Not significant	9 (5 filtered)	14646 (14323 filtered during preprocessing)	14796
Total:	36	14804	14840

This allows to find 185 significantly expressed *m/z* between these two conditions with 89 overexpressed with the dopant and 96 underexpressed. It is to be noted that each *m/z* signal on the raw spectra is almost every time described by 2 or sometimes even 3 bins and that all of the 9 signals described in the **Figure 29** have several isotopes. All the peaks already described were significantly found except for the peaks at 371 Da which is usually filtered out of our analysis because it usually corresponds to a contaminant. There is a high number (158) of False Positives but 137 of them have a FC<1.5 which leads to the following recommendation to consider valuable, only the differential results having an adjusted p-value ≤ 0.05 and an absolute FC (**FC_{abs}**) ≥ 1.5. Doing so are presented the results in the **Table 7**.

Table 7: Summarising table of the differential analysis showing the number of peaks truly in the dopant found significantly expressed in the dopped sebum paper, grouped according to the previous recommendations.

	In the dopant	**Not in the dopant**	Total:
Sign & FC_{abs}>1.5	23	21	44
Not significant or FC_{abs}<1.5	13	14783	14796
Total:	36	14804	14840

Based on these results, the sensibility and the specificity of this experiment are Se=23/36=64%, and specificity Sp=14783/14804=99%, a Positive Predictive Value (**PPV**) of PPV=23/44=52% and a Negative Predictive Value (**NPV**) of NPV=14783/14796=99%.

In more concrete terms, these values mean respectively:

- 64% of the standard peaks were declared significant with a FC>1.5

- 99% of the peaks which are not part of the dopant are not significant or at least filtered by the FC
- 52% of the significant peaks with a FC>1.5 are from the standard mix
- 99% of the non-significant peaks or filtered by the FC are not characteristic of the mix

The PPV is quite low but can be explained by the standard peaks applied intensity threshold which was subjectively chosen at 1500 a.u. If we would have used a lower threshold, more peaks from the standard mix would have been significant increasing this PPV value. Analysis are being conducted to come up with an objective and algorithmic solution to evaluate the noise depending on the mass and creating a dynamic threshold.

2. "SpiderValid": First clinical validation study

The first clinical study was carried out the week of 20/05/2019 on 23 volunteers with healthy skin on the forearms and mixed skin on the face and is entitled: "Evaluation of the technical feasibility of *in vivo* measurements by SpiderMass on the forearms of a panel of volunteers and technical feasibility of *ex vivo* measurements on samples of normal/mixed or oily skin on the forehead". The main objective of this study was validate the SpiderMass system ability to detect signals from a SC impregnated products and compare the signals obtained between treated (T) and untreated (NT) areas, 10 min after application and the whipping of the forearm.

This first study has been the occasion to develop the statistical workflow with the service biostatisticians using R language (see Experimental Procedure I.B.3– "**Data analysis**"). The average spectra of all the volunteers in the study showing the characteristic peaks for each of the conditions are presented in **Figure 30**. The panels correspond to a zoom on the mass range comprising the majority of the peak's characteristic of each of the 3 conditions.

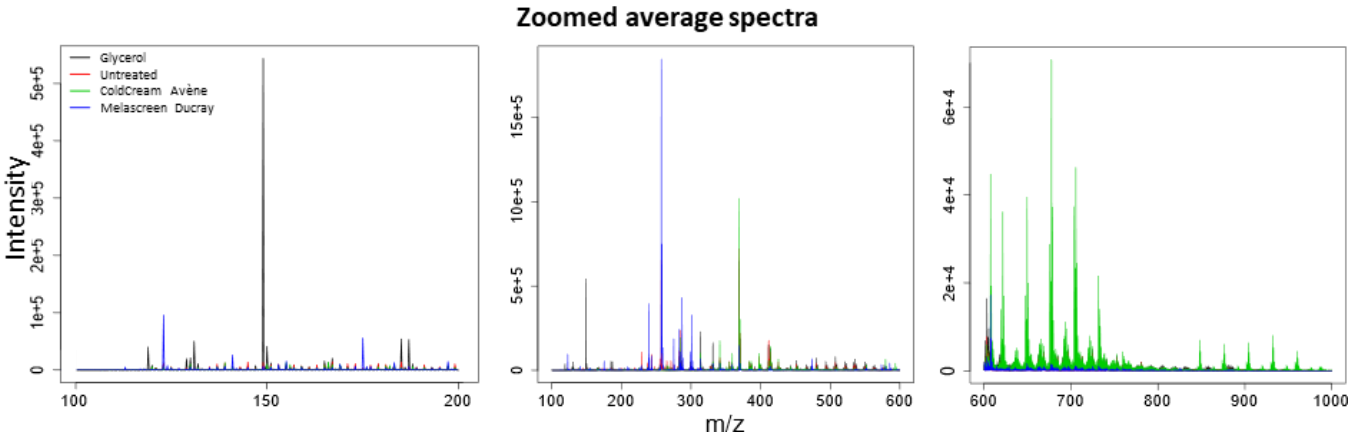

Figure 30: Average spectra of all the volunteers in the SpiderValid study showing the characteristic peaks of each condition. Black: Glycerol, Red: Untreated, Green: Cold Cream from Avene and Blue: Melasreen from Ducray. **Left panel:** Zoom in the 100-200 MR showing the majority of peaks characteristic of the Glycerol. **Central Panel:** Zoom 100-600 showing the majority of peaks characteristic of Melascreen and **Right Panel:** Zoom 600-1000 showing the majority of peaks characteristic of Cold Cream

After filtering out the 10% lower intensity peaks, the remaining 6579 peaks were used in the principal component analysis ("PCA") which is presented in **Figure 31**.

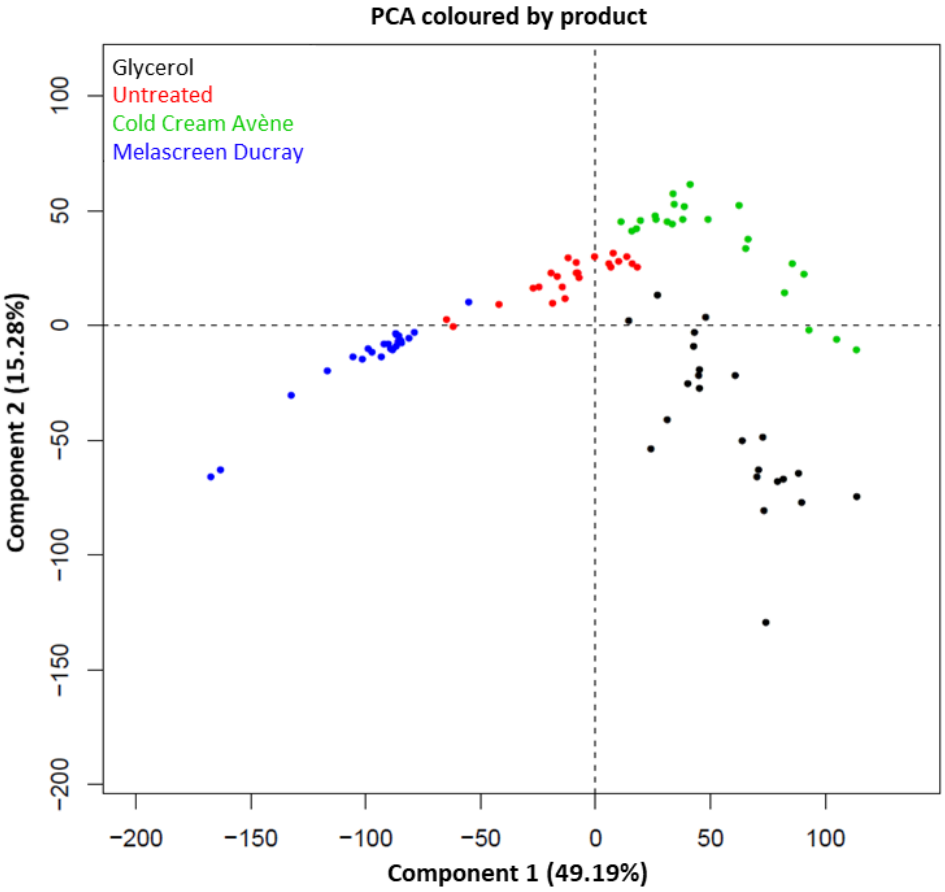

Figure 31: First two PCA dimensions of the volunteer's zones, coloured according to the condition. Black: Glycerol, Red: Untreated, Green: Cold Cream from Avene and Blue: Melasreen from Ducray

A clear separation of the different conditions is observed on the PCA map with the individuals grouped together. To meet the main objective of the study, differential analyses with 2-by-2 comparisons were performed. For each of the 6579 peaks, a mixed model explaining the intensity of the peak with site and product as fixed effects and patient as random was fitted. This way, 6071 peaks were found to be significantly discriminant between the ColdCream group and the NT condition, 5723 between Melascreen and NT and 3556 between glycerine and NT. The *m/z* values of the 5 peaks with a FC greater than 10 and with the lowest adjusted p-value are given in **Table 8**.

Table 8: List of the 5 most significant peaks in the differential analysis against the NT zone. Ranked in each column by decreasing FC value

Cold Cream (*m/z*)	Melascreen (*m/z*)	Glycérol (*m/z*)
703.7	473.5	119.1
931.9	287.9	75.1
675.7	113.1	149.5
959.9	301.9	131.1
875.9	585.7	187.1

For the two used creams, these peaks correspond to their constituents, which will need to be validated by MS/MS. The characteristic peaks of glycerol correspond to undissociated clusters of molecules, or to fragments of glycerol (e.g. loss of water).

The secondary objective was to evaluate the system ability to analyse sebum by absorbent paper sampling on the forehead and evaluate the Pearson correlation between FFA/TG ratio and specific masses observed by the SpiderMass. It was found that 974 masses were significantly positively correlated to the FFA/TG ratio while 3674 masses were negatively correlated. As shown in the **Figure 32**, a total of 442 masses possessed a ρ correlation values above 0.8 or under -0.8: 286 values are positively correlated and have all a *m/z* under 284 (assigned as FA 18:0 +1 isotope) and 156 signals are negatively correlated and all have a *m/z* value between 421 and 1424.

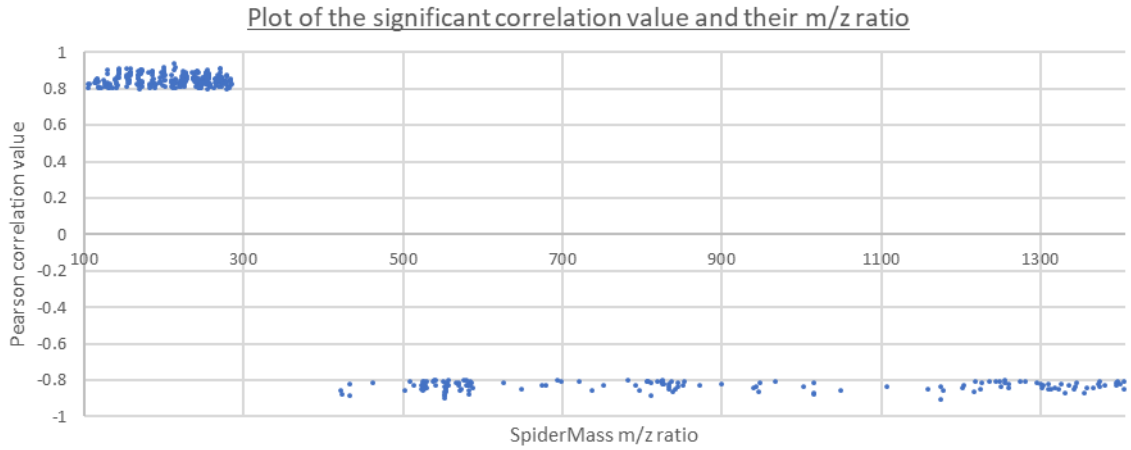

Figure 32: Plot showing the significant Pearson correlation values of *m/z* and FFA/TG ratios. All the 286 values with a ρ coefficient ≥ 0.8 are under the *m/z* value 284. All the 156 signals negatively correlated with a ρ value ≤ -0.8 are above the *m/z* value 421.

Under *m/z* 300, the signal can be assigned to FFA. We can observe on this plot, groups of dots spaced by 14 Da corresponding to a variation of one CH_2 in the aliphatic chain length. The group of masses just above *m/z* 500 are typically DG (551 Da, DG32:0 i.e.) when the masses just under the *m/z* 900 are usually TG and WE (at 805 Da, TG48:1 i.e.) The signals above *m/z* 1100 are quite surprising as the intensities in these regions are low. During this study, the HI on the forearm and the LI on the forehead have been taken and doesn't correlate with observed SpiderMass signals (data not shown).

3. Study of the intrinsic and extrinsic aging of the skin

This study called "SpiderCompar" was conducted on young and mature female subjects recruited during summer 2020. The analyses were directed onto characteristically different areas of the body, namely the forehead and forearm to have an oily and a dry skin area. On the forearm, two zones were analysed on the inner and outer side of the arm to compare UV-exposed and not exposed areas. The SpiderMass prototype has been used to study the molecular changes in the SC constituting lipids and the skin surface lipids by the mean of different sampling modalities.

The primary endpoint of this study is to compare the obtained epidermis molecular profiles according to the sampling method (absorbent paper or scotch tape) and the measurement system (Lille or Toulouse) along with a LC-MS identification of the skin lipids. The secondary endpoints are:

- To study the impact of several factors on the epidermis SpiderMass molecular profiles: (i) UV related ("extrinsic") ageing by the topographic area (inner or outer face of the right forearm). (ii) natural ("intrinsic") ageing related to age on the same area
- Assessing the effect of biometrological parameters on the studied areas and obtained results: (i) Hydration index by corneometry, (ii) Lipid level by sebumetry and (iii) overall lipid quantity by fibred FTIR.

The questions about the two-system comparison is under analyses right now and are not presented in this thesis, as well as the differential analyses of all the comparison made here. The complete results are being incorporated in an article.

a) Forehead sebum profile

i. Positive mode analysis

For this question, sebum has been sampled from the volunteer's forehead, FTIR measured and submitted to SpiderMass analysis. In **Figure 33,** the TIC distribution of all the studied volunteers is presented as well as the corresponding average MS spectra which are coloured according to the groups.

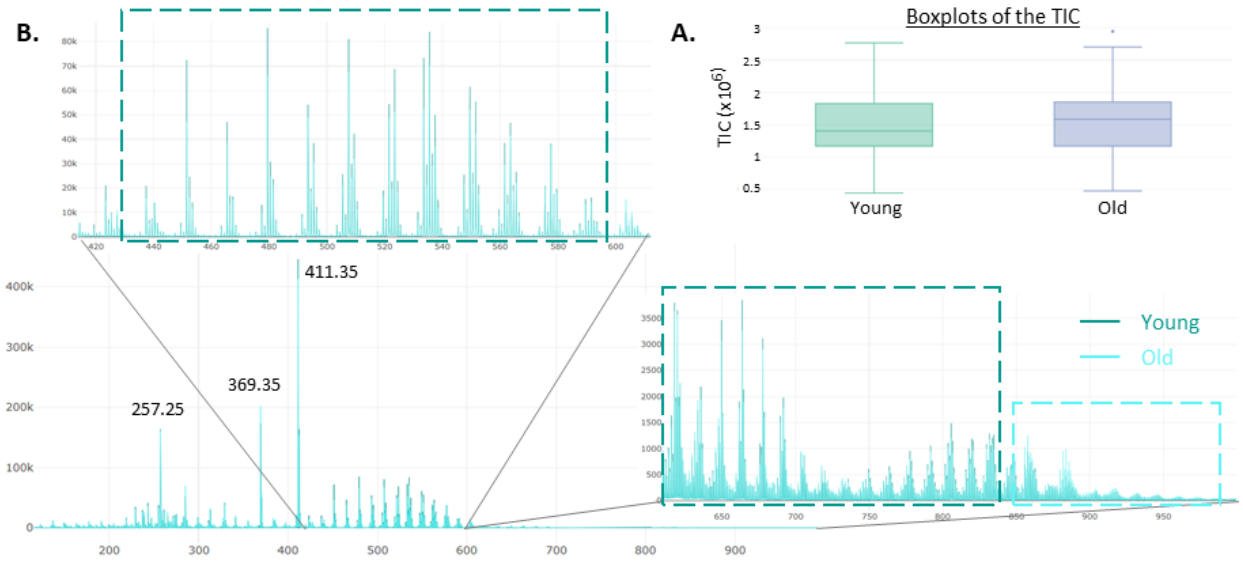

Figure 33: Global TIC distribution of the study volunteers and positive mode average spectra on paper sampled sebum. **A.** The TIC distribution according to the group doesn't show significant difference which indicate a modification of the profiles but not the general quantity of sampled sebum. **B.** Background subtracted, normalised, and averaged spectra from 100 to 1000 Da showing the typical profiles obtained from sebum and coloured according to the groups (Dark blue = Young and Cyan = Old). The more intense peaks are found within the 200 to 415 Da and the region containing the highest number of peaks is between 450 and 900 Da. Peaks at 257, 369 and 411 Da have been identified respectively as lignoceric acid, cholesterol, and squalene. The Dashed squares correspond to regions where the peaks are differentially observed and are coloured depending on the more intense condition.

The TIC distribution doesn't show differences which indicates that any modification of the profiles will not be coming from the general quantity of measured signals. The spectra from *m/z* 100 to 1000 are showing the typical profiles and are coloured according to the groups (Dark blue = Young and Cyan = Old). The dashed squares correspond to regions where the peaks are differentially observed and are coloured according to the most intense condition. Signals were found to be differently expressed on the average spectra and that distinguish the sebum of old and young subjects with a decrease in intensity of the signals between *m/z* 400 and 800 in the old subjects and between *m/z* 800 and 1000 for the young. There are no visible differences in the signals at *m/z* 257 and 411 but there is a visible difference on the cholesterol abundance, with an increase

in the old volunteers. We can note that contrary to the *in vivo* spectra, on this sebum sampling, the squalene peak is far more intense, and the general intensities are higher.

The PCA representation of these sebum impregnated paper in **Figure 34** shows little separation of the volunteers based on their groups and a spreading of some volunteers on the negative (left) part of the first component. Colouring the PCA by the SBR shows the first component variability is explained by this parameter. The labels indicate the volunteer's number and the associated SBR value between parentheses, thus showing that the lowest SBR values correspond to the outliers which are on the left. On **Figure 34C**, a second round of analysis in which the files having a SBR value under 3 has been filtered, and in which we kept only the 6000 more intense *m/z*. This improves the separation but doesn't cluster all the volunteers based on their groups.

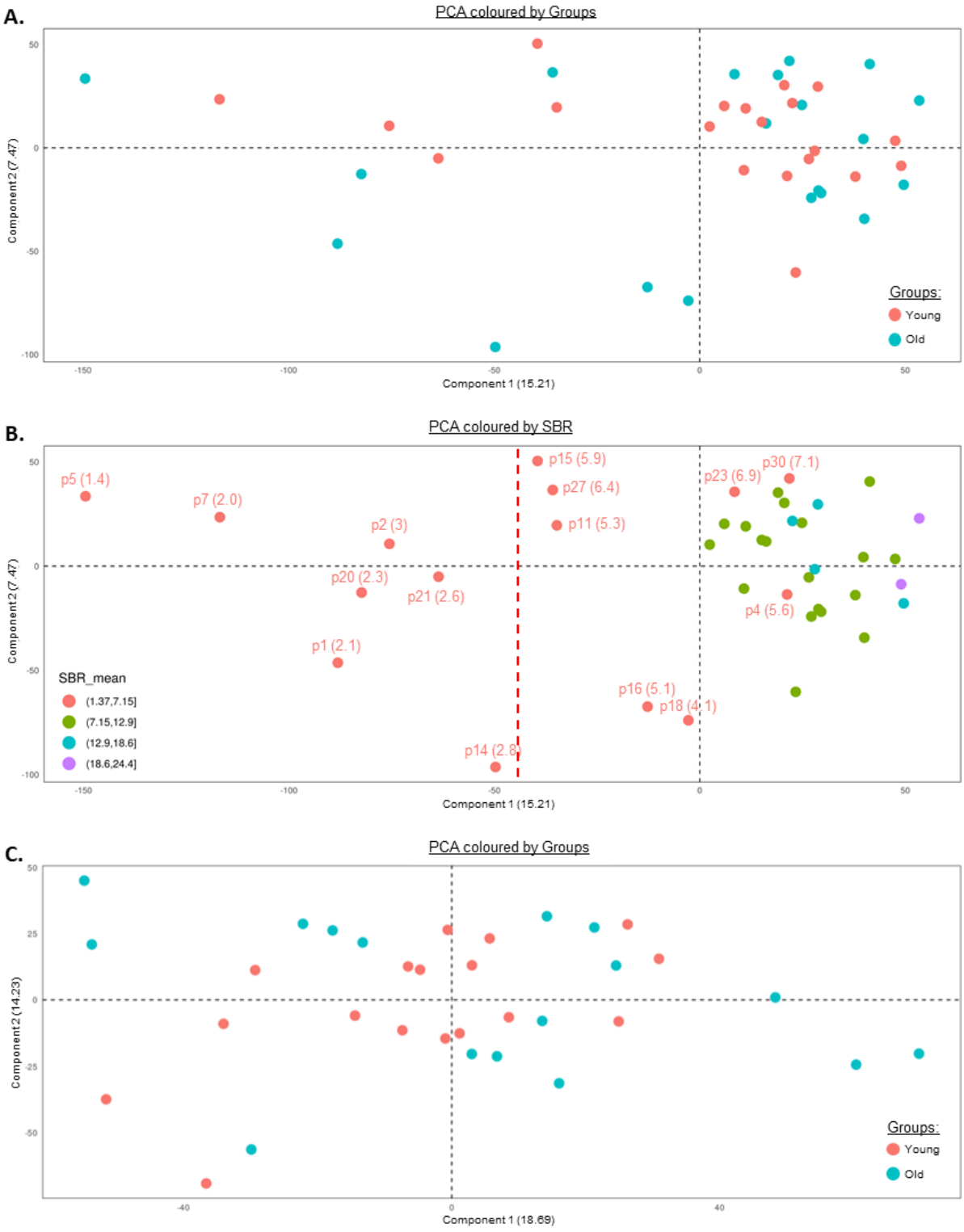

Figure 34: PCA representation of the SpiderCompar sebum impregnated paper data. **A.** The PCA coloured by the groups shows little separation of the volunteers and a spreading of some volunteers on the negative part of the first component. **B.** Colouring the PCA by the SBR shows the first component variability is explained by this parameter. The labels indicate the volunteer's number and the associated SBR value between parentheses, showing the lowest SBR values conducting to outliers on the left. **C.** PCA representation of the Dataset on a second round of analysis in which the files having a SBR value under 3 has been filtered, and in which we kept only the 6000 more intense masses. This improves the separation but doesn't cluster all the volunteers based on their groups.

i. Negative mode analysis

The analysis in positive mode allows us to see biologically interesting molecules like Squalene and cholesterol which are more complicated to observe in negative mode. In the Toulouse PFDC research Center, the MS is of an old generation instrument (QTOF) equipped with Time-Of-Flight technology. Unfortunately, because of this, switching from Positive to Negative is time consuming (around 15minutes) and leads to mass decalibration. This is the reason why we only conducted all the *in vivo* measurements in positive mode during the clinical studies and kept the negative analyses for the *ex vivo* experiments. The **Figure 35** shows the typical profiles obtained from sebum in negative mode.

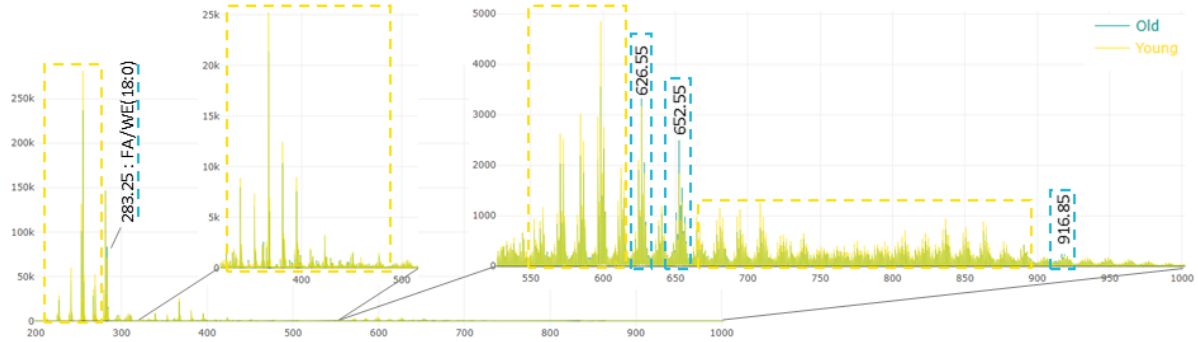

Figure 35: Negative mode average spectra on paper sampled sebum. The background subtracted, normalised, and averaged spectra from 100 to 1000 Da showing the typical profiles obtained from sebum and coloured according to the groups (Blue = Old and Yellow = Young). The Dashed squares correspond to regions where the peaks are differentially observed and are coloured depending on the more intense condition. The signal at 283 Da is assigned to stearic acid or a C18 Wax Ester. Peaks at 626, 652 and 916 Da still needs to be identified as the assignment gave no results

In this figure, the averaged spectra are coloured according to the groups (Blue = Old and Yellow = Young). The Dashed squares correspond to regions where the peaks are differentially observed and are coloured depending on the more intense condition. The signal at *m/z* 283 is assigned to stearic acid or a C18 Wax Ester. Peaks at *m/z* 626, 652 and 916 would need to be fragmented as the assignment gave no results. On the majors peaks, LipidMaps Database[193,194] has been used to assign the masses and are presented in the **Appendix 11**.

The annotations indicate that the ions below *m/z* 600 correspond mostly to FFAs and WEs and are overexpressed in young subjects. In the *m/z* 650 to 900 region, the signals are mostly attributed to ceramides and which are fund to be overexpressed in young subjects.

b) In vivo forehead profile

In these experiments, the volunteer's forehead was submitted to the *in vivo* SpiderMass analysis. The lipids profiles from the skin are rich and present complex spectra. The SMA software was used to pre-process the data (irradiation period detection, background subtraction, normalisation, log transformation), assess the quality and the bias in the Dataset and conduct exploratory experiment. The **Figure 36** shows a typical *in vivo* MS spectra obtained from the forehead skin and PCA analysis.

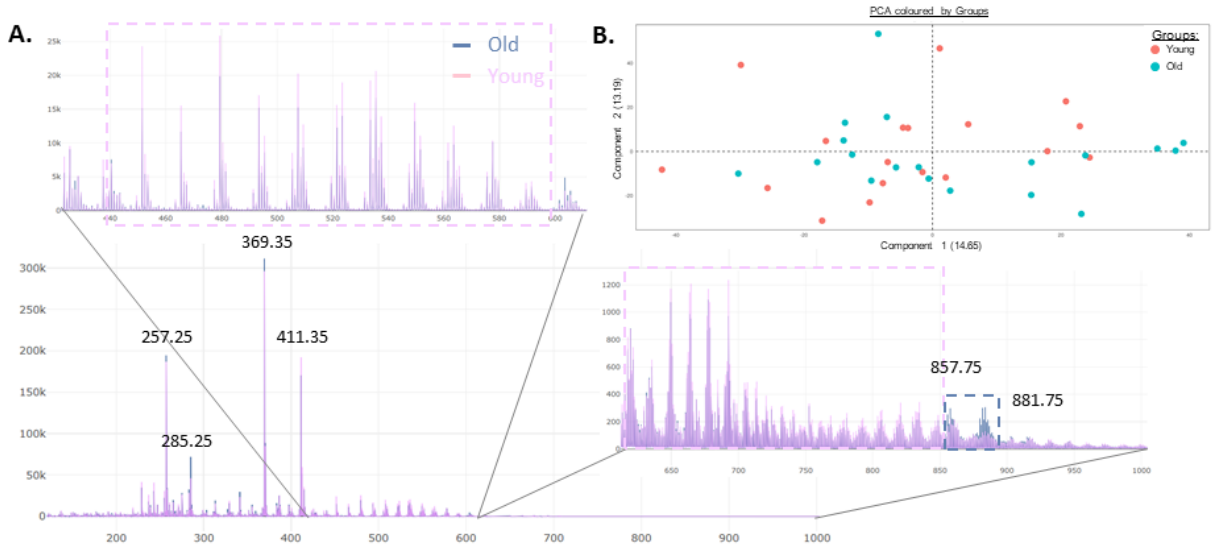

Figure 36: *In vivo* spectra obtained from the forehead skin and PCA analysis. **A.** Binned, background subtracted, normalised, and averaged spectra from 100 to 1000 Da showing the typical profiles obtained from skin and coloured according to the groups (Dark blue = Old and purple = Young). The more intense peaks are found within the 200 to 415 Da and the region containing the highest number of peaks is between 450 and 900 Da. Peaks at *m/z* 257, 369 and 411 have been identified respectively as palmitic acid (FA 16:0), cholesterol, and squalene. *m/z* at 285, 857 and 881 corresponds to stearic acid (FA18:0), TG52:3 and TG 54:5. The dashed squares correspond to regions where the peaks are differentially observed and are coloured depending on the more intense condition. **B.** PCA representation coloured by the groups (Red = Young, Blue = Old) showing the repartition of the volunteers.

The panel **A.** showed the binned, background subtracted, normalised, and averaged spectra from 100 to 1000 Da coloured according to the groups (Dark blue = Old and purple = Young) shows. The more intense peaks are found within the 200 to 415 Da and the region containing the highest number of peaks is between 450 and 900 Da. Peaks at 257, 369 and 411 Da have been identified respectively as palmitic acid (FA 16:0), cholesterol, and squalene by comparison using MetFrag[195] on the MSMS generated spectra. On the majors peaks, LipidMaps Database[193,194] has been used to assign the masses and are presented in the **Appendix 10**. It is to be noted that since SpiderMass is based on the direct analysis without LC-MS, several assignations are possible for each mass. We can rule out that in our spectra, we observe mainly FFAs in the *m/z* 100- 400 range, mainly DGs and WEs in the *m/z* 400-600 range, and Cer & TGs between *m/z* 600 and 1000. At *m/z* 285, 857 and 881 respectively signals are assigned to stearic acid (FA18:0), TG52:3 and TG 54:5. The dashed squares correspond to regions where the peaks are differentially observed and are coloured depending on the most intense condition. On the average spectra discriminative signals of the skin of Old versus Young subjects are observed, with a decrease in intensity of the signals within the *m/z* 400 -800 range for the old subjects and a decreased signal intensity within the *m/z* 800 -1000 range for the young ones. There are no visible differences for the signals at *m/z* 257 and 411 but there is a visible difference on the cholesterol abundance, with an increase in the old volunteers. The panel **B.** shows the PCA representation coloured by the groups (Red = Young, Blue = Old) showing the repartition of the volunteers. On this PCA there is a beginning of a separation, but this is not striking. This can be explained by the fact PCA analysis is not supervised contrary to LDA or

LASSO, which consider the classes when conducting the dimensionality reduction. This method allows to show important global variations but not minor changes of intensities on several masses.

c) In vivo forearm analysis

Contrary to the forehead analysis, forearm present two distinct zones respectively the inner and outer side allowing to study the capacity of the SpiderMass system to observe UV-related extrinsic aging of the skin. Triplicates of the measures were realised on each zone for every subjects. Then all the *in vivo* acquisitions were analysed and normalised together. This exploratory analysis aimed at outlying the differences between the 4 conditions (old/internal, old/external, young/internal, young/external) without going into differential analysis that are ongoing. First, in the **Figure 37**, averaged spectra are shown comparing the age groups without distinctions of the zones, and then the zones without distinction of the age.

The averaged MS spectra coloured according to the groups (Black = Old and Pink = Young) allows to observe several trends: peaks in the *m/z* 450-600 range and in the 650-850 range are more intense in the young group. The old group shows higher intensities in the lower MR and on discrete cluster of peaks at *m/z* 603, 857 and 881 respectively assigned to DG 36:2, TG 52:3 and TG 54:5. In the panel **B.**, the averaged spectra coloured according to the zones (Orange = Internal and Green = External) lead to the following observations: peaks in the *m/z* 450 to 600 range are more intense on the external side of the arm while peaks in the *m/z* 350 to 440 range and in the *m/z* 650 to 800 are more intense on the internal side of the arm.

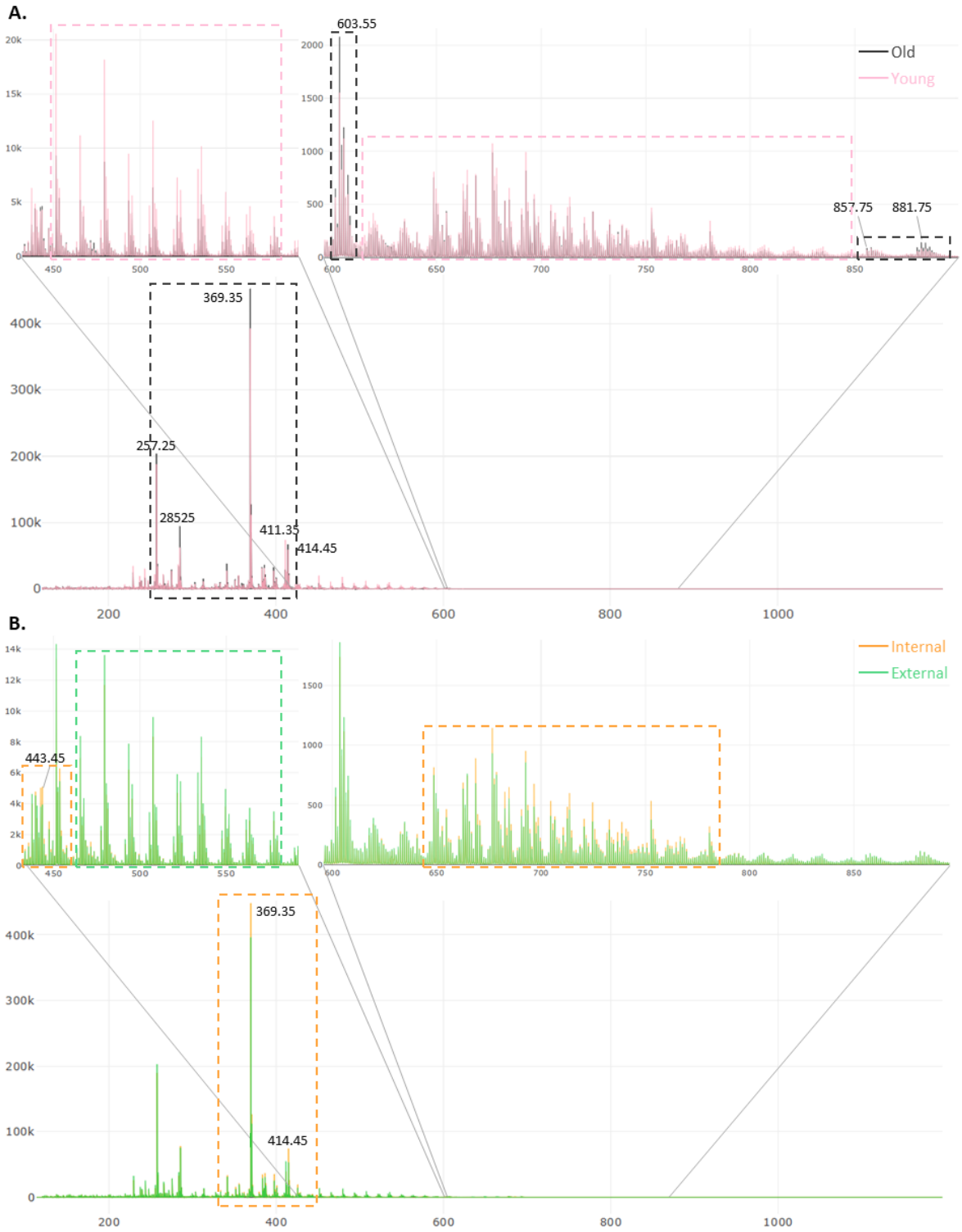

Figure 37: In vivo spectra from 100 to 1000 Da obtained from the forearm skin coloured by the groups and by the zones. Labelled peaks or Dashed squares correspond to regions where intensities are differentially observed and are coloured depending on the more intense condition. **A.** Averaged spectra coloured according to the groups (Black = Old and Pink = Young). It is possible to observe several tendencies: peaks in the 450 to 600 and in the 650 to 850 ranges are more intense in the Young group. The Old group shows higher intensities in the lower MR and on discrete cluster of peaks at 603, 857 and 881 Da respectively assigned to DG 36:2, TG 52:3 and TG 54:5. **B.** Averaged spectra coloured according to the zones (Orange = Internal and Green = External). It is possible to observe several tendencies: peaks in the 450 to 600 Da range are more intense on the external side of the arm while peaks in the 350 to 440 Da range and in the 650 to 800 Da are more intense on the internal side of the arm.

In the **Figure 38**, the averaged spectrum has been constructed using the class, which correspond to the combination of the groups and the zones.

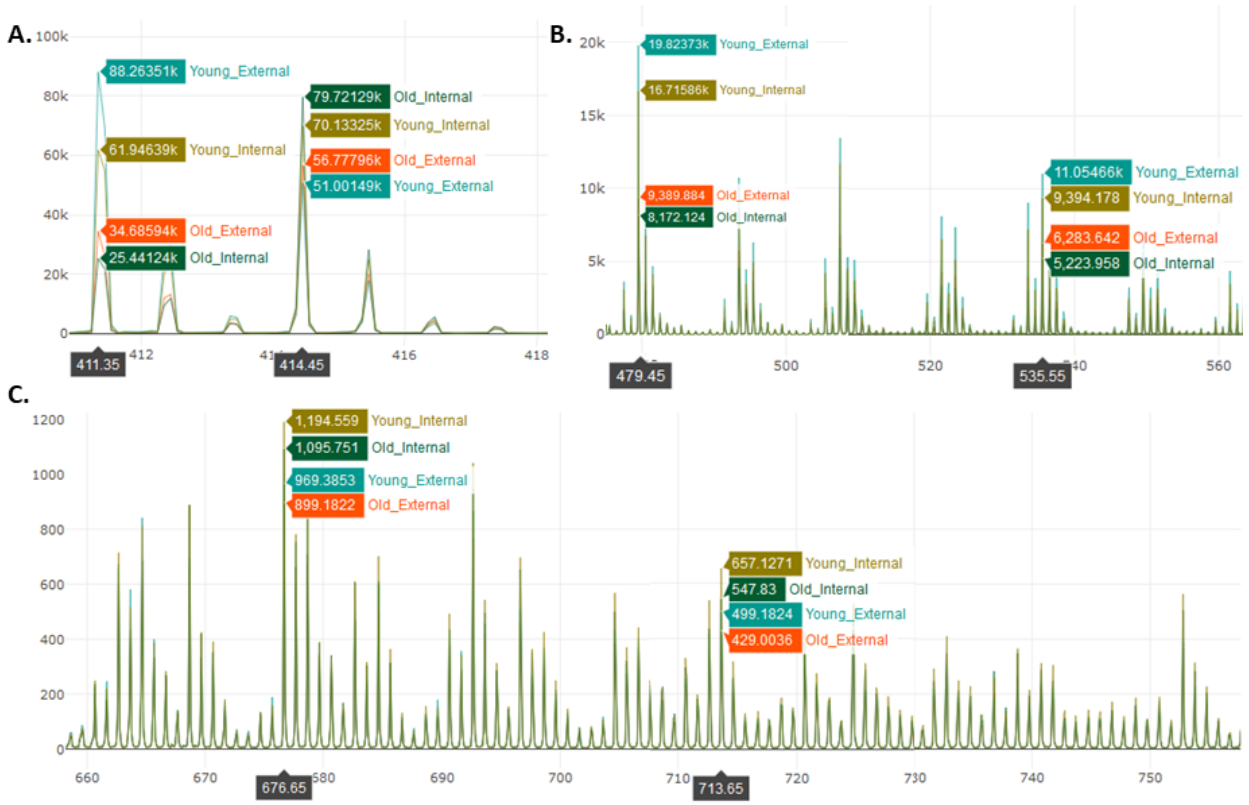

Figure 38: In vivo forearm skin spectra coloured by the classes and zoomed on regions of interests to show 6 different peaks variation. **A.** Zoomed spectra on the 411 and 414 Da peaks showing more abundance of the squalene on the young volunteers and the external zones. The signal at 414 could be assigned to a FA or WE 26:0 **B.** Zoomed spectra on a part of the 450-600 region where WE and DG are found. Display of the intensity of 2 random peaks at 479.45 Da that can be assigned to WE 32:1 and at 535.55 Da to WE 36:1. **C.** Zoomed spectra on a part of the 660-1000 Da region where Cer, long FA esters and TG are found. The peak at 676.65 Da correspond to a Cer 44:2;O2 and 713.65 Da to a FA esters of hydroxy FA ("FAHFA") 48:3;O.

For the sake of clarity, this figure presents only zoomed regions and the labels and intensities on some selected peaks. As the peaks at the lower mass range (<400) shows some level of variations but with small FC, they were not shown. The panel **A.** depicts the evolution of the Squalene (*m/z* 411.40) and the adjacent peak at *m/z* 414.40. The abundance of the squalene is higher in the young volunteers and in the external zones. The identification of the *m/z* 414.40 need to be checked as its evolution has been observed several time correlating with the *m/z* 411.40 (squalene) which should not be particularly the case if the 414 was only a FA or a WE as it is now assigned. It is to be noted that the oxidosqualene at *m/z* 427 Da shows a higher abundance on young subjects and on the external zones (data not shown). This molecule derives from the Squalene by the action of the squalene monooxygenase and is the substrate of various enzymes participating in the cholesterol biosynthesis pathway. It is also a molecule involved in the skin protection against oxidative stress. In the panel **B.**, the spectrum is zoomed in the *m/z* 450-600 range where most of the WE and DG are found. Two peaks are

labelled respectively at *m/z* 479.45 that can be assigned to WE 32:1 and at *m/z* 535.55 that was identified to be WE 36:1. In panel **C.** the spectra show the *m/z* 660-1000 range where most Ceramides, long FA esters and TG are found. The peak at *m/z* 676.65 corresponds to a Cer 44:2;O2 and at *m/z* 713.65 to a FA esters of hydroxy FA ("FAHFA") 48:3;O. The DG36:2 at *m/z* 603.65 shown in **Figure 37A** is more abundant on the internal zone of the old group and lowest at the internal zone of the young group with a FC of 1.5. There is almost no different expression between Internal and external zones on the old group but a slight one in the young volunteers.

The PCA analysis of this dataset is the one giving the better separations of the groups and the classes as shown in **Figure 39.**

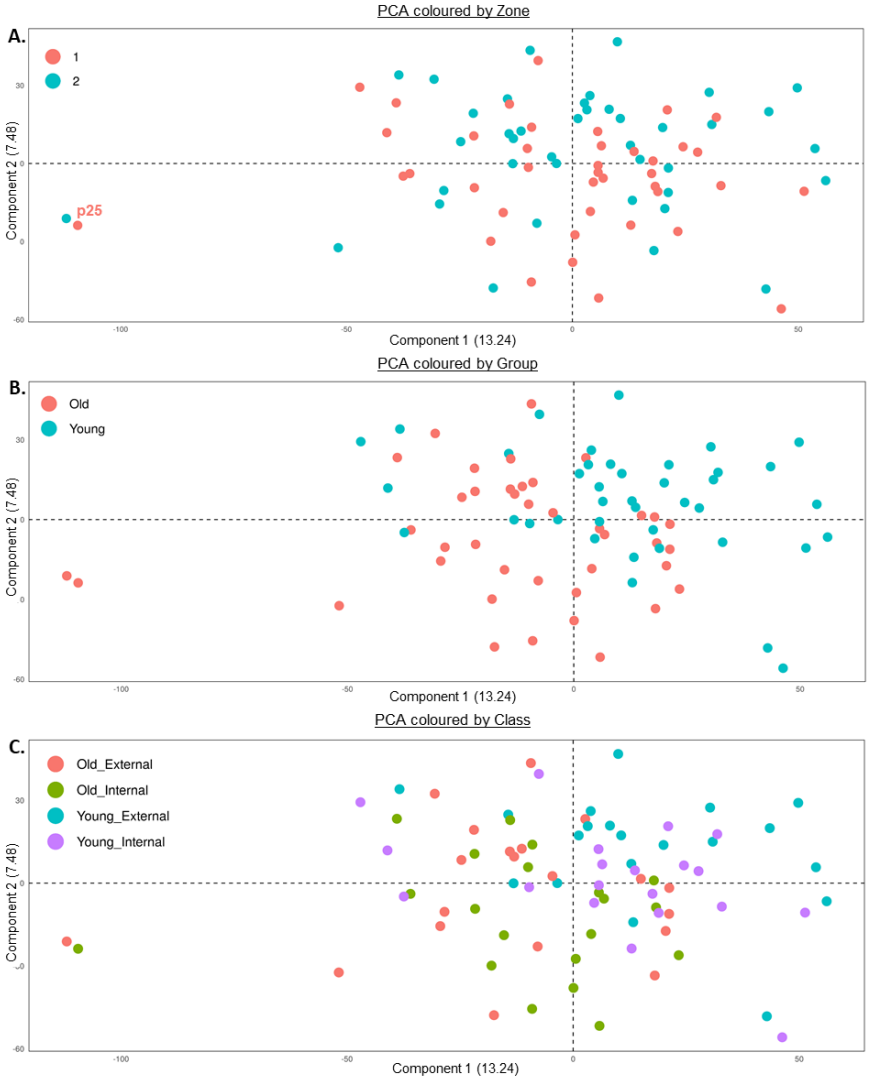

Figure 39: PCA representation of the forearm vivo dataset. **A.** PCA coloured by the zones shows little separation of the zones and 2 outliers points corresponding to p25 z01 (innerside) and z02 (outerside) **B.** PCA coloured by the age group shows a better separation of the age groups indicating that the age effect is greater on the data than of the zones **C.** PCA representation of their classes depending on the groups and zones. The class differentiation is difficult to observe even if it seems the distinction between Internal and external is easier to see on the young subjects.

In this figure, the PCA coloured by the zones shows little to no separation of the zones and 2 outliers dots corresponding to p25 z01 (innerside) and z02 (outerside) In the panel **B.** the PCA is coloured by the age group and shows a better separation of the age groups indicating that the age effect is greater on the data than of the zones. In panel **C.** The PCA is coloured according to the classes. The class differentiation is difficult to observe even if it seems the distinction between Internal and external is easier to see on the young subjects.

The dendrogram of the volunteers arranges the acquisitions based on their similarities and is presented in **Figure 40**.

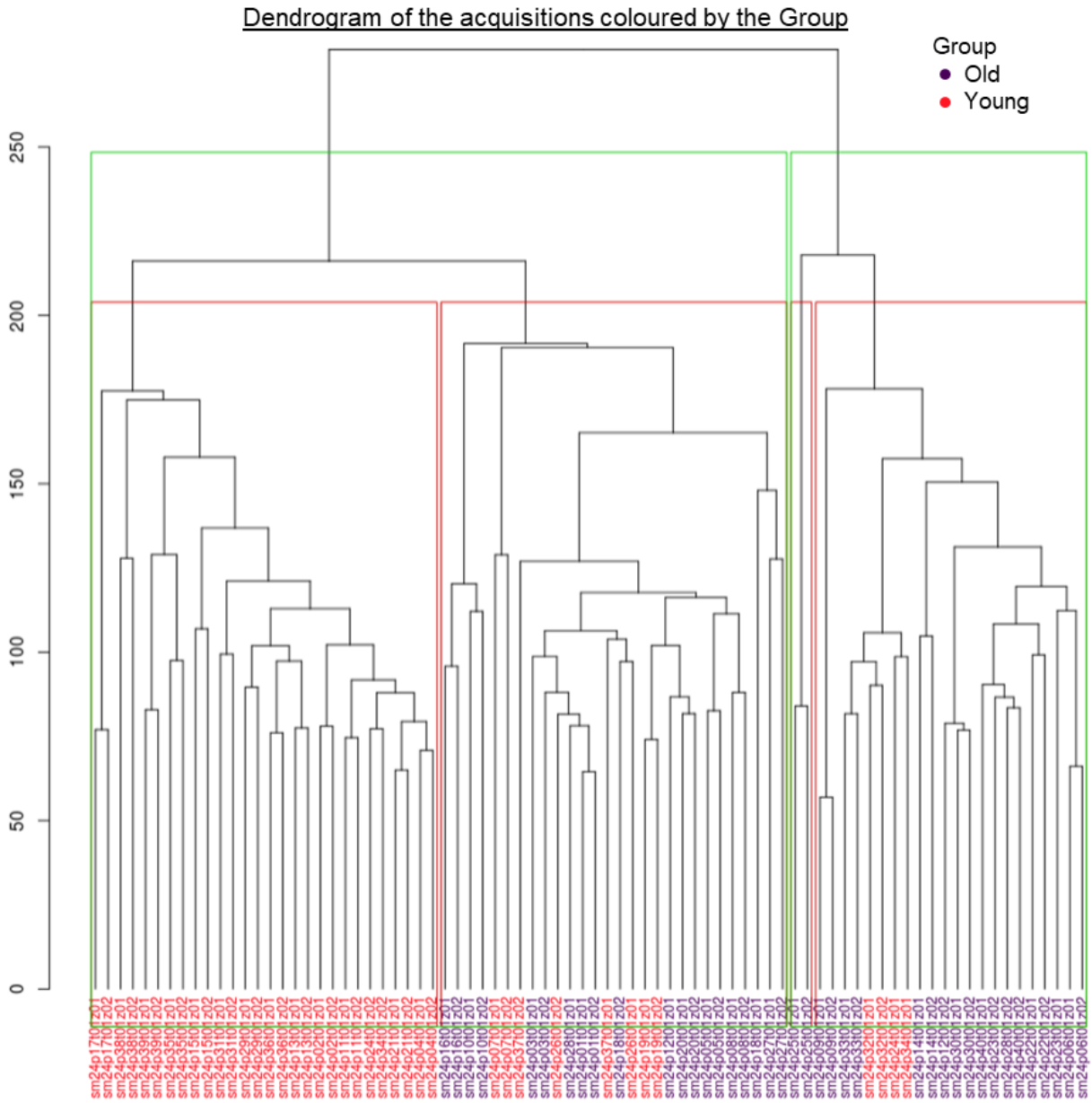

Figure 40: Dendrogram representation of the similarities between the acquisitions, coloured according to the groups. The scale at the left part correspond to the distance coefficient between the acquisitions. The red and green squares represent the optimal separation of the cohort if respectively 4 or 2 groups were to be made. One of the red groups correspond only to p25 which confirms once again its different profile. The separation according to the groups is quite good. It is not possible to observe de distinction between the zones as most of the two acquisitions from each volunteer are grouped together.

This dendrogram represents the similarities between the acquisitions, coloured according to the groups. The scale at the left part correspond to the distance coefficient between the acquisitions. The red and green squares represent the optimal separation of the cohort if respectively 4 or 2 groups were to be made. One of the red groups correspond only to p25 which confirms once again its different profile. The separation according to the groups is quite good. It is not possible to observe a real distinction between the zones as most of the two acquisitions from each volunteer are grouped together. This suggest that the inter-subject variability is more important than the inter zone variability on the same volunteer.

D. Conclusion and discussion

The laser system received in Toulouse did not fully meet the specifications issued for the Lille system. To be able to start my thesis, this system was accepted but some modifications had to be made with the help of the manufacturer for it to reach the desired characteristics in terms of energy per laser shot. The OPO box had to be remanufactured because it created a low-quality shaped beam, with three bundles that was problematic: it created "hot spots" on the injection face of the fibre that degraded it. Since the box has been changed, the beam profile has a higher quality and doesn't cause unexpected burning of the fibre, but the biggest concerns come from the modification of the inside architecture of the system. Indeed, between the 2 years separating the buying of our two lasers, OPOTEK had upgraded some element's position which lead to a more a divergent beam. With an identical fibre injection system than in Lille, this notably more divergent and wider beam prevents from getting completely inside the fibre, impeaching to obtain laser energies in the same level that we have in Lille. It is important to consider these differences between the prototypes. The laser energy obtained during the SMPatho study present in Chapter VI equals 0.8mJ/Pulse which means we have a laser fluence around 0.7 J/cm² on a 400µ diameter spot. This means we have a laser fluence 20 times less intense on the Toulouse system. This can explain some of the ablation variability but fortunately, for *in vivo* experiment and absorbent paper, the laser energy reaches a high enough level to allow to conduct experiments. For tapes experiment, the system provides just needed energy which need to be carefully monitored to avoid losing energy and affecting the results. To date, most of the major issues encountered with the laser have been addressed. A change in the actual arrangement of the elements inside the laser is not feasible so we are working to improve the injection system instead as well as completely connecting the fibres for them to be really plug and play and ease the maintenance.

As the Toulouse system is used intensively on volunteers, products, optimisations, and feasibility studies, it is necessary to be simple to operate and to allow the generation of quality data, free of as many experimental effects as possible. Developments during my thesis have enabled to obtain a more reproducible and user-friendly measurement system, taking into account the distance between the subject and the laser. On the control software, it is planned to work on a coupling with the mass spectrometer to be able to automatically trigger the acquisitions. To continue the quality assessment and control of the system, a small application named "SMA QC" was developed to follow, as the system is used, different parameter like the intensity of the calibrant, the level of background noise, the TIC and the laser energy. This database allows easy evaluation of the experimental parameters occurring during the clinical studies.

From a regulatory point of view, an external safety consultancy has assessed the system as being class 1M, i.e. not dangerous under classic conditions of use. This is confirmed by the low ablation depth of 4µm per

laser shot on skin. However, it would be interesting to evaluate which parameters may have an impact on this depth depending on the characteristics of the skin such as thickness, state of the skin barrier or hydration.

The APCI interface that has been developed is functional and provides good sensitivity. It will be necessary to make it more robust with stronger and better machined parts. Some leaks lead to a decrease in the efficiency of the suction. The effect of operating parameters such as the suction and solvent type and flow rate, the vaporisation temperature or the voltage applied to the corona needle were evaluated and showed little to no effect at the early development stage of the prototype. A recent experiment conducted after the upgrade of a part of the system on the effect of solvent showed promising results to reduce, for example, the in-source fragmentation. This opens the way to more fundamental experiments on the effects of the various parameters influencing the ionisation which we foresee to help observing other classes of molecules that are not yet accessible today, such as phospholipids, or porphyrins which is a marker of C. acnes presence. It is for example crucial to evaluate the effect of the source temperature on the degradation of thermolabile molecules. It has been shown for example that Vit-D can hardly be observed above a temperature of 325°C using APCI[196]. These developments will certainly improve the intensity of the observed signals and the overall sensitivity of the system by lowering the detection limit of the standard which on the cholesteryl palmitate is already as a respectable level of 50 pg.

Finally, it will allow to find parameters for better repeatability and reproducibility to increase the chances of observing fine biological effects. This will be directly observable on our QCs which depicts a high level of instrument variability (around 30%). Let's not forget that at the time of this evaluation, we were still in the adjustment of some parameters partially explaining part of the more important instrumental variability. There is also a need to evaluate whether the preparation of the samples or the choice of the standard itself is the best. To this aim, RAMAN imaging could be used to first assess the homogeneity of the QC and we may need to evaluate the interest of a multicomponent QC for finer evaluations of the system state.

The statistical analysis strategies use classical pre-processing routines for MS generated data but has been embodied in a web-based software to ease its use for non-R users. The data preparation software now allows to be independent of statisticians for our routine exploratory analyses that do not require their expertise. These first analysis results allow us to better understand how the whole system works and what its capacities are. The sebum dopped paper experiment is crucial to understand what should and shouldn't be taken as a true positive result and in this case, gave us guidelines not to conclude on false positive signals. Eleonore Gravier, one of the statisticians in the team worked extensively on the implementation on a centroid data processing approaches which has shown to be challenging. Indeed, classical centroid workflow are used on LCMS dataset or high mass precision instruments. Each of these two requirements induces specific needs for the data to be processed which are not fulfilled with the SpiderMass prototype. Without going into detail, this approach uses the centroided data and reconstitute gaussians to count all the pics and determining which

needs to be kept. When the standard mix experiment with the profile mode gave an SE/SP/PPV/NPV of 64/99/52/99, we obtained 60/97/60/97 with this modality showing a good similarity to the profile mode. This workflow has the potential to greatly increase the power of our analyses for the detection of molecules of interest and better prepare the identification of these molecules.

As it could be seen, the exploratory analyses such as PCAs do not always allow us to observe a separation of our conditions as in the case of the SpiderValid study, but that effects are indeed found to be highly significant in differential analyses. In this study the analyses demonstrate the ability of the system to distinguish areas based on the specificity of their molecular content from different treatments. For the two used creams, these peaks correspond to their constituents, which will need to be validated by MS/MS. The characteristic peaks of glycerol correspond to undissociated clusters of molecules, or to fragments of glycerol (e.g. loss of water). This was also the occasion to show on non-acneous skin, that the FFA/TG ratio is correlated to the SpiderMass results which is really promising for several applications. In addition, this study allowed us to demonstrate the safety of laser ablation for patients. The patients were followed by a dermatologist after the experiments and the adverse effects were limited to 3 volunteers and never more than the appearance of a slight erythema that disappeared within hours of the analysis. We have not yet found the exact criteria explaining the skin reaction because the volunteers who've shown a reaction were not patients with problematic skins. In general, the effects that we observe are coming from signals that have minor variations and therefore have less weight in the PCA. On way to improve that would be to conduct reduced PCA where each of the peaks would have the same weight. As already mentioned, the differential analyses allow for finer effects to emerge since several factors are considered in the differential analysis, such as batches, basal intensity value, TIC and laser energy. Finally, PCA is an unsupervised analysis which means that a very strong effect (other than the one of interest) can mask the effect of interest, whereas differential analysis is a supervised analysis.

The SpiderCompar study presented in this chapter has the principal goal to compare the TLS and LIL systems by sharing analysis of samples. This axis is being done so the exploratory results were shown for the *in vivo* and sebum measurements. This study has been the occasion to assign all the major observed peaks in positive and negative mode and that shows we observe mainly FFAs and WE followed by DG/TG and to a less extend ceramides.

Contrary to the *in vivo* measurements, analysis of the sebum impregnated papers has shown a general increase in intensities and a higher detection of the squalene which is described as one of the major constituents of the sebum. There is no TIC difference between the conditions which will need further examination as others groups have shown a general decrease in the amount of sebum with passing age[197]. In the average spectra, we find signals that seem to be differently expressed and that distinguish the sebum of old and young subjects with a decrease in intensity of the signals between *m/z* 400 and 800 in the old subjects

and between *m/z* 800 and 1000 in young ones. There are no visible differences on the signals at *m/z* 257 and 411 but there is a visible difference on the cholesterol abundance, with an increase in the old volunteers. These described variations need to be put in the perspective of the validation study which advises to keep only signal differentiating by a FC>1.5, which is not often the case in this situation, where most of the described peaks bares a FC between 1.3 and 1.5.

This fact will need to be addressed during the differential analysis because the linear model will adjust the intensities based on experimental factors like the SBR. The negative mode analysis of these papers shows a general tendency for the young groups to have more intense peaks and only some specific peaks more abundant for the old group that gave no convincing assignment results and need to be fragmented for identification. On the forearm, the results also indicate a general decrease in most of the observed lipids except for the smaller masses and 3 groups of peaks assigned to a DG and 2 TGs. We will need to investigate what could be the role of these specific molecules. These qualitative results go well with the described literature. Indeed, the main class of sebum lipid is the TG and all its hydrolysis products, the DGs, MGs, FFAs and glycerol. It has been shown that a general decrease of TGs with age can be due to an increase in their hydrolysis which could be explained by the modification of the microflora in older skins[142,198]. There is also a depicted decrease of WE secretion rate correlated with the increasing age that have been seen here as well[199]. Indeed, there is a known decline in the sebaceous gland activity with age which appears to be even more important in women than in men[199] and probably linked to the level of circulating androgenous hormones[200]. The inner and outer difference in the subject is less marked and more difficult to observe. Still, we can say there is a tendency to reduced intensities in the TG regions of the spectra (650 to 800 Da) on the external side of the arm, along with an increase in the DG region of the spectra (450 to 650 Da).

There are still a lot of additional analyses to be conducted on this study, but the first exploratory results are really encouraging to show how deep the SpiderMass is able to look at variations in the skin lipid variations. A first level of analysis will be the differential tests of the internal and external zones as well as the age effect on the measures. Then a lot of more technical questions will be addressed to compare the modalities of sampling, and the differences between the LIL and TLS systems.

Chapter VI

Study of Skin Chronic Inflammatory Dermatosis by the SpiderMass

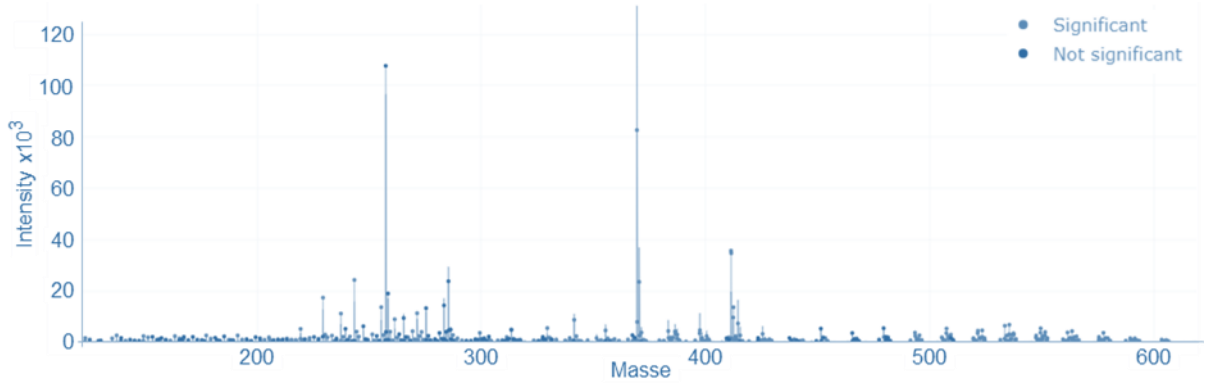

Log2(TIC) corrected, average mass spectrum on which is superimposed the significancy of each signal for the specific Acne RZ Vs LZ comparison.

Philippe Saudemont, Célia Ipinazar, Jérôme Filiol, Éric Cros, Éléonore Gravier, Amaury Alves, Aimée Simcic-Mori, Christophe Lauze, Thérèse Nocera, Alexia Brocario, Gwendal Josse & Isabelle Fournier

CHAPTER VI: Study of skin chronic inflammatory dermatosis by the SpiderMass

A. Introduction

As described in the state of the art, a high number of dermatosis have an inflammatory aspect but the ones described here are all chronic inflammatory dermatosis. They imply the dysregulation of several factors and amongst which, the lipids play a central role as immunomodulators.

This chapter is describing the results obtained from the main study of my PhD named "SMPatho" entitled: "Exploratory study, using real-time mass spectrometry to analyse the molecular profiles of the epidermis (particularly lipid profiles) of subjects with chronic inflammatory dermatosis versus control group" (declared on ClinicalTrial, n° NCT04472546). This study is conducted in the Toulouse PFDC Research Center by the Dr Thérèse Nocera principal investigator. It aims at characterising the molecular profiles obtained by the SpiderMass system on the main dermatosis investigated by Pierre Fabre Dermocosmetic. Indeed, the company is developing several dermatologic and cosmetic products to alleviates the symptoms of those pathologies and obtaining efficacy biomarkers that can be easily monitored when a specific product is applied is the final objective.

For this clinical trial, the subjects were divided into 5 groups: 1/ Acne of the face, 2/ Atopic Dermatitis of the upper limb, 3/ Vulgar plaque Psoriasis, 4/ Telangiectasic erythrocouperosis with papule of the face (rosacea), and 5/ Seborrheic Dermatitis of the scalp. Each group contains 2 subgroups, one is for the volunteers affected by the dermatosis and the other is for the associated control (**CTL**) subjects. It is to be noted that the inclusion for the rosacea was too much delayed due to the Covid-19 situation and is therefore not included in this thesis.

This is an exploratory study in which all the objectives have the same level of importance, they are define as follow:

- Characterise the molecular signals (particularly lipidic) of subjects with or without dermatosis
- Study the impact of several factors on the molecular profiles of the epidermis (in particular lipids) of healthy subjects or subjects with dermatosis: i) The dermatosis; ii) Topographical areas (lesion, peri-lesion and reference); iii) Gender, and iv) Age
- Study the molecular profiles of the epidermis (especially lipids) according to the method of sample collection (absorbent paper, *in vivo* and/or by scotch tape) and the measurements of the obtained signals (FTIR or SpiderMass)

- Evaluate biometrological parameters on the studied areas: i) Hydration; ii) Pathophysiological state of the skin barrier in subjects with atopic dermatitis of the upper limbs and the associated CTL subgroup; iii) Sebum levels in subjects with facial acne, erythrocouperosis telangiectasia with papule of the face and seborrheic dermatitis of the scalp and their associated CTL subgroups
- Obtain illustrative photographs of lesion and peri-lesion areas

We had planned to compare the 5 dermatoses by using their CTL groups as a normalising element but due to extensive technical problems and modifications in the analytical method for the acne and AD groups so this question won't be addressed.

B. Experimental procedure

1. Volunteer population profile

The study was carried out in compliance with the Declaration of Helsinki (1964) and its successive revisions, the Good Clinical Practices (EMA/CHMP/ICH/135/1995) and the current French regulations. The measures taken to protect the personal data and confidentiality are in accordance with the European Regulation 2016/679/EU of 27/04/2016 on the protection of individuals regarding the processing of personal data and the free movement of such data (GPDR). The protocol and associated documents (including the information and consent form) were submitted to the Nord-Ouest Persons Protection Committee before implementation. This clinical study was not started until the CPP had given a favourable opinion and the volunteers were given clear information about the study before deciding whether to participate.

As this is an exploratory study and in the absence of data from the literature, there is no rational basis for calculating the number of subjects. 22 subjects per subgroup were included in order to obtain 20 analysable subjects (assuming that the quality of the *in vivo* measurement is insufficient for 10% of the measurements). This number seems enough to show a difference between the dermatosis's subgroups and their associated CTL subgroup.

Each subgroup contained 22 subjects as well as their associated CTL leading to a maximum number of included subjects at 220 (currently, 4 dermatoses have been completed and 180 subjects recruited). The subjects of a subgroup and their CTL are recruited in parallel, have the same age range (as defined in the subgroup inclusion criteria) and had to be as gender-balanced as possible with a difference in male/female distribution allowed between the dermatosis subgroup and its associated CTL of ±3. In addition, the difference between the inclusion date of the first subject in each dermatosis subgroup and the inclusion of the first subject in the associated CTL subgroup could not exceed 2 weeks. This condition was also applicable for the inclusion of the last subject in each subgroup. The detailed eligibility criteria are presented in the **Appendices: SMPatho "Eligibility criteria**".

a) Acne and CTL subgroups

Details about the acne groups cohort is described in the **Table 9**. Majority of the subjects were women (72.73% in acne; 77.27% in CTL) with a median age of 22 years for the acne cohort and 27 years for the associated CTL cohort.

Table 9: General population description of the Acne and Associated CTL subgroups

	Acne n = 22	Acne associated CTL n = 22
DEMOGRAPHIC DATA		
Age, med (min - max)	22 (18 – 31)	27 (22 – 30)
Female, n (%)	16 (72.73)	17 (77.27)
Phototype:		
- I (always burns, never tans), n (%)	1 (4.5)	0 (0)
- II (usually burns, tans with difficulty), n (%)	3 (13.64)	4 (18.18)
- III (sometimes mild burn, gradually tans), n (%)	16 (72.73)	13 (59.09)
- IV (rarely burns, tans with ease), n (%)	2 (9.09)	5 (22.73)
CONTRACEPTION		
Women of childbearing potential, n (%)	16 (72.73)	17 (77.27)
Not applicable (male), n (%)	6 (27.27)	5 (22.73)
Contraceptive method		
- Hormonal or intrauterine, n (%)	10 (62.50)	11 (64.71)
- Other, n(%)	6 (37.50)	6 (35.29)
DERMATOSIS HISTORY		
Duration (year), med (min - max)	7 (3 – 18)	*NA*
Main locations		
- Forehead, n (%)	19 (86,36)	*NA*
- Cheek, n (%)	18 (81,82)	*NA*
- Chin, n (%)	8 (66,67)	*NA*
Global Acne Evaluation (GAE) score		
- Mild, n (%)	10 (45,45)	
- Moderate, n (%)	11 (50,00)	
- Severe, n (%)	1 (0,05)	

There is a significant 3.2 years difference (t-test, $p<0.001$) between the 2 subgroups mean age as visible in the **Figure 41**. But this age difference was evaluated as non-critical by the investigator as all the patients were recruited in the age range defined by the protocol and in this range, there is no difference in the acne aetiology or symptoms.

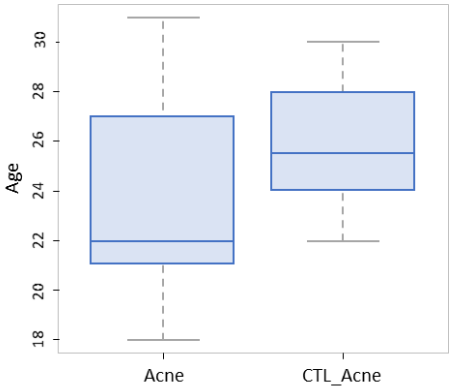

Figure 41: Boxplot representation of the age in the 2 acne subgroups showing the difference in their respective distributions.

According to Fitzpatrick's classification, a majority of the subjects had a type III phototype (72.73% Acne / 59.09% CTL). For the acne

volunteers, the median duration of the dermatosis was 7 years and it was located mainly on the forehead for 86.36% of subjects, the cheek (81.82%) and the chin (66.67%).

At inclusion, subjects had to have mild to severe facial acne, with a Global Acne Evaluation (**GAE**) score of 2 to 4 on a scale ranging from 0 (no lesion) to 5 (very severe). The score was "mild" for 10 subjects (45.45%), "moderate" for 11 subjects (50%) and "severe" for 1 subject (0.05%).

b) AD and CTL subgroups

This group population is detailed in the **Table 10**. Majority of the subjects were women (90.48% in AD; 77.27% in CTL) with a median age of 26 years for the AD cohort and 37.5 years for the associated CTL cohort which is significantly different (Analyse of Variance, **ANOVA**, p<0.0001) and illustrated in the **Figure 42**.

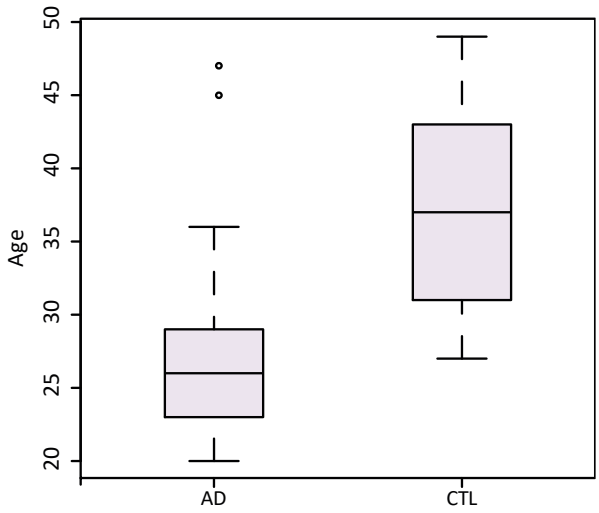

Figure 42 :Boxplot representation of the age in the 2 AD subgroups showing the difference in their respective distributions.

Table 10: General population description of the Atopic Dermatitis and Associated CTL subgroups

	Atopic Dermatitis n = 21	AD Associated CTL n = 22
DEMOGRAPHIC DATA		
Age, med (min – max)	26 (20 – 47)	37.50 (27 – 49)
Femme, n (%)	19 (90.48)	17 (77.27)
Phototype		
- II (usually burns, tans with difficulty), n (%)	4 (19.05)	2 (9.09)
- III (sometimes mild burn, gradually tans), n (%)	12 (57.14)	20 (90.91)
- IV (rarely burns, tans with ease), n (%)	5 (23.81)	0 (0)
CONTRACEPTION		
Women of childbearing potential, n (%)	18 (85.71)	17 (77.27)
Not applicable (male), n (%)	2 (9.52)	5 (22.73)
Contraceptive method		
- Hormonal or intrauterine, n (%)	11 (61.11)	9 (52.94)
- Other, n (%)	7 (38.89)	8 (47.06)
DERMATOSIS HISTORY		
Duration (year), med (min – max)	23 (1 – 47)	
Main locations		
- Scalp, n (%)	0 (0)	
- Forehead, n (%)	1 (4,76)	
- Cheek, n (%)	1 (4,76)	
- Forearm (external face), n (%)	14 (66,67)	
- Forearm (internal face), n (%)	21 (100)	
- Elbow crease, n (%)	21 (100)	
- Elbow, n (%)	2 (9,52)	
Global SCORAD, med (min – max)	28.70 (17.2 – 38.9)	
- Extent (% of affected skin), med (min - max)	5.20 (1 – 12)	
- Intensity of the clinical signs, med (min - max)	6 (3 – 9)	
- Sum of the subjective signs, med (min - max)	6.30 (1.50 – 13.20)	

The severity of AD is evaluated using the international SCORing of AD index (**SCORAD**) developed by the European Task Force on Atopic Dermatitis[201]. The extent of the dermatosis is graded between 0 and 100% depending on the affected surface of the body. The intensity of the SCORAD index consists of six items: erythema, oedema/papulation, excoriations, lichenification, oozing/crusts and dryness. Each item is graded on a 0 to 3 scale (absent, light, moderate and severe). The subjective items include pruritus and sleeplessness and are graded on a 10 cm visual analogue scale by the volunteer. The SCORAD index formula is: A/5 + 7B/2 + C. In this formula A is defined as the extent (0-100), B is defined as the intensity (0-18) and C is defined as the subjective symptoms (0-20). The maximum possible SCORAD score is 103 and, in our case, the mean value was at 28.7 with a minimal value at 17.2 and a maximal value at 38.9. As a reminder, the eligibility criteria were set between 15 and 40 (See appendices SMPatho study, **Eligibility criteria**).

In this group, 1 subject from the AD subgroup was removed from the cohort (p41) as it's averaged TIC was under 3.10^4 a.u. which is considered too low to obtain good quality spectra.

c) Psoriasis and CTL subgroups

The general population description of the Psoriasis and Associated CTL subgroups is detailed in the **Table 11**. In each subgroup, the male/female distribution was similar and evenly distributed (54.55% female in the Pso group and 50% in the CTL). The median age was 38 years for the Pso cohort and 44 years for the CTL. Moreover, according to Fitzpatrick's classification, the majority of subjects had a phototype III (77.27% Pso; 81.82% CTL). Finally, the median duration of the psoriasis was 20 years. At inclusion, it was mainly located on the elbow (86.36%) and the outer surface of the forearm (68.18%). The Investigator Global Assessment (**IGA**) is scored by the investigator on a scale from 0 (clear) to 5 (very severe). Around half of the Pso volunteers showed a Mild IGA score (54.55%) and the other half a moderate score (45.45%).

Table 11: General population description of the Psoriasis and Associated CTL subgroups

	Psoriais n = 22	Pso Associated CTL n = 22
DEMOGRAPHIC DATA		
Age, med (min – max)	38 (24 – 53)	44 (20 – 53)
Femme, n (%)	12 (54,55)	11 (50)
Phototype		
- II (usually burns, tans with difficulty), n (%)	3 (13.64)	3 (13.64)
- III (sometimes mild burn, gradually tans), n (%)	17 (77.27)	18 (81.82)
- IV (rarely burns, tans with ease), n (%)	2 (9.09)	1 (4.55)
CONTRACEPTION		
Women of childbearing potential, n (%)	10 (45.45)	9 (40.91)
Not applicable (male), n (%)	12 (54.55)	13 (59.09)
Contraceptive method		
- Hormonal or intrauterine, n (%)	2 (20)	4 (44.44)
- Surgical	0 (0)	2 (22.22)
- Other, n (%)	8 (80)	3 (33.33)
DERMATOSIS HISTORY		
Duration (year), med (min – max)	20 (4 – 45)	
Main locations		
- Forearm (external face), n (%)	15(68.18)	
- Elbow, n (%)	19 (86.36)	
Investigator Global Assessment (IGA)		
- Mild, n (%)	12 (54.55)	
- Moderate, n (%)	10 (45.45)	

d) SD and CTL subgroups

The general population description of the SD and associated CTL subgroups are described in the **Table 12**. Most of the subjects were women (77.27% both in the SD and CTL), with a mean age of 30.5 years for the SD and 35 years for the CTL cohort. According to Fitzpatrick's classification, the majority of the subjects had a phototype III (72.73% SD; 86.36% CTL). In the SD, the mean duration of the dermatosis was 10 years. For all subjects, it was located on the scalp, but a minority also had it on the forehead (18.18%) and cheek (9.09%). At inclusion, subjects had to have mild to moderate SD, with an IGA score of 2 to 3 on a rating scale ranging from 0 (absent) to 5 (severe). The IGA score was "mild" for 10 subjects (45.45%) and "moderate" for 12 subjects (54.55%)

Table 12: General population description of the Seborrheic Dermatitis and Associated CTL subgroups

	Seborrheic dermatitis n = 22	SD Associated CTL n = 22
DEMOGRAPHIC DATA		
Age, med (min – max)	30,5 (20 – 44)	35 (24 – 44)
Femme, n (%)	17 (77.27)	17 (77.27)
Phototype		
- II (usually burns, tans with difficulty), n (%)	6 (27.27)	3 (13.64)
- III (sometimes mild burn, gradually tans), n (%)	16 (72.73)	19 (86.36)
CONTRACEPTION		
Women of childbearing potential, n (%)	17 (77.27)	17 (77.27)
Not applicable (male), n (%)	5 (22.73)	5 (22.73)
Contraceptive method		
- Hormonal or intrauterine, n (%)	7 (41.18)	11 (64.71)
- Other, n (%)	10 (58.82)	6 (35.29)
DERMATOSIS HISTORY		
Duration (year), med (min – max)	10 (0 – 30)	
Main locations		
- Scalp, n (%)	22 (100)	
- Forehead, n (%)	4 (18.18)	
- Cheeks	2 (9.09)	
Investigator Global Assessment (IGA)		
- Mild, n (%)	10 (45.45)	
- Moderate, n (%)	12 (54.55)	

2. Sample collection and measurements

Along with the SpiderMass measurements, D-squams and sebum sampling by absorbent paper were performed. In this study 3 zones were studied: on the dermatosis affected area a lesion zone (named **LZ**), a peri-lesion (**PLZ**) just beside and a reference zone (**RZ**) located on the inner side of the forearm for all the

subjects. For the CTL group, there is only the lesion and reference zones. Biometrological measurements were added depending on the groups and when pertinent: Lipid index measurement on the face, HI on dry areas of the limbs and TEWL for AD. A summary of the site of collection and measurements depending on the groups are displayed in **Table 13**. The text in red indicates the lesion and peri-lesion locations while the text in green correspond to the reference zone.

Table 13: Description of the site of collection and measurements depending on the groups. The text in Red correspond to the lesion and peri-lesion while the text in Green correspond to the Reference zone

	IL Sebumeter®	Absorbent paper	IH Corneometer®	TEWL Aquaflux®	D-Squam	*In vivo* SpiderMass
Acne + Associated CTL	Face	Face			Face Forearm (internal face)	
Atopic Dermatitis + Associated CTL			Upper limb (except hands)	Upper limb (except hands)	Upper limb (except hands) Forearm (internal face)	
Erythrocouperosis + Associated CTL	Face	Face			Face Forearm (internal face)	
Psoriasis + Associated CTL					Upper / lower limb (except hands / feet) Forearm (internal face)	
Seborrheic Dermatitis + Associated CTL	Scalp	Scalp			Scalp Forearm (internal face)	

The classical unrolling of a visit was always the same and is presented in the **Table 14**. After discussing the protocol and the consent form, the visit starts by the taking photographs, then the SpiderMass *in vivo* measurements were conducted before taking the biometrological indicators and the samples (D-squams or absorbent paper).

Table 14: Course of a visit listing the different measures and samplings to be done and their orders depending on the groups

Acne + Associated CTL	Atopic Dermatitis + Associated CTL	Erythrocouperosis + Associated CTL	Psoriasis + Associated CTL	Seborrheic Dermatitis + Associated CTL
1. Photographs 2. *In vivo* 3. LI 4. Absorbent paper 5. D-Squams	1. Photographs 2. *In vivo* 3. HI 4. TEWL 5. D-Squams	1. Photographs 2. *In vivo* 3. LI 4. Absorbent paper 5. D-Squams	1. Photographs 2. *In vivo* 3. D-Squams	1. Photographs 2. *In vivo* 3. LI 4. Absorbent paper 5. D-Squams

For all the sampling and measures please refer to the according paragraph in the **Chapter V: Study Design**.

.

a) Trans Epidermal Water Loss measurement

The TEWL was measured using an Aquaflux™ (Biox Systems Ltd.) and represent the condition of the skin barrier function. It is assessed by measuring the passive diffusion of body water vapor through the SC. The evaporation flux is measured by a relative humidity and temperature sensor placed between the skin surface and a cooling plate (-7.6°C) that forms the Aquaflux™ condenser-chamber. The more altered the skin, the higher the TEWL value is. For healthy forearms skin in adults, the usual TEWL is around 10-15 g/m²/h. The Aquaflux™ is controlled by an internal software used in the PFRC that help conducting the calibration and the measures. For the latter, the probe just needs to be held in place on the skin and the button pressed. Then after the flux stabilisation, the TEWL value is displayed.

3. Data analysis

a) Biometrological criteria:

The expression of the biometrological variables have been described in the form of tables showing the number of people, the mean, the standard deviation, the median, the CI95%, and the minimum and maximum. The comparison between the dermatosis subgroup and its CTL subgroup were done using an ANOVA with the zone (if relevant) and subgroup factors as fixed effects. If relevant, the gender can be added as a fixed effect.

b) Biological criteria:

After the pre-processing and exploratory analysis stages, the analyses of variance were performed to compare the intensity of each peak between:

- **The dermatosis subgroup and its associated CTL on *in vivo* data**. The subgroup variable (dermatosis/CTL) was included as a fixed effect.
- **The three zones**. The zone variable (lesion / peri-lesion / reference) was included as fixed effect. The subject variable was included as random effect. The 2-by-2 comparisons of the three zones was carried out by tests on the differences of the adjusted means.
- **The five dermatoses.** The dermatosis variable (acne / atopic dermatitis / psoriasis / erythrocouperosis telangiectasia with papule of the face / seborrheic dermatitis) was included as fixed effect. The 2-by-2 comparisons of the five dermatoses was carried out by tests on the differences of the adjusted means.
- **The five CTL subgroups.** The CTL subgroup variable (acne / atopic dermatitis / psoriasis / erythrocouperosis telangiectasia with papule of the face / seborrheic dermatitis) was included as fixed effect. The 2-by-2 comparisons of the five CTL was carried out by tests on the differences of the adjusted means.
- **With age, gender and age*sex interaction**.

- **The dermatosis subgroup and its associated CTL**. The subgroup variable (dermatosis / CTL) was included as a fixed effect.
    - Only on absorbent paper data and independently on acne, erythrocouperosis telangiectasia with papule of the face, and seborrheic dermatitis.
    - On the scotch data for the five dermatosis subgroups and their associated CTL. Based on the analyses of the *in vivo* data, further analyses can be performed to identify molecules of defined mass.

For all the above analyses, a Benjamini and Hochberg multiple test correction was performed on the p-values of all peaks. In all these comparisons, if relevant, the site variables (the "lesion" zone, can be on different site depending on the dermatosis) HI, LI, TEWL, age, gender, batch (e.g. mass spectrometer run) have shown an effect on lipidomic profiles in the above exploratory analyses, they were included as fixed effects in addition to the variables listed above.

C. Results

The 2 main questions to be answered are the following:

- Is there any difference between the LZ from the dermatosis subgroup and the associated LZ from the associated CTL subgroup?
- Are there any differences between the LZ/PLZ/RZ in the dermatosis and in the CTL subgroups?

1. Acne

Following the designed statistical procedure, a first round of data quality result was generated right after the pre-processing. These allowed to observe several biases in our dataset that were expected because of the experimental variations. Indeed, on the 107 acquisitions of this group 102 were generated with a first developed movement scheme of the laser characterised by a stop in-between each ablation spots. This method was evaluated during the recruitment of this first group as less effective than a continuous laser movement. We had planned to finish the whole group using the same method but unfortunately it has not been the case and 5 measures were realised with the new laser movement. Moreover, at the beginning of this first group, we were using a 3.5m long 600 µm core diameter fibre ("LVF-600-3.5-a"), which broke and was replaced with a 1 m long 600µm core fibre ("LVF-600-1-a") we had in stock, while waiting for new fibres from the manufacturer. It could only provide us with 400 µm core diameter fibres, that we took in 4m long as well.

In the following paragraphs, I exemplify the classical strategy that we use to evaluate the impact of such parameters on our measurements. **Figure 43** shows the relation between the fibre reference, TIC and Fluence. Here the fluence is approximated by dividing the measured energy at the output of the fibre by the core diameter of the fibre itself. This is a good approximation of the real fluence values which would need to

be calculated by dividing the energy by the actual ablation spot size on the volunteer which could not be measured during the study.

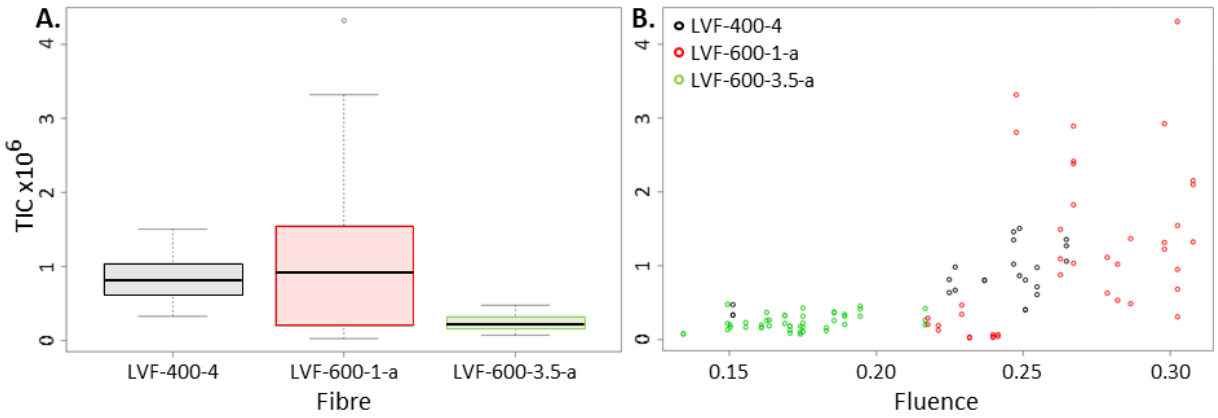

Figure 43: TIC and Fluence representation effect of the fibre reference. **A.** Boxplot depicting the TIC distribution according to the fibre reference. **B.** Plot showing the relation between the TIC and the Fluence coloured by fibre. The LVF-600-3.5-a shows the more limited distribution but also the smallest fluence and TIC values. The LVF-600-1-a is the one allowing to get the highest Fluence values but is also the one with the most scattered TICs.

In the panel **A.** a boxplot shows the TIC distribution according to the fibre reference and in panel **B.** is a plot showing the relation between the TIC and the Fluence coloured by the fibre. This shows that the LVF-600-3.5-a have a more limited distribution but on the other hand the smallest fluence and TIC values. The LVF-600-1-a is the one allowing to obtain the highest fluence values but has the most scattered TIC. This can be explained by the difficulty to correctly position the volunteer under the moving arm of the laser with a so small length fibre.

This is even more obvious when looking at the heatmap presented in **Figure 44** which shows the Ward-Pearson Hierarchical Clustering of the 100 peaks showing the highest Inter-Quartile Range (**IQR**) in which we coloured the subjects with their respective fibre. There are 2 clear groups separating the masses: the group 1 gather the *m/z* > 440 Da which means intensities are low with the LVF-600-3.5-a fibre and the group 2, with the masses < 440 Da. After normalisation the lower fluences leads to higher intensities in the higher m/z range indicating that the lowest laser energies lead to lower intensities of the higher masses in the raw spectra.

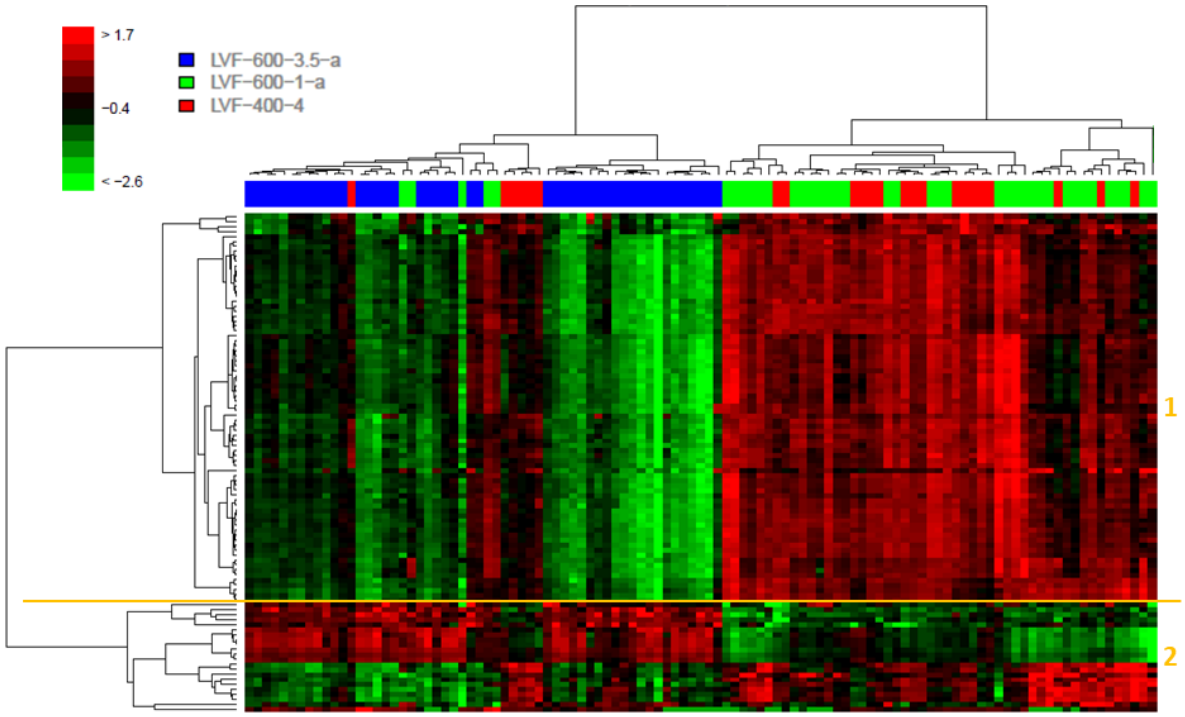

Figure 44: Heatmap of the 100 highest IQR masses coloured by the fibre showing a clear distinction between the subjects grouped by the fibre. There are 2 mains groups separating the masses: the group 1 gather the *m/z* > 440 Da which present mainly lower intensities with the LVF-600-3.5-a fibre and the group 2, with the *m/z* < 440 Da.

As the TICs are low by the conjugation of the fibre and the point-by-point movement method of the probe, this dataset is the one showing the lowest intensities. On the average spectra we can observe the classical *in vivo* profile and huge variation in intensities which is an indicator of important variability, amplified by the TIC normalisation. The low intensities in this dataset have the effect to remove a high number of 428 signals out of 14800 bins after pre-processing and filtering (non-Log2 intensities <500 a.u. are filtered out). The PCA analysis shown in **Figure 45** confirms the effect of the instrumental parameters on the measures. In the panel **A.** The PCA is coloured by the fibre showing the principal source of variability in the dataset and a clear separation between the LVF-600-3.5-a and the two others. In panel **B.** the PCA is coloured by the zones showing the difference between the face and the arm is the second principal source of variability. In the panel **C.** the PCA is coloured by the groups, showing no clear distinction between the Acne LZ and the CTL associated LZ.

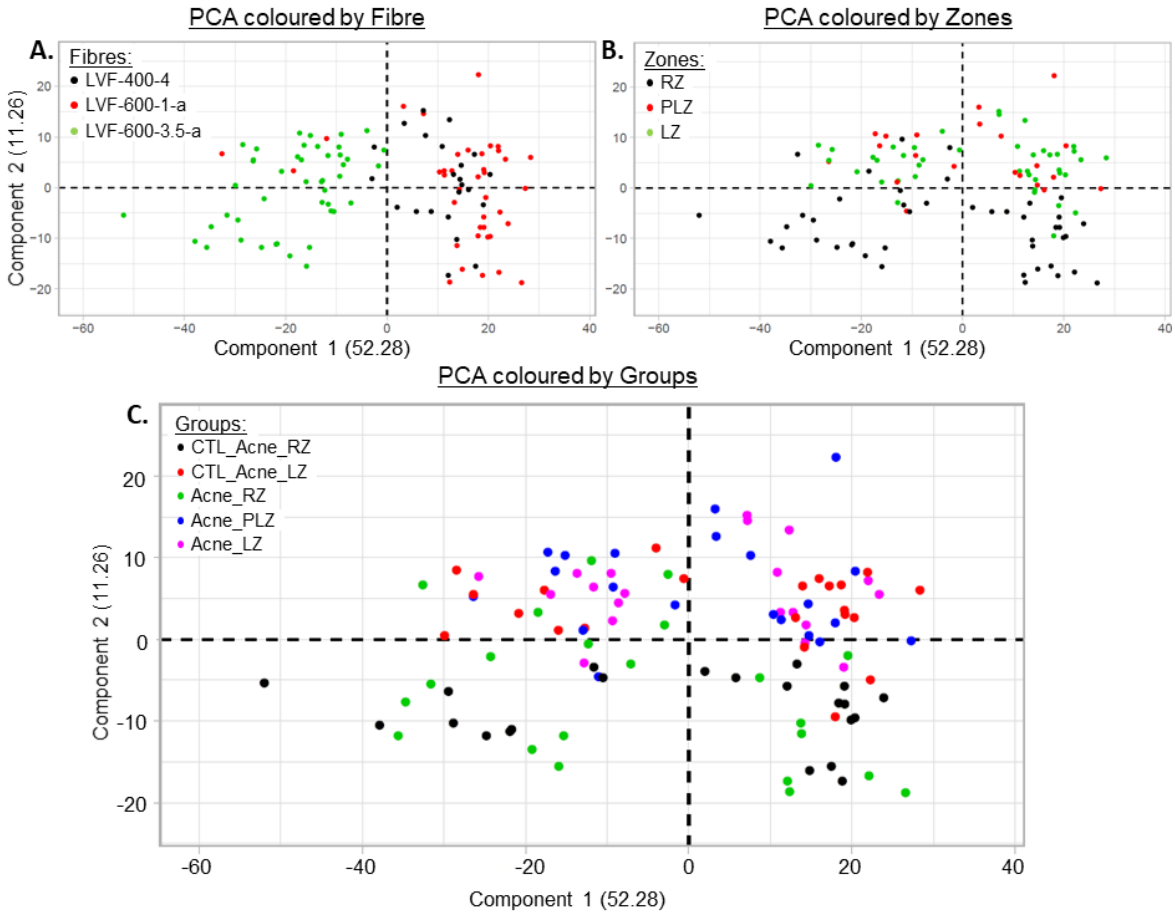

Figure 45: PCA representation of the acne *in vivo* dataset. **A.** PCA coloured by the fibre showing the principal source of variability in the dataset and a clear separation between the LVF-600-3.5-a and the two others. **B.** PCA coloured by the zones showing the difference between the face and the arm is the second principal source of variability. **C.** PCA coloured by the groups showing no clear distinction between the Acne LZ and the CTL associated LZ.

Based on this first round of results showing strong experimental effects, it was decided to first adjust the linear models on the Log2(TIC)[n] as it is quite of an end-result influenced by all the experimental factors. We have tested to adjust as well on the laser fibre, or on both at the same time. The differential analysis was not able to show any differences between the LZ in the dermatosis and CTL subgroup nor between the LZ and PLZ on the Acne volunteers. Thus, we tried to adjust the model on the TIC but without normalising the data to evaluate and limit the artificial effect of increasing the intensities of the smallest masses and *vice versa*.

The distribution of the biometrical measurements (LI and FFA/TG ratios) planned on this group are presented in **Figure 46**. For botch LI and FFA/TG ratio, the variation between the subgroups was evaluated as not significant respectively by the Pooled t-test on the IL data and the Welch-Satterthwaite test for the FFA/TG data.

[n] During the pre-processing, the intensities are Log2 transformed to comply with the normal distribution hypothesis needed for several statistical tests used hereafter. Correcting by the Log2(TIC) is needed to keep a linear relationship with the Log2 of the intensities.

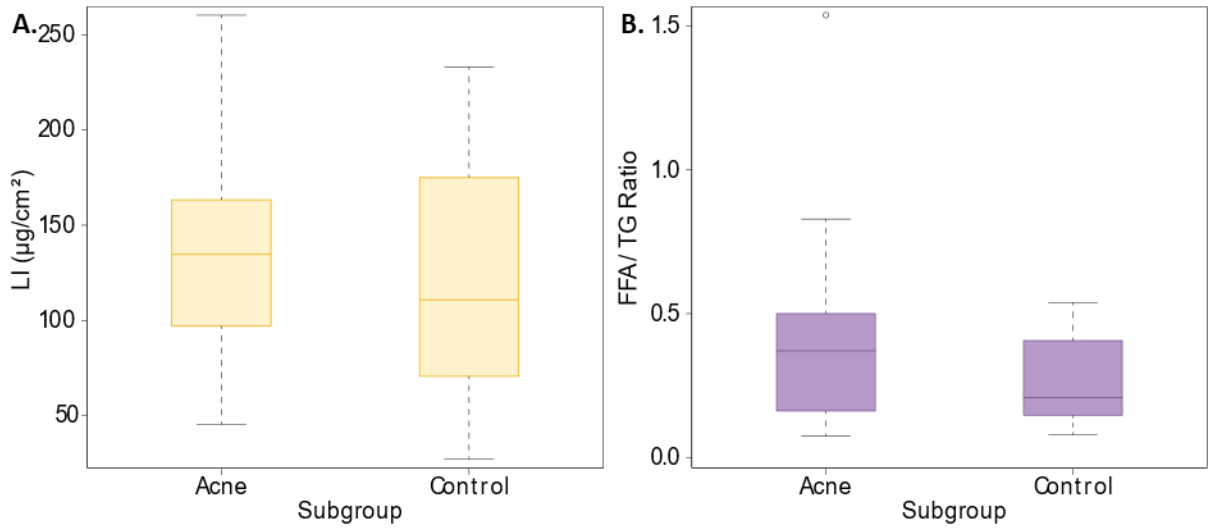

Figure 46: Boxplot representation of the LI and FFA/TG measurements in the acne group. **A.** boxplot of the LI in the 2 subgroups showing no significant differences **B.** FFA/TG ratio in the 2 subgroups showing no significant differences.

Finally, we noticed that the FFA/TG ratio between the acne and CTL subgroup was not significant which means we had CTL subjects with an acneous like FFA/TG Ratio and acne subjects with a non acneous ratio. In a complementary analysis, we decided to limit the number of volunteers in each group to keep only the 15 highest ratio of the acne subgroup and the 15 lowest ratios on the normal group, but this strategy did not give better results. The only comparison in which we were able to see significant peaks is the one comparing the LZ and the RZ in both subgroups. A summary of the number of significant peaks obtained in the different adjustments are presented in the **Table 15**.

Table 15: Summary of the number of significant comparisons for each analysis detailed by the type of adjustment. LZ= Lesion zone, PLZ= Peri-Lesion Zone and RZ = Reference zone.

	TIC	TIC + Fibre	Fibre	No normalisation	FTIR driven selection
Acne Vs CTL: LZ	0	0	0	0	0
Acne Vs CTL: RZ	0	0	0	0	0
Acne: LZ Vs RZ	270	269	264	280	263
Acne: LZ Vs PLZ	0	0	0	0	0
Acne: PLZ Vs RZ	274	271	273	274	275
CTL: LZ Vs RZ	269	265	258	265	225

To exemplify one of the differential analyses, I have chosen the comparison between the RZ and the "LZ" of the CTL subgroup adjusted by the Log2(TIC). This comparison gives 269 significant peaks among which are 178 under-expressed and 91 over-expressed signals on the LZ. This comparison allows to observe the difference more precisely between forearm and forehead. To filter-out the signals of interest, we use the selection criteria described in the **Table 16.**

Table 16: Selection criteria to filter out the most significant peaks from the raw tables obtained during the differential analyses.

Parameter	Value
Non Log2 Average Intensity	>1000 a.u.
Adjusted p-value	<0.05
Absolute Fold Change (FCabs)	>1.5
Bin reduction	Keep the highest intensity peak on several following bins[o]
Isotopic reduction	Keep the monoisotopic peak when several 1 Da spaced peaks are significant[p]

This resulted in 45 peaks that are displayed in the **Table 17**: 13 are under expressed and 32 are overexpressed on the forehead. Amongst the peaks that are overexpressed on the forehead we can observe at least 12 peaks tentatively assigned to DGs which are a sign of a more intense bacterial lipasic activity on the oily skin of the face. It is to be noted that due to the low peaks intensities above the m/z value 600, no masses are found significant in this result.

Table 17: Selected significant peaks in the LZ Vs RZ comparison in the CTL subgroup with tentative assignments. The peaks are ordered by increasing FC value. *m/z* = observed binned *m/z* value. AveExpr = Average Expression. p.value.adj = adjusted p-value, FC = Fold Change. NA = "Not assigned", the assignment is undergoing.

m/z	AveExpr	p.value.adj	FC	Tentative assignment
397.45	7177	1.8E-08	-2.4	Ergosterol / VitD2 / FA 26:0 (++) / WE 26:0 (++)
414.45	10914	6.1E-06	-2.4	NH4+ Adduct of FA/WE 26:0 ??
383.35	6117	7.5E-07	-2.1	NA
351.35	2149	6.0E-06	-2.0	NA
425.45	4440	3.5E-07	-2.0	NA
400.45	3195	1.0E-05	-2.0	NA
428.45	1429	1.0E-05	-1.9	NA
387.35	3907	2.0E-05	-1.9	NA
333.35	1270	6.4E-06	-1.7	NA
386.45	4179	1.8E-04	-1.7	NA
369.35	104173	3.3E-04	-1.6	FA 24:0 / MG 20:0 / Chole (++)
385.35	2107	3.8E-04	-1.6	NA
439.45	1315	1.4E-05	-1.6	NA
177.15	2157	1.2E-05	1.5	NA
493.45	2922	2.3E-03	1.5	WE 33:1 ?
233.25	2091	1.7E-06	1.5	FA 13:1;O ?
505.45	1494	7.8E-05	1.5	WE 34:0

[o] When binning, it is not rare that a gaussian peak on the profile mode is separated into adjacent bins, even with adapted binning size. Keeping only the more intense bin when several are following is done to keep only the one corresponding to the apex of the signal.

[p] If we take 3 successive peaks, and the signal in the middle is less intense than its two neighbours, there is a high chance it is the +1 Da isotope of the first peak, and then it can be filtered out. Specifically, when dealing with lipids, peaks separated from 2 Da are usually characterised by the addition of one insaturation on the lower mass signal which means we cannot filter out the +2 Da isotope from 3 successive peaks.

m/z	AveExpr	p.value.adj	FC	Tentative assignment
495.45	2075	3.5E-03	1.5	DG 28:0
507.45	2766	2.0E-04	1.6	WE 34:1
191.15	2112	2.7E-05	1.6	NA
219.25	4155	1.5E-04	1.6	Squalene degradation fragment ? WE 15:3-H2O ?
329.25	1125	2.0E-04	1.6	FA 20:0;O
243.25	19552	1.3E-03	1.6	NA
255.25	10831	1.8E-03	1.7	FA 16:1
535.55	5116	5.9E-05	1.7	WE 36:1
231.25	1470	7.3E-05	1.7	FA 13:0;O
521.55	3373	1.2E-05	1.7	WE 35:1 ?
237.25	8853	1.6E-03	1.7	FA 16:1 -H2O
273.25	3080	7.9E-07	1.7	NA
411.45	25795	5.5E-05	1.8	Lanosterol / FA 27:0 / DihydroLanoesterol / Squalene (++)
519.55	1120	1.7E-05	1.8	NA
261.25	6767	1.2E-05	1.8	NA
533.55	4471	2.0E-06	2.0	WE 36:2 ?
579.55	1035	4.3E-05	2.1	DG 34:0 ?
561.55	2546	3.6E-06	2.1	DG 38:2 ?
509.45	1969	1.5E-05	2.1	DG 29:0
563.55	2893	1.0E-05	2.1	DG 38:1
549.55	3603	5.5E-06	2.1	DG 32:1
547.55	1715	3.1E-06	2.1	DG 32:2 ?
565.55	1471	8.9E-06	2.2	DG 38:0 ?
523.45	2972	1.9E-05	2.3	DG 29:2 ?
551.55	2536	1.2E-05	2.3	DG O-32:2
577.55	2330	1.0E-05	2.3	DG 34:1
575.55	1283	4.7E-06	2.3	DG 34:2 ?
537.45	2098	5.5E-06	2.5	FAHFA 34:2;O

The boxplot of the 8 most significant peaks showing either the 4 lowest (397.45, 425.45, 383.35, and 351.35) or the 4 highest FC values (273.25, 233.25, 533.55, 547.55) were selected and are displayed along with the *m/z* 411.45 in **Appendix I.D.2 - Acne supplementary results.**

Based on these results, we generated an average mass spectrum (adjusted by the Log2(TIC)) on which we superimposed the significancy of each comparison for the specific question. The spectrum obtained from the LZ Vs RZ comparison in CTL subgroup subjects is shown in **Figure 47.**

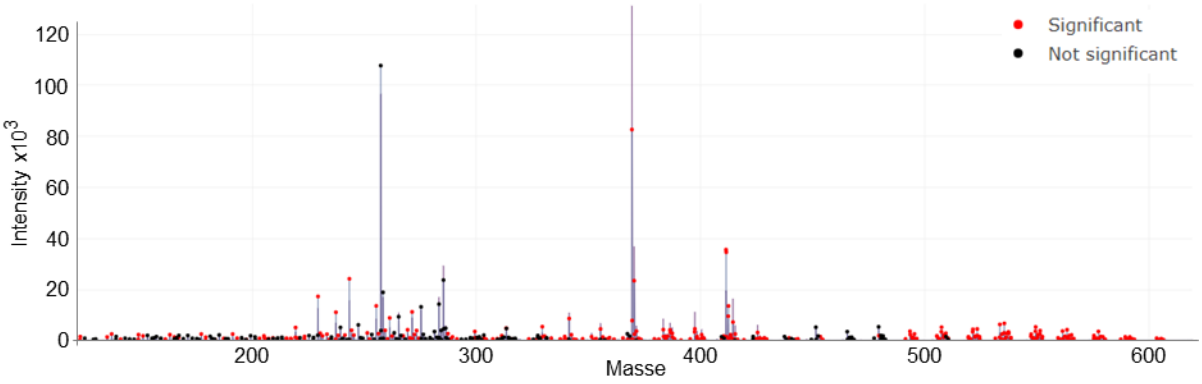

Figure 47: Log2(TIC) corrected, average mass spectrum on which is superimposed the significancy of each signal for the specific Acne RZ Vs LZ comparison.

This type of plot enables the immediate visualisation of the spectral ranges showing the significant variations between two conditions and many signals are found to contribute to the non-similarities between the forearm and forehead skin. The use of Venn diagrams to show the robustness of the results in the LZ vs RZ comparison in both Acne and CTL subgroups and are shown in **Figure 48**. Around 80% of the results are similar between the subgroups on the same question with only 28 (19+9) masses are not common between the CTL and the Acne.

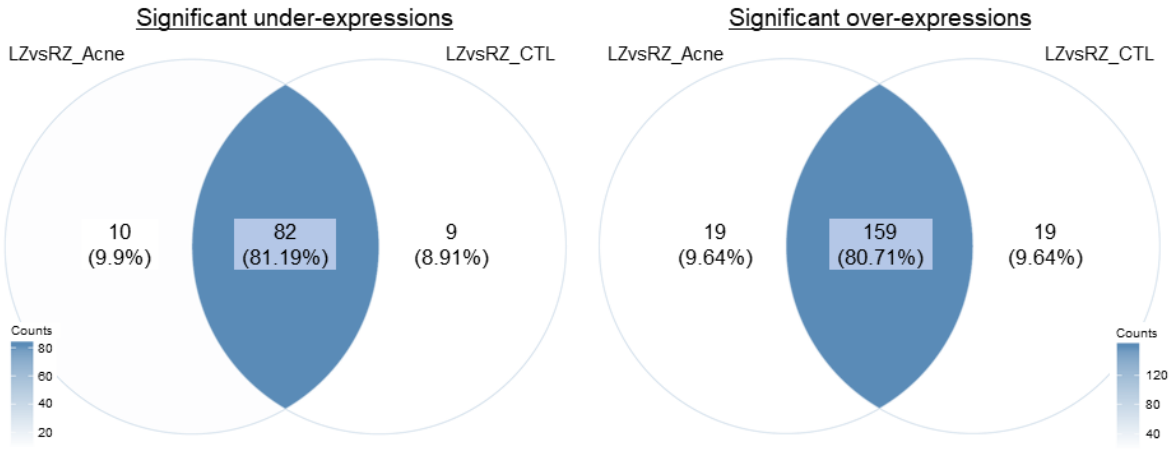

Figure 48: Venn diagrams showing the robustness of the results in the LZ vs RZ comparison in both Acne and CTL subgroups. Around 80% of the results are similar between the groups on the same question.

The analysis on the absorbent papers have shown no results which is attributed to the important variations that occurred in the experimental factors.

2. Atopic dermatitis

The biometrological measurements used to characterise to subject's skin state are consistent to what was expected. Indeed, the boxplots presented in **Figure 49** shows the significant differences in the HI and the TEWL between the two subgroups.

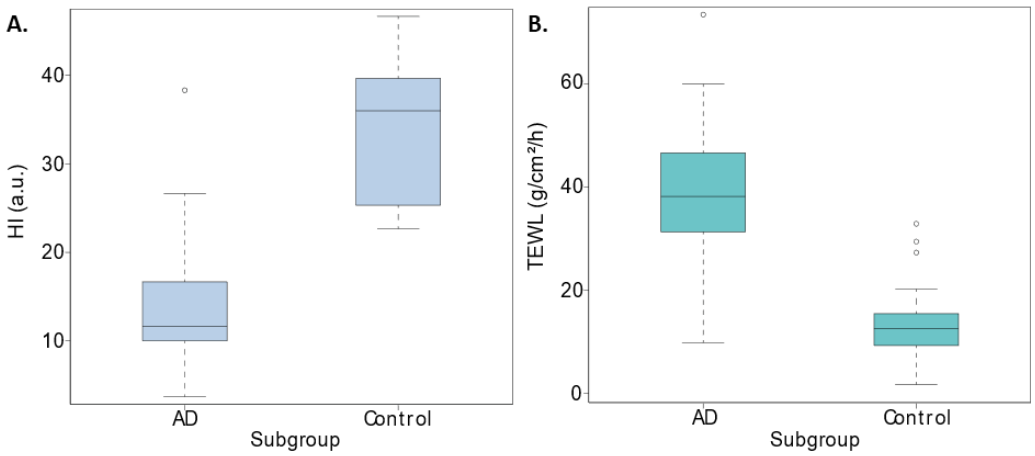

Figure 49: Boxplot representation of the HI and TEWL measurements in the AD group. **A.** Boxplot of the HI in the 2 subgroups showing a significantly higher HI in the control subgroup **B.** Boxplot of the TEWL in the 2 subgroups showing a significantly lower TEWL in the control subgroup.

In the panel **A.** the boxplot of the HI allows to distinguish the differences in its distribution between the two subgroups. The average value of the AD volunteers is 14.27 vs 33.58 a.u. for the CTL subjects which is significantly lower (ANOVA, p-value <0.0001), indicating a drier skin in the AD subgroup. It is to be noted that most of the subjects have a very dry skin (HI<35) which is normal for measures on the arm known to be dry areas. The panel **B.** shows that the average TEWL is 14.23 for the CTL and 38.70 g/m²/h for the AD subjects which is significantly higher (ANOVA, p-value <0.0001), confirming the skin barrier function is altered in the AD subjects.

During the data pre-processing, we filtered the masses whose average intensity (on non-Log2 data) was <500 a.u. Thus, a total of 838 signals were kept. This increased number compared to the acne analysis (with the same intensity threshold) is indicating higher averaged intensities in this dataset. At the data quality step, some graphs pointed out 2 mains sources of variability which are visible in the **Figure 50**.

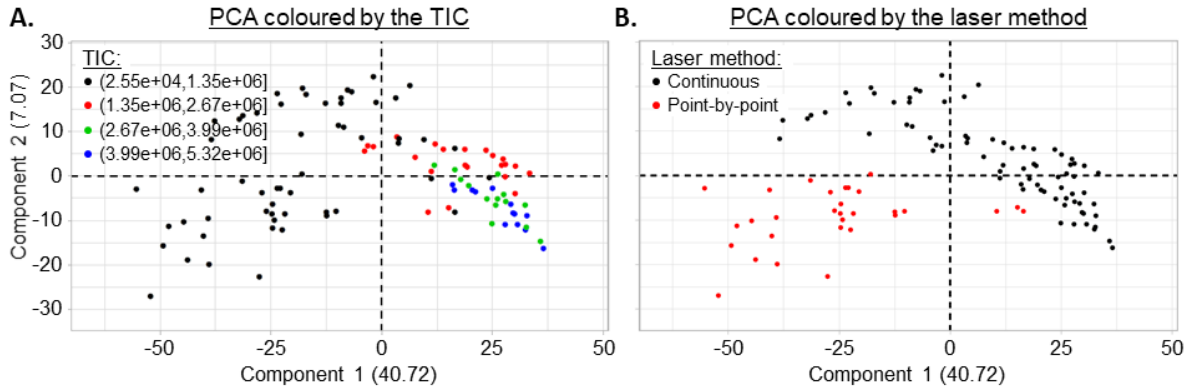

Figure 50: PCA 2D representation of the AD *in vivo* dataset. **A.** PCA coloured by the average TIC which seems to be the principal source of variability. **B.** PCA coloured by the laser method showing this is the second source of variability in the dataset

Indeed, the panel **A.** shows that there is an important effect of the TIC on the first dimension of the PCA, and the panel **B.** shows an effect of the laser method as the second source of variability in this dataset.

Even if the data is normalised by the TIC, this step is not powerful enough to erase the TIC linked variations in the MS spectra. This can be explained by looking at the average spectra and the dendrograms (data not shown) which shows that the more the TIC increase and the more masses above 600 Da are intense[q]. Regarding the laser method, it is to be noted that the AD group was recruited partially at the same time than the acne one so common biases can be found in this dataset such like the laser movement method. Here we have more acquisitions generated with the old "point-by-point" method which increase the effect of the difference between the two methods contrarily to the acne group for which the method had little to no impact.

The difference between the LZ of the AD and CTL volunteers are better observable if we keep only the 42 LZ related acquisitions. Doing so a new PCA was generated with points coloured by the subgroup as shown in the **Figure 51**.

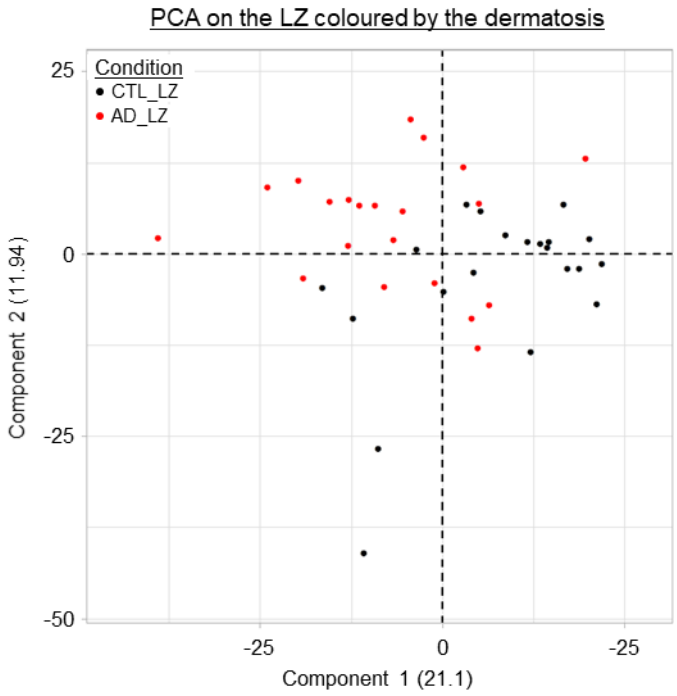

Figure 51: PCA 2D representation of the LZ subset coloured by the subgroup. A separation between the AD and CTL LZ can be seen on the first dimension

The **Figure 51** shows that the main source of variability is induced by the subgroup as it is on the first PCA dimension.

The exploratory analyses conclusions led us to conduct the differential analysis with a Log2(TIC) and a laser method correction. As mentioned in the experimental procedure of this chapter, the age difference is important in this group. Thus, for each question implying the two subgroups, the impact of the age was studied. When comparing the LZ / PLZ and RZ between the AD and CTL subjects, we obtained respectively 3%, 2% and 11% of the masses showing an intensity significantly impacted by the age (data not shown). When more than 5% of the *m/z* showed a significant link between the intensity and age, the analyses were adjusted by the age factor[r]. It means that only the RZ comparison between AD and CTL were adjusted by the age.

[q] This led us to use the ratio between the m/z intensities above 600 and all the intensities of the spectrum as a quality indicator (data not shown).

[r] We choose a 5% threshold because in a context of multiple testing like here, if a significance level of 5% is chosen, it means 5% of the tests are accepted to be false positives.

Following these differential analyses, we noticed that a specific acquisition from p51 showed an outlier's response for many signals, with intensity values being artificially put to 0 during the pre-processing[s]. This sample has been removed and a second round of analysis has been conducted, summarised in the **Table 18** hereafter.

Table 18: Summary of the significant peaks obtained in each comparison for the AD group. "AD_LZvsRZ" is the comparison between the LZ and RZ inside of the AD subgroup. "AD_PLZvsRZ" is the comparison between the PLZ and RZ inside of the AD subgroup. "AD_LZvsPLZ" is the comparison between the LZ and PLZ inside of the AD subgroup. "CTL_LZvsRZ" is the comparison between the LZ and RZ inside of the CTL subgroup. "LZ_ADvsCTL" is the comparison of the LZ between the two subgroups. "RZ_ADvsCTL" is the comparison of the RZ between the two subgroups and "PLZ_ADvsLZ_CTL" is the comparison of the PLZ of the AD subject and the LZ of the CTL subjects. The "Raw" columns correspond to all the obtained significant signals, the underexpressed signals are in the "-" column and the overexpressed are in the "+" column. The "Filtered" columns correspond to the peak selection described earlier in the **Table 16**.

	Raw			Filtered		
	-	+	Total	-	+	Total
AD_LZvsRZ	122	152	**274**	15	14	**29**
AD_PLZvsRZ	15	82	**97**	0	1	**1**
AD_LZvsPLZ	86	35	**121**	0	1	**1**
CTL_LZvsRZ	63	50	**113**	1	2	**3**
LZ_ADvsCTL	170	62	**232**	25	36	**61**
RZ_ADvsCTL	0	0	**0**	0	0	**0**
PLZ_ADvsLZ_CTL	52	8	**60**	28	2	**30**

The "Raw" columns correspond to all the obtained significant signals, the underexpressed signals are in the "-" column and the overexpressed are in the "+" column. The "Filtered" columns correspond to the peak selection described earlier in **Table 16**. This stringent filtering allows to be confident that the selected peaks are true positive results. As expected, this table shows the mains differences are coming from : i) the LZ comparisons between the AD and CTL patients ("LZ_ADvsCTL"), with 61 significant and filtered signals; ii) the comparison of AD PLZ and CTL LZ, with 30 signals; and iii) from the comparison of the LZ and RZ inside the AD subgroup. For a better visualisation of these results the comparisons showing the most significant and filtered signals were put under the form of a schematic in **Figure 52**.

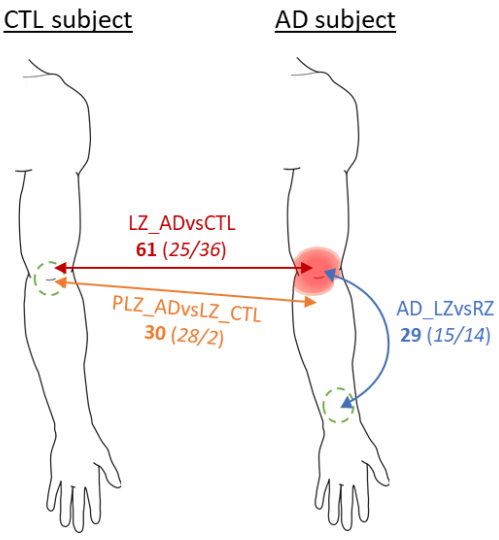

[s] This phenomenon is typical from samples showing an aberrant blank level leading to 0s when subtracted from the signal.

Figure 52: Schematic of the main observed differences in the AD group. The LZ comparisons between the AD and CTL patients ("LZ_ADvsCTL"), with 61 significant and filtered signals; ii) the comparison of AD PLZ and CTL LZ, with 30 signals ("PLZ_ADvsLZ_CTL"); and iii) from the comparison of the LZ and RZ inside the AD subgroup ("AD_LZvsRZ") with 29 signals. The bold number represent the total number of significant and filtered signals and between parenthesis are respectively the number of overexpressed and underexpressed signals.

The only signal differing the LZ from the PLZ is the *m/z* 520.45 which is 1.6 times less intense in the PLZ than LZ and can be assigned to a lysophosphocholines (LPC18:2) this peak is also significantly 2.2 times lowered between the RZ and the LZ. The only 2 signals differing in the AD_PLZvsRZ comparison is the *m/z* 159.05 1.8 times lowered in the ZPL, and 547.45 which is 1.5 more intense in the PLZ than the RZ and could be assigned to a FAHFA 35:4;O. For the LZ comparison between the AD and CTL subjects, the 5 peaks with the lowest negative FC are 379.45, 442.45, 414.45, 397.35, and 428.45 while the 5 highest positive FC are *m/z* 145.15, 201.15, 123.05, 603.55, and 229.55. It can be observed the signal at *m/z* 130.05 which can be assigned to the pyroglutamic acid is 2.5 times less intense in the LZ of AD volunteers. This molecule is part of the **NMF** which could explain the degradation of the skin barrier function. The raw results showed in the **Table 18** shows a more elevated number of significant peaks that are underexpressed which is relevant with the general inhibitory profiles described for AD[172].

The analysis of these results is still ongoing to look at more molecules, which ones are up or down regulated and compare this to the literature.

3. Psoriasis

No biometrological measurements are planned on this groups of subjects. The filtering step during the pre-processing was conducted slightly different for this group as we are not using anymore a constant threshold of 500 a.u intensity but rather a decreasing linear threshold. It is defined at 1000 a.u. at the beginning of the *m/z* range and at 25 a.u. by the end of the *m/z* range. This allowed to be more representative of what's in the raw data in our selection and keep the small intensities that have a good signal to noise ratio at higher *m/z* and were previously filtered out. By doing so, we kept 929 *m/z* out of the 14 900 in the mass spectra. This dataset has a better quality as the same laser method and laser fibres have been used. The exploratory analysis shown in the **Figure 53** allows to observe the main effect, along the first dimension is the one from the TIC. The zone effect (RZ, PLZ and LZ) is the one ruling the second dimension as it could be expected. It is important to note that the PCA coloured by zones is merging the information of the CTL and AD subjects without being able to distinguish for example, the LZ from the AD volunteers, from the associated LZ on a CTL volunteer.

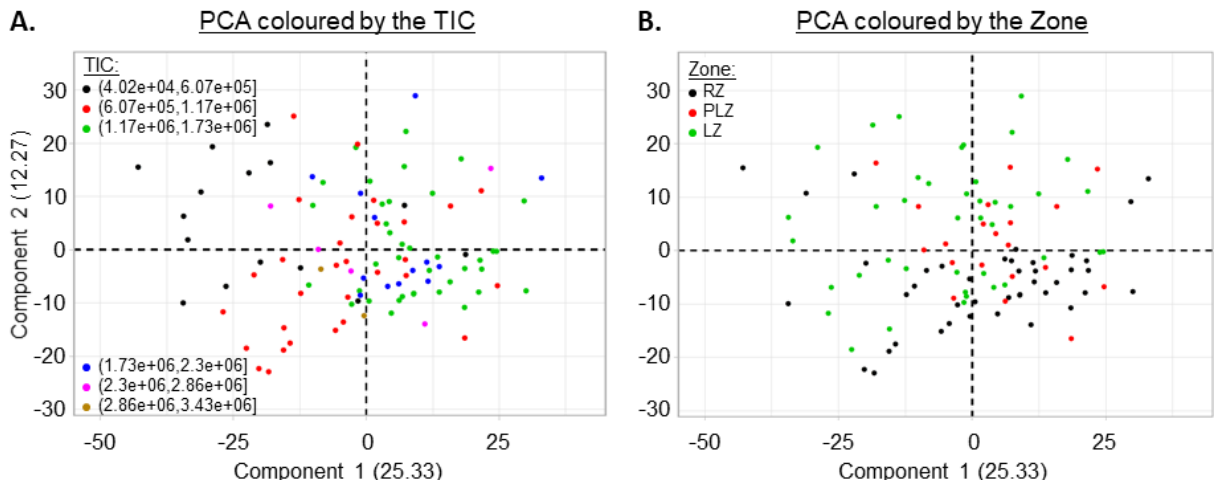

Figure 53: PCA 2D representation of the Pso *in vivo* dataset. **A.** PCA coloured by the average TIC which seems to be the principal source of variability. **B.** PCA coloured by the Zone showing this is the second source of variability in the dataset

The coloration of the PCA plot by class presented in **Figure 54** allows to make this distinction and shows a neat separation of the Pso LZ and PLZ from the CTL zones and in a less extend to the Pso RZ which bodes well for the following differential analyses.

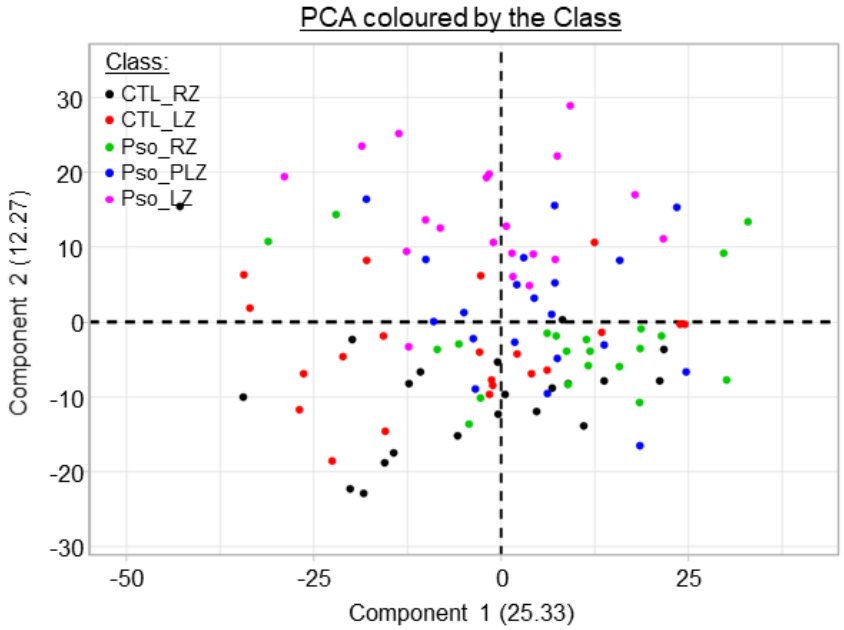

Figure 54: PCA 2D representation of the Pso *in vivo* dataset coloured by the class. As It was possible to guess from the PCA coloured by the zone, we can observe a neat separation of the Pso LZ and PLZ from the CTL zones and in a less extend to the Pso RZ.

The differential analysis has been conducted and the results are summarised in the **Table 19** hereafter.

Table 19: Summary table of the significant peaks obtained in each comparison for the Pso group. "PSO_LZvsRZ" is the comparison between the LZ and RZ inside of the PSO subgroup. "PSO_PLZvsRZ" is the comparison between the PLZ and RZ inside of the PSO subgroup. "PSO_LZvsPLZ" is the comparison between the LZ and PLZ inside of the PSO subgroup. "CTL_LZvsRZ" is the comparison between the LZ and RZ inside of the CTL subgroup. "LZ_PSOvsCTL" is the comparison of the LZ between the two subgroups. "RZ_PSOvsCTL" is the comparison of the RZ between the two subgroups and "PLZ_PSOvsLZ_CTL" is the comparison of the PLZ of the PSO subject and the LZ of the CTL subjects. The "Raw" columns correspond to all the obtained significant signals, the underexpressed signals are in the "-" column and the overexpressed are in the "+" column. The "Filtered" columns correspond to the peak selection described earlier in the **Table 16**.

	Raw			Filtered		
	-	+	Total	-	+	Total
PSO_LZvsRZ	404	183	**587**	61	24	**85**
PSO_PLZvsRZ	91	33	**124**	5	5	**10**
PSO_LZvsPLZ	301	128	**429**	45	15	**60**
CTL_LZvsRZ	91	64	**155**	12	10	**22**
LZ_PSOvsCTL	172	151	**323**	59	33	**82**
RZ_PSOvsCTL	3	161	**164**	1	28	**29**
PLZ_PSOvsLZ_CTL	0	2	**2**	0	1	**1**

All the peaks won't be described here but instead we choose the 5 ones having the highest absolute FC value whether they were under or overexpressed in the LZ comparison between the PSO and CTL subgroups ("LZ_PSOvsCTL").

Table 20: Selected significant peaks in the LZ comparison between the PSO and CTL subgroups with tentative assignments. The 5 extreme FC peaks are ordered by increasing FC values. *m/z* = observed binned *m/z* value. AveExpr = Average Expression. p.value.adj = adjusted p-value, FC = Fold Change. NA = "Not assigned", the assignment is undergoing.

m/z	AveExpr	p.value.adj	FC	Tentative assignment
414.45	21162	4.49E-08	-6.27	$[FA/WE\ 26:0 + NH_4]^+$
400.45	7142	1.64E-07	-5.42	$[FA/WE\ 25:0 + NH_4]^+$
442.45	1801	1.17E-08	-4.25	$[FA/WE\ 28:0 + NH_4]^+$
425.45	8709	2.23E-08	-3.70	$[FA/WE\ 28:0 + H]^+$
386.45	7796	6.44E-06	-3.24	NA (Fragment ?)
664.65	1272	8.27E-05	2.49	$[Cer\ 42:1;O4 + H - H_2O]^+$ or $[Cer\ 43:1;O2 + H]^+$
520.55	2138	1.88E-07	2.62	$[Cer\ 34:1;O2 + H - H_2O]^+$ or $[WE\ 34:3 + NH_4]^+$
676.65	1344	1.31E-04	2.69	$[Cer\ 44:2;O2 + H]^+$
369.75	6355	7.05E-05	3.34	Cholesterol or FA 24:0
648.65	1572	3.01E-07	3.92	$[Cer\ 42:2;O2 + H]^+$

In this LZ comparison between the groups the *m/z* 414 is really stepping out once again with the highest FC value insisting on the necessity to conduct identification of this compound. There is a trend in this differential analysis to observe underexpressed signals with masses under *m/z* 500 and overexpressed values with higher *m/z*. The assigned pyroglutamic acid is found significantly down regulated with a 1.9 FC but only when comparing the LZ and RZ in the Pso patients. At *m/z* 369 nominal mass, there is a high number of compounds that can be found, and interestingly there is often in our comparison a specific mass at *m/z* 370.05 that is significant and with a high absolute FC value. This is the only case in the *m/z* range where several signals are found within a 1 *m/z* window. This signal would require complementary studies to be identified. The

analysis of these results is still ongoing to look at more molecules, identify the ones listed here and compare this to the literature.

4. Seborrheic dermatitis

The specificity of this groups is coming from the location of the lesion sites which are on the scalp. On a physiological point of view, this represents a totally different biome and we expect to have different signal coming out of this group. As the Psoriasis one, here we had used only one laser method and one fibre, but unfortunately, we faced electronical card instabilities during this period which led to several manufacturer interventions, volunteers needing to come several times which clearly induced a date related instrumental bias.

The biometrological measurements constated of LI and FFA/TG ratio. On average, the FFA/TG ratio determined by FTIR on the absorbent paper samples is 1.25 for SD subjects and 1.12 for the associated CTL. No significant difference in the FFA/TG ratio was observed (t-test, p-value > 0.05) between the DS subgroup and its associated control. On average, the amount of lipids of sebaceous origin on the scalp measured by the LI is 42.21 µg/cm² for the SD cohort and 36.93 µg/cm² for the associate CTL. No significant differences in the amount of sebum was observed (t-test, p-value > 0.05) between the DS subgroup and its associated control.

The SpiderMass *in vivo* dataset presented here has been pre-processed as described with an intensity threshold set at 1200 a.u. at the beginning of the *m/z* range and 75 a.u. at the end of the *m/z* range leaving 624 peaks. The data quality and exploratory analyses showed in the **Figure 55** demonstrated a putative TIC and date effect on the variability. The dates were grouped depending on the instrument maintenance.

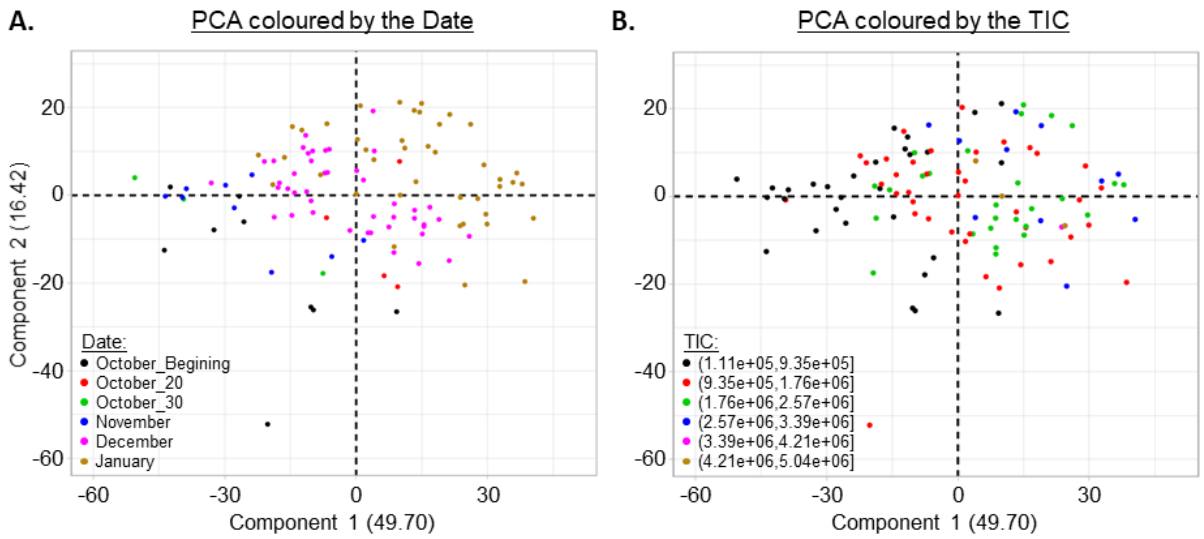

Figure 55: PCA 2D representation of the SD *in vivo* dataset. **A.** PCA coloured by the date groups depending on instrument events which seems to be the principal source of variability. **B.** PCA coloured by the average TIC showing its important effect

The PCA representation coloured by the class in **Figure 56** which correspond to the detail of the zones and the subgroups shows a neat distinction between the forearm and the scalp but little to no differences between the subgroups on the LZ.

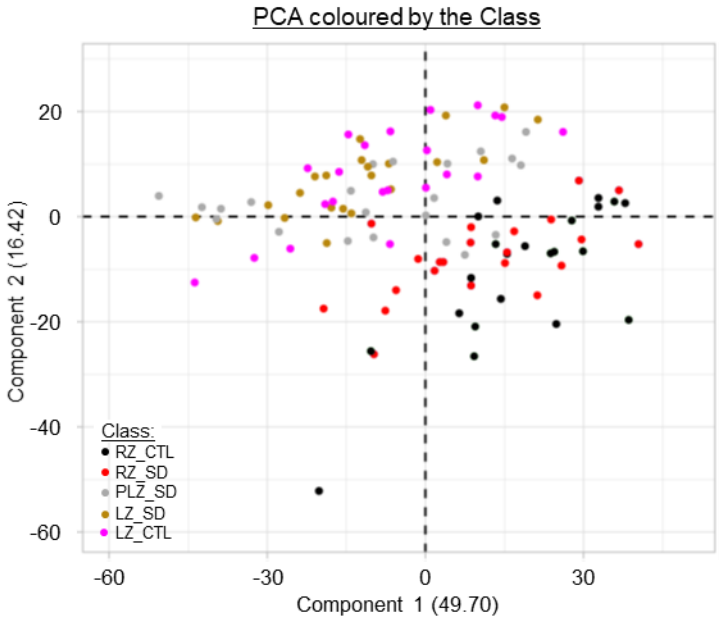

Figure 56: PCA 2D representation of the SD *in vivo* dataset coloured by the class which correspond to the detail of the zones and the subgroups. It shows a neat distinction between the forearm and the scalp but little to no differences between the subgroups on the LZ.

Based on these observations, 3 rounds of differential analysis have been conducted, the first adjusting on the TIC, the second on the date and the third, on both. The summary **Table 21** present all the significant results obtained in each situation.

Table 21: Summary table of the raw significant results obtained in each differential analysis, classified by the applied adjustment factor (TIC, Date or both). The first number correspond to the total significant peaks and between parenthesis are displayed respectively the number of underexpressed and overexpressed signals.

	TIC	Date	TIC + Date
SD_LZvsRZ	443 (226/217)	463 (247/216)	427 (240/187)
SD_PLZvsRZ	32 (31/1)	29 (28/1)	32 (31/1)
SD_LZvsPLZ	408 (220/188)	444 (248/196)	406 (243/163)
CTL_LZvsRZ	505 (223/282)	523 (239/284)	495 (241/254)
LZ_SDvsCTL	0 (x/x)	0 (x/x)	0 (x/x)
RZ_SDvsCTL	0 (x/x)	0 (x/x)	0 (x/x)
PLZ_SDvsLZ_CTL	0 (x/x)	0 (x/x)	0 (x/x)

Based on these results it seems the date adjustment is the one giving the highest number of results as well as limiting the number of adjustment factors. It is to be noted that no matter the adjustment, no significant variations were observed from the comparison of the LZ and RZ between the SD and CTL groups as well as the comparison between the PLZ in SD and the LZ in CTL subgroup.

Based on this observation, the filtering step has been conducted on the raw results obtained from the Date adjustment model and are presented in **Table 22**.

Table 22: Summary table of the significant peaks obtained in each comparison for the SD group adjusted with the Date factor. "SD_LZvsRZ" is the comparison between the LZ and RZ inside of the SD subgroup. "SD_PLZvsRZ" is the comparison between the PLZ and RZ inside of the SD subgroup. "SD_LZvsPLZ" is the comparison between the LZ and PLZ inside of the SD subgroup. "CTL_LZvsRZ" is the comparison between the LZ and RZ inside of the CTL subgroup. "LZ_SDvsCTL" is the comparison of the LZ between the two subgroups. "RZ_SDvsCTL" is the comparison of the RZ between the two subgroups and "PLZ_SDvsLZ_CTL" is the comparison of the PLZ of the SD subject and the LZ of the CTL subjects. The "Raw" columns correspond to all the obtained significant signals, the underexpressed signals are in the "-" column and the overexpressed are in the "+" column. The "Filtered" columns correspond to the peak selection described earlier in the **Table 16**.

	Raw			Filtered		
	-	+	Total	-	+	Total
SD_LZvsRZ	247	216	**463**	86	59	**145**
SD_PLZvsRZ	248	196	**444**	91	51	**142**
SD_LZvsPLZ	28	1	**29**	13	0	**13**
CTL_LZvsRZ	239	284	**523**	92	103	**195**
LZ_SDvsCTL	0	0	**0**	0	0	**0**
RZ_SDvsCTL	0	0	**0**	0	0	**0**
PLZ_SDvsLZ_CTL	0	0	**0**	0	0	**0**

To characterise the lesion area, it will here be necessary to compare the LZ and PLZ only, as the difference between the scalp and the forearm is not informative of the pathology. As the list is short, all the selected significant peaks with tentative assignment are presented in **Table 23**. In this table, the peak at *m/z* 520.55 has been added even if filtered-out as it is the only significantly overexpressed mass.

Table 23: Selected significant peaks in the LZ and PLZ comparison in the SD subgroup with tentative assignments. The peaks are ordered by increasing FC values. The peak at 520.55 has been added even if filtered-out as it is the only significantly overexpressed mass. *m/z* = observed binned *m/z* value. AveExpr = Average Expression. p.value.adj = adjusted p-value, FC = Fold Change. NA = "Not assigned", the assignment is undergoing.

m/z	AveExpr	p.value.adj	FC	Tentative assignment
414.45	17097	1.65E-02	-2.5	$[FA/WE\ 26:0 + NH_4]^+$
400.45	4298	2.39E-02	-2.2	$[FA/WE\ 25:0 + NH_4]^+$
407.45	1192	2.39E-02	-2.1	$[FA\ 28:0 + H - H_2O]^+$
386.45	5166	2.27E-02	-2.1	NA (Fragment ?)
379.35	2977	2.39E-02	-2.0	$[FA\ 25:2 + H]^+$ or $[ST\ 28:3;O + H - H_2O]^+$ or $[FA\ 26:0 + H - H_2O]^+$
361.35	2797	2.39E-02	-2.0	$[FA\ 25:2 + H - H_2O]^+$
416.45	1358	1.65E-02	-2.0	$[FA\ 25:0;O + NH_4]^+$
442.45	1790	1.65E-02	-1.9	$[FA/WE\ 28:0 + NH_4]^+$
397.35	6986	4.52E-02	-1.9	$[ST\ 28:3;O + H]^+$ / $[FA\ 28:5 + H - H_2O]^+$ / $[MG\ O\text{-}22:1;O + H - H_2O]^+$
333.35	4886	4.83E-02	-1.8	$[SPB\ 18:1;O3 + NH_4]^+$
443.45	1177	2.39E-02	-1.8	NA (Fragment ?)
384.45	1035	2.39E-02	-1.7	NA (Fragment ?)
426.45	2051	2.75E-02	-1.6	$[FA/WE\ 27:1 + NH_4]^+$
520.55	3435	1.65E-02	1.3	$[Cer\ 34:1;O2 + H - H_2O]^+$ or $[WE\ 34:3 + H + NH_4]^+$

All the significant *m/z* are observed here between the *m/z* 333 and 443 range[t] and correspond mainly to FFA or WE underexpressed on the lesion area. The ST 28:3;O could correspond to the ergosterol which is a precursor of vit D2 but also the ubiquitous substitute of cholesterol in fungi and yeast targeted by antifungal therapeutics. One would expect this molecule to be overexpressed in the lesion site of SD so more investigations are needed. The SPB 18:1;O3 could be a dehydrophytosphingosine which is an AML with anti-inflammatory properties and is found here underexpressed on the lesioned area.

We need to be careful in our conclusion here as we can conclude on the differences between the lesioned scalp and the PLZ area, but we cannot conclude on the molecular difference between SD lesioned scalp and normal scalp on CTL subjects.

D. Conclusion and discussion

This chapter demonstrated how we came up with a general workflow to assess the quality of our data, correct the possible sources of biases and display the huge amount of obtained results on each question addressed by the SpiderMass. The SMPatho clinical trial has been greatly affected by the COVID-19 situation with several periods of lock-down, which, coupled with the difficulties to find the volunteers and the instrumental problems, delayed the recruitment a lot (when the study was designed, the "last person out" was

[t]It is to be noted that here we decided to keep two peaks distant by 1 Da, the m/z 442 and m/z 443 contrary to the previous presented filtering criteria as they do no seems to be isotopes. Indeed the intensity ratio between the peaks does correspond to the natural occurring isotopic distribution we would expect at this mass.

expected around the final months of last year). Indeed, the rosacea groups is prepared for September, and is foreseen complicated as we will need to get the right volunteers in our PFDC panel.

The acne group is the one that faced the more difficulties and led to the highly structured data quality verification we have now. Still, the only results are coming from the molecular distinction between the face lipids and the forearm ones. This could be explained by another factor which is specific to this kind of dermatosis where the lesions are discrete. Indeed, we analysed a 1cm diameter surface with the papule / pustule in the middle. The lesion is small compared to the analysed surface, and if the inflammatory signals are restrained to a specific area then we average it completely. Two directions could thus be considered, the first is to use imaging modalities to observe the distribution of the signal on the skin surface, by transforming some of the SMPatho acquired data into images. The second direction would be to reduce the analysed area to the centremost region of the papule. A small clinical study ("SpiderAcneDos" is being conducted right now with a specific protocol in this direction. We evaluate the possibility to shoot still on the same location to dig toward the core of the inflamed zone as well as sampling the comedo for direct analysis. However, the results obtained by comparing the forehead and the forearm on CTL subjects are comparable to the ones observed on the Chapter V of this thesis and would be interesting to compare.

The Atopic Dermatitis group has shown good results despite the instrumental effect that occurred. The described down expression profile was observed in all the comparison involving LZ and PLZ on AD subjects which is correlated to what's described in the literature with at least 60 filtered peaks differentially expressed between the LZ on the CTL and AD subgroup. The 547 Da signal observed overexpressed in the PLZ of the AD patients can be assigned to a FAHFA 35:4;O. Such lipids are known to have some anti-inflammatory functions so it would be particularly interesting to look for this molecules level in the other dermatosis[202]. The increasing in the FFA content that we observed in the AD dataset has been described in the literature[203]. It is supposed to trigger the FFA4 receptor which in the physio-pathological context induces an inflammatory response. The inhibition of this receptor has been shown to improve the AD lesions in mice[203] for example. The sphingosine that is tentatively observed in the SD groups has been described in the patients with AD as well. In this situation the diminution of expression has been linked to a general vulnerability of the SC as well as a diminution of the ceramides level[173]. Farwanah et colleagues have analysed the composition of healthy VS non lesioned skin from AD volunteers by LC-MS and have shown no differences in the main lipid classes constituting the SC lipids (ceramides, cholesterol and FFA). This is consistent with the 0 significant signals that were obtained in the "RZ_ADvsCTL" comparison. Instead, last year, Yokose and colleagues report significant lipids ratio modifications of some ceramides. They conclude the ratio between the [NP] ceramides the [NS] ceramides[u]

[u] This classification of the ceramides describes their structure. The 'N' stands for the Non-OH fatty acids linked to the 'P' for a Phytosphingosine base or 'S' for a Sphingosine base.

can be used as a potential marker for skin keratinocytes differentiation and to define the barrier-disruption level in Pso and AD patients as well as in healthy skin[204]. It would be interesting to have a deeper inspection of our assignment to investigate whether we are able to find these results as well. A last very important element that we observe is the diminution of the *m/z* 130.05 signal between LZ zones in AD and CTL volunteers which is assigned to the pyroglutamic acid. It belongs to the NMFs and is tightly linked to the barrier potential of the skin and its capacity to retain water. Several low mass elements are down regulated as well and would need to be further investigated. For the moment we are limited in their observation and fragmentation as our mass spectrometer is not made to observe *m/z* under 100.

Psoriasis is a multiorgan disease not affecting only the skin but also various other organs because of a global modification of the lipid biosynthesis in psoriatic patients[205]. In the SMpatho study, the psoriasis groups gave a variety of significant results which at first sight looks interesting. Our results shows a global decrease of FA (or wax esters) on the Pso LZ as well as an increase in cholesterol which was also previously described elsewhere[205]. An increase in C12:0, C16:0, C18:0, C18:1, C24:0 and C24:1 ceramides was proposed and would be interesting to verified[161].

As described in the results, the Seborrheic Dermatitis group gave results only on comparison in which the measures were paired together on the same patient. This can be explained by the high supposed inter-individual variability. Another possible explanation would come from the second visits needed for some volunteers that randomly affected a majority of SD subject. This may have created an unwanted batch effect lowering the power of our analysis when we adjust by the date. The results have shown a general decrease in the FFA level as well as interesting *m/z* tentatively assigned to ergosterol, specific of yeasts, as well as a sphingosine base. In vitro and *in vivo* studies demonstrated the strong both anti-inflammatory and anti-microbial activity of phytosphingosines[206] that was here detected underexpressed in the LZ. The increased hydrolysation of skin lipids produce FFA and lower the relative quantity of TGs leaving behind irritating and unsaturated FFA such as oleic acid (*m/z* 283) and that the main difference between dandruff-affected and non-affected scalp zones was the peroxidation of squalene[183]. In the comparison between the LZ and PLZ we cannot observe a significant difference on the oleic acid for example (adjusted p-value=9.04E-01, FC=1.05), maybe it would have been interesting for that group to define a non-lesioned zone, far for the LZ contrary to the PLZ which was close to the LZ measurement.

The subject's reaction to laser exposure, was still a running interrogation as we only had the SpiderValid study as data, and in particular we wanted to assess the reaction on injured skin. During this study, out of the included 176 subjects, only 6 (3.4%) showed light to mild erythema that were visible more than 15 minutes after the laser, which reassures us that the technology is not invasive.

This study needed to start rapidly after the system has been evaluated with the SpiderValid study and we learned a lot as we were recruiting. We improved the system, its maintenance, the method, and the

statistical workflow leading to improved ways of working, more robust and reproducible results. There are still a lot to do as we are now sitting on a wealth of data waiting to be refined and transformed into knowledge. These observations will be used in a second time to evaluate whether some of the build-up indicators can be followed to appreciate the efficiency of some products. For example, the *m/z* 414 appears to be as interesting as the squalene at *m/z* 411 and will need to be further studied. While we are generating a lot of QC data, evaluated on their own, still we don't use them to correct the observed biases. Statistical development will need to be explored in that respect.

Another approach which has not been assessed at all during this PhD, is the capability to classify the subjects and predict their clinical status. For example, one can imagine an indicator evaluating the probability of an incoming AD flares based on the measured inflammatory state.

Chapter VII

General Conclusion and Discussion

CHAPTER VII: General Conclusions and Outlooks

The extraordinary technological breakthroughs that happened over the last 20 years has initiated a paradigm shift in medical practices and clinical research that were before relying solely on examination and patients' medical history. Most of it started with the DNA sequencing technology, the era of genetic studies and the rise of the genomics that has engaged towards the personalised and precision medicine. The idea behind is that every patient would be sequenced, and the treatment adapted consequently. The era of genomic has given the research and medical communities a deep understanding of the backbone governing physiology and pathology. However, if mutations can help refining the care of certain patients it was shown to be insufficient to address all of them. Therefore, large scale measurements of gene products such as metabolites (including lipids) and proteins has also started to be conducted, and precision medicine will probably have to rely on the integration of the different -omics data to really tackle the precision medicine leading to the era of Transomics.

Applied to the skin, Mills et colleagues proposed in 2018 a set of genes, named the "unhealthy skin signature" which were demonstrated to be dysregulated in several dermatosis including SD, Psoriasis, AD and acne. They describe an upregulation of immune response associated genes and a down regulation of filament related genes[207]. But in the same time, genomic has equally shown its inability to tackle the goal of personalised medicine by itself[208]. One mutated gene doesn't necessarily lead to a modified protein, and even less necessarily to a modified phenotype because of all the steps involved in between. Indeed, the expression of a gene, its transcription to RNA and further maturation, the following translation to protein (or ghost proteins) and then its activation and degradation shows all some degrees of regulations. Moreover, contrary the ERBB2 gene mutation, there is a low incidence of most of the putative genomic alteration with small numbers of patients which hinder the clinical trials power and recruitment adding logistical challenges to the scientific ones[208]. Therefore, a growing number of studies aim at also screening at the RNA, proteins level and expression and metabolites. By measuring the lipids and metabolites we are looking at the end-effectors of all the biosynthesis pathways, getting us closer to the phenotype even if it has been shown that some lipid and metabolites can regulate genes activity as well[209]

The development of high-throughput MS-based approaches as led to large scale proteomic screening and, on the other hand, the development of AIMS sources has definitely brought MS into the clinical lab and soon to the patient bedside. The *in situ* analysis are powerful ways to observe the pathophysiological context much closer and avoids biases related to sample handling. Despite important advantages related to the limited sample preparation of the AIMS technologies which make them fast and easy to operate, they show a poor ionisation efficiency has much of other modalities, combines with other drawbacks like i) the important ion suppression, ii) the limited selectivity (coming from the absent sample pre-treatment and extraction) and iii)

the inability to distinguish by itself isomeric or isobaric molecules without analytes modifications. This leads generally to a partial observation of the major molecules in the samples; for example, in the case of the SpiderMass and close AIMS technics, the analysis is mainly directed towards lipids and small metabolites. To improve the ionisation yield, on tissue derivatisation[209] or doping of the solvent system with strong proton donor like TFA[210] have been proposed for MS imaging. The ion suppression and isobaric challenges can be counteracted by adding an ion mobility separation[211]. Whether it is in the mass spectrometer or added in front of it like the recently developed FAIMS interface by ThermoFisher scientific. Recent work with this FAIMS interface demonstrates a very good sensitivity and an equal number of identified proteins with 5 times less material and shorter and a gradient duration reduced by 25%[212]. These factors makes the majority of AIMS techniques blind to a vast majority of low abundance compounds : On more than 115k metabolites in the Human Metabolite DataBase ("HMDB")[213], LC-MS allows usually to detect a thousand of them per analysis, when AIMS approaches gives usually hundreds at the same time which correspond to the level also described in this thesis. Yet most of AIMS technologies haven't been tested in these new configurations which is really promising and thus in their conventional operation mode lower abundance compounds would be more easily observed

The work presented here aimed first at developing a SpiderMass system first for the use in a per-operatory context, on *ex vivo* dog patient's sarcoma biopsies. It led to a successful demonstration of the system capability even if some flaws still remain to be corrected for an extensive use by the surgeon. This taught us the fibre part needed to be improved, to become plug-and-play and more rugged. Along with the presentation of the method as a protocol, it also described the preliminary steps necessary toward duplicating it. The SpiderMass technology has been reproduced guided by different instrument needs and constraints in the Pierre Fabre Skin Research Centre and then we validated several aspects of the new system through clinical studies. Contrary to the research lab, the environment of clinical trials adds several challenges. This includes working with volunteers, dermatologists, panel administrator, clinical study expert, data manager and biostatisticians each of them having their own motivations, problematic, and needs. Everything is planned and there is no place for improvisation making the instrumental maintenance a real challenge.

When everything didn't go as expected, because of instrumental problems (or a worldwide pandemic.), then it is necessary to find solutions to correct those biases. This has been made by the necessary development of several statistical tools and workflow from scratch to generate knowledge from data and evaluate its quality. To that regard, the QC strategy will need to be further developed and refined because it is a mandatory aspect for the future of the SpiderMass device in the clinical context for diagnosis. Other statistical approaches using machine learning are possible and will need to be implemented if we want to discriminate conditions based on the obtained molecular profile. For example, the use of discriminant analysis coupled to Principal Least Square (PLS-DA) is related to PCA and allows to define predictors. But when the PCA only reduces the high

dimensionality of variables, based on their covariation, the PLS further evaluate the ability of the new components to predict. This type of directed analysis has the advantages of being able to discard the orthogonal variability linked to instrumental effects and detect the co-variating peaks which lead to a "denoised" model. This kind of PLS-DA models has been recently used i.e. to discriminate different Malassezia species and observe the lipid variations of these yeasts[214]. We have used another type of statistical approaches relying on deep learning with convolutional neuronal network (**CNN**) on the dog sarcoma cohort[1]. Contrary to the usual machine learning approaches, the CNN can learn representations from raw data without the need of time-consuming pre-processing steps to remove biases and artifacts. Still the CNN need a big quantity of data which is not a common situation in MS especially in our case but can be found in the imaging experiments. This is why, the originality of this work comes from the cumulative learning of the CNN over various MALDI MSI datasets to accumulate knowledge on the representation, before transferring onto the dog sarcoma dataset acquired with the SpiderMass. In this research article, the PCA/LDA accuracy of 93% on the dog sarcoma has been improved to 98% using the developed CNN. This work is a promising strategy to improve the classification accuracy on small numbers of samples and is currently being applicated to the dataset from SMPatho.

The results obtained in Toulouse have shown the capability of the system to be used in diverse studies ranging from standard analysis and structural analysis to skin disease molecular characterisation, the analysis of UV-related molecules modifications (data not shown), and direct bacterial identification strategies (data not shown). The general observed trend is not yet corresponding to the described lipid abundance diminution because it would need to use semiquantitative strategies, but rather comes from the observation of lipids being up or downregulated in specific regions of the mass spectra. In general, many skin diseases present similar trends that will lessen the use of lipids for disease-specific recognition, but at the same time it is great to be able to follow the response to dermo-cosmetic product, on several diseases using the same set of signals.

Compared to other skin analysis methods, here the SpiderMass measures are done *in vivo* without requiring any biopsy to be performed and by a simple click of a button which brings the possibility to quickly analyse samples or skin and give complex spectra. Contrary to the oncology-oriented prototype, here the problematic is not fast diagnosis, so the processing has not been developed for real-time result guidance. Other non-invasive techniques were used in the research centre for skin study like the FTIR presented in this manuscript, but these spectroscopic modalities don't allow to identify molecules and observe fine changes in molecular profiles.

One of those fines changes that will need to be explored in the future is the skin lipids modifications by oxidative stress. Indeed, the skin is an organ frequently exposed to oxidative, chemical, and thermal stresses, and to injury and inflammation. These stresses lead to lipids modification constituting what is known

as the epilipidome[v]. Not too much is realised in that way, and the SpiderMass could be used to study their dynamics and biological consequences.

The dermatoses that have been addressed in this work are all considered to a certain extent as a real burden by the World Health Organisation. This is why Pierre Fabre Dermo-Cosmetic company purpose is to take care of life, from health to beauty. And that is why the company's motto is: “Every time we care for a single person, we make the whole world better”.

[v] For a review on the skin epilidome, the reader is referred to the minireview by Gruber et al.[215]

Appendices

Appendices

A. General timeline of the significant MS ionisation developments

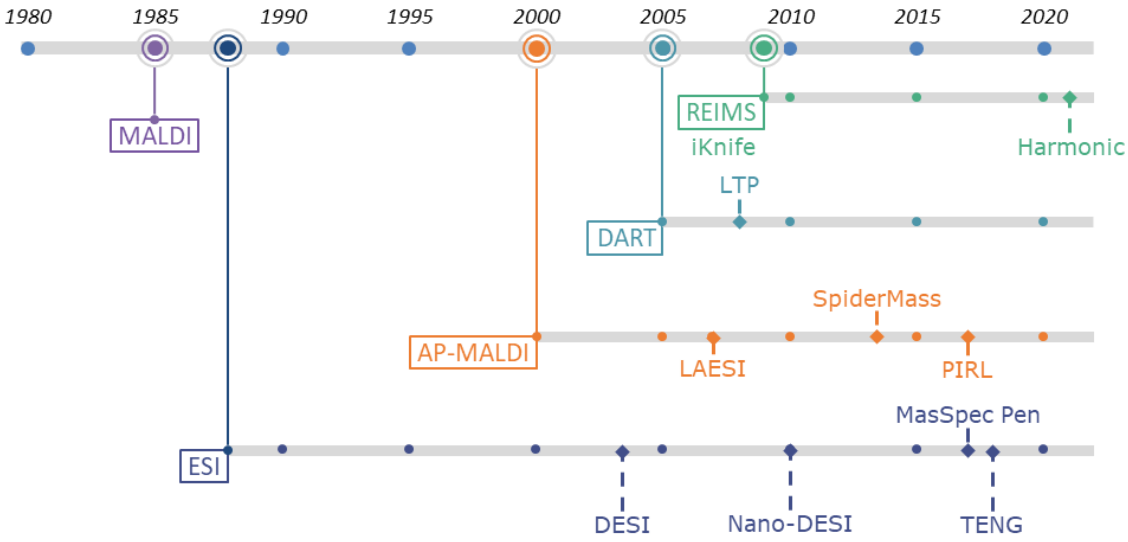

Appendix 1: Timeline of the significant events in the evolution of MS ionisation sources presented in this thesis toward AIMS and intraoperative techniques. Development of MALDI and ESI have empowered the uses of MS and have been the starting point of a lot of different technological developments. The liquid extraction / ionisation techniques are derived from ESI and consist of DESI/nano-DESI, MasSpec Pen and substrate spray methods like TENG-MS. The plasma-based techniques are mainly represented by DART but also LTP. The laser-based techniques come from the first AP-MALDI experiments and gave birth to LAESI, SpiderMass and PIRL-MS. Finally, the alternatives methods have been implemented by the REIMS developments coupled to surgical scalpel, the iKnife, and recently the Harmonic scalpel. Adapted from Ogrinc et al.[111]

A. MOLO software screenshots

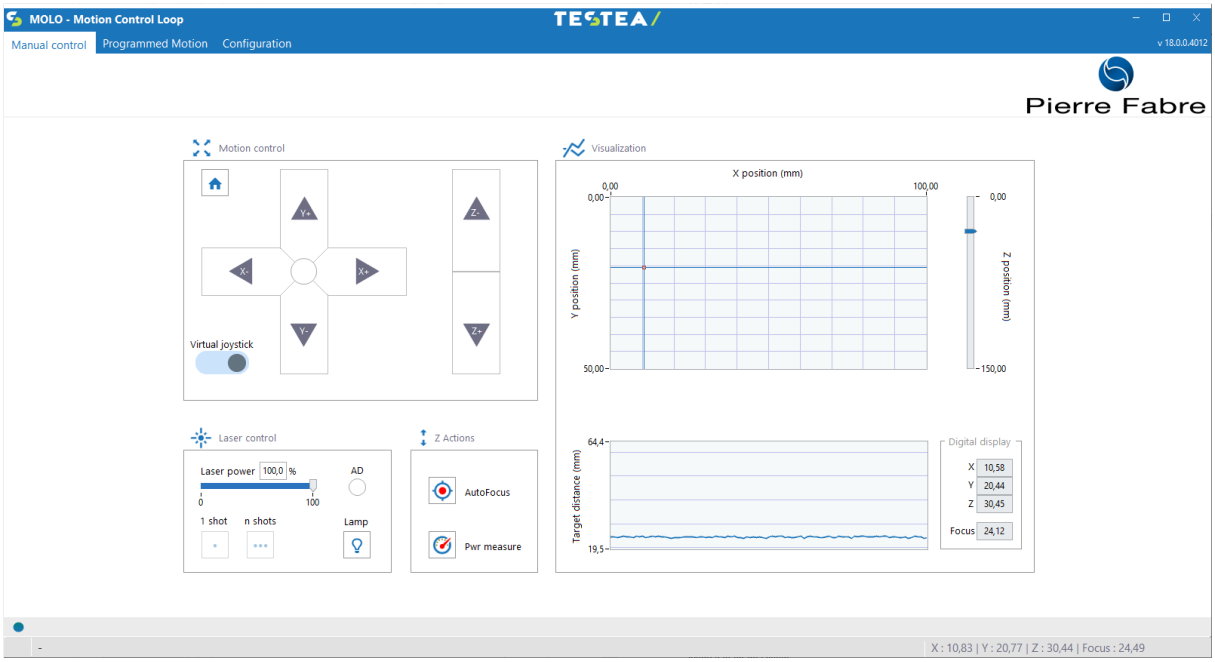

Appendix 2: Screen print of the MOLO ablation control software with here the manual control window. On the left are the laser positioning and firing controls and on the right the position indicators

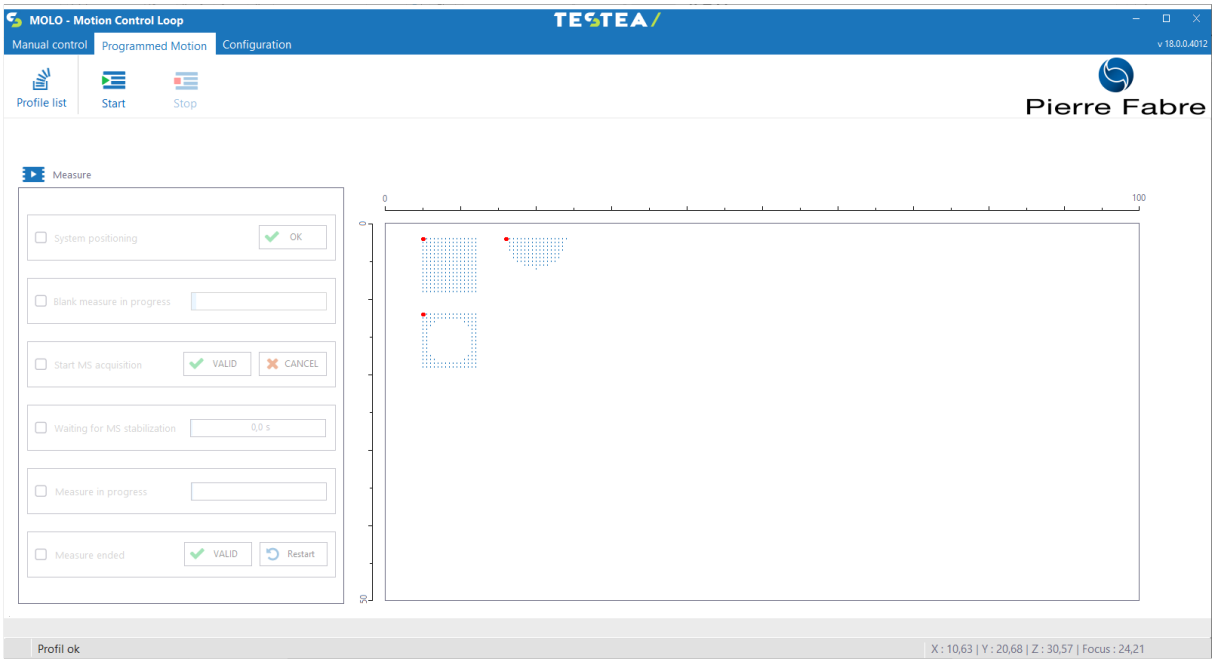

Appendix 3: Screen print of the MOLO ablation control software with here the programmed movement window. After selecting a scheme from a list, several steps of the measurement are displayed on the screen. The steps are displayed one after the other on the left-hand side of the screen and the right-hand side is used to give visual indications. The individual steps first consist of positioning the system using the manual control page shown in **Appendix 2**. After a blank displacement on the zones that will be analysed later, the software asks the user to validate that the acquisition on the spectrometer is launched to trigger a waiting period of 30 seconds. Finally, the software indicates in real time the position of the system and the number of laser shots remaining. The last step allows the user to restart the same measurement scheme or to exit it.

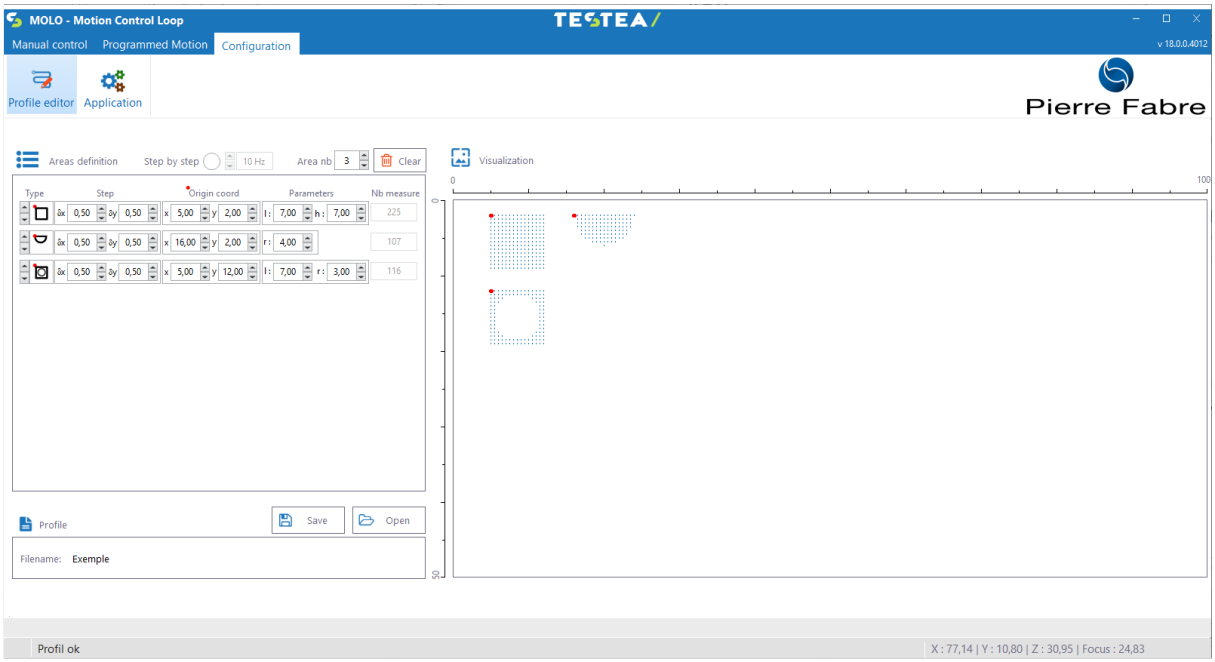

Appendix 4: Screen print of the MOLO ablation control software with the window to create measurement diagrams and configuring the software. The space on the right is the motor working area where shapes can be positioned with dimensions entered on the left side of the screen. The configuration tab allows the user to set various parameters such as the laser wavelength, the movement speeds of the motors, and the parameters for calculating the distance from the sensor

B. SMA software screenshots

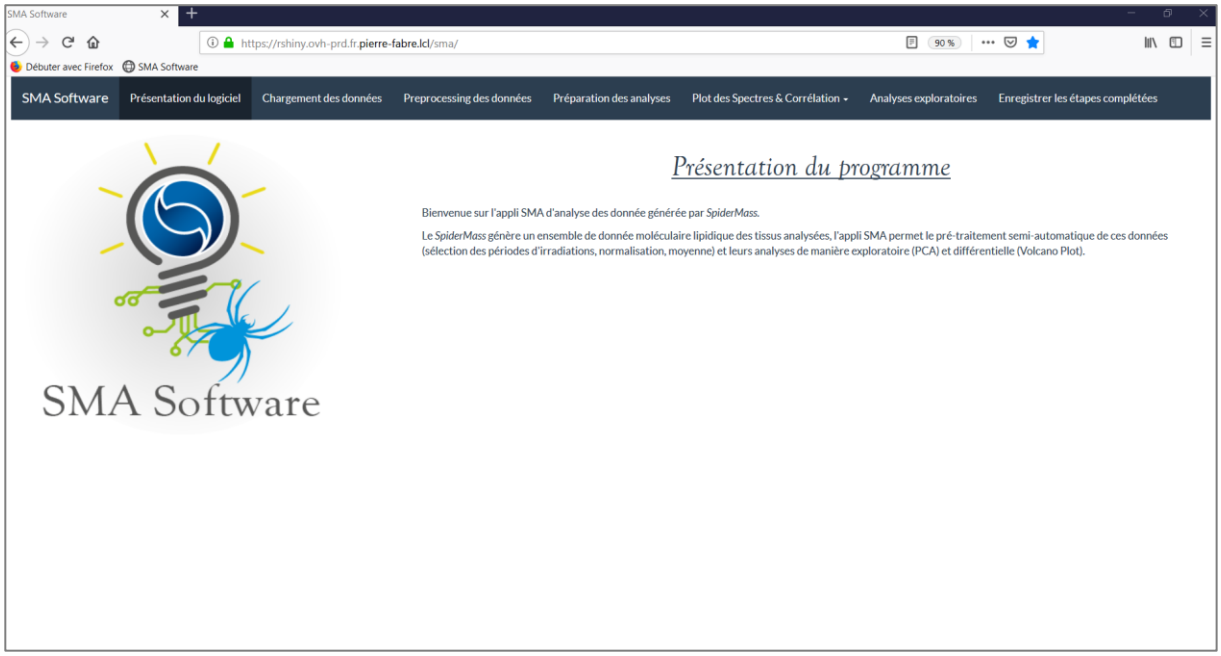

Appendix 5: Screen print of the SMA software to prepare the SpiderMass data. Presentation page of the program. The top banner shows the different tabs that can be used from left to right, in chronological order. The last tab, for saving analyses in progress, can be used at any time.

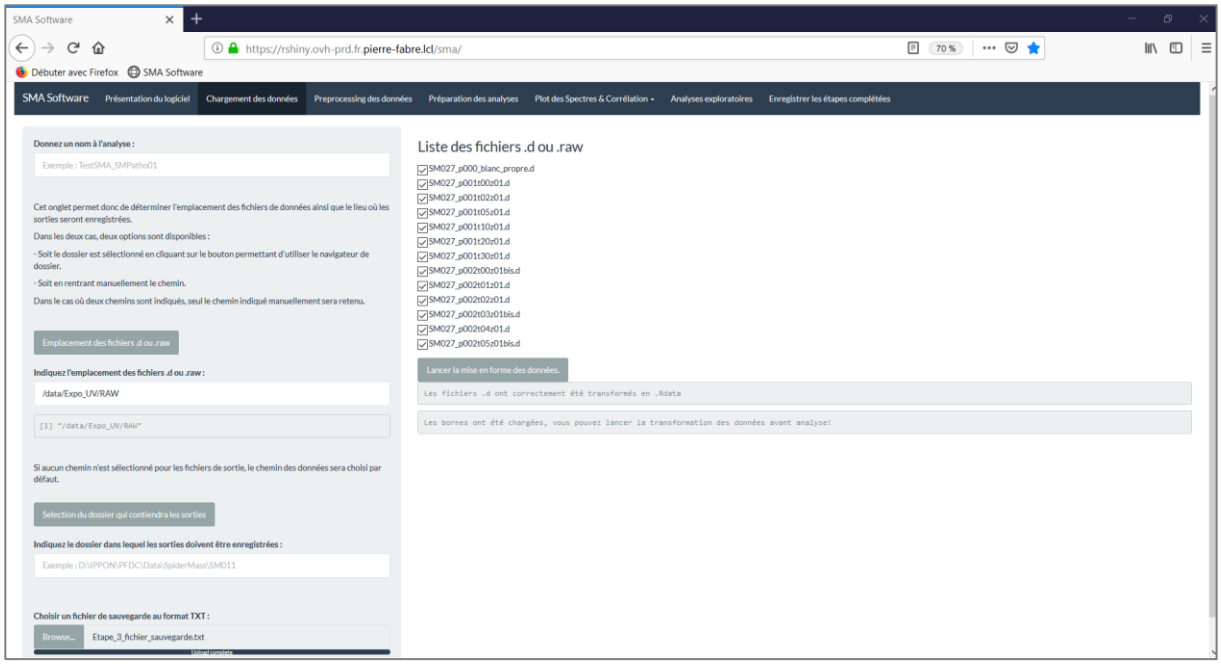

Appendix 6: Screen print of the SMA software to prepare the SpiderMass generated data. The data and acquisition management page. On this page, an analysis can be saved and reloaded.

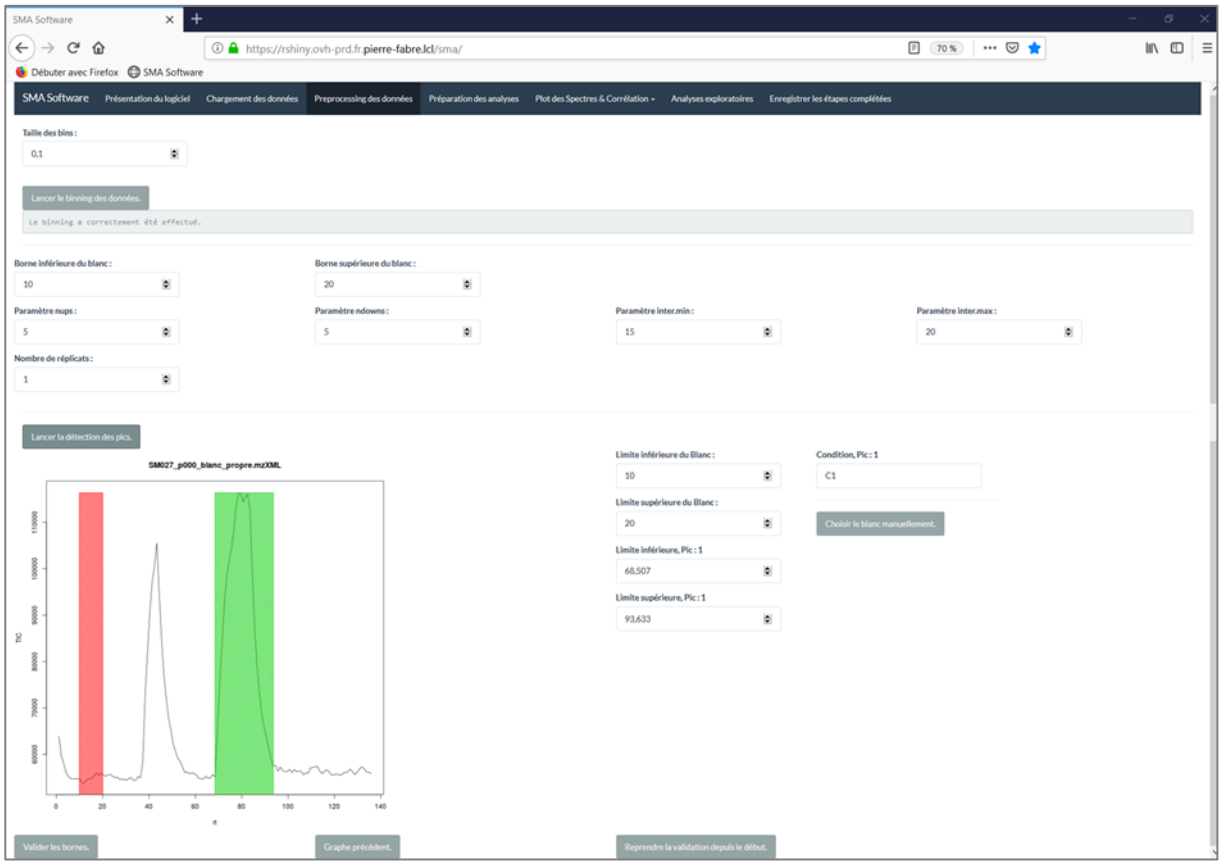

Appendix 7: Screen print of the SMA software to prepare the SpiderMass generated data. File binning and irradiation period selection page

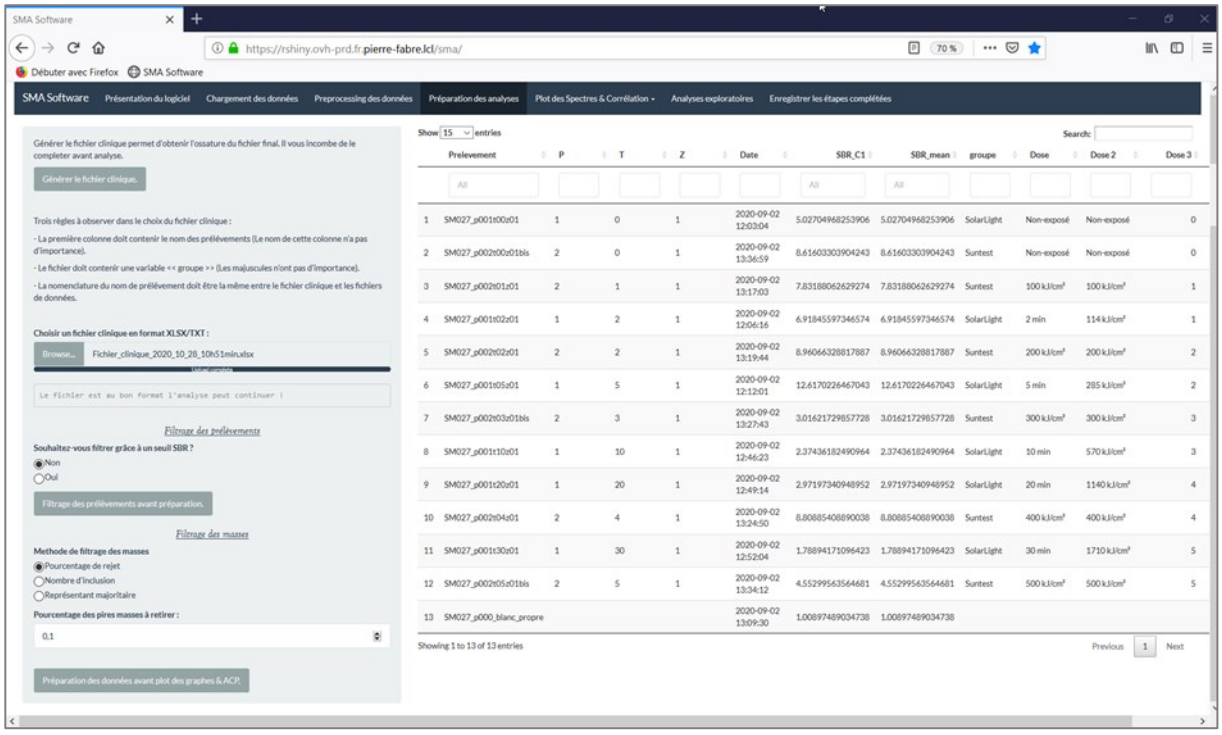

Appendix 8: Screen print of the SMA software to prepare the SpiderMass generated data. Management page for the "clinical" information associated with the analysed files. This example shows all the columns with information automatically filled in, such as the SBR or average TIC, or information filled in by the user, such as the different groups to colour the PCA. It is at this stage that different filtering can be applied to the data.

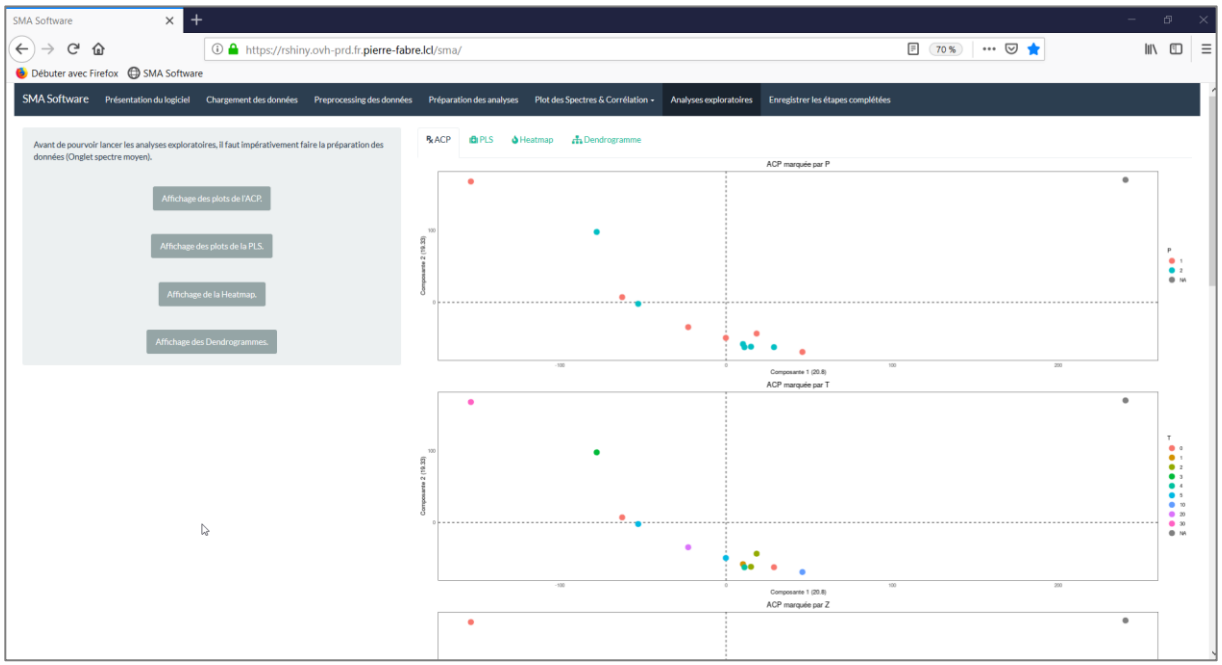

Appendix 9: Screen print of the SMA software to prepare the SpiderMass generated data. Presentation page for exploratory analyses such as PCA, PLS-DA, HeatMap or clustering.

C. SpiderCompar

1. Eligibility criteria

a) Inclusion criteria

Subjects with all of the following criteria may be included:

Population criteria:

- For Group 1 subjects: Female, aged 18 to 25 inclusive.
- For Group 2 subjects : Female, aged 55 to 65 inclusive.
- Subjects with a phototype II to IV according to the Fitzpatrick classification
- For women of childbearing potential: use of a method of contraception for at least 4 weeks, assessed as effective by the investigator.
- Subject who has given written consent to participate in the study.
- Subject affiliated to a social security scheme or beneficiary of such a scheme.

Criteria related to pathologies:

- Subject with areas under study (forehead, inner and outer surface of the right forearm) without lesions or other skin markings (tattoos, erythema, etc.).

b) Non-inclusion criteria

Subjects with at least one of the following criteria are not included:

Population criteria

- For women of childbearing potential: Pregnancy or breastfeeding.
- Simultaneous participation in another study or during an exclusion period.
- Subject unable to comply with protocol requirements.
- Subject who is linguistically or psychologically incapable of signing the informed consent.
- Subject deprived of liberty by judicial or administrative decision, under guardianship or curatorship.

Criteria related to pathology and skin condition :

- Allergy to ethyl acetate.
- Numerous large surface nevi or ephelides in the test areas (face and right forearm).
- Dermatological pathology (eczema, psoriasis, acne...) or any type of complication in at least one study area (such as excoriation, primary bacterial, viral, fungal or parasitic infection, etc.) as determined by the investigator.

- Solar erythema or other markings (tattoos, scars, etc.) on the experimental area that may interfere with the evaluation of skin reactions (pigmentation disorders, etc.).
- General pathology that may affect the outcome of the study.

Criteria for treatments and cosmetics :

- Application of water, topical product or make-up to at least one study area following the last wash the evening before the inclusion visit.
- Anti-inflammatory treatment (steroidal or non-steroidal) taken daily and repeatedly for more than 5 consecutive days in the week preceding the inclusion visit.

2. Table of SpiderCompar study positive ions tentative annotations

Appendix 10: Table of the tentative annotations of the SpiderCompar study positive ions

Binned *m/z*	Observed *m/z*	Matched *m/z*	Ion	Neutral mass	Mass diff	Diff ppm	Assigned
145.15	145.12	145.1223	[M+H]+	144.1151	0.0023	-16	FA 8:0
	149.05	149.019					
150.15	150.106		[M+H]+	149.0988			
171.15	171.135	171.138	[M+H]+	170.1308	0.003	-18	FA 10:1
205.15	205.189	205.1789	[M+H]+	204.1725	0.0101	49	MG O-8:0
219.15	219.203		[M+H]+	218.1958			
231.15	231.204	231.1955	[M+H]+	230.1882	0.0085	37	FA 13:0;O
237.25	237.221	237.2213	[M+H-H2O]+	254.2151	0.0003	-1	FA 16:1
239.25	239.237	239.2369	[M+H-H2O]+	256.2307	0.0001	0	FA 16:0
255.25	255.235	255.2319	[M+H]+	254.2247	0.0032	12	FA 16:1
257.25	257.246	257.2475	[M+H]+	256.2403	0.0015	-6	FA 16:0
285.25	285.28	285.2788	[M+H]+	284.2716	0.0088	4	FA 18:0
313.25	313.274	313.2737	[M+H-H2O]+	330.2675	0.0003	1	MG 16:0
313.25	313.297	313.3101	[M+H]+	312.3029	0.0131	-42	FA 20:0
325.25	325.299	325.3101	[M+H]+	324.3029	0.0111	-34	FA 21:1
329.35	329.31	329.305	[M+H]+	328.2978	0.005	15	FA 20:0;O
331.25	331.279	331.2843	[M+H]+	330.2771	0.0053	-16	MG 16:0
341.35	341.305	341.3414	[M+H]+	340.3342	0.0364	-107	FA 22:0
341.35	341.305	341.305	[M+H-H2O]+	358.2988	0	0	MG 18:0
361.35	361.38	361.3465	[M+H-H2O]+	378.3403	0.0335	93	
369.35	369.348	369.3727	[M+H]+	368.3655	0.0247	-67	FA 24:0
369.35	369.348	369.3363	[M+H-H2O]+	386.3301	0.0117	32	MG 20:0
369.35	369.348	369.3516	[M+H-H2O]+	386.3454	0.0036	-10	ST 27:1;O
397.35	397.402	397.404	[M+H]+	396.3967	0.002	-5	WE 26:0
397.35	397.402	397.404	[M+H]+	396.3967	0.002	-5	FA 26:0
397.35	397.402	397.3465	[M+H]+	396.3392	-0.0555	140	Ergosterol
397.35	397.402	397.3465	[M+H]+	396.3392	-0.0555	140	Vit D2
411.35	411.397	411.3621	[M+H-H2O]+	428.3559	0.0349	85	ST 29:2;O2
411.35	411.397	411.4197	[M+H]+	410.4125	0.0227	-55	FA 27:0
411.35	411.397	411.3833	[M+H-H2O]+	428.3771	0.0137	33	MG O-23:1;O
411.35	411.397	411.3985	[M+H]+	410.3913	0.0015	-4	Squalene
411.35	411.397	411.3985	[M+H-H2O]+	428.3923	0.0015	-4	ST 30:1;O
414.45	414.429	414.4305	[M+NH4]+	396.3967	-0.0015	-4	FA ou WE 26:0
427.35	427.383	427.3934	[M+H]+	426.3862	0.0104	-24	2,3-oxydosqualene / 2,3-epoxysqualene
440.45	440.391	440.4098	[M+NH4]+	422.376	#VALEUR!	-43	FA 27:2;O
451.45	451.45	451.4509	[M+H]+	450.4437	0.0009	-2	WE 30:1
465.45	465.464	465.4665	[M+H]+	464.4593	0.0025	-5	WE 31:1
467.45	467.408	467.4095	[M+H-H2O]+	484.4128	0.0015	-3	DG 26:0
467.45	467.45	467.4823	[M+H]+	466.4751	0.0323	-69	WE 31:0

Binned *m/z*	Observed *m/z*	Matched *m/z*	Ion	Neutral mass	Mass diff	Diff ppm	Assigned
467.45	467.45	467.4459	[M+H-H2O]+	484.4492	0.0041	9	FA 30:0;O2
479.45	479.481	479.4822	[M+H]+	478.475	0.0012	-3	WE 32:1
493.45	493.494	493.4978	[M+H]+	492.4906	0.0038	-8	WE 33:1
495.45	495.439	495.4408	[M+H-H2O]+	512.4441	0.0018	-4	DG 28:0
495.45	495.496	495.5136	[M+H]+	494.5064	0.0176	-36	WE 33:0
507.55	507.508	507.5135	[M+H]+	506.5063	0.0055	-11	WE 34:1
509.45	509.451	509.4564	[M+H]+	508.4492	0.0054	-11	FAHFA 32:2;O
509.45	509.451	509.42	[M+H]+	508.4128	0.031	61	DG 28:2
509.45	509.451	509.4564	[M+H-H2O]+	526.4597	0.0054	-11	DG 29:0
521.55	521.514	521.5291	[M+H]+	520.5219	0.0151	-29	WE 35:1
523.45	523.469	523.4357	[M+H]+	522.4285	0.0333	64	DG 29:2
523.45	523.469	523.4721	[M+H-H2O]+	540.4754	0.0031	-6	DG 30:0
535.55	535.533	535.5448	[M+H]+	534.5376	0.0118	-22	WE 36:1
537.45	537.486	537.4877	[M+H]+	536.4805	0.0017	-3	FAHFA 34:2;O
537.45	537.486	537.4513	[M+H]+	536.4441	0.0347	65	DG 30:2
537.45	537.486	537.4877	[M+H-H2O]+	554.491	0.0017	-3	DG 31:0
549.55	549.485	549.4877	[M+H-H2O]+	566.491	0.0027	-5	DG 32:1
549.55	549.545	549.5604	[M+H]+	548.5532	0.0154	-28	WE 37:1
551.45	551.493	551.5034	[M+H]+	550.4962	0.0104	-19	DG O-32:2
551.45	551.493	551.4823	[M+H]+	550.4751	0.0108	19	Retinyl oleate
551.45	551.493	551.467	[M+H]+	550.4598	0.026	47	DG 31:2
551.45	551.493	551.5034	[M+H-H2O]+	568.5067	0.0104	-19	DG 32:0
563.55	563.495	563.5034	[M+H-H2O]+	580.5067	0.0084	-15	DG 33:1
563.55	563.571	563.5761	[M+H]+	562.5689	0.0051	-9	WE 38:1
577.55	577.513	577.519	[M+H-H2O]+	594.5223	0.006	-10	DG 34:1
577.55	577.574	577.5917	[M+H]+	576.5845	0.0177	-31	WE 39:1
591.55	591.533	591.5347	[M+H-H2O]+	591.5347	0.0017	-3	DG 35:1
591.55	591.595	591.6074	[M+H]+	590.6002	0.0124	-21	WE 40:1
603.55	603.54	603.4983	[M+H]+	602.4911	0.0417	69	DG 35:4
603.55	603.54	603.5347	[M+H-H2O]+	620.538	0.0053	9	DG 36:2
603.55	603.54	603.5499	[M+H-H2O]+	620.5532	0.0099	-16	CE 16:2
605.55	605.552	605.5139	[M+H]+	604.5067	0.0381	63	DG 35:3
605.55	605.552	605.5503	[M+H-H2O]+	622.5536	0.0017	3	DG 36:1
605.55	605.552	605.5656	[M+H-H2O]+	622.5689	0.0136	-22	CE 16:1
607.55	607.564	607.5296	[M+H]+	606.5224	0.0344	57	DG 35:2
607.55	607.564	607.566	[M+H-H2O]+	624.5693	0.002	-3	DG 36:0
607.55	607.564	607.5812	[M+H-H2O]+	624.5845	0.0172	-28	CE 16:0
649.65	649.606	649.5918	[M+H]+	648.5846	0.0142	22	CE 18:2
649.65	649.606	649.6129	[M+H-H2O]+	666.6162	0.0069	-11	DG 39:0
663.65	663.62	663.6286	[M+H-H2O]+	680.6319	0.0086	-13	DG 40:0
663.65	663.62	663.6438	[M+H-H2O]+	680.6471	0.0238	-36	CE 20:0
668.65	668.649	668.6551	[M+H]+	667.6479	0.0061	-9	Cer 42:0;O3
676.65	676.658	676.6602	[M+H]+	675.653	-0.002	-3	Cer 44:2;O2
677.65	677.675	677.6442	[M+H-H2O]+	694.6475	0.0308	45	DG 41:0
692.65	692.654	692.6551	[M+H-H2O]+	709.6584	0.0011	-2	Cer 44:1;O4

Binned *m/z*	Observed *m/z*	Matched *m/z*	Ion	Neutral mass	Mass diff	Diff ppm	Assigned
724.75	724.714	724.7177	[M+H]+	723.7105	0.0037	-5	Cer 46:0;O3
777.65	777.692	777.6967	[M+H]+	776.6895	0.0047	-6	TG 46:1
778.65	778.68	778.6555	[M+H-H2O]+	795.6588	0.0245	31	HexCer 41:2;O2
805.75	805.703	805.728	[M+H]+	804.7208	0.025	-31	TG 48:1
806.65	806.68	806.6422	[M+H-H2O]+	823.6455	0.0378	47	PC O-40:4
855.75	855.746	855.7436	[M+H]+	854.7364	0.0024	3	TG 52:4
857.75	857.761	857.7593	[M+H]+	856.7521	0.0017	2	TG 52:3
859.75	859.772	859.7749	[M+H]+	858.7677	0.0029	-3	TG 52:2
879.75	879.728	879.7436	[M+H]+	878.7364	0.0156	-18	TG 54:6
881.75	881.751	881.7593	[M+H]+	880.7521	0.0083	-9	TG 54:5
883.75	883.766	883.7749	[M+H]+	882.7677	0.0089	-10	TG 54:4
885.75	885.797	885.7906	[M+H]+	884.7834	0.0064	7	TG 54:3

3. Table of SpiderCompar study negative ions tentative annotations

Appendix 11: Table of the tentative annotations of the SpiderCompar study negative ions

Binned *m/z*	Observed *m/z*	Matched *m/z*	Ion	Neutral mass	Mass diff	Diff ppm	Assigned
199.15	199.159	199.170	[M-H]-	200.178	0.011	-57	FA 12:0
199.15	199.159	199.170	[M-H]-	200.178	0.011	-57	WE 12:0
213.15	213.178	213.186	[M-H]-	214.193	0.008	-38	FA 13:0
213.15	213.178	213.186	[M-H]-	214.193	0.008	-38	WE 13:0
213.15	213.178	213.150	[M-H]-	214.157	0.028	133	FA 12:1;O
213.15	213.178	213.140	[M-H-H2O]-	231.141	0.038	178	FA 12:2
213.15	213.178	213.140	[M-H-H2O]-	231.141	0.038	178	WE 12:2
225.15	225.176	225.186	[M-H]-	226.193	0.010	-44	FA 14:1
225.15	225.176	225.186	[M-H]-	226.193	0.010	-44	WE 14:1
227.25	227.194	227.202	[M-H]-	228.209	0.008	-34	FA 14:0
227.25	227.194	227.202	[M-H]-	228.209	0.008	-34	WE 14:0
241.25	241.21	241.217	[M-H]-	242.225	0.007	-30	FA 15:0
241.25	241.21	241.217	[M-H]-	242.225	0.007	-30	WE 15:0
241.25	241.21	241.171	[M-H-H2O]-	259.172	0.039	160	FA 14:2
241.25	241.21	241.171	[M-H-H2O]-	259.172	0.039	160	WE 14:2
253.25	253.207	253.217	[M-H]-	254.225	0.010	-41	WE 16:1
253.25	253.207	253.217	[M-H]-	254.225	0.010	-41	FA 16:1
255.25	255.224	255.233	[M-H]-	256.240	0.009	-35	FA 16:0
255.25	255.224	255.233	[M-H]-	256.240	0.009	-35	WE 16:0
267.25	267.221	267.233	[M-H]-	268.240	0.012	-45	WE 17:1
267.25	267.221	267.233	[M-H]-	268.240	0.012	-45	FA 17:1
267.25	267.221	267.187	[M-H-H2O]-	285.188	0.034	127	FA 16:3
267.25	267.221	267.187	[M-H-H2O]-	285.188	0.034	127	WE 16:3
269.25	269.243	269.249	[M-H]-	270.256	0.006	-21	FA 17:0
269.25	269.243	269.249	[M-H]-	270.256	0.006	-21	WE 17:0
269.25	269.243	269.203	[M-H-H2O]-	287.204	0.040	150	FA 16:2
269.25	269.243	269.203	[M-H-H2O]-	287.204	0.040	150	WE 16:2
279.25	279.228	279.233	[M-H]-	280.240	0.005	-18	FA 18:2
279.25	279.228	279.233	[M-H]-	280.240	0.005	-18	WE 18:2
281.25	281.239	281.249	[M-H]-	282.256	0.010	-34	FA 18:1
281.25	281.239	281.249	[M-H]-	282.256	0.010	-34	WE 18:1

Binned *m/z*	Observed *m/z*	Matched *m/z*	Ion	Neutral mass	Mass diff	Diff ppm	Assigned
283.25	283.253	283.264	[M-H]-	284.272	0.011	-40	FA 18:0
283.25	283.253	283.264	[M-H]-	284.272	0.011	-40	WE 18:0
283.25	283.253	283.207	[M-H]-	284.214	0.046	163	ST 20:3;O
295.25	295.252	295.218	[M-H-H2O]-	313.219	0.034	114	FA 18:3
295.25	295.252	295.218	[M-H-H2O]-	313.219	0.034	114	ST 18:0;O2
295.25	295.252	295.218	[M-H-H2O]-	313.219	0.034	114	WE 18:3
295.25	295.252	295.264	[M-H]-	296.272	0.012	-42	FA 19:1
295.25	295.252	295.264	[M-H]-	296.272	0.012	-42	WE 19:1
297.25	297.271	297.234	[M-H-H2O]-	315.235	0.037	124	FA 18:2
297.25	297.271	297.234	[M-H-H2O]-	315.235	0.037	124	WE 18:2
297.25	297.271	297.280	[M-H]-	298.287	0.009	-30	FA 19:0
297.25	297.271	297.280	[M-H]-	298.287	0.009	-30	WE 19:0
307.25	307.252	307.264	[M-H]-	308.272	0.012	-40	FA 20:2
307.25	307.252	307.264	[M-H]-	308.272	0.012	-40	WE 20:2
309.25	309.273	309.280	[M-H]-	310.287	0.007	-22	FA 20:1
309.25	309.273	309.280	[M-H]-	310.287	0.007	-22	WE 20:1
339.35	339.319	339.327	[M-H]-	340.334	0.008	-23	FA 22:0
339.35	339.319	339.327	[M-H]-	340.334	0.008	-23	WE 22:0
353.35	353.329	353.297	[M-H-H2O]-	371.298	0.032	92	FA 22:2
353.35	353.329	353.297	[M-H-H2O]-	371.298	0.032	92	WE 22:2
353.35	353.329	353.343	[M-H]-	354.350	0.014	-38	FA 23:0
353.35	353.329	353.343	[M-H]-	354.350	0.014	-38	WE 23:0
353.35	353.329	353.285	[M-H]-	354.292	0.044	125	ST 25:3;O
367.35	367.343	367.358	[M-H]-	368.365	0.015	-41	FA 24:0
367.35	367.343	367.358	[M-H]-	368.365	0.015	-41	WE 24:0
367.35	367.343	367.322	[M-H]-	368.329	0.021	58	FA 23:1;O
381.35	381.364	381.374	[M-H]-	382.381	0.010	-26	FA 25:0
381.35	381.364	381.374	[M-H]-	382.381	0.010	-26	WE 25:0
381.35	381.364	381.337	[M-H]-	382.345	0.027	70	FA 24:1;O
381.35	381.364	381.316	[M-H]-	382.324	0.048	125	ST 27:3;O
381.35	381.364	381.328	[M-H-H2O]-	399.329	0.036	95	FA 24:2
381.35	381.364	381.328	[M-H-H2O]-	399.329	0.036	95	WE 24:2
395.35	395.383	395.332	[M-H]-	396.339	0.044	129	ST 28:3;O
395.35	395.383	395.390	[M-H]-	396.397	0.007	-16	FA 26:0
395.35	395.383	395.390	[M-H]-	396.397	0.007	-16	WE 26:0
409.35	409.395	409.405	[M-H]-	410.412	0.010	-25	FA 27:0
409.35	409.395	409.405	[M-H]-	410.412	0.010	-25	WE 27:0
409.35	409.395	409.369	[M-H]-	410.376	0.026	64	FA 26:1;O
409.35	409.395	409.348	[M-H]-	410.355	0.047	116	ST 29:3;O
409.35	409.395	409.359	[M-H-H2O]-	427.360	0.036	87	FA 26:2
409.35	409.395	409.359	[M-H-H2O]-	427.360	0.036	87	WE 26:2
415.35	415.346	415.358	[M-H]-	416.365	0.012	-29	FA 28:4
415.35	415.346	415.358	[M-H]-	416.365	0.012	-29	ST 28:1;O2
415.35	415.346	415.322	[M-H]-	416.329	0.024	58	ST 27:2;O3
415.35	415.346	415.349	[M-H-H2O]-	433.350	0.003	-6	ST 28:2;O
415.35	415.346	415.333	[M-H-H2O]-	433.334	0.013	31	FA 24:1;O2
415.35	429.362	429.385	[M-H-H2O]-	447.386	0.023	-54	FA 26:0;O
415.35	429.362	429.328	[M-H-H2O]-	447.329	0.034	79	FA 28:6
415.35	429.362	429.328	[M-H-H2O]-	447.329	0.034	79	ST 28:3;O2
429.35	429.362	429.374	[M-H]-	430.381	0.012	-27	FA 29:4
429.35	429.362	429.374	[M-H]-	430.381	0.012	-27	ST 29:1;O2
449.45	449.429	449.436	[M-H]-	450.444	0.007	-16	FA 30:1
449.45	449.429	449.436	[M-H]-	450.444	0.007	-16	WE 30:1

Binned *m/z*	Observed *m/z*	Matched *m/z*	Ion	Neutral mass	Mass diff	Diff ppm	Assigned
451.45	451.444	451.452	[M-H]-	452.459	0.008	-18	FA 30:0
451.45	451.444	451.452	[M-H]-	452.459	0.008	-18	WE 30:0
459.35	459.337	459.348	[M-H]-	460.355	0.011	-24	ST 29:2;O4
459.35	459.337	459.312	[M-H]-	460.319	0.025	55	ST 28:3;O5
459.35	459.337	459.375	[M-H-H2O]-	477.376	0.038	-82	FA 30:5
459.35	459.337	459.375	[M-H-H2O]-	477.376	0.038	-82	ST 30:2;O2
477.45	477.455	477.468	[M-H]-	478.475	0.013	-27	FA 32:1
477.45	477.455	477.468	[M-H]-	478.475	0.013	-27	WE 32:1
584.45	584.456	584.4201	[M-H-H2O]-	602.421	0.036	61	LPE O-24:0;O
584.45	584.465	584.4201	[M-H-H2O]-	602.421	0.045	77	LPE O-24:0;O
596.45	596.461	596.4201	[M-H-H2O]-	614.421	0.041	69	LPC 22:0

D. SMPatho study

1. Eligibility criteria

a) Inclusion criteria

Population related criteria

For any subject to be included in the study, he must meet the following criteria:

- Given written consent to participate in the study
- Phototype II to IV according to the Fitzpatrick classification
- Affiliated to a social security scheme or beneficiary of such a scheme
- **Erreur ! Nom de propriété de document inconnu.**For women of childbearing potential: use of a contraception method for at least 4 weeks, assessed as effective by the investigator

For subjects in the facial acne subgroup and their associated control subgroup:

- Male or female, aged 18 to 30 included

For subjects in the upper limb atopic dermatitis subgroup and their associated control subgroup:

- Male or female, aged 20 to 50 included

For subjects in the limb plaque psoriasis subgroup and their associated control subgroup:

- Male or female, aged 20 to 55 included

For subjects in the telangiectatic erythrocouperosis and papule of the face subgroup and their associated control subgroup:

- Male or female, aged between 30 and 55 included

For subjects in the seborrheic scalp dermatitis subgroup and their associated control subgroup:

- Male or female, aged 20 to 45 included

Dermatoses related criteria

For subjects in the facial acne subgroup:

- Subject with mild to severe facial acne, whose GAE (Global Acne Evaluation) score on the face is 2 to 4 on a scale of 0 (no lesion) to 5 (very severe)
- Subject with at least one area on the face:
  - Lesional at the immediate border of a papule
  - Peri-lesional in the vicinity of inflammatory lesions (papule; about 1cm)
- Subject with a lesion-free area on the inner side of the forearm for reference measurement

For subjects in the upper limb atopic dermatitis subgroup:

- Subjects with mild to moderate localized atopic dermatitis of the upper limbs with a SCORAD between 15 and 40 included with:
  - For drought a score ≥ 2 on a scale ranging from 0 (absent) to 3 (severe)
- Subject with at least one inflammatory flare of atopic dermatitis on the upper limbs within 2 years prior to the day of inclusion
- Subject with at least one area on an upper limb (excluding the hand):
  - Lesional defined by the following SCORAD target signs between 3 and 12:
    - Erythema 1 to 3
    - Drought ≥2
    - Oedema / papule 0 to 3
    - Oozing or scabby lesions of 0
    - Excoriation of 0
    - Lichenification from 0 to 3

      On a scale from 0 (absent) to 3 (severe)
  - Peri-lesional near the lesion area (about 1cm)
- Subject with a lesion-free area on the inner side of the forearm for reference measurement

For subjects in the limb plaque psoriasis subgroup:

- Mild to moderate plaque psoriasis with an Investigator Global Assessment (IGA) score between 2 and 3 on a scale of 0 (clear) to 5 (very severe)
- Subject with at least one area on an upper limb (excluding the hand) or lower limb:
  - Lesional:
    - Crack-free and crust-free
    - With an erythema score ≥ 1 on a scale ranging from 0 (absent) to 3 (severe)
    - With a peeling score between 1 (mild) and 2 (moderate) on a scale ranging from 0 (absent) to 3 (severe)
    - With an oedema score of 0 (absent) on a scale of 0 (absent) to 3 (severe)
  - Peri-lesional:
    - Crack-free and crust-free
    - Close to the lesion area (of the order of 1cm)
- Subject with a lesion-free area on the inner side of the forearm for reference measurement

For subjects in the erythrocouperosis telangiectasia and papule of the face subgroup:

- Subject with mild to moderate erythrocouperosis telangiectasia and papules of the face with an IGA score between 2 and 3 on a scale of 0 (absent) to 4 (severe)
- Subject with at least one area on the face:
    - Lesional: immediate border of papule with a persistent erythema score ≥ 1 on a rating scale ranging from 0 (absent) to 3 (severe)
    - Peri-lesional:
        - In the vicinity of inflammatory lesions (papules; about 1cm)
        - Variant of at least 1 point less on the erythema score than the lesion area
- Subject with a lesion-free area on the inner side of the forearm for reference measurement

For subjects in the seborrheic scalp dermatitis subgroup:

- Mild to moderate seborrheic dermatitis of the scalp with an IGA score between 2 and 3 on a scale of 0 (absent) to 4 (severe)
- Subject with at least one area of the scalp:
    - Lesional:
        - with an erythema score ≥ 1 on a scale of 0 (absent) to 3 (severe)
        - with clinically visible scaling
    - Peri-lesional near the injury area (about 1cm)
- Subject with a lesion-free area on the inner side of the forearm for reference measurement

b) Exclusion criteria

Population related criteria

- For women of childbearing potential: pregnancy or breastfeeding
- Subject with linguistic or psychological incapacity to understand the information given and to sign the informed consent
- Subject who, in the opinion of the investigator, is unable to comply with the protocol requirements
- Subject deprived of liberty by judicial or administrative decision, under guardianship or curatorship
- Subject in a position of potential conflict of interest and/or family member of any person involved in the clinical trial at the investigator site
- Subject participating, having participated in the previous weeks or months, or planning to participate in another clinical trial that may interfere with the study, as determined by the investigator

Criteria related to pathology and skin condition

- Subjects with premature skin ageing related to a genetic disease
- Subject with solar erythema in at least one study area
- Subjects with tattoos or scars or any other dermatological signs on at least one study area that may interfere with the study in the opinion of the investigator
- Subject with autoimmune disease
- Subject with any type of complication in at least one study area (such as excoriation, primary bacterial, viral, fungal or parasitic infection, etc.) as determined by the investigator

Criteria for control subgroup

- Subject with a dermatosis or any type of lesion in the area corresponding to the lesion, peri-lesion or reference area of the associated dermatosis subgroup that may interfere with the study in the opinion of the investigator

Criteria for chronic inflammatory dermatoses

For subjects in the facial acne subgroup:

- Subjects with other dermatoses (chronic/acute, inflammatory, infectious, immune) on the face that may interfere with the study in the opinion of the investigator.

For subjects in the upper limb atopic dermatitis subgroup:

- Subject with other dermatosis (chronic/acute, inflammatory, infectious, immune) on the upper limb(s) under study that may interfere with the study in the opinion of the investigator.

For subjects in the limb plaque psoriasis subgroup:

- Subject with isolated palmoplantar psoriasis
- Subjects with an isolated form of non-plaque skin psoriasis (guttate, pustular, erythrodermic or inverted fold psoriasis)
- Subject with other dermatosis (chronic/acute, inflammatory, infectious, immune) on the upper and/or lower limb(s) under study that may interfere with the study in the opinion of the investigator.

For subjects in the erythrocouperosis telangiectasia and papule of the face subgroup:

- Subjects with other dermatoses (chronic/acute, inflammatory, infectious, immune) on the face that may interfere with the study in the opinion of the investigator.

For subjects in the seborrheic scalp dermatitis subgroup:

- Seborrheic dermatitis under medical treatment
- Subjects with other dermatoses (chronic/acute, inflammatory, infectious, immune) on the scalp that may interfere with the study in the opinion of the investigator (e.g. contact dermatitis or alopecia)

Criteria for treatments and cosmetics

For all subjects

- Oral use of isotretinoin or acitretin (oral vit-A and derivatives) within 6 months prior to the inclusion visit or on the day of the visit
- Topical retinoid treatment in at least one study area that may influence outcome in the opinion of the investigator in the month prior to the inclusion visit or on the day of the visit
- Phototherapy treatment on at least one study area within 4 weeks prior to the inclusion visit or on the day of the visit
- Topical or oral treatment established or modified in the previous weeks or about to be established or modified during the study, which may interfere with the results of the study in the opinion of the investigator (e.g. modifying skin characteristics: pigmentation inducing treatment, keratolytic,...)

- Anti-inflammatory treatment (steroidal or non-steroidal) taken daily and repeatedly for more than 5 consecutive days in the week before the inclusion visit
- Application of any topical vitamin D treatment to at least one study area within 3 weeks prior to the inclusion visit or on the day of the visit
- Application of topical dermocorticoids or topical immunomodulators (tacrolimus), antifungals, local antibiotics to at least one study area within 3 weeks prior to the inclusion visit or on the day of the visit
- Application of water, product or topical treatment to at least one study area following the last wash the night before the visit
- Application of water, topical product or make-up to at least one study area on the day of the inclusion visit

For subjects in the seborrheic scalp dermatitis subgroup and its associated control subgroup:

- Use on the scalp of any product that may be active on scaly conditions, to be rinsed or applied (anti-dandruff shampoos, anti-fungal shampoos, vinegar rinses, essential oils, etc.) within the 2 weeks preceding the inclusion visit or on the day of the visit
- Any technique aimed at modifying the colour or condition of the hair (colouring, bleaching, perming, straightening, etc.) carried out in the 2 weeks preceding the visit or on the day of the visit
- Scalp wash performed within 2 days prior to the inclusion visit or on the day of the visit

2. Acne supplementary results

Appendix 12: Boxplot of the 8 more significant peaks showing whether the 4 lowest (397.45, 425.45, 383.35, and 351.35) in green or the 4 highest FC values (273.25, 233.25, 533.55, 547.55) in blue according to the results presented in the Table 17. The 411.45 has been added for its interest.

Bibliography

Bibliography

1. Saudemont, P. *et al.* Real-Time Molecular Diagnosis of Tumors Using Water-Assisted Laser Desorption/Ionization Mass Spectrometry Technology. *Cancer Cell* **34**, 840-851.e4 (2018).
2. Vos, T. *et al.* Years lived with disability (YLDs) for 1160 sequelae of 289 diseases and injuries 1990–2010: a systematic analysis for the Global Burden of Disease Study 2010. *The Lancet* **380**, 2163–2196 (2012).
3. Leung, A. K. C., Hon, K. L. E. & Robson, W. L. M. Atopic dermatitis. *Adv Pediatr* **54**, 241–273 (2007).
4. Lynn, D. D., Umari, T., Dunnick, C. A. & Dellavalle, R. P. The epidemiology of acne vulgaris in late adolescence. *Adolesc Health Med Ther* **7**, 13–25 (2016).
5. Chiu, L. S., Chow, V. C. Y., Ling, J. M. L. & Hon, K. L. Staphylococcus aureus carriage in the anterior nares of close contacts of patients with atopic dermatitis. *Arch Dermatol* **146**, 748–752 (2010).
6. Williams, J. V., Vowels, B. R., Honig, P. J. & Leyden, J. J. S. aureus isolation from the lesions, the hands, and the anterior nares of patients with atopic dermatitis. *Pediatr Dermatol* **15**, 194–198 (1998).
7. World Health Organization. *Global report on psoriasis*. (World Health Organization, 2016).
8. Tucker, D. & Masood, S. *Seborrheic Dermatitis*. *StatPearls [Internet]* (StatPearls Publishing, 2020).
9. Palamaras, I., Kyriakis, K. P. & Stavrianeas, N. G. Seborrheic dermatitis: lifetime detection rates. *Journal of the European Academy of Dermatology and Venereology* **26**, 524–526 (2012).
10. Sanders, M. G. H., Pardo, L. M., Franco, O. H., Ginger, R. S. & Nijsten, T. Prevalence and determinants of seborrhoeic dermatitis in a middle-aged and elderly population: the Rotterdam Study. *British Journal of Dermatology* **178**, 148–153 (2018).
11. Agrawal, K. *et al.* Effects of atopic dermatitis and gender on sebum lipid mediator and fatty acid profiles. *Prostaglandins, Leukotrienes and Essential Fatty Acids* **134**, 7–16 (2018).
12. Ní Raghallaigh, S., Bender, K., Lacey, N., Brennan, L. & Powell, F. C. The fatty acid profile of the skin surface lipid layer in papulopustular rosacea: Fatty acid profile in papulopustular rosacea. *British Journal of Dermatology* **166**, 279–287 (2012).
13. van Smeden, J. & Bouwstra, J. A. Stratum Corneum Lipids: Their Role for the Skin Barrier Function in Healthy Subjects and Atopic Dermatitis Patients. in *Current Problems in Dermatology* (ed. Agner, T.) vol. 49 8–26 (S. Karger AG, 2016).
14. Katona, M., Dénes, J., Skoumal, R., Tóth, M. & Takáts, Z. Intact skin analysis by desorption electrospray ionization mass spectrometry. *Analyst* **136**, 835–840 (2011).
15. Chen, H., Talaty, N. N., Takáts, Z. & Cooks, R. G. Desorption electrospray ionization mass spectrometry for high-throughput analysis of pharmaceutical samples in the ambient environment. *Anal. Chem.* **77**, 6915–6927 (2005).
16. Talaty, N., Takáts, Z. & Cooks, R. G. Rapid in situ detection of alkaloids in plant tissue under ambient conditions using desorption electrospray ionization. *Analyst* **130**, 1624–1633 (2005).
17. Takáts, Z., Wiseman, J. M. & Cooks, R. G. Ambient mass spectrometry using desorption electrospray ionization (DESI): instrumentation, mechanisms and applications in forensics, chemistry, and biology. *J Mass Spectrom* **40**, 1261–1275 (2005).
18. Morelato, M. *et al.* Screening of gunshot residues using desorption electrospray ionisation-mass spectrometry (DESI-MS). *Forensic Sci. Int.* **217**, 101–106 (2012).
19. Fredman, G., Skov, L., Mann, M. & Dyring-Andersen, B. Towards Precision Dermatology: Emerging Role of Proteomic Analysis of the Skin. *Dermatology* 1–10 (2021) doi:10.1159/000516764.

20. Schäfer, K.-C. *et al. In vivo*, *in situ* tissue analysis using Rapid Evaporative Ionization Mass Spectrometry. *Angew. Chem. Int. Ed. Engl.* **48**, 8240–8242 (2009).
21. Balog, J. *et al.* Intraoperative Tissue Identification Using Rapid Evaporative Ionization Mass Spectrometry. *Science Translational Medicine* **5**, (2013).
22. St John, E. R. *et al.* Rapid evaporative ionisation mass spectrometry of electrosurgical vapours for the identification of breast pathology: towards an intelligent knife for breast cancer surgery. *Breast Cancer Res.* **19**, 59 (2017).
23. Zhang, J. *et al.* Nondestructive tissue analysis for ex vivo and in vivo cancer diagnosis using a handheld mass spectrometry system. *Sci Transl Med* **9**, (2017).
24. Fatou, B. *et al.* In vivo Real-Time Mass Spectrometry for Guided Surgery Application. *Sci Rep* **6**, 25919 (2016).
25. Berkenkamp, S., Karas, M. & Hillenkamp, F. Ice as a matrix for IR-matrix-assisted laser desorption/ionization: mass spectra from a protein single crystal. *Proc. Natl. Acad. Sci. U.S.A.* **93**, 7003–7007 (1996).
26. Leisner, A., Rohlfing, A., Berkenkamp, S., Hillenkamp, F. & Dreisewerd, K. Infrared laser post-ionization of large biomolecules from an IR-MALD(I) plume. *J. Am. Soc. Mass Spectrom.* **15**, 934–941 (2004).
27. Witt, L. *et al.* Water ice is a soft matrix for the structural characterization of glycosaminoglycans by infrared matrix-assisted laser desorption/ionization. *Anal. Chem.* **86**, 6439–6446 (2014).
28. Fatou, B. *et al.* Real time and in vivo pharmaceutical and environmental studies with SpiderMass instrument. *Journal of Biotechnology* **281**, 61–66 (2018).
29. Kendall, A. C. & Nicolaou, A. Bioactive lipid mediators in skin inflammation and immunity. *Prog. Lipid Res.* **52**, 141–164 (2013).
30. Kiezel-Tsugunova, M., Kendall, A. C. & Nicolaou, A. Fatty acids and related lipid mediators in the regulation of cutaneous inflammation. *Biochem. Soc. Trans.* **46**, 119–129 (2018).
31. Nicolaou, A. Eicosanoids in skin inflammation. *Prostaglandins Leukot. Essent. Fatty Acids* **88**, 131–138 (2013).
32. Squires, G. Francis Aston and the mass spectrograph. *J. Chem. Soc., Dalton Trans.* 3893–3900 (1998) doi:10.1039/A804629H.
33. Karas, M. & Hillenkamp, F. Laser desorption ionization of proteins with molecular masses exceeding 10,000 daltons. *Anal. Chem.* **60**, 2299–2301 (1988).
34. Fenn, J. B., Mann, M., Meng, C. K., Wong, S. F. & Whitehouse, C. M. Electrospray ionization for mass spectrometry of large biomolecules. *Science* **246**, 64–71 (1989).
35. Griffiths, J. A brief history of mass spectrometry. *Anal Chem* **80**, 5678–5683 (2008).
36. Cooks, R. G., Ouyang, Z., Takats, Z. & Wiseman, J. M. Ambient Mass Spectrometry. *Science* **311**, 1566–1570 (2006).
37. Takáts, Z., Wiseman, J. M., Gologan, B. & Cooks, R. G. Mass spectrometry sampling under ambient conditions with desorption electrospray ionization. *Science* **306**, 471–473 (2004).
38. Cody, R. B., Laramée, J. A. & Durst, H. D. Versatile new ion source for the analysis of materials in open air under ambient conditions. *Anal. Chem.* **77**, 2297–2302 (2005).
39. Van Berkel, G. J., Sanchez, A. D. & Quirke, J. M. E. Thin-Layer Chromatography and Electrospray Mass Spectrometry Coupled Using a Surface Sampling Probe. https://pubs.acs.org/doi/pdf/10.1021/ac020540%2B (2002) doi:10.1021/ac020540+.
40. Smoluch, M., Mielczarek, P. & Silberring, J. Plasma-based ambient ionization mass spectrometry in bioanalytical sciences. *Mass Spectrometry Reviews* **35**, 22–34 (2016).
41. Kuo, T.-H., Dutkiewicz, E. P., Pei, J. & Hsu, C.-C. Ambient Ionization Mass Spectrometry Today and Tomorrow: Embracing Challenges and Opportunities. *Anal. Chem.* **92**, 2353–2363 (2020).

42. Huang, M.-Z., Cheng, S.-C., Cho, Y.-T. & Shiea, J. Ambient ionization mass spectrometry: A tutorial. *Analytica Chimica Acta* **702**, 1–15 (2011).
43. Feider, C. L., Krieger, A., DeHoog, R. J. & Eberlin, L. S. Ambient Ionization Mass Spectrometry: Recent Developments and Applications. *Anal Chem* **91**, 4266–4290 (2019).
44. Roach, P. J., Laskin, J. & Laskin, A. Nanospray desorption electrospray ionization: an ambient method for liquid-extraction surface sampling in mass spectrometry. *Analyst* **135**, 2233–2236 (2010).
45. Owlstone Medical. New "MasSpec Pen" handheld tissue analysis for in vivo and ex vivo cancer detection. https://www.owlstonemedical.com/about/blog/2017/sep/26/new-masspec-pen-handheld-tissue-analysis-vivo-and-/.
46. Bernier, M. C. *et al.* Triboelectric Nanogenerator (TENG) Mass Spectrometry of Falsified Antimalarials. *Rapid Commun Mass Spectrom* (2018) doi:10.1002/rcm.8207.
47. Tillner, J. *et al.* Faster, more reproducible DESI-MS for biological tissue imaging. *2098* (2017) doi:10.1007/s13361-017-1714-z.
48. Chan, C.-C., Bolgar, M. S., Miller, S. A. & Attygalle, A. B. Desorption ionization by charge exchange (DICE) for sample analysis under ambient conditions by mass spectrometry. *J Am Soc Mass Spectrom* **21**, 1554–1560 (2010).
49. Chan, C.-C., Bolgar, M. S., Miller, S. A. & Attygalle, A. B. A combined desorption ionization by charge exchange (DICE) and desorption electrospray ionization (DESI) source for mass spectrometry. *J Am Soc Mass Spectrom* **22**, 173–178 (2011).
50. Haddad, R., Sparrapan, R. & Eberlin, M. N. Desorption sonic spray ionization for (high) voltage-free ambient mass spectrometry. *Rapid Communications in Mass Spectrometry* **20**, 2901–2905 (2006).
51. Eberlin, L. S., Ferreira, C. R., Dill, A. L., Ifa, D. R. & Cooks, R. G. Desorption electrospray ionization mass spectrometry for lipid characterization and biological tissue imaging. *Biochim Biophys Acta* **1811**, 946–960 (2011).
52. Chen, H., Venter, A. & Cooks, R. G. Extractive electrospray ionization for direct analysis of undiluted urine, milk and other complex mixtures without sample preparation. *Chem Commun (Camb)* 2042–2044 (2006) doi:10.1039/b602614a.
53. Gaisl, T. *et al.* Real-time exhaled breath analysis in patients with cystic fibrosis and controls. *J Breath Res* **12**, 036013 (2018).
54. Kertesz, V. & Van Berkel, G. J. Fully automated liquid extraction-based surface sampling and ionization using a chip-based robotic nanoelectrospray platform. *J Mass Spectrom* **45**, 252–260 (2010).
55. Quanico, J. *et al.* Development of liquid microjunction extraction strategy for improving protein identification from tissue sections. *J Proteomics* **79**, 200–218 (2013).
56. Pagnotti, V. S., Chubatyi, N. D. & McEwen, C. N. Solvent Assisted Inlet Ionization: An Ultrasensitive New Liquid Introduction Ionization Method for Mass Spectrometry. *Anal. Chem.* **83**, 3981–3985 (2011).
57. Sans, M. *et al.* Performance of the MasSpec Pen for Rapid Diagnosis of Ovarian Cancer. *Clin. Chem.* **65**, 674–683 (2019).
58. Keating, M. F. *et al.* Integrating the MasSpec Pen to the da Vinci Surgical System for In Vivo Tissue Analysis during a Robotic Assisted Porcine Surgery. *Anal. Chem.* **92**, 11535–11542 (2020).
59. Zhang, J. *et al.* Direct Molecular Analysis of In Vivo and Freshly Excised Tissues in Human Surgeries with the MasSpec Pen Technology. *medRxiv* 2020.12.14.20248101 (2020) doi:10.1101/2020.12.14.20248101.
60. Wang, H., Liu, J., Cooks, R. G. & Ouyang, Z. Paper Spray for Direct Analysis of Complex Mixtures Using Mass Spectrometry. *Angewandte Chemie International Edition* **49**, 877–880 (2010).

61. Manicke, N. E., Abu-Rabie, P., Spooner, N., Ouyang, Z. & Cooks, R. G. Quantitative analysis of therapeutic drugs in dried blood spot samples by paper spray mass spectrometry: an avenue to therapeutic drug monitoring. *J Am Soc Mass Spectrom* **22**, 1501–1507 (2011).
62. Dulay, M. T. & Zare, R. N. Polymer-spray mass spectrometric detection and quantitation of hydrophilic compounds and some narcotics. *Rapid Commun Mass Spectrom* **31**, 1651–1658 (2017).
63. Straub, R. F. & Voyksner, R. D. Negative ion formation in electrospray mass spectrometry. *Journal of the American Society for Mass Spectrometry* **4**, 578–587 (1993).
64. Salentijn, G. Ij., Oleschuk, R. D. & Verpoorte, E. 3D-Printed Paper Spray Ionization Cartridge with Integrated Desolvation Feature and Ion Optics. *Anal. Chem.* **89**, 11419–11426 (2017).
65. Hu, B., So, P.-K., Chen, H. & Yao, Z.-P. Electrospray Ionization Using Wooden Tips. *Anal. Chem.* **83**, 8201–8207 (2011).
66. Pavlovich, M. J., Musselman, B. & Hall, A. B. Direct analysis in real time-Mass spectrometry (DART-MS) in forensic and security applications. *Mass Spectrom Rev* **37**, 171–187 (2018).
67. Pierce, C. Y. *et al.* Ambient generation of fatty acid methyl ester ions from bacterial whole cells by direct analysis in real time (DART) mass spectrometry. *Chem Commun (Camb)* 807–809 (2007) doi:10.1039/b613200f.
68. Busman, M., Liu, J., Zhong, H., Bobell, J. R. & Maragos, C. M. Determination of the aflatoxin AFB1 from corn by direct analysis in real time-mass spectrometry (DART-MS). *Food Addit Contam Part A Chem Anal Control Expo Risk Assess* **31**, 932–939 (2014).
69. Vaclavik, L., Cajka, T., Hrbek, V. & Hajslova, J. Ambient mass spectrometry employing direct analysis in real time (DART) ion source for olive oil quality and authenticity assessment. *Analytica Chimica Acta* **645**, 56–63 (2009).
70. Harper, J. D. *et al.* Low-temperature plasma probe for ambient desorption ionization. *Anal. Chem.* **80**, 9097–9104 (2008).
71. Maiman, T. H. Stimulated Optical Radiation in Ruby. *Nature* **187**, 493–494 (1960).
72. Honig, R. E. & Woolston, J. R. Laser-Induced Emission of Electrons, Ions, And Neutral Atoms from Solid Surfaces. *Appl. Phys. Lett.* **2**, 138–139 (1963).
73. Singh, J. P. & Thakur, S. N. *Laser-induced breakdown spectroscopy*. (2020).
74. Azov, V. A., Mueller, L. & Makarov, A. A. Laser ionization mass spectrometry at 55: Quo Vadis? *Mass Spec Rev* mas.21669 (2020) doi:10.1002/mas.21669.
75. Laiko, V. V., Baldwin, M. A. & Burlingame, A. L. Atmospheric pressure matrix-assisted laser desorption/ionization mass spectrometry. *Anal. Chem.* **72**, 652–657 (2000).
76. Kompauer, M., Heiles, S. & Spengler, B. Atmospheric pressure MALDI mass spectrometry imaging of tissues and cells at 1.4-µm lateral resolution. *Nature Methods* **14**, 90–96 (2017).
77. Ding, X., Liu, K. & Shi, Z. Laser Desorption/Ablation Postionization Mass Spectrometry : Recent Progress in Bioanalytical Applications. *Mass Spec Rev* mas.21649 (2020) doi:10.1002/mas.21649.
78. Nemes, P. & Vertes, A. Laser ablation electrospray ionization for atmospheric pressure molecular imaging mass spectrometry. *Methods Mol. Biol.* **656**, 159–171 (2010).
79. Compton, L. R., Reschke, B., Friend, J., Powell, M. & Vertes, A. Remote laser ablation electrospray ionization mass spectrometry for non-proximate analysis of biological tissues. *Rapid Commun. Mass Spectrom.* **29**, 67–73 (2015).
80. Li, H. & Vertes, A. Solvent gradient electrospray for laser ablation electrospray ionization mass spectrometry. *Analyst* **142**, 2921–2927 (2017).

81. Kooijman, P. C. *et al.* A novel dual ionization modality source for infrared laser ablation post-ionization mass spectrometry imaging to study fungicide metabolism and transport. *International Journal of Mass Spectrometry* **465**, 116602 (2021).
82. Saudemont, P. *et al.* Real-Time Molecular Diagnosis of Tumors Using Water-Assisted Laser Desorption/Ionization Mass Spectrometry Technology. *Cancer Cell* **34**, 840-851.e4 (2018).
83. Seddiki, K. *et al.* Cumulative learning enables convolutional neural network representations for small mass spectrometry data classification. *Nature Communications* **11**, 5595 (2020).
84. Jowett, N. *et al.* Bone Ablation without Thermal or Acoustic Mechanical Injury via a Novel Picosecond Infrared Laser (PIRL). *Otolaryngology -- Head and Neck Surgery* **150**, 385–393 (2014).
85. Kwiatkowski, M. *et al.* Ultrafast extraction of proteins from tissues using desorption by impulsive vibrational excitation. *Angew Chem Int Ed Engl* **54**, 285–288 (2015).
86. Woolman, M. *et al.* Rapid determination of medulloblastoma subgroup affiliation with mass spectrometry using a handheld picosecond infrared laser desorption probe. *Chem. Sci.* **8**, 6508–6519 (2017).
87. Woolman, M. *et al.* Picosecond Infrared Laser Desorption Mass Spectrometry Identifies Medulloblastoma Subgroups on Intrasurgical Timescales. *Cancer Res* **79**, 2426–2434 (2019).
88. Woolman, M. *et al.* Optimized Mass Spectrometry Analysis Workflow with Polarimetric Guidance for *ex vivo* and *in situ* Sampling of Biological Tissues. *Sci Rep* **7**, 468 (2017).
89. Schluter, M. *et al.* Towards OCT-Navigated Tissue Ablation with a Picosecond Infrared Laser (PIRL) and Mass-Spectrometric Analysis. *Annu Int Conf IEEE Eng Med Biol Soc* **2019**, 158–161 (2019).
90. Katz, L. *et al.* Dual Laser and Desorption Electrospray Ionization Mass Spectrometry Imaging Using the Same Interface. *Anal Chem* **92**, 6349–6357 (2020).
91. Woolman, M. *et al. In situ* tissue pathology from spatially encoded mass spectrometry classifiers visualized in real time through augmented reality. *Chem. Sci.* **11**, 8723–8735 (2020).
92. Hamad, A. H. Effects of Different Laser Pulse Regimes (Nanosecond, Picosecond and Femtosecond) on the Ablation of Materials for Production of Nanoparticles in Liquid Solution. *High Energy and Short Pulse Lasers* (2016) doi:10.5772/63892.
93. Strittmatter, N. *et al.* Analysis of intact bacteria using rapid evaporative ionisation mass spectrometry. *Chem Commun (Camb)* **49**, 6188–6190 (2013).
94. Manoli, E. *et al.* Validation of Ultrasonic Harmonic Scalpel for Real-Time Tissue Identification Using Rapid Evaporative Ionization Mass Spectrometry. *Anal. Chem.* **93**, 5906–5916 (2021).
95. Abu-Rabie, P., Sheelan, D., Laures, A., Spaull, J. & Dowell, S. Increasing the discrimination power of Rapid Evaporative Ionization Mass Spectrometry (REIMS) in analytical control tissue quality screening and cell line sample identification. *Rapid Commun. Mass Spectrom.* (2019) doi:10.1002/rcm.8525.
96. Guitton, Y. *et al.* Rapid evaporative ionisation mass spectrometry and chemometrics for high-throughput screening of growth promoters in meat producing animals. *Food Addit Contam Part A Chem Anal Control Expo Risk Assess* **35**, 900–910 (2018).
97. Rigano, F. *et al.* Rapid evaporative ionization mass spectrometry coupled with an electrosurgical knife for the rapid identification of Mediterranean Sea species. *Anal Bioanal Chem* (2019) doi:10.1007/s00216-019-02000-z.
98. Song, G. *et al.* In Situ Method for Real-Time Discriminating Salmon and Rainbow Trout without Sample Preparation Using iKnife and Rapid Evaporative Ionization Mass Spectrometry-Based Lipidomics. *J. Agric. Food Chem.* **67**, 4679–4688 (2019).
99. Verplanken, K. *et al.* Rapid evaporative ionization mass spectrometry for high-throughput screening in food analysis: The case of boar taint. *Talanta* **169**, 30–36 (2017).

100. Alexander, J. *et al.* A novel methodology for in vivo endoscopic phenotyping of colorectal cancer based on real-time analysis of the mucosal lipidome: a prospective observational study of the iKnife. *Surg Endosc* **31**, 1361–1370 (2017).
101. Balog, J. *et al.* In vivo endoscopic tissue identification by rapid evaporative ionization mass spectrometry (REIMS). *Angew. Chem. Int. Ed. Engl.* **54**, 11059–11062 (2015).
102. Phelps, D. L. *et al.* The surgical intelligent knife distinguishes normal, borderline and malignant gynaecological tissues using rapid evaporative ionisation mass spectrometry (REIMS). *Br. J. Cancer* **118**, 1349–1358 (2018).
103. Vaysse, P.-M. *et al.* Stromal vapors for real-time molecular guidance of breast-conserving surgery. *Sci Rep* **10**, 20109 (2020).
104. Tzafetas, M. *et al.* The intelligent knife (iKnife) and its intraoperative diagnostic advantage for the treatment of cervical disease. *Proc Natl Acad Sci U S A* **117**, 7338–7346 (2020).
105. Robb, null, Covey, null & Bruins, null. Atmospheric pressure photoionization: an ionization method for liquid chromatography-mass spectrometry. *Anal Chem* **72**, 3653–3659 (2000).
106. Schäfer, K.-C. *et al.* Real Time Analysis of Brain Tissue by Direct Combination of Ultrasonic Surgical Aspiration and Sonic Spray Mass Spectrometry. *Anal. Chem.* **83**, 7729–7735 (2011).
107. McEwen, C. N., Pagnotti, V. S., Inutan, E. D. & Trimpin, S. New Paradigm in Ionization: Multiply Charged Ion Formation from a Solid Matrix without a Laser or Voltage. *Anal. Chem.* **82**, 9164–9168 (2010).
108. Pagnotti, V. S., Inutan, E. D., Marshall, D. D., McEwen, C. N. & Trimpin, S. Inlet Ionization: A New Highly Sensitive Approach for Liquid Chromatography/Mass Spectrometry of Small and Large Molecules. *Anal. Chem.* **83**, 7591–7594 (2011).
109. Horan, A. J., Apsokardu, M. J. & Johnston, M. V. Droplet Assisted Inlet Ionization for Online Analysis of Airborne Nanoparticles. *Anal. Chem.* **89**, 1059–1062 (2017).
110. Zhang, J., Sans, M., Garza, K. Y. & Eberlin, L. S. Mass Spectrometry Technologies To Advance Care For Cancer Patients In Clinical And Intraoperative Use. *Mass Spec Rev* mas.21664 (2020) doi:10.1002/mas.21664.
111. Ogrinc, N., Saudemont, P., Takats, Z., Salzet, M. & Fournier, I. Cancer Surgery 2.0: Guidance by Real-Time Molecular Technologies. *Trends in Molecular Medicine* (2021) doi:10.1016/j.molmed.2021.04.001.
112. Stücker, M. *et al.* The cutaneous uptake of atmospheric oxygen contributes significantly to the oxygen supply of human dermis and epidermis. *J Physiol* **538**, 985–994 (2002).
113. Nemes, Z. & Steinert, P. M. Bricks and mortar of the epidermal barrier. *Experimental & Molecular Medicine* **31**, 5–19 (1999).
114. Rawlings, A. V. & Harding, C. R. Moisturization and skin barrier function. *Dermatol Ther* **17 Suppl 1**, 43–48 (2004).
115. Riethmuller, C. *et al.* Filaggrin breakdown products determine corneocyte conformation in patients with atopic dermatitis. *Journal of Allergy and Clinical Immunology* **136**, 1573-1580.e2 (2015).
116. Kawana, M., Miyamoto, M., Ohno, Y. & Kihara, A. Comparative profiling and comprehensive quantification of stratum corneum ceramides in humans and mice by LC/MS/MS[S]. *Journal of Lipid Research* **61**, 884–895 (2020).
117. Duplan, H. & Nocera, T. [Skin hydration and hydrating products]. *Ann Dermatol Venereol* **145**, 376–384 (2018).
118. Sütterlin, T., Tsingos, E., Bensaci, J., Stamatas, G. N. & Grabe, N. A 3D self-organizing multicellular epidermis model of barrier formation and hydration with realistic cell morphology based on EPISIM. *Scientific Reports* **7**, 43472 (2017).
119. Lambers, H., Piessens, S., Bloem, A., Pronk, H. & Finkel, P. Natural skin surface pH is on average below 5, which is beneficial for its resident flora. *International Journal of Cosmetic Science* **28**, 359–370 (2006).
120. Schürer, N. pH and Acne. *Curr Probl Dermatol* **54**, 115–122 (2018).

121. Yazdanparast, T. *et al.* Comparison of biophysical, biomechanical and ultrasonographic properties of skin in chronic dermatitis, psoriasis and lichen planus. *Medical Journal of The Islamic Republic of Iran (MJIRI)* **32**, 630–634 (2018).
122. Angelova-Fischer, I., Fischer, T. W., Abels, C. & Zillikens, D. Accelerated barrier recovery and enhancement of the barrier integrity and properties by topical application of a pH 4 vs. a pH 5·8 water-in-oil emulsion in aged skin. *British Journal of Dermatology* **179**, 471–477 (2018).
123. Proksch, E., Brandner, J. M. & Jensen, J.-M. The skin: an indispensable barrier. *Experimental Dermatology* **17**, 1063–1072 (2008).
124. Percoco, G. *et al.* Antimicrobial peptides and pro-inflammatory cytokines are differentially regulated across epidermal layers following bacterial stimuli. *Exp Dermatol* **22**, 800–806 (2013).
125. Zasloff, M. Antimicrobial Peptides of Multicellular Organisms: My Perspective. in *Antimicrobial Peptides: Basics for Clinical Application* (ed. Matsuzaki, K.) 3–6 (Springer, 2019). doi:10.1007/978-981-13-3588-4_1.
126. Fleming, A. & Wright, A. E. On a remarkable bacteriolytic element found in tissues and secretions. *Proceedings of the Royal Society of London. Series B, Containing Papers of a Biological Character* **93**, 306–317 (1922).
127. Ragland, S. A. & Criss, A. K. From bacterial killing to immune modulation: Recent insights into the functions of lysozyme. *PLOS Pathogens* **13**, e1006512 (2017).
128. Wang, X.-P. *et al.* The interleukin-6 cytokine system regulates epidermal permeability barrier homeostasis. *J Invest Dermatol* **123**, 124–131 (2004).
129. Jensen, J. M., Schütze, S., Förl, M., Krönke, M. & Proksch, E. Roles for tumor necrosis factor receptor p55 and sphingomyelinase in repairing the cutaneous permeability barrier. *J Clin Invest* **104**, 1761–1770 (1999).
130. Wood, L. C., Jackson, S. M., Elias, P. M., Grunfeld, C. & Feingold, K. R. Cutaneous barrier perturbation stimulates cytokine production in the epidermis of mice. *J Clin Invest* **90**, 482–487 (1992).
131. Burtenshaw, J. M. L. The Mechanism of Self-Disinfection of the Human Skin and its Appendages. *Epidemiology & Infection* **42**, 184–210 (1942).
132. Drake, D. R., Brogden, K. A., Dawson, D. V. & Wertz, P. W. Thematic review series: skin lipids. Antimicrobial lipids at the skin surface. *J. Lipid Res.* **49**, 4–11 (2008).
133. Nakatsuji, T. *et al.* Sebum Free Fatty Acids Enhance the Innate Immune Defense of Human Sebocytes by Upregulating β-Defensin-2 Expression. *J Invest Dermatol* **130**, 985–994 (2010).
134. Chen, C.-H. *et al.* An innate bactericidal oleic acid effective against skin infection of methicillin-resistant Staphylococcus aureus: a therapy concordant with evolutionary medicine. *J Microbiol Biotechnol* **21**, 391–399 (2011).
135. Desbois, A. P. & Smith, V. J. Antibacterial free fatty acids: activities, mechanisms of action and biotechnological potential. *Appl Microbiol Biotechnol* **85**, 1629–1642 (2010).
136. Cundell, A. M. Microbial Ecology of the Human Skin. *Microb Ecol* **76**, 113–120 (2018).
137. Shu, M. *et al.* Fermentation of Propionibacterium acnes, a Commensal Bacterium in the Human Skin Microbiome, as Skin Probiotics against Methicillin-Resistant Staphylococcus aureus. *PLoS One* **8**, (2013).
138. Byrd, A. L., Belkaid, Y. & Segre, J. A. The human skin microbiome. *Nature Reviews Microbiology* **16**, 143–155 (2018).
139. Flowers, L. & Grice, E. A. The Skin Microbiota: Balancing Risk and Reward. *Cell Host & Microbe* **28**, 190–200 (2020).
140. Schuessler, M., Astecker, N., Herzig, G., Vorisek, G. & Schuster, I. Skin is an autonomous organ in synthesis, two-step activation and degradation of vitamin D(3): CYP27 in epidermis completes the set of essential vitamin D(3)-hydroxylases. *Steroids* **66**, 399–408 (2001).

141. Murakami, M. *et al.* Cathelicidin anti-microbial peptide expression in sweat, an innate defense system for the skin. *J Invest Dermatol* **119**, 1090–1095 (2002).
142. Pappas, A. Epidermal surface lipids. *Dermatoendocrinol* **1**, 72–76 (2009).
143. Picardo, M., Ottaviani, M., Camera, E. & Mastrofrancesco, A. Sebaceous gland lipids. *Dermato-Endocrinology* **1**, 68–71 (2009).
144. Ohsawa, K., Watanabe, T., Matsukawa, R., Yoshimura, Y. & Imaeda, K. The possible role of squalene and its peroxide of the sebum in the occurrence of sunburn and protection from the damage caused by U.V. irradiation. *J Toxicol Sci* **9**, 151–159 (1984).
145. Jourdain, R. *et al.* Exploration of scalp surface lipids reveals squalene peroxide as a potential actor in dandruff condition. *Arch Dermatol Res* (2016) doi:10.1007/s00403-016-1623-1.
146. Fluhr, J. W., Darlenski, R. & Surber, C. Glycerol and the skin: holistic approach to its origin and functions. *Br J Dermatol* **159**, 23–34 (2008).
147. Packer, L., Weber, S. U. & Thiele, J. J. Sebaceous Gland Secretion is a Major Physiologic Route of Vitamin E Delivery to Skin. *Journal of Investigative Dermatology* **113**, 1006–1010 (1999).
148. Knox, S. & O'Boyle, N. M. Skin lipids in health and disease: A review. *Chemistry and Physics of Lipids* **236**, 105055 (2021).
149. Lovászi, M., Szegedi, A., Zouboulis, C. C. & Törőcsik, D. Sebaceous-immunobiology is orchestrated by sebum lipids. *Dermato-Endocrinology* **9**, e1375636 (2017).
150. Bhate, K. & Williams, H. C. Epidemiology of acne vulgaris. *Br J Dermatol* **168**, 474–485 (2013).
151. Heng, A. H. S. & Chew, F. T. Systematic review of the epidemiology of acne vulgaris. *Scientific Reports* **10**, 5754 (2020).
152. Zouboulis, C. C. Endocrinology and immunology of acne: Two sides of the same coin. *Exp Dermatol* (2020) doi:10.1111/exd.14172.
153. Designua. Type of acne pimples (2015). Accessed online the 2021-04-26 from <https://www.shutterstock.com/fr/image-vector/types-acne-pimples-healthy-skin-whiteheads-248595325>
154. Camera, E. *et al.* Use of lipidomics to investigate sebum dysfunction in juvenile acne. *Journal of lipid research* **57**, 1051–1058 (2016).
155. Zhou, M., Gan, Y., He, C., Chen, Z. & Jia, Y. Lipidomics reveals skin surface lipid abnormity in acne in young men. *Br J Dermatol* **179**, 732–740 (2018).
156. Zhou, M. *et al.* Skin surface lipidomics revealed the correlation between lipidomic profile and grade in adolescent acne. *Journal of Cosmetic Dermatology* **19**, 3349–3356 (2020).
157. Simonart, T. Newer Approaches to the Treatment of Acne Vulgaris. *Am J Clin Dermatol* **13**, 357–364 (2012).
158. Jagdeo, J. *et al.* Light-emitting diodes in dermatology: A systematic review of randomized controlled trials. *Lasers Surg Med* (2018) doi:10.1002/lsm.22791.
159. Griffiths, C. E. M., Armstrong, A. W., Gudjonsson, J. E. & Barker, J. N. W. N. Psoriasis. *The Lancet* **397**, 1301–1315 (2021).
160. Takahashi, T. & Yamasaki, K. Psoriasis and Antimicrobial Peptides. *Int J Mol Sci* **21**, (2020).
161. Checa, A. *et al.* Circulating levels of sphingosine-1-phosphate are elevated in severe, but not mild psoriasis and are unresponsive to anti-TNF-α treatment. *Scientific Reports* **5**, 12017 (2015).
162. Mysliwiec, H. *et al.* Abnormal serum fatty acid profile in psoriatic arthritis. *Arch Med Sci* **15**, 1407–1414 (2019).
163. Es, F. *et al.* [Features of distribution of free and esterified cholesterol in the epidermis, biological membranes and plasma lipoproteins in psoriasis]. *Klin Lab Diagn* 38–43 (1996).
164. Khyshiktuev, B. S., Karavaeva, T. M. & Fal'ko, E. V. [Variability of quantitative changes in short-chain fatty acids in serum and epidermis in psoriasis]. *Klin Lab Diagn* 22–24 (2008).

165. Menter, A. *et al.* Joint AAD-NPF guidelines of care for the management and treatment of psoriasis with biologics. *J Am Acad Dermatol* **80**, 1029–1072 (2019).
166. Langan, S. M., Irvine, A. D. & Weidinger, S. Atopic dermatitis. *The Lancet* **396**, 345–360 (2020).
167. Løset, M., Brown, S. J., Saunes, M. & Hveem, K. Genetics of Atopic Dermatitis: From DNA Sequence to Clinical Relevance. *DRM* **235**, 355–364 (2019).
168. Palmer, C. N. A. *et al.* Common loss-of-function variants of the epidermal barrier protein filaggrin are a major predisposing factor for atopic dermatitis. *Nat Genet* **38**, 441–446 (2006).
169. Kim, B. E. *et al.* Side-by-Side Comparison of Skin Biopsies and Skin Tape Stripping Highlights Abnormal Stratum Corneum in Atopic Dermatitis. *J Invest Dermatol* **139**, 2387-2389.e1 (2019).
170. Berdyshev, E. *et al.* Lipid abnormalities in atopic skin are driven by type 2 cytokines. *JCI Insight* **3**,.
171. Janssens, M. *et al.* Increase in short-chain ceramides correlates with an altered lipid organization and decreased barrier function in atopic eczema patients. *Journal of Lipid Research* **53**, 2755–2766 (2012).
172. Danso, M. *et al.* Altered expression of epidermal lipid bio-synthesis enzymes in atopic dermatitis skin is accompanied by changes in stratum corneum lipid composition. *Journal of Dermatological Science* **88**, 57–66 (2017).
173. Arikawa, J. *et al.* Decreased Levels of Sphingosine, a Natural Antimicrobial Agent, may be Associated with Vulnerability of the Stratum Corneum from Patients with Atopic Dermatitis to Colonization by Staphylococcus aureus. *J Invest Dermatol* **119**, 433–439 (2002).
174. Takigawa, H., Nakagawa, H., Kuzukawa, M., Mori, H. & Imokawa, G. Deficient Production of Hexadecenoic Acid in the Skin Is Associated in Part with the Vulnerability of Atopic Dermatitis Patients to Colonization by Staphylococcus aureus. *DRM* **211**, 240–248 (2005).
175. Murata, Y. *et al.* Abnormal expression of sphingomyelin acylase in atopic dermatitis: an etiologic factor for ceramide deficiency? *J Invest Dermatol* **106**, 1242–1249 (1996).
176. Hara, J., Higuchi, K., Okamoto, R., Kawashima, M. & Imokawa, G. High-expression of sphingomyelin deacylase is an important determinant of ceramide deficiency leading to barrier disruption in atopic dermatitis. *J Invest Dermatol* **115**, 406–413 (2000).
177. Honda, T. & Kabashima, K. Prostanoids and leukotrienes in the pathophysiology of atopic dermatitis and psoriasis. *International Immunology* **31**, 589–595 (2019).
178. Skowron, K. *et al.* Human Skin Microbiome: Impact of Intrinsic and Extrinsic Factors on Skin Microbiota. *Microorganisms* **9**, (2021).
179. Ständer, S. Atopic Dermatitis. *N Engl J Med* **384**, 1136–1143 (2021).
180. Czarnowicki, T., He, H., Krueger, J. G. & Guttman-Yassky, E. Atopic dermatitis endotypes and implications for targeted therapeutics. *Journal of Allergy and Clinical Immunology* **143**, 1–11 (2019).
181. Elgash, M., Dlova, N., Ogunleye, T. & Taylor, S. C. Seborrheic Dermatitis in Skin of Color: Clinical Considerations. *J Drugs Dermatol* **18**, 24–27 (2019).
182. Wikramanayake, T. C., Borda, L. J., Miteva, M. & Paus, R. Seborrheic dermatitis-Looking beyond Malassezia. *Exp Dermatol* **28**, 991–1001 (2019).
183. DeAngelis, Y. M. *et al.* Isolation and expression of a Malassezia globosa lipase gene, LIP1. *J Invest Dermatol* **127**, 2138–2146 (2007).
184. Thayikkannu, A. B., Kindo, A. J. & Veeraraghavan, M. Malassezia-Can it be Ignored? *Indian J Dermatol* **60**, 332–339 (2015).
185. Fatou, B. *et al.* Dispositif D'analyse Moleculaire in Vivo En Temps Reel. (2014).
186. Ash, C., Dubec, M., Donne, K. & Bashford, T. Effect of wavelength and beam width on penetration in light-tissue interaction using computational methods. *Lasers Med Sci* **32**, 1909–1918 (2017).

187. Dreisewerd, K. Recent methodological advances in MALDI mass spectrometry. *Anal Bioanal Chem* **406**, 2261–2278 (2014).
188. Fatou, B. *et al.* Remote Atmospheric Pressure Infrared Matrix-Assisted Laser Desorption-Ionization Mass Spectrometry (Remote IR-MALDI MS) of Proteins. *Mol. Cell Proteomics* **17**, 1637–1649 (2018).
189. Ogrinc, N. *et al.* Robot-Assisted SpiderMass for in vivo Real-Time Topography Mass Spectrometry Imaging. *bioRxiv* 2020.12.15.422889 (2020) doi:10.1101/2020.12.15.422889.
190. Creytens, D. What's new in adipocytic neoplasia? *Virchows Arch* **476**, 29–39 (2020).
191. Azzopardi, J. G., Iocco, J. & Salm, R. Pleomorphic lipoma: a tumour simulating liposarcoma. *Histopathology* **7**, 511–523 (1983).
192. Chambers, M. C. *et al.* A cross-platform toolkit for mass spectrometry and proteomics. *Nature Biotechnology* **30**, 918–920 (2012).
193. Sud, M. *et al.* LMSD: LIPID MAPS structure database. *Nucleic Acids Res* **35**, D527-532 (2007).
194. Fahy, E., Sud, M., Cotter, D. & Subramaniam, S. LIPID MAPS online tools for lipid research. *Nucleic Acids Res* **35**, W606-612 (2007).
195. Ruttkies, C., Schymanski, E. L., Wolf, S., Hollender, J. & Neumann, S. MetFrag relaunched: incorporating strategies beyond in silico fragmentation. *Journal of Cheminformatics* **8**, 3 (2016).
196. Jäpelt, R. B., Silvestro, D., Smedsgaard, J., Jensen, P. E. & Jakobsen, J. LC–MS/MS with atmospheric pressure chemical ionisation to study the effect of UV treatment on the formation of vitamin D3 and sterols in plants. *Food Chemistry* **129**, 217–225 (2011).
197. Rigal, A. *et al.* Skin surface lipid composition in women: increased 2,3-oxidosqualene correlates with older age. *European Journal of Dermatology* **30**, 103–110 (2020).
198. Passi, S., De Pità, O., Puddu, P. & Littarru, G. P. Lipophilic antioxidants in human sebum and aging. *Free Radic Res* **36**, 471–477 (2002).
199. Jacobsen, E. *et al.* Age-related changes in sebaceous wax ester secretion rates in men and women. *J Invest Dermatol* **85**, 483–485 (1985).
200. Elsaie, M. L. Hormonal treatment of acne vulgaris: an update. *Clin Cosmet Investig Dermatol* **9**, 241–248 (2016).
201. Oranje, A. P., Glazenburg, E. J., Wolkerstorfer, A. & de Waard-van der Spek, F. B. Practical issues on interpretation of scoring atopic dermatitis: the SCORAD index, objective SCORAD and the three-item severity score. *Br J Dermatol* **157**, 645–648 (2007).
202. Brejchova, K. *et al.* Understanding FAHFAs: From structure to metabolic regulation. *Prog Lipid Res* **79**, 101053 (2020).
203. Son, S.-E., Park, S.-J., Koh, J.-M. & Im, D.-S. Free fatty acid receptor 4 (FFA4) activation ameliorates 2,4-dinitrochlorobenzene-induced atopic dermatitis by increasing regulatory T cells in mice. *Acta Pharmacol Sin* **41**, 1337–1347 (2020).
204. Yokose, U. *et al.* The ceramide [NP]/[NS] ratio in the stratum corneum is a potential marker for skin properties and epidermal differentiation. *BMC Dermatol* **20**, 6 (2020).
205. Pietrzak, A., Michalak-Stoma, A., Chodorowska, G. & Szepietowski, J. C. Lipid Disturbances in Psoriasis: An Update. *Mediators of Inflammation* **2010**, e535612 (2010).
206. Pavicic, T., Wollenweber, U., Farwick, M. & Korting, H. C. Anti-microbial and -inflammatory activity and efficacy of phytosphingosine: an in vitro and in vivo study addressing acne vulgaris. *International Journal of Cosmetic Science* **29**, 181–190 (2007).
207. Mills, K. J., Robinson, M. K., Sherrill, J. D., Schnell, D. J. & Xu, J. Analysis of gene expression profiles of multiple skin diseases identifies a conserved signature of disrupted homeostasis. *Experimental Dermatology* **27**, 1000–1008 (2018).

208. Arnedos, M. *et al.* Precision medicine for metastatic breast cancer—limitations and solutions. *Nat Rev Clin Oncol* **12**, 693–704 (2015).
209. Harkin, C. *et al.* On-tissue chemical derivatization in mass spectrometry imaging. *Mass Spectrom Rev* (2021) doi:10.1002/mas.21680.
210. Wang, X., Hou, Y., Hou, Z., Xiong, W. & Huang, G. Mass Spectrometry Imaging of Brain Cholesterol and Metabolites with Trifluoroacetic Acid-Enhanced Desorption Electrospray Ionization. *Anal Chem* **91**, 2719–2726 (2019).
211. Shrestha, B. & Vertes, A. High-Throughput Cell and Tissue Analysis with Enhanced Molecular Coverage by Laser Ablation Electrospray Ionization Mass Spectrometry Using Ion Mobility Separation. *Anal. Chem.* **86**, 4308–4315 (2014).
212. FAIMS Pro Duo Interface for mass spectrometry - FR. //www.thermofisher.com/fr/fr/home/industrial/mass-spectrometry/liquid-chromatography-mass-spectrometry-lc-ms/lc-ms-accessories/field-asymmetric-ion-mobility-spectrometry-faims.html.
213. Wishart, D. S. *et al.* HMDB 4.0: the human metabolome database for 2018. *Nucleic Acids Res* **46**, D608–D617 (2018).
214. Celis Ramírez, A. M. *et al.* Analysis of Malassezia Lipidome Disclosed Differences Among the Species and Reveals Presence of Unusual Yeast Lipids. *Front. Cell. Infect. Microbiol.* **10**, (2020).
215. Gruber, F., Marchetti-Deschmann, M., Kremslehner, C. & Schosserer, M. The Skin Epilipidome in Stress, Aging, and Inflammation. *Front Endocrinol (Lausanne)* **11**, (2021).

List of publications

List of publications

A. Publications in this thesis

1. Ogrinc N & **Saudemont** P, Balog J, Robin Y-M, Gimeno J-P, Pascal Q, et al. Water-assisted laser desorption/ionization mass spectrometry for minimally invasive *in vivo* and real-time surface analysis using SpiderMass. Nat Protoc [Internet]. 2019 Nov [cited 2020 Jan 30];14(11):3162–82. Available from: http://www.nature.com/articles/s41596-019-0217-8
2. **Saudemont** P & Quanico J, Robin Y-M, Baud A, Balog J, Fatou B, et al. Real-Time Molecular Diagnosis of Tumors Using Water-Assisted Laser Desorption/Ionization Mass Spectrometry Technology. Cancer Cell [Internet]. 2018 Nov;34(5):840-851.e4. Available from: https://doi.org/10.1016%2Fj.ccell.2018.09.009

B. Other publications

3. Ogrinc N, **Saudemont** P, Takats Z, Salzet M, Fournier I. Cancer Surgery 2.0: Guidance by Real-Time Molecular Technologies. Trends in Molecular Medicine [Internet]. 2021 May 5 [cited 2021 May 7]; Available from: https://doi.org/10.1016/j.molmed.2021.04.001
4. Ogrinc N, Kruszewski A, Chaillou P, **Saudemont** P, Lagadec C, Salzet M, et al. Robot-Assisted SpiderMass for *in vivo* Real-Time Topography Mass Spectrometry Imaging. bioRxiv [Internet]. 2020 Dec 16 [cited 2021 Jun 7];2020.12.15.422889. Available from: https://www.biorxiv.org/content/10.1101/2020.12.15.422889v1
5. Seddiki K, **Saudemont** P, Precioso F, Ogrinc N, Wisztorski M, Salzet M, et al. Cumulative learning enables convolutional neural network representations for small mass spectrometry data classification. Nature Communications [Internet]. 2020 Nov 5 [cited 2021 Apr 16];11(1):5595. Available from: https://www.nature.com/articles/s41467-020-19354-z
6. Wisztorski M, **Saudemont** P, Aboulouard S, Cardon T, Narducci F, Robin Y-M, et al. Preneoplastic lesions fimbria pan-proteomic studies establish the fimbriectomy benefit for BRCA1/2 patients and identify early diagnosis markers of HGSC. bioRxiv [Internet]. 2020 Oct 4 [cited 2021 Jun 8];2020.10.04.325100. Available from: https://www.biorxiv.org/content/10.1101/2020.10.04.325100v1
8. Fatou B, **Saudemont** P, Duhamel M, Ziskind M, Focsa C, Salzet M, et al. Real time and *in vivo* pharmaceutical and environmental studies with SpiderMass instrument. J Biotechnol. 2018 Sep 10;281:61–6. Available from: https://doi.org/10.1016/j.jbiotec.2018.06.339
9. Fatou B, Ziskind M, **Saudemont** P, Quanico J, Focsa C, Salzet M, et al. Remote Atmospheric Pressure Infrared Matrix-Assisted Laser Desorption-Ionization Mass Spectrometry (Remote IR-MALDI MS) of Proteins. Mol Cell Proteomics. 2018 Aug;17(8):1637–49. Available from: https://doi.org/10.1074/mcp.TIR117.000582
10. Duhamel M, Fatou B, **Saudemont** P, Wisztorski M, Rhun EL, Maurage CA, et al. Bringing mass spectrometry from pathologist bench to patient bedside. Journal of Biotechnology [Internet]. 2016 Aug;231:S11. Available from: https://doi.org/10.1016%2Fj.jbiotec.2016.05.065
11. Fatou B, **Saudemont** P, Leblanc E, Vinatier D, Mesdag V, Wisztorski M, et al. In vivo Real-Time Mass Spectrometry for Guided Surgery Application. Sci Rep [Internet]. 2016 May [cited 2019 Jul 4];6(1):25919. Available from: http://www.nature.com/articles/srep25919

Acknowledgment

Acknowledgement

First and foremost, I will start by being grateful to the problems that fell upon me during this thesis like the unforeseen instrumental problems leading to a full year without any mass spectra, several study interruption, or the days and days of fibre polishing (Thank you Kleber!) It really helps me not to forget to which extent research consist of solving problems as well as expanding knowledge. I won't thank the COVID-19 for the various impact it had on the world, our personal lives, and the 6 months delay it induced in the SMPatho volunteer's recruitments. Finally, I won't thank the ransomware cyber-attack conducted from REvil toward PFDC that lead to 2 months of complete jeopardy at least on the data and tool access, not completely solved to this day, which was great at a time of writing a PhD Thesis.

Michel and Isabelle I am grateful for the trust you put in me when you let me work on the SpiderMass so long time ago now (and I guess I succeeded to keep it with the journey we are going in!) Particularly, thank you Isabelle for helping me develop my scientific skills and for all the discussions we can have, you revealed the most talkative part in me!

Gwendal, the first time I saw you in PRISM lab I remember talking with you in the meeting room and then realising after that it was in fact a job interview! Thank you for letting me discover the several aspects linked to the work in a big group work environment. Your enthusiasm is always a source of motivation to go beyond, and even if it often lead us say, "*Toujours plus !*", at the end we succeeded.

Églantine, meeting you has been the greatest part of my transition from school to work. During my two years working with you I learned a lot and I will never forget that you were always there to discuss when it was not easy. I wouldn't be writing this thesis if you were not there at that time.

Antonella, you are the one I know since the longest time in the lab, and I am glad we met. We spend so much good times that I wouldn't have enough space here to write everything down (and as we are two Dolly, I am not sure to be able to remember everything anyway…). I remember the good ol'days we spend with Tanina, but also the difficulties we faced together.

The pirates, Melanie, Lauranne and Flore, thank you for all the good moment we shared, I guess it was quite a good thing for everyone that we were not physically present in the same room for those 3 years !!

In the end, I am one of the ancients of the SpiderMass project, and I would like to thank all the people I worked with during these years, Benoit, Jusal, Anna, Nina, Lucas and Léa. I am glad we worked together.

Benoit, the lab is quieter since you left and it's a shame. You knew how to make everyone laugh and discussing with you was always a pleasure. Even when I rediscovered my CJSM presentation in front of everyone, after we completely modified it late in the night after a few drinks! Nina, we are working together since quite a long time now, even if it has been from abroad at the beginning, I like the discussions we can have because we think alike on a lot of aspects! And we always find a small song to complain with.

"It's a never ending stooooooryyyyyyyyy"

I would like to thank the people with whom I share the same office: Alice, Diego, Sylvain and Kamel, that I started to know more recently. It always a pleasure to talk or go outside the lab to enjoy the sun before we are able to go outside for drinks!

I am grateful to all the other people in the lab: Marie, Julien, Maxence, Louise, Frank, Christophe, JP, Christelle, Jacopo, PE, Etienne and Estelle. Every one of you deserve the best and it has always been a pleasure to talk to you all. Specifically, I have a thought for Annie, often described as the mom of the lab, I can confirm I got this feeling as well when we worked together. I miss you!

Irène, je ne sais pas ce que je te trouve non plus 😉 mais on rigole toujours bien ensemble, toujours prêt à tailler le bout de gras, surtout si ça parle de pipette! Special thanks to Tristan always ready to grab a beer and some cheese, I miss those times! And a thought for you Soulaimane, we haven't the opportunity to work a lot with you but you know what I think about you and all you projects!

This period would have been the same without the amazing people a had the opportunity to meet in Toulouse. I remember my first week in Pierre Fabre, and after 3 days I already had the feeling to know some of you since a long time. Specifically, Célia and Aurélie, AKA "The Raman sisters", you are work machines and you lifted me up. You are examples to me, and it saddens me not to be able to hear you every morning. Amaury, I mean, you know... We are alike and you are about to be my bestman, do I need (and do we want?) to say more here?! Pieces of me stayed in Toulouse because of you 3, and it is still hurting.

Special thought to the other member of the 2BTN team: Christophe, Jimmy, Jérôme, Éric, Sylvie Laurence and Clara. It has always been a pleasure to discuss, take time, and go out for drinks and restaurants with you. Special thanks to Éléonore, we spent a lot of time discussing about the MS signal processing, and I think we both learned a lot! I will always be grateful for the time you gave me and the rigor you taught me about statistics!

The 2BTN team spirit is strong thanks to common interests we share all about good food, good drinks and Salzuflen speaking! The watchword we came up with sums it up quite well… *"Bibendo Doctus Fies".*

" - ZIZI !!!! - COIN COIN !!!"

I wish to thank most of the people I worked with in the Pierre Fabre skin research centre in the magnificent Hotel-Dieu building. Special thought to Alexia, it is always a pleasure to work and discuss with you. Without you, the SMpatho study wouldn't exist and you did a crazy job there! Also, thank you Thérèse for your availability and everything you taught me about dermatology. The SMpatho study has been a journey, and we have (almost) gone through it even if it has not always been easy!

The work presented here wouldn't have been possible without the common effort of a lot of persons, and I feel extremely blessed while writing this thesis to be its spearhead. As the proverb says:

"If you want to go fast, go alone. If you want to go far, go together"

This leads me to thank the people with whom I had the opportunity to work in Oncovet: Dominique, Emmanuel, Mélanie. These time in the clinic have gone so fast, I would have liked to do so much more, but for sure, it is only a matter of time! Special thoughts as well to Delphine and Yves-Marie from the COL, working with you remembered my times working in the pathology lab and how much I liked it.

On my journey since I finished my MD, I did the crazy choice to accept being part of the Ourcon V organisation committee. It was a real challenge for me, and I wasn't at my best at that time, so it has been complicated to keep up with you guys. But I think at the end we did well, and I am grateful now as it led me far out of my comfort zone (but isn't it there you grow up the most?) I spent great time with all of you: Florian, Brenda, Lieke, Alina, Irena, Keely and Pieter! I will never forget drinking and partying with somities of the MSI community

Writing and thinking in English stop here for me as I will finish these "Remerciements" in French! Je me souviens avoir sérieusement hésité à accepter ce doctorat, je doutais de pouvoir quitter la ville dans laquelle j'avais toujours vécu, l'environnement connu du laboratoire et mon domaine d'étude pour aller seul à l'autre bout de la France, pour travailler sur quelque chose de totalement nouveau. Cela me permet de me remercier, merci Philippe pour ton manque de confiance en toi et pour tous les doutes qui t'habitent. Ta capacité à TOUT oublier, et le perfectionnisme qui te pousse à l'immobilisme mais surtout, il faut que je remercie ton envie constante de vouloir te dépasser et aller plus loin. L'écriture de cette thèse a regroupé un bon nombre de qui est le plus compliqué pour moi dans mon travail, ce qui me rend extrêmement heureux d'y être arrivé.

D'un point de vu un peu plus personnel, je voulais remercier les différentes familles que j'ai pu me constituer au cours du temps et qui m'ont aidé à arriver jusqu'ici. Merci aux Gang of peaches pour tout ce que l'on a échangé depuis le lycée, cela représente beaucoup pour moi de pouvoir vous compter parmi mes amis.

Dédicace spéciale à Sonia qui m'a aidé à passer cette période de rédaction en venant se confiner dans notre abri de jardin ! Merci pour les massages et pour ces session #InstaFood.

Merci à Denise et René pour leur accueil quand je suis parti à Toulouse, j'ai adoré pouvoir discuter avec vous, partager vos souvenirs et aller à la fête de l'ail ensemble. Vous avez été comme des grands parents pour moi pendant mon passage à Toulouse, et je pense souvent à vous.

Merci à Didier et Patricia, même si ce n'était pas prévu comme ça, le temps que j'ai passé avec vous a été super, merci encore pour votre accueil ! Fabien et Dorothée, je suis content d'avoir eu enfin l'occasion de vous voir plus longtemps que sur un WE dans le nord. Nos soirée jeux me manques ! Merci également au reste de la famille avec qui j'ai pu partager notamment mon amour pour le fromage !

Merci à toi Thibaut. Tu as toujours été là pour me supporter dans les moments difficiles, me pousser à ne pas abandonner et aller plus loin. Cela n'a pas toujours été évident et tu as tenu face à mon mauvais caractère ! Merci à mes beaux-parents préférés, Sylvie et Dominique, vous être des personnes au cœur pure et cela me ressource à chaque fois que l'on peut se voir !

Et pour finir merci à ma marraine et mon parrain, vous avez toujours été là pour moi, et je regrette de ne pas pouvoir passer plus de temps en votre compagnie ! Bientôt le permis 😉

Maman, tu le dis toi-même, dès le plus jeune âge je ne voulais pas devenir policier ou astronaute comme les autres enfants, je voulais « découvrir de nouveau virus et de nouveaux vaccins ». Je me souviens que pendant toute mon enfance, dès que je prenais le métro je rêvais d'aller jusqu'à la « cité des scientifique » (l'arrêt de métro du campus de l'université de Lille). Quand on y passait par l'autoroute pour aller chez Mémé, cet endroit me semblai directement vivre dans un futur utopique. Finalement, m'y voilà 20 ans après et c'est grâce à toi. Tu m'as aidé à devenir qui je suis aujourd'hui et sans toi, cela n'aurait pas été possible !

Je souhaite terminer cette thèse avec une pensée pour ma grand-mère, je sais qu'elle aurait été emplie de fierté de voir où j'en suis aujourd'hui. Peu de jours passent sans que je n'aie une pensée pour toi.

Summary

Our skin is the interface between our body and our environment, a supple barrier with sensory, regulatory, protective, and immune functions. Originally considered inert, it is seen as a dynamic and complex landscape where many interactions take place. Acne, atopic dermatitis, psoriasis, and seborrheic dermatitis are chronic inflammatory conditions that affect the skin. The factors for their development involve the skin flora, the immune system, and a disturbance in the skin physiology itself. One of the key players are lipids, which have barrier, protective and immune functions. Lipidomic, which is part of the field of metabolomic, is the study of these lipids. Unlike genes, metabolites are characterised by their dynamism and so observing their evolution as close to the skin as possible is very important to understand their subtle changes. Mass spectrometry is one of the most widely used technologies for metabolomic analysis and has many advantages in terms of sensitivity, versatility, and reproducibility. However, conventional vacuum or atmospheric pressure approaches requires technicality and time as the collected sample must be prepared before analysis. The use of conventional mass spectrometry can therefore be time consuming and the ethical justification of biopsies in clinical studies is sometimes raised. Finally, conventional mass spectrometry is not suitable for *in vivo* and real-time applications. The Lille PRISM laboratory presented in 2016 a new technology called SpiderMass™, to improve the analytical performance for *in vivo* and non-invasive mass spectrometry analysis under real-time conditions. The aim of this thesis project is to adapt a SpiderMass™ for dermo-cosmetic use in clinical studies of chronic inflammatory dermatoses. After describing the research and development that led me to this project, this manuscript describes the achievements related to the main objectives of the thesis. They first consisted in developing a SpiderMass™ prototype adapted to dermo-cosmetics, evaluating, and validating it in clinical studies at the Pierre Fabre Dermo-Cosmetics skin research centre. This prototype was then used in the context of the study of skin ageing and in a large-scale study submitted on 220 volunteers for the study of chronic inflammatory dermatoses. The results show the great capacity of the system to be used to study the physiopathology of the skin and to find biomarkers of interest for the evaluation of the effectiveness of products in development in various situations such as ageing and chronic inflammation.

Résumé

Notre peau est l'interface entre notre corps et notre environnement, une barrière souple dotée de fonctions sensorielles, régulatrices, protectrices et immunitaires. Considérée à l'origine comme inerte, elle est aujourd'hui considérée comme un paysage dynamique et complexe où se déroulent de nombreuses interactions. L'acné, la dermatite atopique, le psoriasis et la dermatite séborrhéique sont des affections inflammatoires chroniques qui touchent la peau. Les facteurs de leur développement impliquent la flore cutanée, le système immunitaire et une perturbation de la physiologie de la peau elle-même. Les lipides, qui ont des fonctions de barrière, de protection et d'immunité, sont l'un des acteurs clés. La lipidomique, qui fait partie du domaine de la métabolomique, est l'étude de ces lipides. Contrairement aux gènes, les métabolites sont caractérisés par leur dynamisme et il est donc très important d'observer leur évolution au plus près de la peau pour comprendre leurs changements subtils. La spectrométrie de masse est l'une des technologies les plus utilisées pour l'analyse métabolomique et présente de nombreux avantages en termes de sensibilité, de polyvalence et de reproductibilité. Cependant, les approches conventionnelles sous vide ou à pression atmosphérique requièrent de la technicité et du temps car l'échantillon collecté doit être préparé avant l'analyse. L'utilisation de la spectrométrie de masse conventionnelle peut donc prendre du temps et la justification éthique des biopsies dans les études cliniques est parfois soulevée. Enfin, la spectrométrie de masse conventionnelle n'est pas adaptée aux applications in vivo et en temps réel. Le laboratoire PRISM de Lille a présenté en 2016 une nouvelle technologie appelée SpiderMass™, afin d'améliorer les performances analytiques pour des analyses de spectrométrie de masse in vivo et non invasives dans des conditions de temps réel. L'objectif de ce projet de thèse est d'adapter un SpiderMass™ pour une utilisation dermo-cosmétique dans le cadre d'études cliniques sur les dermatoses inflammatoires chroniques. Après avoir décrit les recherches et développements qui m'ont conduit à ce projet, ce manuscrit décrit les réalisations liées aux objectifs principaux de la thèse. Elles ont d'abord consisté à développer un prototype de SpiderMass™ adapté à la dermo-cosmétique, à l'évaluer, et à le valider dans des études cliniques au sein du centre de recherche cutanée Pierre Fabre Dermo-Cosmétique. Ce prototype a ensuite été utilisé dans le cadre de l'étude du vieillissement cutané et dans une étude à grande échelle soumise sur 220 volontaires pour l'étude des dermatoses inflammatoires chroniques. Les résultats montrent la grande capacité du système à être utilisé pour étudier la physiopathologie de la peau et à trouver des biomarqueurs d'intérêt pour l'évaluation de l'efficacité de produits en développement dans diverses situations telles que le vieillissement et l'inflammation chronique.